TECHNISCHE UNIVERSITÄT MÜNCHEN

Fakultät für Medizin

Defining the roles of Kindlin-2 and PAT2 in adipose tissue plasticity and amino acid sensing, respectively

Jiefu Wang

Vollständiger Abdruck der von der Fakultät für Medizin der Technischen Universität München zur Erlangung des akademischen Grades eines Doktors der Naturwissenschaften genehmigten Dissertation.

Vorsitzender: Prof. Dr. Percy A. Knolle

Prüfer der Dissertation: 1. TUM Junior Fellow Dr. Siegfried Ussar

2. Prof. Martin Klingenspor

Die Dissertation wurde am 24.09.2019 bei der Technischen Universität München eingereicht und durch die Fakultät für Medizin am 10.03.2020 angenommen.

Eidesstattliche Erklärung

Ich erkläre an Eides statt, dass ich die bei der Fakultät für Medizin zur Promotionsprüfung vorgelegte Arbeit mit dem Titel:

“Defining the roles of Kindlin-2 and PAT2 in adipose tissue plasticity and amino acid sensing, respectively”

am Institut für Diabetes und Adipositas (Helmholtz Zentrum München) unter der Anleitung und Betreuung durch Dr. Ussar ohne sonstige Hilfsmittel erstellt und bei der Abfassung nur die gemäß § 6 Abs. 6 und 7 Satz 2 angegebenen Hilfsmittel benutzt habe.

Ich habe keine Organisation eingeschaltet, die gegen Entgelt Betreuerinnen und Betreuer für die Anfertigung von Dissertationen sucht, oder die mir obliegenden Pflichten hinsichtlich der Prüfungsleistungen für mich ganz oder teilweise erledigt.

Ich habe die Dissertation in dieser oder ähnlicher Form in keinem anderen Prüfungsverfahren als Prüfungsleistung vorgelegt.

Die vollständige Dissertation wurde noch nicht veröffentlicht.

Ich habe den angestrebten Doktorgrad noch nicht erworben und bin nicht in einem früheren Promotionsverfahren für den angestrebten Doktorgrad endgültig gescheitert.

Die öffentlich zugängliche Promotionsordnung der TUM ist mir bekannt, insbesondere habe ich die Bedeutung von § 28 (Nichtigkeit der Promotion) und § 29 (Entzug des Doktorgrades) zur Kenntnis genommen. Ich bin mir der Konsequenzen einer falschen Eidesstattlichen Erklärung bewusst.

Mit der Aufnahme meiner personenbezogenen Daten in die Alumni-Datei bei der TUM bin ich einverstanden.

München, den Jiefu Wang

I. Abbreviations

WAT	White adipose tissue
BAT	Brown adipose tissue
UCP-1	Uncoupling protein 1
ATP	Adenosine triphosphate
PPARγ	Peroxisome proliferator-activated receptor γ
C/EBPs	CCAAT/enhancer-binding proteins
HFD	High fat diet
CD	Chow diet
SCF	Subcutaneous fat
PGF	Perigonadal fat
mRNA	Message ribonucleic acid
ECM	Extracellular matrix
cDNA	Complementary deoxyribonucleic acid
ANOVA	Analysis of variance
H&E	Hematoxylin and eosin
GTT	Glucose tolerance testing
ITT	Insulin tolerance test
SLC	Solute carrier
WB	Western blot
PAT	Proton coupled amino acid transporter
mTORC1	mammalian target of rapamycin complex 1 or mechanistic target of rapamycin complex 1
S6K	phosphorylation of S6 Kinase
LC3	microtubule-associated protein light chain 3
Co-IP	Co-immunoprecipitation
DMEM	Dulbecco's Modified Eagle Medium
V-ATPase	Vacuolar adenylpyrophosphatase
BN-PAGE	Blue native polyacrylamide gel electrophoresis
EM	Electron microscope
qPCR	Quantitative polymerase chain reaction
EGFP	Enhanced green fluorescent protein
FITC	Fluorescein isothiocyanate
LAMP	Lysosomal-associated membrane protein
MS	Mass spectrometry

II. Abstract

In modern society, obesity has become a severe worldwide health problem and related diseases like metabolic syndrome and type 2 diabetes are intractable challenges for public health. Adipose tissues are one of the most important metabolic organs and the main energy storage tissues. In my dissertation I studied the functions of two important proteins; Kindlin-2 and PAT2 in adipose tissues.

Kindlin-2 is a broadly expressed protein, with essential functions in many tissues and during embryonic development. Kindlin-2, as an integrin activator, plays a crucial role in ECM signal transduction, but its function in adipose tissue is less known. In my study, Kindlin-2 knockout in adipose tissue causes lipodystrophy. Furthermore, angiogenesis in adipose tissue and whole body glucose homeostasis are also affected by Kindlin2 knockout. Moreover, unlike in other tissues, loss of Kindlin-2 in fat, reduces protein levels of some integrin subunits.

PAT2 is a proton coupled amino acid transporter and was identified as a surface marker for brown adipocytes. However, its function in adipocytes is unknown. Several functions of PAT2 are revealed in my study. PAT2 regulates amino acid depletion induced autophagy. PAT2 knockdown or overexpression both lead to impaired autophagy. This function is through modulating acidification of the V-ATPase in brown adipocytes. I show that PAT2 is necessary for V-ATPase assembly in brown adipocytes and enhances V-ATPase activity upon amino acid starvation. Loss of PAT2 causes impaired V-ATPase assembly and the proton pumping activity.

In addition I show that the translocation of PAT2 from the cell surface to the lysosome is triggered by amino acid depletion or the inhibition of mTORC1. PAT2 also regulates mitochondrial function and cellular amino acid sensitivity in the brown adipocyte.

My study demonstrates the importance of Kindlin-2 in adipose tissues and the crucial role of PAT2 in brown adipocyte to nutrient homeostasis and development. These two proteins can be the targets for the therapy of obesity related diseases. Research of Kindlin-2

and PAT2 function are helpful to understand the physiological functions of adipose tissues in more detail.

III. Zusammenfassung

In der heutigen Gesellschaft sind Adipositas, sowie die damit assoziierten Erkrankungen, wie das metabolische Syndrom und Typ 2 Diabetes zu einem globalen Problem und einer Herausforderung für die öffentliche Gesundheit geworden. Fettgewebe sind eine der wichtigsten metabolische Gewebe und der Hauptspeicherort für überschüssige Energie. In meiner Arbeit habe ich mich mit der Funktion von zwei wichtigen Proteinen, Kindlin-2 und PAT2, im Fettgewebe beschäftigt.

Kindlin-2, welches ein breites Expressionsmuster zeigt, hat essentielle Funktionen in einer Vielzahl von Organen und während der Embryonalentwicklung.

Kindlin-2, als ein zentrales Element der Integrinaktivierung, spielt eine zentrale Rolle in der Signaltransduktion der Extrazellulären Matrix. Die Funktion von Kindlin-2 im Fettgewebe ist bislang jedoch nur lückenhaft untersucht worden. In meinen Studien konnte ich zeigen, dass der Knockout von Kindlin-2 im Fettgewebe zu einer Lipodystrophie führt. Des Weiteren führt der Verlust von Kindlin-2 im Fettgewebe zu Störungen der Vaskularisierung und der Glukosehomöostase. Außerdem führt der Verlust von Kindlin-2 im Fettgewebe, im Gegensatz zu anderen bereits untersuchten Organen, zu einer Reduktion der Proteinlevels einiger Integrinuntereinheiten.

PAT2 ist ein Protonen gekoppelter Aminosäuretransporter, welcher in vorhergehenden Studien als spezifischer Oberflächenmarker für braune Adipozyten identifiziert wurde. Bislang ist jedoch sehr wenig über die Funktion von PAT2 im braunen Fettgewebe bekannt. In meinen Studien konnte ich mehrere Funktionen und Regulationen von PAT2 aufzeigen. PAT2 reguliert die durch Aminosäuredepletion induzierte Autophagie. Dadurch kommt es sowohl bei der Überexpression als auch der Depletion von PAT2 zu einer Störung der Autophagie. Mechanistisch beruht dies auf einer Regulation der vATPase abhängigen Azidifizierung in braunen Adipozyten. Ich zeige, dass PAT2 eine wichtige Rolle in der Assemblierung der vATPase und der Aktivierung der vATPase während eines Amionsäuremangels spielt. Des Weiteren zeige ich, dass die Translokation von PAT2 von

der Zelloberfläche zum Lysosom durch Aiminosäuredepletion oder die Inhibition von mTORC1 ausgelöst wird. PAT2 reguliert auch mitochondriale Funktion und zelluläre Amionsäuresensitivität in braunen Adipozyten.

Meine Studien zeigen die Bedeutung von Kindlin-2 im Fettgewebe und die Rolle von PAT2 in braunen Adipozyten in Bezug auf Nährstoffhomäostase und Entwicklung. Diese zwei Proteine stellen zwei potentielle Angriffspunkte für die Therapie von Adipositas bezogenen Erkrankungen dar. Forschung an Kindlin-2 und PAT2 hilft die physiologische Funktion des Fettgewebes besser zu verstehen.

IV. List of tables

V. List of figures

VI. Table of contents

1 Introduction

1.1 Adipose tissue development and function

1.1.1 Adipose tissue and its function

Adipose tissue is a complex organ which has essential effects on physiology and pathophysiology. Adipose tissue has been regarded as a loose connective tissue, which is composed of adipocytes mostly (Birbrair et al 2013). Besides, adipose tissue also contains some other kinds of cells, these cells are referred to as stromal vascular fraction (SCF), which comprises a mix of cells, such as preadipocytes, mesenchymal stem cells (MSC), vascular endothelial cells and its progenitor cells. Additional, some immune cells like T cells, B cells, mast cells and adipose tissue macrophages are also included. Preadipocytes in SCF will differentiate into adipocyte upon some particular conditions.

In most mammals, two major adipose tissue types can be distinguished, WAT and BAT (Saely et al 2012). The adipocytes which compose WAT are called white adipocytes, accordingly, BAT is comprised of brown adipocytes. White adipocytes contain a single lipid droplet, which consists of triglycerides and occupies more than 90% of the cell volume. So the size of white adipocyte is variable because it depends on the size of the lipid droplet. In contrast, brown adipocyte store triglycerides in multiple small vacuoles. Furthermore, white adipocytes have thin, elongated mitochondria, whereas brown adipocytes contain large, spherical, laminar cristae packed and usually numerous mitochondria. Also, much more capillary and nerve supply can be found in BAT than WAT (Cinti 2009). The denser mitochondria and stronger vascularization result in the characteristic brown color of BAT (Saely et al 2012).

Adipocytes form discrete adipose depots during development. These depots are divided into subcutaneous and visceral depots. For rodents, subcutaneous depots include anterior and posterior depots, visceral depots include even more types, such as mediastinal, omental, mesenteric, perirenal, retroperitoneal, perigonadal and perivesical depots. Some fat depots are connected closely with skeletal muscle, some are in bone marrow, parathyroid

gland, parotid gland, pancreas, lymph nodes and some other organs (Cinti 2009). These depots are intrinsically different on physiological functions (Rosen & Spiegelman 2014). Almost all of these depots are comprised of both white adipocytes and beige (brown like) adipocytes. The relative proportion is depended on several factors, such as age, sex, environment temperature, nutritional status, strain and species (Cinti 2005). According to quantitative anatomical data of adult Sv129 female mice (Murano et al 2009, Murano et al 2008), white adipocytes are more numerous in posterior subcutaneous, mesenteric and retroperitoneal depots, brown adipocytes are most abundant in anterior subcutaneous, mediastinal and abdominopelvic depots. The discrete depots of BAT were reported in mice and infant including interscapular, axillary, and perirenal BAT depots. In adult humans, BAT depots were reported to reside in different locations including cervical, supraclaviscular, axillary, paravertebral, and abdominal subcutaneous regions (Ikeda et al 2018).

In the past for a long time, functions of adipose tissue were thought to include conserving excessive energy in the form of lipid, cushion and thermal insulation (Kershaw & Flier 2004, Rosen & Spiegelman 2014). In recent studies, adipose tissues are more and more regarded as endocrine organs, secreting many kinds of hormones, such as leptin, tumor necrosis factor α (TNFα), interleukin-6 (IL-6), macrophages and monocyte chemoattractant protein-1 (MCP-1), plasminogen activator inhibitor-1 (PAI-1), adiponectin, adipsin and acylation stimulating protein (ASP), resistin and proteins of renin angiotensin system (RAS) and several kinds of enzymes for steroid metabolism. Besides, numerous receptors are expressed in adipose tissue including insulin receptor, glucocorticoid receptor, leptin receptor, several catecholamine receptors, etc. These receptors let adipocytes to respond to different signals from many other organs (Kershaw & Flier 2004). Most of the hormones and receptors in adipose tissue are regulating or are regulated by the nutritional status of the organism. For example, energy homeostasis and reproduction can be affected by adipose tissue (Rosen & Spiegelman 2014). Actually, adipose tissue is integrally involved regulating neuroendocrine and immune system funciton (Kershaw & Flier 2004).

In addition, BAT is well known for its function in thermoregulation. Besides shivering thermogenesis, thermal energy produced by BAT is an important thermal source. The signals triggering BAT thermogenesis are mainly cold exposure and adaptive/facultative diet induction (Cannon & Nedergaard 2011, Himms-Hagen 1989). It is well-accepted that BAT thermogenic activity depends on UCP-1 function (Schulz & Tseng 2013), which has been regarded as a BAT marker (Mattson 2010). UCP-1 can uncouple oxidative ATP production by making a short-circle for proton from intermembrane space to matrix in mitochondria, which dissipates the energy stored as proton gradient by the electron transportation chain as heat (Cannon & Nedergaard 2004, Gesta et al 2007).

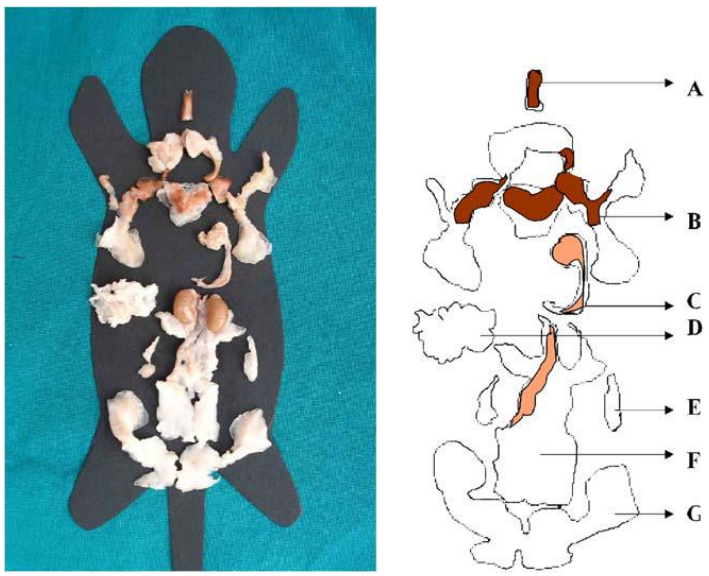

Figure 1.1 Fat depots in the mouse. Tissues are dissected from Sv129 adult mouse maintained at 29 °C for 10 days. A: deep cervical. B: anterior subcutaneous (interscapular, subscapular, axillo-toracic, superficial cervical). C: visceral mediastinic. D: visceral mesenteric. E: visceral retroperitoneal. F: visceral perirenal, periovaric, parametrial and perivescical. G: posterior subcutaneous (dorso-lumbar, inguinal and gluteal). The areas of WAT or BAT are shown in white or brown color. (Cinti 2005)

1.1.2 The development of adipose tissue

Most of the adipose tissues derive from mesoderm (Enerback 2009), albeit adipocytes of non-mesoderm origin have also been reported (Monteiro et al 2009). BAT appears in midgestation during the fetal development, which is earlier than WAT (Saely et al 2012). Previous publications indicate that the origins of WAT vary in different depots (Billon &

Dani 2012, Chau et al 2014, Sanchez-Gurmaches & Guertin 2014). Different depots emerge in different stages of development (Han et al 2011, Jiang et al 2014), subcutaneous depots develop prior to visceral depots (Tchkonia et al 2002, Wang et al 2013b). The prominent interscapular BAT derives from a tripotent engrailed 1 (EN1) positive cell lineage of dermomytome, which can also develop into dermis and skeletal muscle (Atit et al 2006). Another difference between BAT and WAT is that the ratio of tissue size to body weight declines after birth for BAT, but WAT depots increase gradually together with age (Cinti 2009).

Although WAT and BAT derive from different precursors, the subsequent adipogenesis of them shares the same main adipogenic transcriptional cascade including PPARγ and C/EBPs (Giralt & Villarroya 2013). PPARγ is indispensable for all kinds of adipogenesis (Barak et al 1999, Rosen et al 1999). PPARγ and C/EBPs coordinately promote and maintain the adipose characteristics (such as specific lipid and glucose metabolism and insulin sensitivity) by regulating the expression of adipogenic genes (Giralt & Villarroya 2013). Beside the same signal cascade, white and brown adipocytes have their own specific transcriptional mechanism to guarantee their characteristics. Two main proteins are reported as the key factors for the cell fate decision between white adipocytes and brown adipocyte, Zn-finger tranScriptional regulator PRD1-BF1-RIZ1 homologous domain containing 16 (PRDM16) (Seale et al 2007) and peroxisome proliferator-activated receptor γ-coactivator-1α (PGC-1α) (Puigserver et al 1998, Uldry et al 2006). Compared to PGC-1α, PRDM16 specifically promotes brown adipocyte development (Seale et al 2008, Seale et al 2007). The mechanism is found to be that PRDM16 binds to C/EBPβ, PPARγ, PPARα and PGC-1α and promotes the expression of brown adipocyte related genes (Hondares et al 2011, Kajimura et al 2009, Seale et al 2007). PGC-1α is shown to coactivate PPARγ and PPARα to maintain mitochondrial biogenesis, oxidative metabolism and thermogenesis (Barbera et al 2001, Puigserver et al 1998).

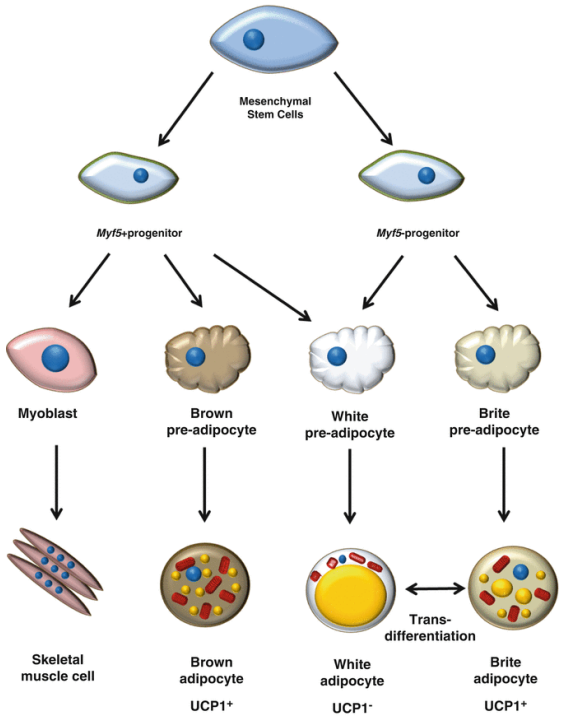

Figure 1.2 Differentiation of stem cell into white, brown, beige adipocytes or myocyte. Base on Myf5 carried on cells, mesenchymal stem cells can differentiate into Myf5 positive and negative cells. Most white adipocytes derive from Myf5 negative precursors but some Myf5 positive precursors can also be induced into white adipocytes. Myf5 positive cells normally give rise to brown adipocytes and myocytes. Brown adipocyte-like beige/brite adipocytes appear during the browning via induction to Myf5 negative progenitors of white adipocytes or white adipocytes transdifferentiation. (Jiménez G 2016)

Many similarities were shown between brown adipocytes and myocytes, such as lipid catabolism, innervation by the sympathetic nervous system, abundant mitochondrial content, facilitation for adaptive thermogenesis (Farmer 2008). Another important point to brown adipocytes and skeletal muscle is that myogenic factor 5 (Myf5) is expressed in both cells (Timmons et al 2007). It is noteworthy that this does not mean that no Myf5 positive progenitor can give rise to white adipocytes, actually, it has been reported that some subsets of white adipocytes derive from Myf5 positive cells (Sanchez-Gurmaches et al 2012). Besides these similarities, myocytes and brown adipocytes were clearly reported to have the same developmental origin (Atit et al 2006). Furthermore, the mechanism of the cell fate decision between myoblast and preadipocytes have also been revealed. Seale and colleagues (Seale et al 2008, Seale et al 2007) showed that PRDM16 bidirectionally regulates the decision between adipogenesis or myogenesis. Brown adipocyte precursors

without PRDM16 loose brown adipocyte characteristics and start to differentiate into myocytes. Similarly, ectopic expression of PRDM16 induces myoblasts transdifferentiation into brown adipocytes. The mechanism was reported as PRDM16 binds to and activates PPARγ (Seale et al 2008). Besides, bone morphogenetic protein 7 (BMP7) was also reported to promote brown adipocyte differentiation by inducing PRDM16 and UCP-1 expression (Tseng et al 2008).

The appearance of brown adipocytes (so called beige adipocytes) in WAT is called WAT browning. WAT browning is always upon several specific stimulations, such as cold exposure (Young et al 1984), chronic treatment of β3 adrenergic receptor activator (Cousin et al 1992) and PPARγ agonists (Ohno et al 2012). One theory for browning of WAT is that the white adipocyte deriving from Myf5 negative stem cell (such as mesenchymal stem cell) can also differentiate into brown adipocytes upon these stimulations (Schulz & Tseng 2013). The new brown adipocytes generated in WAT is called beige or brite adipocytes to distinguish them from constitutive brown adipocytes in typical BAT depots (Ishibashi & Seale 2010, Petrovic et al 2010, Wu et al 2012). Several similar proteins which regulate cell fate decision between brown and white adipocytes are also reported for regulating WAT browning, including bone morphogenic protein family (Tseng et al 2008), C/EBPβ, PRDM16 (Kajimura et al 2009) and PGC-1α (Giralt & Villarroya 2013). Another opinion believes that WAT browning is via transdifferentiation of white adipocytes into beige adipocytes (Barbatelli et al 2010). It has been reported that some brown/beige adipocyte-like cells show intermediate characteristics and morphology between white and brown/beige adipocytes (Barbatelli et al 1993, Himms-Hagen et al 2000). Some data using genetic labeling also support the possibility of bidirectional transdifferentiation between beige and white adipocytes (Rosenwald et al 2013). Some reports illustrated that both these two browning ways exist *in vivo* but in different depots. β3 adrenergic receptor activation induced WAT browning is reported via transdifferentiation in inguinal WAT but through regulation of proliferation and adipogenesis of progenitors in epididymal WAT (Lee et al 2012).

1.2 Kindlin-2 is a broadly expressed integrin activator

1.2.1 Extracellular matrix and integrin

ECM is a non-cellular component which exists in almost every kind of tissues. It provides an extracellular physical framework for the cellular component. The ECM also transduces essential signals into the cells to regulate important biological functions like tissue morphogenesis, differentiation and homeostasis. With a specific composition and topological structure, ECM in different tissues or organs is different, which is formed during development through crosstalk between various cellular components (Frantz et al 2010). ECM is also dynamic, whose structure and properties can be modulated upon different conditions by ECM remodeling via multiple ways (Theocharis et al 2016).

The composition of ECM includes two main classes, proteoglycans and hyaluronan, fibrous proteins (Heldin & Pertoft 1993, Jarvelainen et al 2009, Laurent & Fraser 1992, Schaefer & Schaefer 2010).

Proteoglycans consist of many kinds of macromolecules. Based on their localization, sequence homology and unique protein modules, proteoglycans can be divided into four kinds, intracellular, cell surface, pericellular-basement membrane and extracellular proteoglycans (Iozzo & Schaefer 2015).

Hyaluronan is a linear glycosaminoglycan with a repeating disaccharide unit of D-glucuronic acid and N-acetyl-D-glucosamine (Theocharis et al 2016). Hyaluronan is the main component of the pericellular matrix for many cells, in which it can bind to its synthases or receptors to affect related functions (Heldin & Pertoft 1993, Knudson & Knudson 1993). Existence of intracellular hyaluronan has also been reported including nucleus hyaluronans (Hascall et al 2004, Li et al 2007). Due to the properties and characters of binding water molecules, hyaluronan provide ECM and even the whole tissue with plasticity. This is the major reason for hyaluronan polymers accumulation during tissue reorganization (Theocharis et al 2016).

The fibrous proteins in the ECM mainly include collagens, elastins, fibronectin and laminins (Frantz et al 2010).

Collagen is the most abundant fibrous protein in interstitial ECM, up to 30% of total protein in human is made up by collagens. The collagen superfamily comprises 28 different collagens which are made up of many distinct peptides in vertebrates. (Frantz et al 2010). Collagens in ECM are normally synthesized and secreted by fibroblasts (De Wever et al 2008). Actually, the arrangement and alignment of collagen fibers in the ECM is influenced by fibroblasts via exerting tension on the matrix to organize collagen into sheets and cables As the main structural component, collagens takes part in many biological processes, such as providing tissue tensile strength, regulating cell adhesion, assisting chemotaxis, supporting migration and direct tissue development (Rozario & DeSimone 2010).

Elastin is the main constituent of elastic fibers which are the large ECM structures providing recoil to tissues suffered from the repeated stretch. The elastin stretch is limited by the associating collagen fibrils (Wise & Weiss 2009). The assembly of elastic fibers is mostly completed in the earlier phase of development, these fibers are very stable and very slow for turnover. (Theocharis et al 2016). Complete repair of damaged elastic fibers is not possible and the repaired fibers cannot function normally in adults (Wagenseil & Mecham 2007).

Fibronectin is expressed in the ECM of many different tissues and plays a crucial role during the development of vertebrates (George et al 1993). According to the solubility, fibronectin can be grouped into soluble plasma fibronectin and cellular fibronectin, the latter part is much more heterogeneous and depending on cell type and species (Theocharis et al 2016). Fibronectin bound by integrins to regulate the binding of fibronectin to cells (Hynes 2002). In addition, sydecans can also bind to fibronectin (Couchman 2010). Actually, the binding between syndecans and fibronectin enhances integrin signaling and cell spreading, which suggests that syndecans act as co-receptors for integrins (Morgan et al 2007, Woods & Couchman 1998).

Laminins are a large class of glycoproteins with a heterotrimeric structure which are found in the basement membrane and assembled along with collagen type IV, nidogens, agrin and perlecan (Durbeej 2010, Iorio et al 2015). The tissue-specific distribution of laminin isoforms suggests that individual laminins play distinct roles in specific tissue functions (Hallmann et al 2005). Laminins are important in early embryonic development and organogenesis (Durbeej 2010). Besides, laminins can modulate angiogenesis by promoting blood vessel growth and maturation (Hallmann et al 2005, Iorio et al 2015).

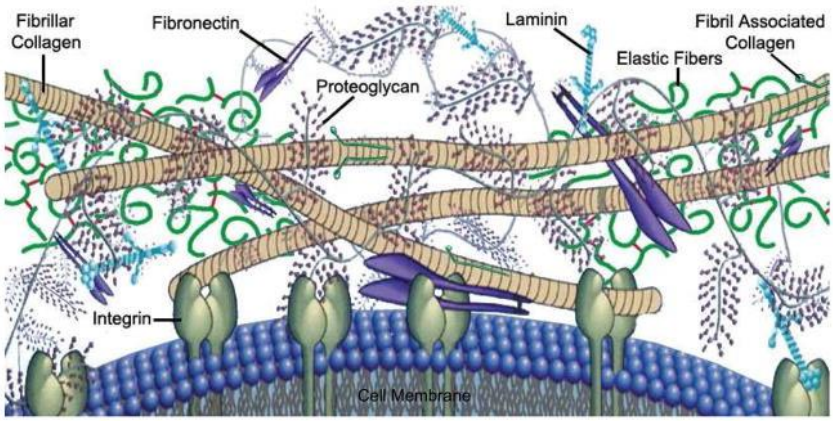

Figure 1.3 Representative cartoon for ECM layout. Binding between cell and ECM, the primary components in a general ECM are indicated. (Aamodt & Grainger 2016)

The ECM also contains some extracellular proteases and extracellular receptors (Theocharis et al 2016). Integrins are the cell surface receptors, which link the actin cytoskeleton with the ECM (Theocharis et al 2016). Integrins are heterodimers which are composed of one α subunit and one β subunit. All the subunits contain a large extracellular domain, one transmembrane helix and a short cytoplasmic domain (Hynes 2002). Eighteen α subunits and 8 β subunits are found in vertebrates, giving rise to 24 integrin heterodimers, each integrin recognizes its specific ligands (Humphries et al 2006, Kinashi 2005, Luo et al 2007).

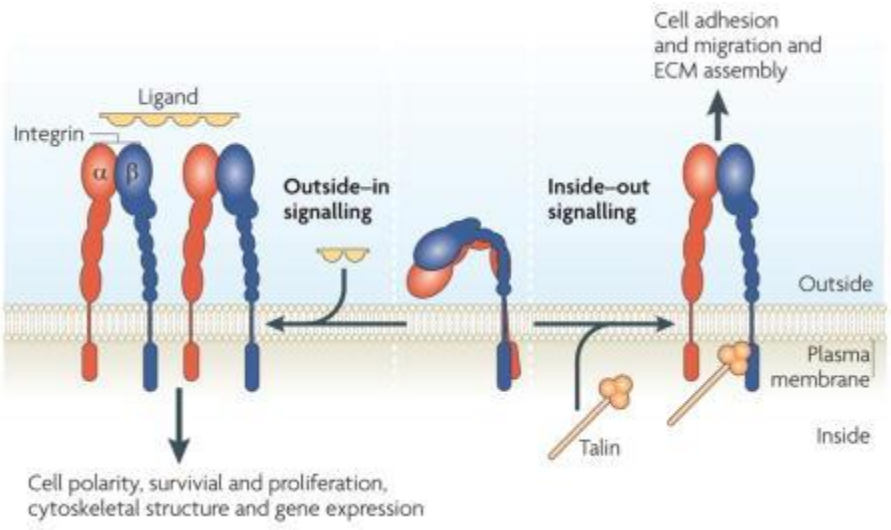

Figure 1.4 Bi-directional signaling of integrins. Integrin can transmit signaling from two directions. Signaling from inward is called “inside-out” signaling, with the assistant of integrin activators, like talin or Kindlins, integrin completes a conformational change to become active for extracellular ligand recognition. During “outside-in” signaling, integrins cluster into focal adhesion due to binding to ligands. Then clustered integrins trigger intracellular downstream signals. “Inside-out” signaling and “Outside-in” signaling affect different biological functions. (Shattil et al 2010)

The functions of integrins are not restricted to cell adhesion, but also include the regulation of cell proliferation, cell differentiation and tissue development (Hu & Luo 2013). One important role of integrins is bi-directional signal transduction across the membrane, referred to as “inside-out” and “outside-in” signaling. (Hu & Luo 2013).

In “inside-out” signaling, talins and Kindlins are supposed to be the crucial factors in activating integrin residing in a low ligand affinity state to facilitate integrin mediated matrix organization and cell adhesion (Hu & Luo 2013). Interaction between talin and the cytoplasmic tail of β integrin is thought to be the last step for integrin activation (Tadokoro et al 2003).

“Outside-in” signaling, referred to the signals transmitted into the cell upon interaction of integrins with the ECM, plays a crucial role in cell mobility, proliferation, differentiation and other processes (Ginsberg et al 2005). Ligand bound integrins cluster into focal adhesions (Choi et al 2008, Geiger et al 2001, Zamir & Geiger 2001), this processing is together with the assembly of the adhesome, which is essential for cells to sense the extracellular environment (Berrier & Yamada 2007, Vicente-Manzanares & Sanchez-Madrid 2004, Zaidel-Bar & Geiger 2010). The adhesome contains numerous proteins, the core proteins are

defined as the proteins that can enable the integrin cytoskeleton coupling, including talin, vinculin, α-actinin and parvin (Horton et al 2015, Legate et al 2009, Morse et al 2014, Zaidel-Bar et al 2007).

1.2.2 Kindlins activate integrins

The Kindlins play an essential role in integrin activation (Larjava et al 2008, Ma et al 2008, Meves et al 2009, Montanez et al 2008, Moser et al 2008, Plow et al 2014, Shi et al 2007, Ye et al 2011). The functions of Kindlins are not only for “Inside-out” signaling regulation but also include “Outside-in” signaling modulation (Feng et al 2012, Montanez et al 2008, Xue et al 2013). The Kindlin protein family consists of Kindlin1, Kindlin-2 and Kindlin3 (Ussar et al 2006). Not all the Kindlins are expressed ubiquitously; Kindlin1 is expressed in epithelial cells, Kindlin-2 has a more broad expression pattern in most mesenchymal derived solid tissues and Kindlin3 is mainly expressed in hematopoietic cells (Malinin et al 2010). Kindlins are such an important protein family that absence of each one leads to diseases, such as abnormal Kindlin1 causes Kindler’s syndrome (actually the name Kindlin is from Kindler’s syndrome) (Jobard et al 2003, Mas-Vidal et al 2010, White & McLean 2005), loss of Kindlin-2 and Kindlin3 is embryonic lethal (Montanez et al 2008, Moser et al 2008) and mutations in human Kindlin3 causes leukocyte adhesion deficiency III (Kuijpers et al 2009, Larjava et al 2008, Mory et al 2008, Svensson et al 2009). The sequences of the three Kindlins are quite conserved. The identity is above 53% which is the least similarity between Kindlin-2 and Kindlin3 (Ussar et al 2006).

Individual Kindlins cannot bind to every β integrin cytoplasmic tail. Kindlin1 can bind to β1, β3 and β6 integrins (Harburger et al 2009, Moslem et al 2017, Rognoni et al 2014) and Kindlin-2 and 3 are reported to bind to integrin β1, β2 and β3 tails (Bledzka et al 2012, Bottcher et al 2012, Harburger et al 2009, Ma et al 2008, Montanez et al 2008, Moser et al 2009, Moser et al 2008).

1.2.3 The function of Kindlin-2

Functional studies on Kindlin-2 are more abundant than on the other two Kindlins (Malinin et al 2010). Besides activating integrins, Kindlin-2 is also believed to play a role in connecting integrins with the actin cytoskeleton (Meves et al 2009, Ussar et al 2006). This association of Kindlin-2 linking to focal adhesions and actin cytoskeleton has been observed (He et al 2011, Shi et al 2007, Tu et al 2003) via the complex of integrin-linked kinase (ILK), particularly interesting new cysteine-histidine-rich protein (PINCH) and Parvin as a bridge (Honda et al 2013). ILK directly binds to Kindlin-2 and focal adhesions bind to parvin (Qadota et al 2012, Schaller 2001, Tu et al 2001). Actually, Kindlin-2 directly interacts with actin and the actin-binding site in the F0 domain affects cell spreading (Bledzka et al 2016). Besides the β integrin and ILK, migfilin is another molecule which can bind to Kindlin-2, modulating cell shape (Tu et al 2003). In addition, recruitment of Kindlin to the cell membrane is assisted by binding of the pleckstrin homology subdomain in F2 and another site in the F0 subdomain to pospholipids (Liu et al 2011, Liu et al 2012, Metcalf et al 2010, Perera et al 2011, Qu et al 2011).

Besides the embryonic lethality of Kindlin-2 knockout in mouse (Montanez et al 2008), Kindlin-2 knockout in zebrafish shows a defective integrin signaling and abnormal cardiac development (Dowling et al 2008). The related *in vitro* studies by utilizing the cells deriving from Kindlin-2 knockout mice or siRNA knockdown cells reported the crucial roles of Kindlin-2 in integrin related functions like cell spread and adhesion (Ma et al 2008, Ussar et al 2006). The malignant transformation of breast cancer cells and leiomyomas can also change the expression pattern of Kindlin-2 (Gozgit et al 2006, Kato et al 2004). These studies implicate an important function of Kindlin-2 in development and diseases. However, the function of Kindlin-2 in adipose tissue is still not clear. A recent publication suggests that Kindlin-2 inhibits adipogenesis of induced pluripotent cell-derived mesenchymal stromal cells (Moslem et al 2017).

1.3 The functions of ECM in angiogenesis and vascularization in BAT

1.3.1 Role of the ECM in angiogenesis

The quiescent blood vessels in adults are normally covered with a basement membrane on the abluminal (basal) surface. This membrane is continuous and comprises many ECM components such as laminins, collagen type IV, nidogens and perlecan (Bix & Iozzo 2008, Hallmann et al 2005, Hayashi et al 1992). Some stimulations like wounding and ischemia induce angiogenic cytokines like Vascular Endothelial Growth Factor (VEGF), which triggers basement membrane degradation for angiogenesis (Chang et al 2009, Rowe & Weiss 2008, Sundberg et al 2001). Then the blood vessels become leaky (Sundberg et al 2001) and start to sprout (Nicosia & Madri 1987). At the same time quiescent endothelial cells are activated (Senger & Davis 2011). About the order of basement membrane degradation and vascular permeability during angiogenesis, one opinion tends to believe degradation is earlier (Senger & Davis 2011) but another thinks the opposite (Bryan & D'Amore 2007). Due to the leaky blood vessels, fibrinogen, vitronectin and fibronectin are extravasated from blood vessels to form a provisional ECM via enzymatic coagulation of fibrinogen to fibrin and transformation of interstitial collagen matrices triggered by vitronectin and fibronectin.This provisional ECM is believed as the necessary environment for blood vessels sprouting (Senger 1996, Senger & Davis 2011, Sundberg et al 2001). The sprouting and further morphogenesis lead to the formation and maturation of new blood vessels. Then these new vessels are covered with a vascular basement membrane together with pericytes which directly regulate this stage, and finally new vessels are stabilized (Benjamin et al 1999, Grant & Kleinman 1997, Senger & Davis 2011, Stratman et al 2009a, Stratman et al 2010).

The ECM plays an important role during the whole angiogenesis. Besides the angiogenic factors, the proliferation and survival of endothelial cells is also controlled by ECM adhesion of endothelial through integrins (Akiyama et al 1989, Giancotti & Ruoslahti 1999, Meredith & Schwartz 1997, Wary et al 1996). On the one hand, integrin mediated adhesion of endothelial cells to the ECM is required for efficient cytokine activation of the extracellular signal-regulated kinase 1 (ERK1)/ERK2 mitogen-activated protein (MAP) kinase

pathway (Aplin et al 1999, Short et al 1998), on the other hand, this pathway promotes proliferation and survival but suppresses apoptosis (Aoudjit & Vuori 2001, Assoian & Schwartz 2001, Ilan et al 1998, Perruzzi et al 2003, Roovers & Assoian 2000, Seger & Krebs 1995, Vinals & Pouyssegur 1999). Actually, for endothelial cells, the cyclin-dependent kinases which regulate proliferation also require adhesion to the ECM for its expression and activation (Assoian 1997, Fang et al 1996, Vinals & Pouyssegur 1999, Zhu et al 1996). Adhesion to the ECM of endothelial cells is also reported to be crucial for blood vessels sprouting through participation of several ECM components (Dejana et al 1985, Nicosia & Madri 1987, Senger et al 2002, van Hinsbergh et al 2001). Because migration of endothelial cells is an important event for sprouting (Ausprunk & Folkman 1977), ECM adhesion is believed to be required for endothelial cells migration. There are also publications reporting the haptotactic migration driven by ECM components independently from cytokines (Senger & Perruzzi 1996, Senger et al 2002).

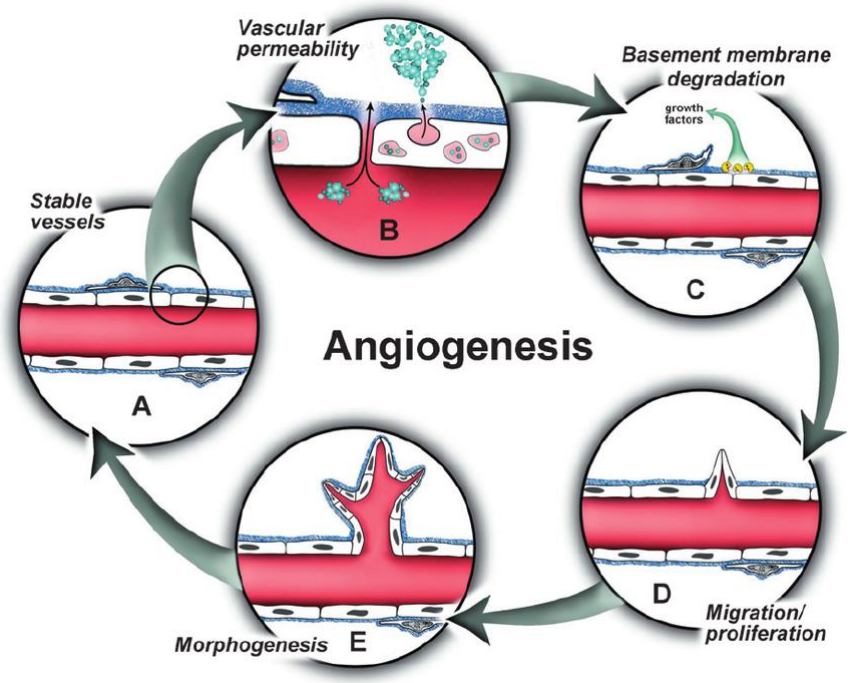

Figure 1.5 Phases of angiogenesis. Stable blood vessels (A) undergoes permeability which leads to extravasate proteins to form provisional ECM (B). (C) The basement membrane is degraded by ECM protease, such as MMPs. Endothelial cells are activated, growth factors are released. (Different opinion indicates membrane degradation phase is earlier than vascular permeability phase, see text). (D) Endothelial cells proliferate and migrate to form lumens. (E) The cord-like structure is formed. And the new blood vessels complete morphogenesis and then maturation. (Bryan & D'Amore 2007)

The role of the ECM is to provide a scaffold which can be utilized to generate a tension guidance network by endothelial cells to form cord-like structures (Davis & Camarillo 1995, Vernon & Sage 1995). Another, ECM can also directly regulate the morphogenesis of endothelial cells (Senger & Davis 2011), for instance, collagen I provides an environment for cord structures to mature to become lumens through intracellular vacuoles variation (Davis & Camarillo 1996) and expansion of lumen via ECM proteolysis (Chun et al 2004, Saunders et al 2006, Stratman et al 2009b). One solid evidence is the expression of collagen I in isolated endothelial cells triggers spontaneous formation of cord structures of these cells *in vitro* (Fouser et al 1991, Iruela-Arispe et al 1991), besides, collagen crosslinking inhibitor proline analogs are also reported to inhibit neovascularization *in vivo* (Ingber & Folkman 1988). This regulation of collage I to morphogenesis is via modulating actin stress fibers by integrins, such as activating Rho, Src (short for sarcoma) and p38 MAP kinase and inhibiting cyclic adenosine monophosphate (AMP) and Rac activity (Liu & Senger 2004, Sweeney et al 2003, Whelan & Senger 2003). Besides the formation of cord-like structures, the ECM also regulates lumen formation via collagen I/fibrin and endothelial cell interactions (Aplin et al 2008, Bayless et al 2000, Davis & Camarillo 1996, Davis et al 2007, Iruela-Arispe & Davis 2009, Koh et al 2008, Nakatsu & Hughes 2008, Nicosia & Madri 1987, Sainson et al 2005, van Hinsbergh et al 2001). The interactions mediated by integrins and Rho GTPases induce ECM proteolysis together with pinocytic vacuole formation and coalescence, which finally forms lumens for new blood vessels generation (Bayless & Davis 2002, Davis & Bayless 2003, Davis & Camarillo 1996, Egginton & Gerritsen 2003, Folkman & Haudenschild 1980, Kamei et al 2006, Lubarsky & Krasnow 2003, Meyer et al 1997, Saunders et al 2006, Senger & Davis 2011, Stratman et al 2009b, Yang et al 1999). The ECM can also function as a reservoir for cytokines. Endothelial cells can respond to several cytokine signals transduced by receptors including integrins in ECM containing these cytokines (such as growth factor and Vascular Endothelial Growth Factor (VEGF)) (Chen et al 2010, Hynes 2009, Somanath et al 2009). It has also been reported that angiogenic cytokines can bind to heparin sulfate

proteoglycans which exist broadly in the ECM and endothelial cell surface (Gerhardt et al 2003, Mitsi et al 2008). In fact, some angiogenic cytokines can directly bind to some components such as collagen I and fibrin/fibronectin matrices (Kanematsu et al 2004). Some similar reports include Angiopoietin-1 associating integrin α5β1 and its receptor (Carlson et al 2001, Cascone et al 2005, Ramirez & Dietz 2007, Ramirez & Dietz 2009, Saharinen et al 2008, Wagenseil & Mecham 2009), TGF-β and BMPs binding to fibrillins. Another more direct evidence is in 3D collagen matrices where some hematopoietic stem cell cytokines (stem cell factor (SCF), interleukin-3 (IL-3) and stromal-derived factor-1 α (SDF-1α)) can modulate blood vessels formation together with pericytes (Stratman et al 2009a). On the contrary, some ECM components can also inhibit angiogenesis by binding to other cytokines such as thrombospondin-1 and thrombospondin-2 which can bind to Fibroblast Growth Factor-2, VEGF and hepatocyte growth factor (Armstrong & Bornstein 2003, Margosio et al 2003). Fibronectin is very important for vasculogenesis as severe defects appear in vascular development in fibronectin knockout mice (Astrof et al 2007, Astrof & Hynes 2009, Francis et al 2002, George et al 1997, George et al 1993).

1.3.2 Vascularization in BAT

BAT is a vascular enriched tissue (Cinti 2005). Besides to transport oxygen and nutrients (Honek et al 2014), vascularization has also been reported to participant in some particular processes, such as browning of WAT (Bukowiecki et al 1980, Cannon et al 1996, Cao 2007, Lim et al 2012, Xue et al 2009). The effects are depicted as cold induced WAT browning can also induce angiogenesis by promoting angiogenic gene expression and inhibiting antiangiogenic gene expression. Further, during browning, angiogenesis is induced via signals transduced by VEGF receptor. Disabled VEGF receptor can also reduce the browning of WAT (Xue et al 2009). Furthermore, *in vitro* experiments indicate that obese/insulin-resistant WAT shows fewer capillaries but more large blood vessels than lean WAT (Spencer et al 2011). But the mechanism of angiogenesis or vasculogenesis in BAT is still not understood. Some phenomena shown in VEGF transgenic mice implicate the relation

between angiogenesis and BAT. Besides enhanced angiogenesis and some other vascular-related effects in both WAT and BAT, VEGF overexpressing mice also show a protection against high fat diet (HFD) induced hypoxia and obesity, and reasonably stronger thermogenesis and energy expenditure (Elias et al 2012). These conclusions reveal the potential participation of angiogenesis in much more BAT functions than previously thought and also implicate that the ECM may regulate BAT not only directly but also indirectly via its effect on angiogenesis. However, the mechanical understanding of angiogenesis in BAT is still rudimentary.

1.4 Amino acid homeostasis and sensing in the cell

1.4.1 Amin acid homeostasis in the cell

The necessity of amino acid to survive, and grow has been noticed since the 1950s (Dulbecco & Freeman 1959, Eagle 1955a, Eagle 1955b, Eagle 1955c). The main functions of amino acids can be depicted as the following several aspects: (1) Twenty proteinogenic L-amino acids act as the basic elements for protein synthesis; (2) In some situations amino acids can be metabolized for energy in some cells; (3) The synthesis of some hormones, neurotransmitters and some other special metabolites depends on amino acids as precursors; (4) Amino acids are the carrier of C1 carbon compounds; (5) Amino acids can directly intermediate tricarboxylic acid (TCA) cycle and gluconeogenesis as anaplerosis; (6) Some metabolic intermediates can also be used for non-essential amino acid synthesis (Broer & Broer 2017). These functions coordinately maintain normal physiological activities and at the same time homeostasis of amino acids.

Amino acids can take part in many different signaling pathways via amino acid binding proteins like some enzymes, transporters and transfer ribonucleic acids (tRNA). Most of these signals are regarded to regulate amino acid homeostasis (Broer & Broer 2017). These parts are discussed individually in the later amino acid sensing chapter.

The regulations of amino acid homeostasis can be divided into three parts: (1) amino acid transporters which are essential for amino acid entrance and exit; (2) amino acid

biosynthesis and degradation; (3) protein biosynthesis and degradation (Broer & Broer 2017).

The concentration of amino acids in the cytosol is much higher than in blood (Bergstrom et al 1974, Hoffmann & Lambert 1983). This phenomenon suggests an active transport of amino acids by amino acid transporters. Since the pioneering research of identifying different amino acid transporters (Christensen 1966), more and more amino acid transporters have been identified and confirmed (Broer & Palacin 2011, Hediger et al 2013, Palacin et al 1998). All these transporters have their own specific affinities for different amino acids and specific expression profiles in different kinds of cells (Broer & Palacin 2011, Perland & Fredriksson 2017). Although there are abundant transporters known, by comparing the expression profiles of all known transporters in 917 cancer cell lines several kinds of transporters are found to be basic transporters for maintaining amino acids homeostasis (Barretina et al 2012, Broer & Broer 2017). This minimal set of transporter includes plasma transporters SLC1A4 (also known as ASCT1), SLC1A5 (also known as ASCT2), SLC7A5 (also known as LAT1), SLC7A6 (also known as y+LAT2), SLC38A1 (also known as sodium-dependent neutral amino acid transporter (SNAT)1), SLC38A2 (also known as SNAT2), SLC38A6 (also known as SNAT6), SLC38A7 (also known as SNAT7) and two lysosome transporters SLC36A4 (also known as PAT4), SLC38A9 (also known as SNAT9). A study deleting SLC1A5 in 143B osteosarcoma cells, which express this minimal set of transporters, revealed some details about the functions of some transporters in this simple set. Some symporters coupled with Na^+ like SLC38A1, which carries small hydrophilic neutral amino acid into cells, make small amino acids accumulate in the cytosol as loaders (Broer et al 2016). Then the antiporters like SLC1A4 and SLC1A5 take up other small amino acids by exporting hydrophilic small amino acids in the cytosol transported by loaders, these antiporters are called exchangers (Arriza et al 1993, Utsunomiya-Tate et al 1996). Besides, transportation of amino acids with large branched chain and aromatic amino acids is depended on a similar exchange system using heterometric amino acid antiporters like

4F2hc-SLC7A5 (Kanai et al 1998, Mastroberardino et al 1998) and 4F2hc-SLC7A8 (also known as LAT2) (Khunweeraphong et al 2012, Segawa et al 1999). Comparing with the loaders, exchangers are the dominating transporters (Broer et al 2016). Some abundant amino acids like glycine, alanine, glutamine and asparagine are used as exchange currency for uptake of other amino acids (Bhutia & Ganapathy 2016, Broer 2014, Krall et al 2016, Pochini et al 2014). It can be supported from other aspects that amino acid starvation is reported as the inducer for nonessential amino acid synthesis (Kilberg et al 2012) and expression of some transporters like SLC38A2 (Gaccioli et al 2006). This mechanism is thought to allow restoring nonabundant amino acids (Broer & Broer 2017). For cationic amino acids such as lysine, arginine and ornithine, the transportation is through multiple ways, for example on the one hand, the cationic amino acid transporters SLC7A1-3 (also known as CAT 1-3) mediates diffusion of these amino acids into nonepithelial cells then these cationic amino acids are accumulated by negative membrane potential (Closs et al 2004, Kavanaugh 1993). On the other hand, SLC7A1 is reported to be induced by amino acid deprivation for amino acids taken up in an exchange way (Hatzoglou et al 2004). It is noteworthy that cationic amino acids can also be transported outward by heterometric antiporters such as 4F2hc-SLC7A6 (Broer et al 2000).

About amino acid biosynthesis is normally activated by amino acid starvation, the asparagine synthesis is the typical pathway whose key enzyme asparagine synthetase can catalyze aspartate to become asparagine by transfer an amino group from glutamine (Balasubramanian et al 2013). In more detail, amino acid deprivation induced transcription of asparagine synthetase is depended on two elements in its promoter; amino acid response element and nutrient response element which can be bound by activating transcription factor (ATF4) (Balasubramanian et al 2013, Kilberg et al 2009). Almost all the amino acid biosynthesis is regulated by ATF4, but amino acids can also regulate ATF4 as feedback (Broer & Broer 2017). In more detail, translation of ATF4 is found to be regulated by amino acids, reversely ATF4 binding sites exist in the promoters of most enzymes which are

essential for the biosynthesis of nonessential amino acids and amino acid transporters. Proline biosynthesis is a typical example (D'Aniello et al 2015, Han et al 2013, Kilberg et al 2016, Phang et al 2015, Tan et al 2011). Besides, aminotransferases are also very important for amino acid biosynthesis and homeostasis. For amino acid *de novo* synthesis from organic acid, aminotransferases are needed to add amino group from MH_4^+ or another amino acid (Hutson et al 2005). For the transfer of amino groups from one amino acid to another, to quickly regulate amino acid homeostasis, aminotransferases are also, of course, the necessities.

Amino acid degradation is always for oxidation producing energy or for anaplerosis of TCA cycle as some intermediates. Amino acids are oxidized by many cells (Broer & Broer 2017), but as introduced in the last chapter, amino acids are not the major fuel in BAT. The mitochondrion is the place where amino acids are oxidized, but the mechanism of how amino acids are transported into mitochondria still lacks sufficient support. Due to the prevalence of branched chain amino acids (BCAAs) oxidation in many cells, more details are known about its mechanism which is regarded to be the important way for balancing the utilization of these essential amino acids among anaplerosis, energy generation and protein synthesis (Ananieva et al 2016, Harper et al 1984). For leucine, isoleucine and valine the branched chain keto-acid dehydrogenase (BCKD) complex is the key enzyme complex (Brosnan & Brosnan 2006), BCKD activity is depended on E1 subunit phosphorylation by BCKD kinase or dephosphorylation by Protein phosphatase 2Cm (PP2Cm) (Lu et al 2009). BCDK kinase and PP2Cm are under the regulation of an allosteric regulator α-ketoisocaproate which is generated from leucine (Broer & Broer 2017). The first step of BCAA metabolism is deamination by transaminase, mitochondrial BCAA transaminase (BCAT2) is regulated by ATF4, which suggests that BCAAs can be the amino donors for synthesis of nonessential amino acids upon particular situations. Leucine of all BCAAs is the most frequently used amino acid for protein synthesis no matter in humans (Mauro & Chappell 2014) or animals (Piper et al 2017). This makes leucine to be an indicator of amino acid levels, which also

explains why BCKD is regulated by leucine derived α-ketoisocaproate. Another example is glutamine, its balance is also regulated by metabolic substrates, transaminase and allosteric regulators, such as glutamine synthetase modulated by ammonia binding (Cooper 1990), glutaminase under allosteric regulation of phosphate (Li et al 2016) and expression regulation of the transcription factor myc (Dang 2011). But the regulations are obviously not limited to these ways, for instance glutaminase can also be regulated by micro-RNA miR-23 via binding the 5′-UTR to degrade its mRNA. Enhancement of glutaminase by myc is reported to be through inhibition of miR-23 induced mRNA degradation (Gao et al 2009). As the most metabolized amino acid, glutamine can be converted into many intermediates of metabolism such as aspartate, asparagine, citrate, oxaloacetate and pyruvate via glutaminolysis (Newsholme et al 1985, Wise et al 2008). This makes glutamine to be important in proliferating cells, for example to many cancer cells glutamine is indispensable (DeBerardinis et al 2007, Wise & Thompson 2010).

The last part affecting amino acid homeostasis is protein biosynthesis and degradation which actually are the leading factors for balancing amino acid utilization and maintenance (Hinnebusch 1994, Hinnebusch et al 2016, Kimball & Jefferson 2005, Kimball & Jefferson 2010). Mechanistic target of rapamycin complex 1 (mTORC1) is one of the most important signaling pathways for protein translation. Typically its regulations are through phosphorylation of 4E binding protein 1 (4E-BP1) and the downstream kinase p70 ribosomal protein S6 kinase beta-1 (S6K1), which can phosphorylate eukaryotic initiation factor (eIF) 4G and programmed cell death protein 4 (PCD4) in turn (Dennis et al 2012). Phosphorylated or nonphosphorylated 4E-BP1 is the switch for initiating translation, unphosphorylated 4E-BP1 can bind to and then sequester eIF4E the subunit of eIF4F complex, which is necessary for translation initiation (Broer & Broer 2017). Nonphosphorylated PCDC4 prevents the eIF4F complex from binding to mRNA by binding to its subunits eIf4A and eIF4G (Yang et al 2003). Besides, the assembly of ribosomes is also regulated by amino acid homeostasis through other amino acid sensing systems such as general control nonderepressable 2 (GCN2)

(sensing cytosol amino acid insufficiency) and protein kinase RNA-like endoplasmic reticulum kinase (PERK) (sensing instance incorrect protein folding) which can phosphorylate GDP- eukaryotic initiation factor 2α (eIF2α). The phosphorylated GDP-eIF2α cannot interact with guanine nucleotide exchange protein eIF2B and then cannot be transformed to GTP-eIF2α. The exchange from GDP-bound eIF2α to GTP-bound eIF2α is the switch for sustained peptide elongation during protein synthesis (Balasubramanian et al 2013, Broer & Broer 2017, Kimball 2001). Additionally, translation of ATF4 is under the regulation of two upostream elements of the open read frame. The second element will stop translation of ATF4 when eIF2α·GTP·Met-tRNA$_i^{Met}$ complex is sufficient (amino acids are sufficient and eIF2α is phosphorylated) and on the contrary, translation can be completed when eIF2α·GTP·Met-tRNA$_i^{Met}$ level is reduced (Broer & Broer 2017, Hinnebusch et al 2016, Somers et al 2013, Vattem & Wek 2004, Young & Wek 2016). These examples show the precise regulations to protein biosynthesis to ensure the homeostasis of amino acid.

The degradation of proteins is an important source of amino acids through recycling and restoring. Protein is degraded through two main pathways, autophagy and the ubiquitin protease system (Cohen-Kaplan et al 2016). Autophagy is introduced in the later individual chapter, so this part mainly talks about ubiquitination degradation. Ubiquitin protease system is always regarded as the digestion way for large protein complexes (Cohen-Kaplan et al 2016, Glickman & Ciechanover 2002). When proteins are ready to be degraded for amino acid recycling, ubiquitin ligases will be marked on these proteins. Next, these proteins start to be unfolded and deubiquitinated followed by hydrolysis from which several short peptides are produced (Finley 2009). These peptides can be degraded furtherly into individual amino acid by cytosol peptidases, some peptides can also be used for another particular purpose as antigenic peptides recognized by the immune system (Goldberg et al 2002). Interestingly, it has been reported in NIH3T3 cells only the levels of asparagine, aspartate and cysteine are decreased by inhibition of the proteasome, which mediates ubiquitin protease degradation (Suraweera et al 2012). This implies different recycling rates for different amino acids. On the

opposite, cytosolic amino acids levels are increased by activated mTORC1 induced expression of proteasomal proteins (Zhang et al 2014). It is further reported that mTORC1 activation induced protein biosynthesis includes proteasomal proteins biosynthesis, which is regarded as the adaption to the increased protein folding and possible misfolding (Zhang & Manning 2015).

These mechanisms together ensure the normal amino acid homeostasis. However, these regulations always do not happen at the same time and the same tissues. Different tissues or organs perform different functions to regulate multiple aspects of amino acid metabolism from food intake to utilization in responding to different stimulations including amino acid depletion or abundance (Broer & Broer 2017). About the particular functions of BAT on systemic amino acid homeostasis, still very little is known.

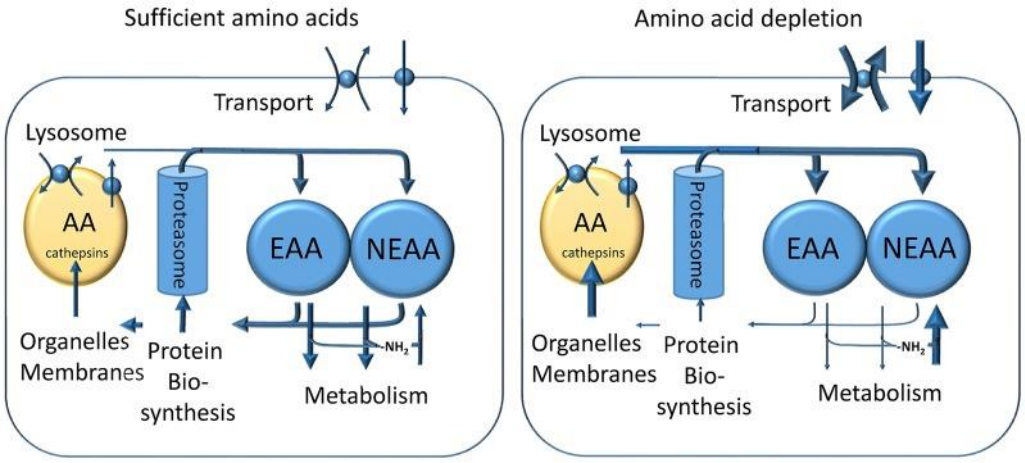

Figure 1.6 Cellular amino acid homeostasis. A constant turnover of proteins is shown in the cell upon sufficient amino acids. Amino acids are mainly stored as the form of proteins. The major net loss is mitochondrial oxidation, which is thought to be compensated by uptake of amino acids by transporters and/or amino acid biosynthesis. Another homeostasis regulation is the exchange of amino from essential amino acids or oxidized amino acids to nonessential amino acids. Once amino acid is depleted, expressions of transporters will be enhanced to import more amino acids. At the same time, proteins degradation will also be enhanced and protein biosynthesis is weakened to recycle more amino acids. Oxidation of amino acids is shut down to the lowest level. (Broer & Broer 2017)

1.4.2 The amino acid sensing system

As a crucial intracellular hub for signaling in response to nutrients, the mTORC1 pathway is a well-accepted amino acid sensing signaling pathway. mTORC1 is the main sensor in it (Avruch et al 2009, Bar-Peled & Sabatini 2014, Goberdhan et al 2016, Jewell et

al 2013, Zheng et al 2016). By regulating the downstream factors, mTOR modulates different cellular responses to adapt to different environmental nutrient status, such as 4E-BP1for protein biosynthesis upon amino acid abundance and ULK1 for autophagy upon amino acid depletion (Dunlop & Tee 2014, Hosokawa et al 2009, Tan & Miyamoto 2016).

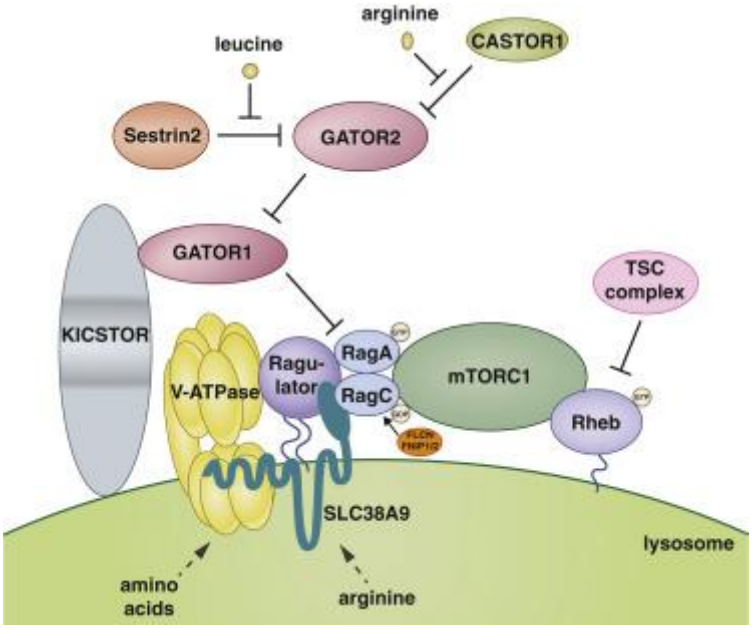

Figure 1.7 Amino acids sensing of mTORC1 signaling. Cytosolic leucine and arginine are sensed through GATOR2 (and/or GATOR1) regulation by Sestrin2 and CASTOR1 homodimer (or CASTOR1 and 2 heterodimers) respectively, finally sensing signaling targets Rag GTPases. Lysosomal amino acids sensing require V-ATPase. Lysosomal arginine can be sensed by SLC38A9. TSC integrating multiple signaling and stimuli regulates mTORC1 through Rheb. (Wolfson & Sabatini 2017)

The tuberous sclerosis complex (TSC) 2 is the key for mTOR to integrate multiple signals (Tee et al 2003), such as AKT and ERK which activate mTORC1 through inhibition of TSC2 by phosphorylation (Dibble & Manning 2013). Conversely, AMPK can activate TSC2 to shut off mTORC1 signaling (Kimura et al 2003, Sengupta et al 2010). The activation or inactivation of TSC2 switches mTORC1 off or on by affecting mTORC1 activator Ras homolog enriched in brain (Rheb), by hydrolyzing Rheb associated GTP to GDP TSC2 that can inactivate Rheb (Broer & Broer 2017). Some other stimuli which do not directly associate with amino acids can also be mediated by TSC such as low energy stress (Inoki et al 2003), hypoxia (Brugarolas et al 2004, Reiling & Hafen 2004) and genotoxic stress (Budanov &

Karin 2008). The subcellular localization of mTORC1 is found to related to amino acid concentration variates (Sancak et al 2010)

mTORC1 only senses selected amino acids in the cytosol or lysosomal lumen directly, such as leucine and arginine (Avruch et al 2009, Bar-Peled & Sabatini 2014).

The amino acid transporter SLC38A9 is regarded to be the primary lysosomal arginine sensor in mTOR signaling. The regulation of SLC38A9 is through interaction with the Rag Ragulator complex (Jung et al 2015, Rebsamen et al 2015, Wang et al 2015b). Lysosomal leucine has been reported to activate mTORC1 (Milkereit et al 2015), but the sensing pathway is still not clear. The V-ATPase is found to be necessary for lysosomal amino acid sensing (Zoncu et al 2011).

Cytosolic amino acid levels are sensed by Rag GTPases. Amino acid starvation induces Rag GTPase activity (Broer & Broer 2017). Cellular Arginine Sensor for mTORC1 (CASTOR) 1 homodimer or CASTOR1 CASTOR2 heterodimer is regarded as the cytosolic arginine sensor, with arginine binding CASTOR1 to regulate mTORC1 (Broer & Broer 2017, Chantranupong et al 2016). For cytosolic leucine sensor in mTORC1, some molecules have been reported including Sestrin2 which bind to leucine to regulate mTORC1 (Hutson et al 2005, Kimball et al 2016, Wolfson et al 2016), but Sestrin as a leucine sensor is still controversial (Lee et al 2016a).

Besides, many other mechanisms have also been reported (Goberdhan et al 2016, Ho et al 2016, Pramod et al 2013). For example, leucyl-tRNA synthetase (LRS) regulates mTORC1 together with Sestrin2 (Han et al 2012, Lee et al 2018). Furtherly, amino acid depended Rag GTPases activation to mTORC1 has also been reported (Petit et al 2013, Tsun et al 2013). Another leucine metabolite acetyl-coenzyme A (AcCoA) is reported to alter mTORC1 activity (Son et al 2018). For glutamine sensing, ARF1 is reported to be involved (Jewell et al 2015), but the sensing pathway is still not clear.

Amino acid sensing of mTOR was reported to associate with PATs, but the details are still unclear (Goberdhan et al 2016, Heublein et al 2010).

1.5 Autophagy clears unnecessary proteins and regenerates amino acid pools

1.5.1 Autophagy background and different types of autophagy

Autophagy is a process of self-degradation in cells, which is crucial for maintaining homeostasis of metabolic substrates in response to nutrient stress. Autophagy also removes misfolded or aggregated proteins, intracellular pathogens and dysfunctional organelles such as mitochondria, endoplasmic reticulum (ER) and peroxisomes (Glick et al 2010). Actually, the substrates of autophagy are very heterogeneous (Galluzzi et al 2017). Autophagy was discovered based on the observation of cargoes in the lysosome, including mitochondria and some other intracellular structures (Deter & De Duve 1967). Autophagy is a very conserved function, its related genes can be found in many different species from slime mold to mammals (Nakatogawa et al 2009).

Autophagy includes three defined types, macroautophagy, microautophagy and chaperone mediated autophagy (Glick et al 2010). Macroautophagy is to degrade the cellular components such as membranes, organelles or protein aggregates. The lysosome finally fuses with vesicles encapsulating cargoes (Yang & Klionsky 2010). Microautophagy is the way to degrade individual proteins, the cargo containing vesicles are fused with the lysosome (Broer & Broer 2017). Chaperone mediated autophagy is for digesting selective cytosolic proteins. Single soluble proteins are directed one by one to the lysosome via the assistance of chaperones and lysosomal surface proteins (Kaushik et al 2011). Usually, macroautophagy is referred to as autophagy (Broer & Broer 2017). So the following introduction about the mechanism of macroautophagy uses autophagy directly instead of macroautophagy.

1.5.2 The classical model of (macro)autophagy

A typical autophagy processing can be divided into two main phases; autophagosome formation and autophagosome-lysosome fusion (Yu et al 2018).

Briefly, the initiating process of autophagosome formation is about the activation and recruitment of a series of autophagy related proteins (ATGs). The related complexes are abundant. (Galluzzi et al 2017).

The initiation of autophagosome formation starts from the activation and translocation of serine threonine kinase complex unc-51 like autophagy activating kinase (ULK) complex to ATG9 docked at the ER (Karanasios et al 2016). Then the class III phosphatidylinositol 3 kinase (PtdIns3K kinase) is recruited to produce phosphatidylinositol 3-phosphate (PtdIns3P) and generate a special structure from the ER called omegasome. The omegasome containing PtdIns3P shows affinity to PtdIns3K complex I due to its highly curved region. PtdIns3K complex I can change the lipid composition of the omegasome to convert it into a phagophore (Yu et al 2018). This conversion process at the same time facilitates the exposure or clustering of PtdIns3P, which recruits WIPI2B. WIPI2B is essential for further recruitment of ubiquitin-like (E3-like) complex ATG12-ATG5-ATG16L1 (Dooley et al 2014, Yu et al 2018). The generation of the omegasome from the ER is inferred to be mediated by (N-ethylmaleimide-sensitive-factor attachment receptor) SNARE in yeast (Lemus & Goder 2016). This is the origin of the ER-derived phagophore, with the ER associated exit sites or ER Golgi intermediate compartment is believed to be the source of it (Davis et al 2017, Puri et al 2013).

However, other sources of the phagophore have also been described (Ge et al 2013). The Golgi and the endosome are the organelles which take part in phagophore formation by interacting with ATG9 (Yu et al 2018). It has been shown that the Golgi complex (Mari et al 2010, Yamamoto et al 2012) and Golgi endosomal system (Ohashi & Munro 2010, Shirahama-Noda et al 2013) are the sources of ATG9 vesicles. Furthermore, Src kinase and ULK1 mediate the trafficking of ATG9 vesicles from the Golgi to the endocytic pool (Zhou et al 2017). Electron tomography suggests several other organelles make contact with autophagosomes during autophagy development besides ER, Golgi and endosome (Biazik et al 2015). Several pathways have been reported for the plasma membrane to contribute to

autophagosome formation. Phospholipids can be transported from the plasma membrane through clathrin mediated endocytosis and driven by ATG16L1 (Ravikumar et al 2010). ADP ribosylation factor 6 (ARF6) also contributes to this process (Moreau et al 2012). Another pathway is that membrane together with ATG9 can traffic from the plasma membrane to the recycling endosome through endocytic trafficking pathways. Then the recycling endosome carrying ATG9 fuses with another ATG16L1 driven recycling endosome to continue transport to the phagophore. (Popovic & Dikic 2014, Puri et al 2013). Homotypic fusion regulated by several SNAREs also happens in ATG16L1 containing recycling endosomes. The fusion of recycling endosomes enables the growth of vesicles and the further recruitment of LC3 to promote the formation of ATG16L1 and LC3 double positive phagophore-like structures (Moreau et al 2014, Moreau et al 2011). Direct transport from the recycling endosome to the forming autophagosome is mediated by sorting nexin 18 (SNX18). TBC1D14 can also promote this process (Orsi et al 2012, Webber & Tooze 2010). The mitochondrion is reported to be another source of autophagosomes during starvation through outgrowth of the mitochondrial outer membrane (Hailey et al 2010). Noticeable, lipid droplets as a neutral lipid store can also contribute to autophagosome formation (Dupont et al 2014, Yla-Anttila et al 2009).

As mentioned above, after the omegasome is generated the ubiquitin-like system ATG5-ATG12-ATG16L1 is recruited for complex initiating and at the same time ATG5-ATG12-ATG16L1 complexes mark the site of autophagosome formation. These two events target small vesicles to the forming autophagosome (Dooley et al 2014). In the conjugation of this complex, ATG7 serves as an E1 ubiquitin activating enzyme-like activator to ATG12 in an ATP dependent manner, then E2-like ubiquitin carrier protein ATG10 links ATG12 and ATG5 covalently. The final conjugation is between the paired ATG5-ATG12 and ATG16L dimer (Glick et al 2010). Another ubiquitin like system, the lipidation of ATG8 (Yu et al 2018) which is also called LC3 processing (Glick et al 2010) also contributes to the initiation of the autophagosome.

Here LC3 processing is introduced as an example. The first step is the cleavage of LC3 by the cysteine protease ATG4 (Kumanomidou et al 2006, Satoo et al 2009). After this step LC3 is termed LC3 I. Then E1-like ATG7 actives LC3 I and E2-like ATG3 conjugates phosphatidylethanolamine (PE) to LC3 I to generate LC3 II, finally LC3 II is recruited to the forming autophagosome by ATG5-ATG12 (Galluzzi et al 2017, Glick et al 2010). Another ATG8 member GABARAP undergoes a similar ubiquitin-like transformation to become GABARAP II which is also involved into autophagosome formation (Kirkin et al 2009).

After maturation, autophagosomes start to engulf cytosol (Gatica et al 2018). This loading process of cargo is thought to be random in response to nutrient deprivation. It is called nonselective autophagy. However, in some situations, certain components need to be cleared specifically, such as aggregates of proteins and dysfunctional or abundant organelles (Jin et al 2013). Several organelles have been reported to be recognized and degraded by selective autophagy, such as mitochondria (Ashrafi & Schwarz 2013), peroxisomes (Hutchins et al 1999), lysosomes (Hung et al 2013), ER and the nucleus (Nakatogawa & Mochida 2015).

Q-SNARE Syntaxin 17 (STX17) normally resides on the ER and mitochondria. STX17, which normally is only on the ER, translocates to ER-mitochondria contact sites upon starvation (Hamasaki et al 2013). Autophagy induces the translocation of STX17 to the autophagosome (Yu et al 2018). The translocation of STX17 is regarded to be induced by the completion or almost completion of the autophagosome, and at the same time STX17 is necessary for autophagosome-lysosome fusion because it ensures only the mature autophagosomes fuses with the lysosome (Itakura et al 2012, Tsuboyama et al 2016).

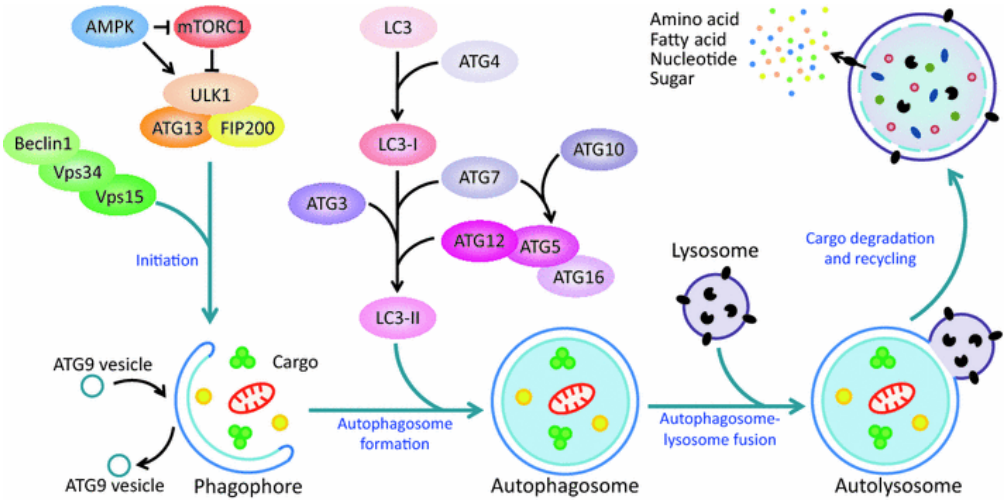

Figure 1.8 Schematic pathway of (macro)autophagy. In responding to upstream signals, assembled ULK1 complex and some other complexes (such as class III PtdIns3 kinase complex) induce the formation of the phagophore. Different sources of membrane contribute to the phagophore/autophagosome formation mainly through ATG9 traffic. By the assistance of two ubiquitin-like systems of ATG5-ATG12-ATG16 (as shown in text normally ATG16L1) and LC3, autophagosome elongates to pack cargoes and finally closes to complete formation. Then autophagosome fuse with lysosome to form autophagolysosome, its cargoes are exposed to lysosomal enzymes to be degraded, the products of degradation are transported out of the lumen. (Cui et al 2016)

Next, the cargo loaded autophagosome fuses with the lysosome/late endosome to complete autophagy. Fusion processes of lysosome and late endosome are regarded to be very similar (Nakamura & Yoshimori 2017). Here the lysosome is used for the introduction. Due to acidification the lysosomes cluster in the peripheral region of the nucleus upon starvation (Heuser 1989), but autophagosomes are formed randomly throughout the cell (Jahreiss et al 2008). To fuse with each other, autophagosomes and lysosomes need to be closed enough. Autophagosomes are linked and then delivered to the perinuclear region along microtubules (Fass et al 2006, Yu et al 2018). Some microtubule motors take part in this transportation, such as Dynein for minus end movement (Jahreiss et al 2008, Kimura et al 2008, Ravikumar et al 2005) and kinesin together with FYVE and coiledcoil domain-containing 1 (FYCO1) for plus end movement (Olsvik et al 2015, Pankiv et al 2010). Besides, actin motors like MYO6/myosin VI and MYO1/myosin I are also reported to be indispensable for fusion (Brandstaetter et al 2014, Tumbarello et al 2012).

Besides cytoskeleton, the tethering factor, SNAREs and phospholipids take part in the complicate fusion process between autophagosome and lysosome (Yu et al 2018).

Tethering factors are various. An important one is homotypic fusion and protein sorting (HOPS) complex (Balderhaar & Ungermann 2013, Rieder & Emr 1997, Seals et al 2000, Solinger & Spang 2013, Wurmser et al 2000). Another tethering complex is the Ras related protein Rab-7 (Rab7) and its adaptors. It is reported that Rab7 recruits pleckstrin homology domain-containing family M member 1 (PLEKHM1) and RILP to bind to vacuolar protein sorting (VPS) 39 and VPS41, the two subunits of HOPS (Wijdeven et al 2016). Rab7-HOPS which can tether membranes of two vesicles has been reported to be required for autophagosome-lysosome fusion (Gutierrez et al 2004, Lurick et al 2017). Rab7 can interact with many different tethering proteins, which is regarded to be important for the specificity of fusion (McEwan et al 2015, Terawaki et al 2015, Wang et al 2016). SNAREs play a core role in autophagosome-lysosome fusion. The interaction between R-SNARE and Q-SNARE, which reside on membranes of different vesicles to form trans-SNARE complex, produces the force needed for fusion (Yu et al 2018). PtdIns3P, Phosphatidylinositol 4-phosphate (PtdIns4P) and Phosphatidylinositol 3,5-bisphosphate (PtdIns(3,5)P2) also contribute to autophagosome-lysosome fusion (Cebollero et al 2012, Chen et al 2012, de Lartigue et al 2009, Nakamura et al 2016, Wang et al 2015a).

The outer membrane of autophagosomes fuses with lysosomes first and then the inner membrane, together with the autophagosomal components, are degraded by the enzymes in the lysosome lumen. The products of degradation are transported out by transporters on the membrane of the autolysosome (Yu et al 2018). The fused vesicle can also be called as autophagolysosome (Klionsky et al 2014).

When autophagy is finished, the last step called autophagic lysosome reformation (ALR) is triggered (Yu et al 2018). The key signal for ALR is the activation of mammalian target of rapamycin (mTOR) (Yu et al 2010).

1.5.3 Initiation regulation and other regulations of (macro)autophagy

As a complex biological process, autophagy includes many steps. Numerous factors and signaling pathways can regulate different steps in different ways. It is impossible to list

all the autophagy regulating elements here. So in this chapter, several relatively direct regulations to autophagy are discussed schematically.

As a mechanism responding to nutrient deprivation, protein aggregation and other stimulations, initiation of autophagy is triggered by multiple signals (Rabinowitz & White 2010). The mTOR signaling pathway is the major signal for autophagy regulation. It is regarded as the hub for integrating various intercellular autophagy related signals (Efeyan & Sabatini 2010). Upon nutrient or growth factors stimulation mTORC1 inhibits ULK1 to weaken autophagy. On the contrary, nutrient depletion or other stresses inactivate mTORC1 to trigger autophagy. Another mTOR complex mTORC2 can positively regulate mTORC1 (Rabinowitz & White 2010). The adenosine monophosphate activated protein kinase (AMPK) pathway is regarded to be a sensor for energy and to function upstream of mTORC1. It is activated by adenosine monophosphate (AMP), indicating low cellular energy levels, to enhance autophagy by inhibiting mTORC1 (Rabinowitz & White 2010, Shackelford & Shaw 2009). AMPK has been also reported to directly phosphorylate ULK1 to induce autophagy (Kim et al 2011).

In addition to classical signaling pathways, other types of regulation have also been reported to trigger autophagy. For example, insulin like growth factor 1- phosphoinositide 3 kinase-Akt (also known as protein kinase B (PKB)) (IGF1-PI3K-Akt) is reported to induce autophagy, not only through mTOR, but also slowly through forkhead box protein O3 (FoxO3) the transcription factor which can be activated to induce the transcription of ATGs genes (Zhao et al 2007). Particularly, mitophagy, the type of autophagy degrading mitochondria, can be induced by hypoxia and hypoxia inducible factors (HIFs) through promoting the transcription of related genes (Zhang et al 2008). Additional, some hormones or metabolites can also trigger autophagy. For instance, glucagon a hormone secreted upon fasting and activation of the adrenergic receptor can trigger autophagy in the liver through activating adenylate cyclase to increase levels of cyclic adenosine monophosphate (cAMP)

(Rabinowitz & White 2010). Ammonia induces autophagy in weakly perfused tissues and tumors (Eng et al 2010).

As mentioned above, to initiate autophagosome formation ATG9 is very important to drive membranes to the recycling endosome or growing autophagosome. This traffic of ATG9 can be regulated by a series of factors including ULK complex (has mentioned), p38α (also known as mitogen-activated protein kinase 14(MAPK14)) (Webber & Tooze 2010), Rab11and TBC1D14 (have mentioned), transport protein particle III (TRAPPIII) (Lamb et al 2016), clathrin coats contained AP2 17 and bax interacting factor 1 (Bif1) -Dynamin 2 (Takahashi et al 2016). The substrate sphingomyelin has also been reported to regulate ATG traffic to recycling endosomes as an inhibitor (Corcelle-Termeau et al 2016). Actually, a more direct regulation is to alter the phosphorylation status of ATG9. The ULK1 complex and AMPK have been suggested to be able to alter it (Corcelle-Termeau et al 2016, Mack et al 2012, Weerasekara et al 2014). Besides, Src kinase and ULK1 can also mediate ATG9 phosphorylation (Zhou et al 2017).

During the fusion phase, Rab7 connects many tethering proteins. As a Ras related GTP binding protein, many GTP/GDP exchange factors (GEFs) and Rab GTPase activating proteins (GAPs) can regulate fusion processes through affecting Rab7 (Hegedus et al 2016, Itoh et al 2011). The regulation of Rab7 can also determine the specificity of fusion between lysosome/late endosome and autophagosomes such as Rab7 effector, ectopic P-granules autophagy protein 5 homolog (EPG5), which binds to the lysosomal/late endosomal Rab7 and R-SNARE VAMP7/8 and at the same time to autophagosomal LC3/LGG-1 (C.elegans homolog of LC3) and STX17-SNAP29 to facilitate recruitment of and further stabilize trans-SNARE complexes to guarantee the specificity of fusion (Wang et al 2016). The SNARE complex is another target for the regulation of fusion. For example, ATG14 promotes fusion by binding to STX17 to stabilize binary Q-SNARE complex STX17-SNAP29 (Diao et al 2015), on the contrary, O-GlcNAcylation (attachment of O-linked N-acetylglucosamine) of

SNAP29 SNARE which is negatively correlated with nutrient levels interferes with the trans-SNARE assembly (Guo et al 2014).

As a special factor, Bafilomycin A1 is a broadly utilized inhibitor for autophagosome-lysosome fusion through the inhibition of Ca^{2+} release from the sarco/endoplasmic reticulum by inhibiting Ca^{2+}-ATPase (SERCA) (Mauvezin & Neufeld 2015)..

1.6 V-ATPase drives acidification

1.6.1 V-ATPase functions

V-ATPases are short for vacuolar H^+-ATPases which are proton pumps. The proton transport activity of these pumps is driven by ATP hydrolysis, V-ATPases broadly reside in many different membranes of many different kinds of cell types (Breton & Brown 2013, Cotter et al 2015, Forgac 2007, Kane 2012, Marshansky et al 2014, Sun-Wada & Wada 2013). The following introduction is mainly about eukaryote V-ATPase. V-ATPase is a large multiprotein complex which comprises two main domains, cytosolic V1 domain, which is responsible for ATP hydrolysis, and the membrane docked V0 domain, which is for proton transmembrane transport (Forgac 2007). Each domain consists of many subunits. V1 domain subunits include A, B, C, D, E, F, G and H. V0 is composed by the conservative subunits a, d, e, c and c'', in yeast another c' subunit is also needed, but in evolutionally higher eukaryotes an accessory protein Ac45 is essential (Forgac 2007).

V-ATPases perform numerous functions in different cells, but the core function is to drive acidification by pumping and accumulating protons (Holliday 2014). Here V-ATPase dependent acidification and other related functions are schematically introduced.

The diverse functions of V-ATPase in endocytosis and exocytosis are mediated through acidification (Forgac 2007). The most well-known acidification by V-ATPase is for endosome and lysosome. The lumen of endosomal organelles is acidified during the endocytosis from the plasma membrane to the lysosome. At the same time acidity of the lumen and assembly of the V-ATPase are continuously enhanced (Lafourcade et al 2008). Actually, decreased pH by acidification in endosomes is important for receptor endocytosis

and vesicular trafficking (Scott & Gruenberg 2011). After internalization, receptor ligand complexes are exposed to the acid endosome lumen, which allows for the release and recycling of the receptor and ligand to the plasma membrane (Maxfield & McGraw 2004). The pH in the lysosome lumen is maintained at 4.5 by the V-ATPase. This is required for acid hydrolase synthesized in Golgi to be transported to and active in the lysosome (Pamarthy et al 2018). Besides, the acid environment in the autophagolysosome lumen during (macro)autophagy is crucial for maintaining activity of digestive enzymes (Saftig & Klumperman 2009), and acidification through the V-ATPase is thought to provide the acid environment for acid hydrolases and cargo degradation (Kissing et al 2015).

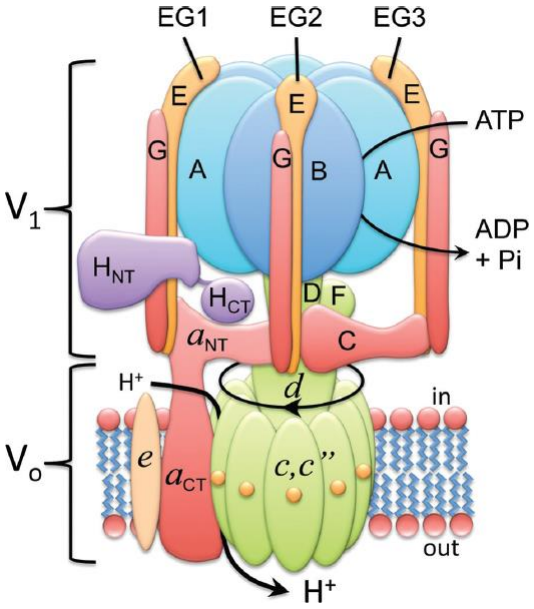

Figure 1.9 Schematic structure and proton transportation mechanism of V-ATPase. V-ATPase mainly consists of two domains, cytosolic V1 domain and integral V0 domain. Each domain is composed by many subunits, subunits A, B, C, D, E, F, G, H for V1 domain, a, c, c'', d, e for V0 domain in animals (Composition may variate in different species, see text). V1 domain is responsible for ATP hydrolysis which drives the rotation of catalytic domain in V1 domain and associated proteolipid ring in V0 domain. Proton enters and binds to proteolipid ring, finally it is released to another side of membrane. (McGuire et al 2017)

The plasma membrane localized V-ATPase functions in proton secretion (Breton & Brown 2007). The acidification of the extracellular lumen by V-ATPase exists in different organs. For example, acid base homeostasis and acidification of urine are regulated by V-ATPase with a subunit isoform 4 in epithelial cells of kidney proximal tubule (Brown et al 2009, Karet 2005). Mutants in V-ATPase subunits cause recessive distal renal tubular

acidosis and deafness (Smith et al 2000). Besides kidney, plasma membrane localized V-ATPase with subunit a isoform 4 is also expressed in the ear. Subunit a isoform 4 knockout mice are found to suffer the severe metabolic acidosis, impaired hearing and smell sense after weaning. These mice can survive only with alkali supplementation (Norgett et al 2012). Furthermore, bone resorption requires V-ATPase acidification of lacunae in osteoclasts (Qin et al 2012) and V-ATPase dysfunction causes osteoporosis (Kartner & Manolson 2014). Additional, sperm maturation and storage induce V-ATPase luminal acidification in clear cells of the epididymis (Jaiswal et al 2015). Plasma localized V-ATPase may take part in proton secretion from the olfactory epithelial cells base (Paunescu et al 2008). Furthermore, deficiency of the B subunit isoform 1 leads to olfactory dysfunction (Paunescu et al 2012). Vision sense related cells are also found to require proton transportation across the cell membrane by V-ATPase. Mutations of V-ATPase lead to ocular pathologies (Shine et al 2014).

On the one hand, V-ATPase plays a crucial role in endocytosis, on the other hand, endocytosis itself can regulate multiple signaling pathways (Marshansky & Futai 2008, Sorkin & von Zastrow 2009). Thus, V-ATPase activity can indirectly regulate signal transduction (Pamarthy et al 2018, Sun-Wada & Wada 2015).

V-ATPase has been reported to regulate Notch signaling (Fischer et al 2012, Lange et al 2011, Lee et al 2010, Sethi et al 2010, Valapala et al 2013). Other signaling associating with V-ATPase are Wnt (Cruciat et al 2010, Gao et al 2010, Ichihara 2012, Rousselle et al 2014) and TGF-β (Cao et al 2012, Fischer et al 2012, Pamarthy et al 2016). Finally, mTOR signaling in response to amino acid stimulation needs to be recruited to the lysosome, which needs the activation of Guanine Exchange Factor (GEF) in Ragulator by V-ATPase (Kim & Guan 2015, Zoncu et al 2011). And interference of subunit C expression is found to reduce activity of mTORC1 (McConnell et al 2017).

1.6.2 Regulation of V-ATPase activity

Assembly and disassociation of the V-ATPase are important ways to regulate V-ATPase activity (Cotter et al 2015). Many factors have been identified to regulate V-ATPase assembly. In yeast Ras/cAMP/ protein kinase A (PKA) signaling facilitates V-ATPase assembly in response to glucose restimulation following glucose starvation (Bond & Forgac 2008). Furthermore, pH is also known to regulate V-ATPase assembly. A neutral extracellular pH is reported to prevent disassembly of the V-ATPase (Diakov & Kane 2010). Increased cytosolic pH also promotes V-ATPase assembly via the PKA pathway (Dechant et al 2010). Furthermore, glycolytic enzymes aldolase (even without catalytic activity) (Lu et al 2007) and phosphofructokinase (Chan & Parra 2014) can directly interact with V-ATPase to facilitate assembly. The regulation of phosphofructokinase is through binding to regulator of the ATPase of vacuolar and endosomal membranes (RAVE) (Chan & Parra 2014). RAVE is a V-ATPase assembly factor (Smardon et al 2014), and is thought to bind to the V1 domain to stabilize the activity of the V-ATPase (Kane 2012).

In mammalian cells PtdIns3K together with ERK mediates V-ATPase dependent intracellular pH change (Marjuki et al 2011). PtdIns3K mediates glucose stimulated V-ATPase assembly (Sautin et al 2005). However, glucose starvation is also reported to increase V-ATPase assembly through the PI3K/Akt pathway. Furthermore, high concentration of glucose and glucose starvation both induce V-ATPase assembly (McGuire & Forgac 2018, Stransky & Forgac 2015). AMPK inhibits proton pumping by phosphorylating subunit A of the V-ATPase, inhibiting V-ATPase assembly (Alzamora et al 2013). EGF also increases V-ATPase assembly and activates mTORC1 (Xu et al 2012). V-ATPase assembly can also be facilitated by amino acid starvation (Stransky & Forgac 2015), it is reasonable to link amino acid starvation and mTOR regulated autophagy generating amino acids, but interestingly amino acid starvation induced V-ATPase assembly show independent of PI3K and mTORC1 (Stransky & Forgac 2015).

There are also some V-ATPase assembly regulators, such as Zinc transporter (ZnT)2 (Rivera et al 2018), Transmembrane protein (TEME)9 (Jung et al 2018), Vacuolar ATPase

assembly integral membrane protein (VMA)21 (Ramachandran et al 2013), Coiled-coil domain-containing protein (CCDC)115 and TEME199 (Miles et al 2017).

Besides assembly regulation, traffic of V-ATPase is another aspect affecting V-ATPase activation, especially in epithelial cells secreting proton because V-ATPase can localize to plasma membrane to pump protons out of cell at least in some cells (Breton & Brown 2013, Cotter et al 2015). The different subunit isoforms also alter V-ATPase activity, for example subunit a was reported to regulate the different cellular destinations of the V-ATPase by expression of different isoforms of subunit a (Breton & Brown 2013, Finnigan et al 2012, Forgac 2007, Sun-Wada & Wada 2013). Different subunit a isoforms are thought to maintain different pHs as a mechanism to modulate V-ATPase activity (McGuire et al 2017).

Actually, some researches have also revealed the direct regulation which is independent of assembly and traffic to V-ATPase activity. For example, Serine/threonine-protein kinase STE20 (STE20) the Cell division control protein 42 homolog (Cdc42) effector in yeast directly regulate V-ATPase activity by interacting with H subunit of V-ATPase (Lin et al 2012). Without altering assembly, Heme Responsive Gene 1 (HRG1) is found to facilitate V-ATPase activity (O'Callaghan et al 2010). Some regulation factors of V-ATPase in the kidney have been identified (Merkulova et al 2015).

As a more fundamental regulation way, mTORC1 can regulate gene expressions of some subunits of V-ATPase mediated by transcription factor EB (TFEB) (Pena-Llopis et al 2011).

1.7 The amino acid transporter PAT2 is specifically expressed in brown adipocytes

PAT2 (also known as SLC36A2 or transmembrane domain rich protein 1 (Tramdorin1)) is a proton coupled amino acid transporter, which belongs to the SLC36 family (Schioth et al 2013, Thwaites & Anderson 2011). The SLC36 family constitutes 4 members, SLC36A1 (PAT1), SLC36A2 (PAT2), SLC36A3 (PAT3) and SLC36A4 (PAT4), which are all proton coupled transporters for small neutral amino acids (Schioth et al 2013). The transport

mechanisms of PAT1, PAT2 and PAT4 have been characterized, but less is known for the orphan transporter PAT3 (Schioth et al 2013, Thwaites & Anderson 2011). PAT1 (Boll et al 2002, Sundberg et al 2008) and PAT4 (Pillai & Meredith 2011, Sundberg et al 2008) are distributed broadly, but PAT2 is not expressed as broadly as PAT1 and PAT4 (Schioth et al 2013, Sundberg et al 2008).

PAT2 mRNA is detected in heart, lung, kidney, skeletal muscle, spleen and brain in mouse (Boll et al 2003, Boll et al 2002, Rubio-Aliaga et al 2004, Vanslambrouck et al 2010). In rat it is found in adipose tissue, spleen, lung, skeletal muscle, kidney, heart and brain (Chen et al 2003, Foltz et al 2004b, Sundberg et al 2008), in human it is in the kidney and skeletal muscle (Bermingham & Pennington 2004a, Nishimura & Naito 2005). PAT2 is also detected in bone marrow and adipose tissue in mice by *in situ* hybridization (Bermingham & Pennington 2004a). PAT2 expression in 3T3-L1 cell line has also been reported (Zebisch & Brandsch 2013). PAT2 is thought to localize to the plasma membrane (Boll et al 2004), and not the lysosome as PAT1 (Bermingham et al 2002). Further research has confirmed the plasma membrane localization and revealed by far highest expression of PAT2 in BAT (Ussar et al 2014).

It has been reported that PGC1 coactivators alter the expression of PAT2 (Uldry et al 2006). The expression of PAT2 is found to be decreased in the sciatic nerves of POU Class 3 Homeobox 1(pou3f1)-null mice (Bermingham et al 2002). PAT2 expression also changes during murine kidney development. PAT2 mRNA levels increase to 5.3 times from day 0 to day 7, then decrease to 20% of the peak at day 14 (Vanslambrouck et al 2010). Comparing to other PATs, PAT2 and PAT1 both show high affinity to glycine, alanine and proline, the differences are shown in the transportation of some modified amino acids (Schioth et al 2013, Thwaites & Anderson 2011). PAT2 has a much narrower substrate specificity than PAT1 (Rubio-Aliaga et al 2004). Comparing with the low affinity high capacity PAT1, the affinity of PAT2 to substrates is found to be higher than PAT1 (Thwaites & Anderson 2011). This may implicate the different roles of PAT2 and PAT1 in cells. Half maximal transport

rates of PAT2 occur in an extracellular pH range from 7.4-9.3 (Boll et al 2002, Foltz et al 2004b, Kennedy et al 2005, Rubio-Aliaga et al 2004). Membrane depolarization is also found to reduce the proton affinity of PAT2 at the range of −120 to −20 mV (Foltz et al 2004b). Additional, the transportation of PAT2 is bidirectional, influx or efflux depends on the concentration gradient of substrate, pH and membrane potential (Edwards et al 2011, Kennedy et al 2005, Rubio-Aliaga et al 2004).

The precise functions of PAT2 are not clear, but some early studies have shown that mutations in PAT2 lead to iminoglycinuria and hyperglycinuria through impaired amino acid absorption in the renal proximal tubule (Broer et al 2008). Molecularly PATs are found to interact with and regulate the mTOR pathway (Goberdhan et al 2005a, Suryawan et al 2013).

2 Material and methods

2.1 Material

2.1.1 PAT2 knockdown and overexpression cell lines

The previously established murine brown preadipocyte cell line BAT1 derived from 8 weeks old C57Bl/6 mouse (Pramme-Steinwachs et al 2017) was used to generate Scramble, PAT2 knockdown and overexpression cell lines.

As the control cell line, the Scramble cell line is BAT1 cell line containing non-target shRNA control pLKO.1-puro plasmid.

PAT2 knockdown cell lines are BAT1 cells containing PAT2 shRNA with different targeting sequences.

PAT2 overexpression cell line is BAT1 cells containing pCDH-CMV-PAT2-HA-puro plasmid.

2.1.2 Wild type mice in the fast experiment

All the wild type mice in the fast experiment are purchased. Mouse lines of these wild type mice are C57/BL6J or C57BL/6N. The ages are eight weeks old.

2.1.3 Adipose tissue specific Kindlin-2 knockout mice

Kindlin2 knockout first allele mouse (Fermt2tm1a(EUCOMM)Wtsi, reporter-tagged insertion with conditional potential) was from IMPC. Colony name: GSF-EPD0087_1_G04-1. Genetic background: C57BL/6NTac/Den.

The mouse was mated with flp mouse to remove LacZ and neo cassettes. The Kindlin-2$f^{l/+}$ $flp^{+/-}$ or Kindlin-$2^{fl/+}$ $flp^{+/-}$ mice were selected. For the following breeding, these mice were mated with each other to get Kindlin-$2^{fl/+}$ or Kindlin-$2^{fl/fl}$ mice without flp. Next, Kindlin-$2^{fl/+}$ or Kindlin-$2^{fl/fl}$ mice were mated with Adiponectin-Cre^{+} mice to get Kindlin-$2^{fl/-}$ Adiponectin-Cre^{+} or Kindlin-$2^{fl/+}$ Adiponectin Cre^{-} mice. Kindlin-$2^{fl/+}$ Adiponectin-Cre^{+} mice were further mated with Kindlin-$2^{fl/+}$ Adiponectin Cre^{-} to get Kindlin-$2^{fl/fl}$ Adiponectin Cre^{+}, Kindlin-$2^{fl/fl}$ Adiponectin Cre^{-} and Kindlin-$2^{fl/+}$ Adiponectin Cre^{+} mice for verifying Kindlin-2 knockout. Finally, Kindlin-2 adipose tissue conditional knockout mice for experiments were from matings of Kindlin-$2^{fl/fl}$ Adiponectin Cre^{+} with Kindlin-$2^{fl/fl}$ Adiponectin Cre^{-}.

Figure 2.1 Gene structure of Fermt2$^{tm1a(EUCOMM)Wtsi}$ mice. (From IMPC website)

2.1.4 Whole body PAT2 knockout mice

The chimera mice generated by PAT2 knockout embryonic stem cells injection were from Dr. Ingo Burtscher as a gift. Then chimera mice were bred with wild type mice, the heterozygotes in the next generation were continuously mated with wild type mice to acquire steady PAT2 heterozygous knockout mice. To remove neo sequence at two terminals, heterozygotes mice were hybridized with Rosa26 Cre mice, Cre recombinase will cut the neo cassette off from two locus of X-over P1 (LoxP) sites in $PAT2^{+/-}$, Cre^{+} mice. Then neo free $PAT2^{+/-}$, Cre^{+} mice were again mate with wild type mice to select neo free $PAT2^{+/-}$, Cre^{-} mice. $PAT2^{-/-}$ mice can be acquired from mating between $PAT2^{+/-}$, Cre^{-} mice. Mouse line is C57/BL6N.

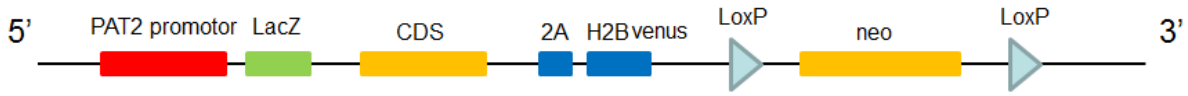

Figure 2.2 Gene structure of PAT2 knockout elements.

2.1.5 Reagents, consumable materials and instruments

Table 2.1 Reagents

Regent	Manufacturer
DMEM, High glucose, GlutaMAX Pyruvate, Dulbecco's Modified Eagle Medium	Thermo Fisher Scientific
Polyfect	Quiagen
PEG-it virus precipitation solution (5 ×)	Biocat
HEPES	Carl Roth
DPBS	Thermo Fisher Scientific
Polybrene Hexadimethrine bromide	Sigma-Aldrich
Puromycin (hydrochloride)	Biomol
Fetal Bovine Serum (FBS)	Thermo Fisher Scientific
100 × Penicillin-Streptomycin (10,000 U/mL)	Thermo Fisher Scientific
Trypsin-EDTA (0.05%), phenol red	Thermo Fisher Scientific
Dimethylsulfoxid (DMSO)	Carl Roth
3-Isobutyl-1-methylxanthine (IBMX)	Sigma-Aldrich
Potassium hydroxide	Carl Roth
Dexamethasone	VWR international (Sigma-Aldrich)
Indomethacin	Santa-Cruz
3,3',5 Triiodo-L-Thyronine (T3)	Merck Millipore
Insulin Solution, Human (10mg/ml)	Sigma-Aldrich
Rosiglitazone	Sigma-Aldrich
DMEM w/o glutamine, w/o amino acids, with 1g/L glucose	GENAXXON bioscience
2-Propanol (Isopropanol)	Merck Millipore
Dialyzed FBS	Thermo Fisher Scientific
D(+)-Saccharose, D(+)-Sucrose	Carl Roth
Ethylendiamin-tetraessigsäure (Ethylenediaminetetraacetic acid (EDTA))	Carl Roth
TRIS, Tris(hydroxymethyl)aminomethane (Tris)	Carl Roth
Hydrochloric acid	Carl Roth
Ficoll 400	Sigma-Aldrich
SDS, Sodium dodecyl sulfate	Carl Roth
Seahorse XFe96 FluxPaks	Agilent Technologies, Seahorse
Oligomycin	Merck Millipore
FCCP, Carbonyl cyanide-4-(trifluoromethoxy)phenylhydrazone	R&D systems
Rotenone	Sigma-Aldrich
Antimycin A from Streptomyces sp.	Sigma-Aldrich
2-Deoxy-D-glucose	ALFA AESAR
D(+)-Glucose	Carl Roth
MEM Amino Acids (50 ×) solution	Sigma-Aldrich
Quant-iT PicoGreen dsDNA reagent	Bio-Rad
iTaq Universal SYBR Green Supermix	Bio-Rad
Hard-Shell 384 well standard PCR plates	Bio-Rad
RNeasy Mini Kit	QIAGEN
QIAGEN Plasmid Plus Midi Kit	QIAGEN

QIAprep Spin Miniprep Kit	QIAGEN
Ethanol	Merck Millipore
Trichlormethan/Chloroform	Carl Roth
QIAzol Lysis Reagent	QIAGEN
Stainless Steel Beads, 5 mm	QIAGEN
High-Capacity cDNA Reverse TranScription Kit	Applied Biosystems
Water for PCR	Merck Millipore
Phosphatase Inhibitor Cocktail 2 aqueous solution	Sigma-Aldrich
Phosphatase Inhibitor Cocktail 3 DMSO solution	Sigma-Aldrich
Protease Inhibitor Cocktail	Sigma-Aldrich
Pierce BCA Protein Assay Kit	Thermo Fisher Scientific
MOPS, 3-(N-morpholino)propanesulfonic acid	Carl Roth
MES, 2-(N-morpholino)ethanesulfonic acid	Carl Roth
NuPAGE 4-12% Bis-Tris Protein Gels	Thermo Fisher Scientific
NativePAGE 3-12% Bis-Tris Protein Gels	Thermo Fisher Scientific
NativePAGE™ Running Buffer Kit	Thermo Fisher Scientific
NativePAGE™ Sample Prep Kit	Thermo Fisher Scientific
Acetic acid 100 %	Carl Roth
Non-fat skimmed milk powder	Biomol
Sodium chloride	Carl Roth
Tween-20	Santa-Cruz
NuPAGE™ LDS Sample Buffer (4 ×)	Thermo Fisher Scientific
Fisher BioReagents EZ-Run Prestained Rec Protein Ladder	Fisher Scientific
NativeMark Unstained Protein Standard	Thermo Fisher Scientific
Albumin Fraktion V	Carl Roth
Immobilon Western Chemiluminescent HRP Substrate, Immobilon Western Chemiluminescent Horseradish Peroxidase Substrate	Thermo Fisher Scientific
Restore PLUS Western Blot Stripping Buffer	Thermo Fisher Scientific
Pierce IP Lysis Buffer	Thermo Fisher Scientific
Protein A/G PLUS-Agarose	Santa-Cruz
Fluorescence Mounting Medium	Dako
Triton™ X-100	Sigma-Aldrich
DAPI, 4',6-Diamidino-2-Phenylindole, Dihydrochloride	Thermo Fisher Scientific
PFA, Paraformaldehyde	Sigma-Aldrich
Live Cell Imaging Solution	Thermo Fisher Scientific
Collagen, Type I solution from rat tail	Sigma-Aldrich
Sodium azide	Sigma-Aldrich
Glycerol	Carl Roth
Kaliumchlorid, Potassium chloride	Carl Roth
Magnesiumchlorid, Magnesium chloride	Carl Roth
αβ-methylene ATP, α,β-Methyleneadenosine 5'-triphosphate	Cayman Chemical
FITC-Dextran, Fluorescein isothiocyanate–dextran average mol wt 70000, (FITC:Glucose = 1:250)	Thermo Fisher Scientific
Glucose 20 % B. Braun Injektionslösung, Glucose 20% Injection	B. Braun
Isotonische Kochsalzlösung 0,9 %, Isotonic saline 0.9%	B. Braun
Insulin Injection	BANF
Glutaraldehyde solution Grade I	Sigma-Aldrich
Ketamin 10%, ketamine 10%	Bremer Pharma

Xylazine HCl Injection 100mg/ml	VETTEK
Evans Blue	Sigma-Aldrich
Xylene (isomers)	Carl Roth
Paraplast	Carl Roth
O.C.T. compound, OCT compound	Tissue-Tek
Agarose, low gelling temperature	Sigma-Aldrich
Mayers Hämalaunlösung, Mayer haematoxylin solution	Merck Millipore
Chromotrope 2R, Chromotrope II	ALFA AESAR
Roti-Mount	Carl Roth
Picric acid solution	Sigma-Aldrich
Formaldehydlösung 37 %, Formaldehyde soution 37%	Carl Roth
Hematoxylin	Carl Roth
Iron(III) chloride, Ferric chloride	Sigma-Aldrich
Methanol	Merck Millipore
Biebrich scarlet	Schubert und Weiss
Fuchsin sauer, acid fuchsin	Schubert und Weiss
Phosphomolybdic acid hydrate, 80%,	Fisher Scientific
Phosphotungstic acid hydrate	Fisher Scientific
Aniline Blue	Fisher Scientific
Direct Red 80, Sirius Red	Sigma-Aldrich
Azocarmine G	Fisher Scientific
Anilin zur Synthese, Aniline for synthesis	VWR international (Merck Millipore)
Orange G	Carl Roth
Methyl Blue	Sigma-Aldrich
MitoTracker Red FM	Thermo Fisher Scientific
Hrodo Red AM Intracellular pH Indicator	Thermo Fisher Scientific
Rapamycin, 2.5 mg/mL in DMSO (2.74 mM)	Sigma-Aldrich
Bafilomycin A1 from *Streptomyces griseus*	Sigma-Aldrich
Concanamycin A	Santa-Cruz
Filipin complex ready made solution 5mg/ml in DMSO	Sigma-Aldrich
Methyl-β-cyclodextrin	Sigma-Aldrich
Chlorpromazine hydrochloride	Sigma-Aldrich
Dynasore hydrate	Sigma-Aldrich
MHY1485	Sigma-Aldrich
3BDO	Sigma-Aldrich
Chow diet	Brogaarden
High fat diet	Brogaarden
AGAROSE MOLECULAR BIOLOGY REAGENT	Sigma-Aldrich
Biomol 1kb DNA Ladder, ready-to-use	Biomol
peqGREEN non-toxic DNA/RNA Dye	PeqLab
G418	Santa-Cruz
autoMACS Running Buffer – MACS Separation Buffer	Miltenyi Biotec
autoMACS Pro Washing Solution	Miltenyi Biotec

1 L PBS (10 ×): Dissolve 80 g NaCl, 2 g KCl, 14.4g Na_2HPO_4, 2.4g KH_2PO_4 in 800 ml double distilled water. Adjust pH to 7.4. Add double distilled water to 1 L.

1 L TBS (10 ×): Dissolve 6.05 g Tris and 8.76 g NaCl in 800 mL double distilled water. Adjust pH to 7.6 with 1 M HCl. Make volume up to 1 L with high purity distilled or deionized water.

RIPA lysis buffer: Dissolve 50mM Tris (pH=7,4), 150mM NaCl, 1mM EDTA, 1% Triton X100 in double stilled water. Store the buffer at 4°C.

Table 2.2 Antibodies

Antibody	Manufacturer	Application and dilution
HA-Tag (6E2) Mouse mAb (HRP Conjugate)	Cell Signaling Technology	WB 1 : 2000
HA-tag Rat	Roche	IP 1 : 200
PPARγ (C26H12) Rabbit mAb	Cell Signaling Technology	WB 1 : 1000
UCP-1 Rabbit	Gift from Prof. Martin Jastroch	WB 1 : 5000
Anti-LAMP1 antibody Rabbit polyclonal	Abcam	WB 1 : 1000 IF 1 : 100
EEA1 Rabbit	Cell Signaling Technology	IF 1 : 100
Golgin-97 (D8P2K) Rabbit mAb	Cell Signaling Technology	IF 1 : 100
COX IV (4D11-B3-E8) Mouse mAb	Cell Signaling Technology	IF 1 : 100
mTOR (7C10) Rabbit mAb	Cell Signaling Technology	WB 1 : 1000 IF 1 : 100
Phospho-mTOR (Ser2448) (D9C2) XP Rabbit mAb	Cell Signaling Technology	WB 1 : 1000
β-Actin (C4) HRP	Santa-Cruz	WB 1 : 5000
Phospho-p70 S6 Kinase (Thr389) (108D2) Rabbit mAb	Cell Signaling Technology	WB 1 : 1000
p70 S6 Kinase (49D7) Rabbit mAb	Cell Signaling Technology	WB 1 : 1000
LC3A/B (D3U4C) XP Rabbit mAb	Cell Signaling Technology	WB 1 : 1000
Anti-LAMP1 antibody [H4A3] Mouse monoclonal	Abcam	IF 1 : 10
RagC (D31G9) XP Rabbit mAb	Cell Signaling Technology	WB 1 : 1000
ATP6V1B2 (D3O7Q) Rabbit mAb	Cell Signaling Technology	WB 1 : 1000
Anti-ATP6V0D1 antibody [EPR18320-38] Rabbit monoclonal	Abcam	WB 1 : 2000
GAPDH Antibody (D-6) HRP	Santa-Cruz	WB 1 : 5000
OxPhos Rodent WB Antibody Cocktail	Thermo Fisher Scientific	WB 1 : 1000
Kindlin-2 Antibody	Cell Signaling Technology	WB 1 : 1000
Integrin β1 (D6S1W) Rabbit mAb	Cell Signaling Technology	WB 1 : 1000
Anti-rabbit IgG, HRP-linked Antibody	Cell Signaling Technology	WB 1 : 5000
goat anti-mouse IgG-HRP	Santa-Cruz	WB 1 : 5000
Alexa Fluor 488 AffiniPure Donkey Anti-Rat IgG (H+L)	Jackson ImmunoResearch	IF 1 : 500
Alexa Fluor 488 AffiniPure Rat Anti-Mouse IgG (H+L)	Jackson ImmunoResearch	IF 1 : 500
Alexa Fluor 647 Goat Anti-Rabbit	Thermo Fisher Scientific	IF 1 : 500

Alexa Fluor 594 AffiniPure Goat Anti-Rabbit IgG (H+L)	Jackson ImmunoResearch	IF 1 : 500

Table 2.3 Instruments

Name	Manufacturer
Iris Scissors - CeramaCut Straight 11.5cm	Fine Science Tools
Student Surgical Scissors	Fine Science Tools
Dumont #5 Forceps - Assorted Styles	Fine Science Tools
Dumont #5 Forceps - Assorted Styles, Biology	Fine Science Tools
Student Dumont Forceps	Fine Science Tools
Dissecting Chisel	Fine Science Tools
Forceps, Pinzetten m. Zähnen 1 : 2, Stahl 18/10, 130mm lang	bochem
Forceps, Pinzette, Stahl 18/10, stumpf, gerade, 105mm lang	bochem
Tube for Potter-Elvehjem Tissue Grinder	Fisher Scientific
ROTMARDER-PINSEL GR.1 / 9MM M.SILBERZWINGE, SCHWARZLACK.STIEL, 1 PAK	Th. Geyer
ROTMARDER-PINSEL GR.2 / 11MM M.SILBERZWINGE, SCHWARZLACK.STIEL, 1 PAK	Th. Geyer
Homogenisatorpistill nach Potter-Elvehjem, Glas 1 ml	Fisher Scientific
CFX384 Touch™ Real-Time PCR Detection System	Bio-Rad
EchoMRI™ 3-in-1 Body Composition Analyzer Product Specifications	EchoMRI
Blood glucose meter, FreeStyle Freedom Lite	FreeStyle
Blood Glucose FreeStyle Lite test strips	FreeStyle
EVOS XL Core Cell Imaging System	Thermo Fisher Scientific
Confocal microscope, Leica TCS SP5	Leica
Tissue Embedding Station	Leica
Rotary Microtome	Leica
Cryostat	Leica
Vibratome	Leica
Upright microscope, Axio Scope.A1 Pol	ZEISS
Living cell imaging system, The Cube & The Box	LIFE IMAGING SERVICES
Eppendorf ThermoMixer	Eppendorf
Heracell™ 240i CO2 Incubators	Thermo Fisher Scientific
Waterbath	Memmert
Ultracentrifuge, Optima MAX-XP	Beckman Coulter
Centrifuge 5430 R	Eppendorf
Electronic multichannel pipettes, Eppendorf Xplorer® plus	Eppendorf
Stepper, Multipette® E3	Eppendorf
Pipettes and multichannel pipettes Eppendorf Research® plus	Eppendorf
ST16R Refrigerated Centrifuge	Thermo Fisher Scientific
Seahorse XFe96 Analyzer	Agilent
XF Prep Station	Agilent
NanoDrop™ 2000 Spectrophotometers	Thermo Fisher Scientific
TissueLyser II	QIAGEN

Tissue homogenizer, POLYTRON® PT 2500 E	Kinematica
Eppendorf 6331 Nexus Gradient MasterCycler Thermal Cycler	Eppendorf
BioImaging gel documentation system	UVP
Agfa Curix 60 (developer)	AGFA
CFX384 Touch™ Real-Time PCR Detection System	Bio-Rad
Probe Sonicator Model 150VT (Ultrasonic Homogenizer)	BioLogics
Plate reader, PHERAstar FS	BMG LABTECH
Flow cytometer, MACSQuant® Analyzer 10	Miltenyi Biotec
2132 Microperpex® Peristaltic Pump	LKB Bromma

Table 2.4 Consumable materials

Name	Manufacturer
Tip, SurPhob Spitzen, 10 µl, extra lang, farblos Low Binding, graduiert,10 Reloads	Biozym
Tip, SurPhob Spitzen, 10 µl, extra lang, farblos graduiert,	Biozym
Multichannel tips, epTIPS set, 0,1 bis 20µl	Schubert und Weiss
Multichannel tips, epTIPS Reloads, PCR clean, 0,1 bis 20µl	Schubert und Weiss
Tips, SurPhob Spitzen, 200 µl, farblos Low Binding, graduiert,10 Racks à 96 Stück	Biozym
Tips, Spitzen, 200 µl, gelb, 10 Reloads	Biozym
Tips, epTIPS Reloads, 200µl, 10 Trays à 96 Spitzen	Schubert und Weiss
Refill Tips Tipone 100-1000 960St	STARLAB
Tips, Quali-Pipettenspitzen, 100-1200µl	Kisker Biotech
Tips, Plastipak TBC-Spritzen 1 ml Luer, 3-tei	Wagner und Munz
Syringes, OMNICAN TUB M KAN 0.33X12	Neolab
Einmalspritzen Injekt Solo, 10ml, Pck à 100 (syringe for filter)	Schubert und Weiss
Combitips, 0,1 ml, biopur, 100 Stk. (for stepper pipette)	Schubert und Weiss
Combitips advanced, 1,0 ml, gelb, biopur, 100 Stk. (for stepper pipette)	Schubert und Weiss
Combitips advanced, 5,0 ml, biopur, 100 Stk. (for stepper pipette)	Schubert und Weiss
Combitips , 10,0 ml, biopur, 100 Stk. (for stepper pipette)	Schubert und Weiss
syringes for filter, NORM-JECT(R) EINMAL-SPRITZEN	Th. Geyer
Tips, Clearline BT- 1250 Filterspitze	Kisker Biotech
EINMALPIPETTE 2ML 1000S	SARSTEDT
EINMALPIPETTE 5ML 200ST	SARSTEDT
Einmalspritzen Injekt Solo, 5ml, Pck à 100 (syringe for filter)	Schubert und Weiss
EINMALPIPETTE 10ML	HMGU Lagermaterial
qPCR plates, Hard-Shell 384-well Plates, white well, clear shell, 50	Bio-Rad

qPCR plates sealing membrane, Microseal 'B' Adhesive Seals, 100	Bio-Rad
BCA plates, MICROPLATTE, 96 WELL, PS, F-BODEN, TRANS	Greiner Bio-One
PCR plates, UltraCruz PCR Plate, 96 well, 0.2ml 25/pack	Santa Cruz
PCR tubes, Multiply-µStrip 0,2ml Kette	SARSTEDT
PCR tubes, Multiply-µStrip Farbmix	SARSTEDT
PCR tube lids, 8er Deckelkette, flach	SARSTEDT
PCR tubes, PCR SoftTubes, 0.2 ml, 1000 Stück	Biozym
Tubes, SafeSeal Gefäß 1,5ml 2000ST	SARSTEDT
Tubes, SafeSeal Reagiergef. 2ml, PP	SARSTEDT
Tubes, EPPENDORF TUBES 5,0ML EPPENDORF QUALITÄT	VWR International (Eppendorf)
Petri dishes, PETRISCHALEN 94X16MM M.NOCK. POLY 480ST	Greiner Bio One International
Bacteria tubes, PP-ROEHRE 14ML FALCON 500ST	Falcon
FACS tubes, Falcon Zellsiebröhrchen 35 µm Zellsieb in 6 ml Rundbodenröhrchen	Schubert und Weiss
Tubes, PS-ROEHRE 15ML FALCON STERIL 500ST	FALCON
Tubes, PP-ROEHRE 50ML FALCON 500ST	FALCON
LABORFLASCHE 100ML	Th. Geyer
UltraCruz Reagent Reservoir, 100ml	Santa Cruz
LABORFLASCHE 250ML	Th. Geyer
LABORFLASCHE 500ML	Th. Geyer
LABORFLASCHE 1000ML	Th. Geyer
LABORFLASCHEN, GL45 Kappe	Th. Geyer
Tips, Rotilabo-Spritzenf. Steril, 0,2ym 50ST	Carl Roth
Tips, MILLEX-GS-SPRITZENFILTER, 0,22µM	Th. Geyer
0.45µm filters, Rotilabo-Spritzenf.Steril, 0,45µm 50ST	Carl Roth
Filters, MF75 Bottle-Top-Filter, 0,2µ, GL 45	Fisher Scientific
Histology cassettes, HISTOSETTE® I Einbettkassette mit anhängendem Deckel, weiss	SIMPORT SCIENTIFIC INC
Coated slides, Objektträger SuperFrost plus, 75x25mm, Pck à 72	Schubert und Weiss
HYPERFILM ECL, 18X24CM, 50 SHEETS	GE Life Sciences
FILTERTIPS TIPONE 10−20µl, filter, rack	HMGU Lagermaterial
Tips, SafeSeal SurPhob Spitzen, 20 µl, steril Filterspitzen, Low Binding, graduiert,10 Racks à 96 Stück	Biozym
Tips, Clearline BT-200 Filterspitze1,0 - 200µl	Kisker Biotech
Tips, Clearline BT-1000 Filterspitze 100 - 1000µl	Kisker Biotech
Injection syringes, Plastipak TBC-Spritzen 1 ml Luer, 3-tei	Wagner und Munz

TC-Platte 96 Well,Standard,F	SARSTEDT
Plates with glass bottom, Cell Imaging Platte, 96W, TCT, Schwarz/Glasboden	Eppendorf
TC-Platte 48 Well, Standard, F	SARSTEDT
TC-Platte 24 Well, Standard, F	SARSTEDT
TC-Platte 12 Well,Standard,F	SARSTEDT
TC-Platte 6 Well,Standard,F	SARSTEDT
10 cm plate, ZELLKULTURSCHALEN 100X15MM 150ST	HMGU Lagermaterial
15 cm plate, ZELLKULTURSCHALEN 140X20MM 80ST	HMGU Lagermaterial
CRYOTUBES 2ML PP STERIL 500ST	Thermo Fisher Scientific
Röhre 120ml, 114x44mm, PP	SARSTEDT
0.22µm filters, Rotilabo-Spritzenf. Steril, 0,2ym 50ST	Carl Roth
Nunc™ Lab-Tek™ II Chambered Coverglass; 8 chamber	Thermo Fisher Scientific
Nunc™ Lab-Tek™ II Chambered Coverglass; 4 chamber	Thermo Fisher Scientific
8-Well ibiTreat	ibidi
CENTRIFUGAL FILTER MODIFIED PES 10K 500U	VWR International
MICROPLATTE, 96 WELL, PS, F-BODEN, TRANS	Greiner Bio-One
Microseal 'B' Adhesive Seals, 100	Bio-Rad
UltraCruz™ PCR Plate, 96 well, 0.2ml 25/pack	Santa Cruz
Immobilon-P 26.5 x 3.75m Roll PVDF .45um	Merck Millipore
Immobilon-P 26.5 x 3.75m Roll PVDF .22um	Merck Millipore
PCR- VERSCHLUSSFOLIE AXYSEAL	VWR International
Coverglasses for EM, Zellkultur-Deckgläser, Thermanox, Ø 13 mm, CC, steril Zellkultur-Deckgläser	FST Thermo Fisher Scientific
Tubes for FACS, Falcon® Round-Bottom Tubes with Cell Strainer Cap, 5 mL	FALCON
Falcon® Cell Strainers, Sterile, Corning®, 100 µm (for primary cell culture)	FALCON
Filter paper, Filterpapiere	neolab
Ultracentrifuge tubes, Microcentrifuge Tubes Clear 1.5mL	Beckman Coulter
Ultracentrifuge tubes, Thickwall Polycarbonate Tube 1ml	Beckman Coulter
Ultracentrifuge tubes, Thinwall Polypropylene Tube 5 ml	Beckman Coulter

2.2 Methods

2.2.1 Establishment of PAT2 knockdown and overexpression cell lines

2.2.1.1 Plasmid

All the lentivirus plasmids for knockdown and control were purchased from Sigma-Aldrich and all the vectors are pLKO.1-puro. The information is shown below.

Name of cell line	Catalog number of the containing plasmid	Targeting sequence
Scramble (Control)	SHC016-1EA	CCGGCAATCAGTCAAGCTCCTGTATCTCGAGATACAGGAGCTTGAC TGATTGTTTTTG
PAT2 knockdown 443	TRCN0000068443	
PAT2 knockdown 444	TRCN0000068444	CCGGCAGACTGAACAAGCCTTTCATCTCGAGATGAAAGGCTTGTTC AGTCTGTTTTTG
PAT2 knockdown 445	TRCN0000068445	CCGGCAGACTGAACAAGCCTTTCATCTCGAGATGAAAGGCTTGTTC AGTCTGTTTTTG
PAT2 knockdown 446	TRCN0000068446	CCGGCAGACTGAACAAGCCTTTCATCTCGAGATGAAAGGCTTGTTC AGTCTGTTTTTG
PAT2 knockdown 447	TRCN0000068447	CCGGACATTGGTTCATCTGGTCAAACTCGAGTTTGACCAGATGAAC CAATGTTTTTTG
PAT1 knockdown 381	TRCN0000068381	CCGGCCTACTATGGAGAGGGCATTACTCGAGTAATGCCCTCTCCAT AGTAGGTTTTTG

PAT2 overexpression plasmid was constructed by using pCDH-CMV-puro vector, PAT2 coding sequence (CDS) together with 3' terminal HA tag sequencing was inserted after cytomegalovirus (CMV) promoter.

2.2.1.2 Lentivirus packaging

6 µg plasmid, 5.4 µg psPAX and 0.6 µg PMD2.G were added to a clean tube. The total volume was adjusted to 100 µl by DMEM, then 40 µl polyfect was added. The solution was mixed on vortex for 10 s and the tube was stood at room temperature for 5 min. The transfection solution was added slowly to the 10 cm plate with confluent HEK293T cells drop by drop to cover all the cells. After maintenance in culture incubator (37°C, 5% CO_2, same conditions for the following) 4 h, 4 ml cell culture medium was added to the plate and then the plate was kept in the incubator overnight. The medium in the plate was filtered by 0.45 µm membrane, filtrate was collected in 50 ml falcon tube and then PEG-it (1 : 5 to final volume) was added. 5 ml new medium with 10 mM HEPES was then added to HEK293T cells, the plate was kept in the incubator overnight. The collection was repeated in the next two days to collect the virus. The virus solution is centrifuged for 30 min at 4°C, 1500 × g and then the pellets was wash with DPBS. The precipitate was resuspended with 200 µl DPBS. The aliquots 4 × 50 µl were stored at –80°C.

2.2.1.3 Infection

The BAT1 cells were seeded into a 12 well plate and kept in the incubator (37°C, 5% CO_2, same conditions for the following) until reaching 70% confluence. The medium was removed and 1 ml new cell culture medium was added to the cells. 50 µl virus solution, 1.5 µl polybrene (final concentration 9 µg/ml) and 500 µl cell culture medium were mixed in a clean tube by inverting several times. The tube was stood at room temperature for 10-15 min. The mixed transfection solution was added to BAT1 cells drop by drop and the cells were kept in the incubator for 24 h. The medium of the transfected cells and non-transfected cells was changed by the new medium with 2.5 µg/ml puromycin. Until no non-transfected cells survive, the positively transfected cells were split with puromycin containing cell culture medium. The cells were stored when reaching enough quantity.

2.2.2 Cell culture

2.2.2.1 Cell culture handling

For an aseptic environment:

Adjust the hood sash to a proper position to maintain laminar aseptic airflow. Avoid cluttering under the hood. All the media (including pipette tips and plates), supplement and reagents should be sterile. All the surface area needs to be sprayed by 70% ethanol.

For cell culture medium preparation:

Normal medium: mix 500 ml DMEM, 50 ml FBS (final concentration 10%), 5 ml 100 × Penicillin and Streptomycin (final concentration 100 unit/ml Penicillin and 100 µg/ml Streptomycin).

Puromycin selective medium: by adding puromycin to normal medium at final concentration of 2.5 µg/ml.

For cell splitting:

Cells were washed by DPBS to cover all the cells, wash and then evacuate the DPBS. Trypsin-EDTA (0.05%) with phenol red was added cover all the cells. (For 15 cm plate 2 ml, 10 cm plate and for smaller plates the reduced volumes) The digestion was

performed in the incubator (37°C, 5% CO2) for 1 - 2 min until most of the cells detached. The 37°C warm normal medium (or selective medium if it is needed) was added to the plate to stop digestion. (Adding 8 ml for 15 cm plate, adjust the volumes for the smaller plates). The cell suspension was pipette up and down several times. The proper volume of the cell suspension was added to new plate according to the needed splitting radio. Then new medium was added to the new plate. (Final volume should fit the plate, 20 ml for 15 cm plate, adjust the volumes for the other plates). The plate was shacked to mix well.

For cell frozen:

The frozen medium was prepared by adding DMSO to normal medium (or selective medium if needed) under the hood, the volume ratio of DMSO to the medium is 1 : 9. Cells were digested as in the cell splitting part. The cell suspension was transferred to a clean tube and then centrifuged for 5 min at 1000 × g at room temperature. The pellet was resuspended by the frozen medium whose volume was according to the number of needed frozen tubes. Each 1 ml aliquot was transferred to each frozen tube. The tubes were put in the frozen box and then stored at –80°C.

For cell thawing:

For each frozen tube, a 15 ml falcon tube with 9 ml 37°C pre-warmed medium was prepared under the hood. The –80°C frozen tube was stirred quickly in 37°C water bath until cell suspensions nearly thaw. The cell suspension was then transferred into the prepared falcon tubes under the hood. After centrifugation 5 min at 1000 × g at room temperature, the pellet was resuspended with needed medium and then needed volume was added to a new plate. The new medium with needed volume was added to the new plate. Then the plate was shacked to mix well.

2.2.2.2 MDI induction protocol for brown preadipocyte cell line adipogenesis induction

Induction medium: 0.5 mM IBMX (dissolved in 0.5N KOH for stocking solution), 5 µM dexamethasone (dissolved in 100% ethanol for stocking solution), 125 µM indomethacin

(dissolved in DMSO for stocking solution), 1 nM T3 (dissolved in 0.1% DMSO (in water) for stocking solution), 100 nM insulin and 1nM rosiglitazone (dissolved in DMSO for stocking solution) are added in normal medium or selective medium.

Differentiation medium: 1 nM T3 (dissolved in 0.1% DMSO (in water) for stocking solution), 100 nM insulin and 1nM rosiglitazone (dissolved in DMSO for stocking solution) are added in normal medium or selective medium.

The appropriate number of preadipocytes is seeded into the plate. After cells reach to 100% confluence, the medium is replaced by induction medium to start MDI induction. After two days, the induction medium is replaced by differentiation medium, and every two days new differentiation medium is changed until the 8th day.

2.2.2.3 Oil Red O staining

Preadipocytes are seeded into a 6 well plate to be induced for differentiation. For around 100 ml Oil Red O working solution, 0.21 g Oil Red O was dissolved in 60 ml 100% isopropanol in a falcon tube, then 40 ml double distilled water was added, the solution was filtered after 20 min standing at room temperature (adjust the weight and volumes if the total volume is different).

For each well, cells were washed twice by PBS and then fixed with 2 ml 10% formalin in PBS for 10 min at room temperature. Then 10% formalin was replaced by 2 ml formalin for 1 h incubation at room temperature. Cells were washed with double distilled water twice and then were incubated with 2 ml 60% isopropanol for 5 min at room temperature. Then cells were dried at room temperature.1 ml Oil Red O working solution was added and dry cells were incubated for 10 min at room temperature. Then 2 ml double distilled water was used to wash the cells four times. Cells with double distilled water were observed and images were acquired under the microscope. Cells were dried at room temperature and then incubated in 1 ml 100% isopropanol for 10 min with gently shake to elute Oil Red O dye. The isopropanol containing Oil Red O dye was Pipette up and down several times to mix it well. 100 µl of the

solution was transferred to one well of a 96 well plate. The optical density was measured at 505 nm. Blank was set as 100 µl 100% isopropanol.

2.2.2.4 Amino acid starvation protocol

Preparation of amino acid free medium: mix 500 ml amino acid free DMEM with 5 ml 100 × Penicillin and Streptomycin (final concentration 100 unit/ml Penicillin and 100 µg/ml Streptomycin). Add puromycin (same concentration with the selective medium) if needed.

Preparation of amino acid free medium with dialyzed FBS: add dialyzed FBS (final concentration 10%) to amino acid free medium.

When cells were ready to be started for amino acid starvation induction, old medium was removed and appropriate volume (depending on the size of the plate) of amino acid free medium with/without dialyzed FBS was used to wash the cells twice. Then amino acid free medium with/without dialyzed FBS was added with the same volume of the old medium. The plate was put back to the incubator (37°C, 5% CO_2).

For adipocytes, amino acid starvation 24 h was started after 8th day of adipogenesis. The cells for amino acid starvation 1h treatment were kept in medium with amino acids until 23th hour amino acid starvation 1 h was started. The control cells were kept in medium with amino acids for all the 24 h.

2.2.2.5 Brown adipocytes primary culture

The digestion buffer was prepared by filtering normal medium containing 1% BSA and 1 mg/ml collagenase IV with a 0.2 µm filter. The BAT from mice at 6-8 weeks old was immersed in PBS in 2 ml tubes on ice. After removing the PBS, the BAT was minced with spring scissor on ice. The minced BAT was transferred to a 10 ml falcon tube with 5 ml digestion buffer. Incubation was performed for 30 min at 37°C, 1000 rpm shaking. Then 5 ml normal medium was added to the tube and then the digestion product was filtered with 100 µm strainer (the flow through was collected) under cell culture hood. The filtrate was centrifuged for 5 min at 4°C, 500 × g. The pellet was resuspended with 1 ml normal medium

under cell culture hood. The suspension with cells was seeded into a 6 well plate for further cell culture.

2.2.3 Fractionation

2.2.3.1 Fractionation for isolation of heavy membrane, mitochondria and cytoplasm

Cells in 15 cm plate were harvested for this fractionation. (Bruce Alberts 2002).

Cells were washed with 5 ml ice cold PBS several times and then were scraped from the plate by using cell Scraper. Cells were further transferred into a clean prechilled 1.5 ml tube on ice for centrifugation 5 min at 4°C 500 × g. The pellet was resuspended with 1 ml ice cold medium I (0.25 M sucrose, 1 mM EDTA and 10 mM Tris-HCl pH 7.4 in double distilled water) and then was homogenized cells by Potter-Elvehjehm grinder. The homogenate was centrifuge for 5 min at 4°C 500 × g. The supernatant was centrifuged for 5 min at 4°C 500 × g again. Then the supernatant was centrifuged for 20 min at 4°C 16000 × g. The pellet as mitochondria fraction (containing plasma membrane and part of lysosome) was resuspended with 50 µl 2 × sample buffer on ice. The supernatant was transferred to a new prechilled clean super speed centrifugation tube on ice and then was centrifuged for 45 min at 4°C 160000 × g. The supernatant as plasma fraction was transferred to a new prechilled clean tube on ice and 1/4 final volume 4 × sample buffer was added on ice. The pellet as membrane fraction (containing microsome and part of lysosome) was resuspended with 50 µl 2 × sample buffer on ice. All fractions were incubated at 70°C for 10 min and then for WB.

2.2.3.2 Fractionation for sucrose gradient centrifugation

Cells in 15 cm plate were harvested for this fractionation. (McKeel & Jarett 1970). The gradient former, peristaltic pump, 5% and 25% Ficoll 400 solution in 250 mM sucrose were used to make Ficoll 400 gradient from 5% to 25% in 5 ml super speed centrifugation tube.

The homogenization was performed according to the protocol of fractionation for isolation of heavy membrane, mitochondria and cytoplasm. The homogenate was centrifuged twice for 10 min at 4°C 1000 × g and the supernatant was further centrifuged for 20 min at

4°C 16000 × g. The supernatant was transferred to another new prechilled clean tube on ice as the supernatant fraction and 1/4 volume 4 × sample buffer of the final volume was added on ice. The pellet was resuspended with 500 µl ice cold medium I (0.25 M sucrose, 1 mM EDTA and 10 mM Tris-HCl pH 7.4 in double distilled water). The suspension was loaded carefully on the top of prechilled Ficoll 400 gradient and then was centrifuged for 30 min at 4°C 100000 × g. The upper layer was transferred to a new prechilled clean tube on ice by a 30G x 1/2" syringe and then medium I was added to dilute the layer as 4 : 1. The tube was centrifuged for 15 min at 4°C 16000 × g. The pellet as membrane fraction (containing lysosome) was resuspended with 75 µl medium II (0.25 M sucrose and 10 mM Tris-HCl pH 7.4 in double distilled water) and 15 µl 4 × sample buffer. The pellet in the Ficoll 400 gradient was resuspended with 500 µl medium I on ice and then was centrifuged for 15 min at 4°C 16000 × g. The pellet as mitochondria fraction was resuspended with 75 µl medium II and 15 µl 4 × sample buffer. All fractions were incubated at 70°C for 10 min and then for WB.

2.2.3.3 Membrane and cytosol isolation

Cells in 6 well plate were harvested for this fractionation. (Stransky & Forgac 2015).

The homogenization was performed according to the protocol of fractionation for isolation of heavy membrane, mitochondria and cytoplasm except the 650 µl fractionation buffer (250 mM sucrose, 1 mM EDTA and 10 mM HEPES in double distilled water) was used for cells in each well. The homogenate was centrifuged twice for 10 min at 4°C 1000 × g and the supernatant was further centrifuged for 30 min at 4°C 100000 × g. Then the supernatant was transferred into 10K Polyethersulfone (PES) Membrane tube to enrich the protein by centrifuging the tube for 10 min at 4°C 14000 × g (adjust the time according to whether the volume meets the requirement (make all the samples to be equal and small volume) in each tube). The solution was transferred to a new prechilled clean tube on ice as cytosol fraction. Then 0.1% SDS and 1/4 final volume 4 × sample bufferwas added. The pellet was resuspended with fractionation buffer and then centrifuged for 30 min at 4°C 100000 × g. The

pellet as membrane fraction was resuspended with 50 µl 2 × sample buffer on ice. 0.1% SDS was added. All fractions were incubated at 70°C for 10 min and then for WB.

2.2.4 Seahorse Mito Stress assay upon starvation

The seahorse XFe96 sensor cartridge was filled with 200 µl calibrant solution for each well and incubated in seahorse prep station at 37°C overnight.

The 4.5 g/l glucose amino acid free DMEM was prepared by adding glucose solution to amino acid free DMEM. The 4.5 g/l glucose DMEM was prepared by adding 1/10 final volume 10 × amino acid mixer to 4.5 g/l glucose amino acid free DMEM.

Preadipocytes were seeded into XF96 cell culture microplate (200 µl medium for each well) and induced for differentiation. 4 wells were at corner emptied as blanks. Cells were then treated with amino acid starvation. For each starvation well and blank well 180 µl 4.5 g/l glucose amino acid free DMEM was added. 180 µl glucose 4.5 g/l DMEM was added to each non-starvation well. The microplate was then incubated in seahorse prep station at 37°C for 1 h.

Compounds were added to ports of the cartridge according to it the following table:

Compound	Concentration in the into (Dilute in amino acid free DMEM)	Port added in	Volume added in	Final concentration
Oligomycin	20 µg/ml	A	20 µl	2 µg/ml
FCCP	10 µM	B	22 µl	1 µM
Rotenone and Antimycin	25 µM	C	25 µl	2.5 µM
2-DG	1 M	D	27 µl	100 mM

The cartridge plate was put into seahorse XF96 analyzer and run the program as follows:

Command	Time (min)	Command	Time (min)
Calibrate	0,00	Wait	0,50
Equilibrate		Measure	2,00
Loop Start	4 Loops	Loop End	
Mix	2,00	Inject C	
Wait	1,00	Loop Start	4 Loops
Measure	2,00	Mix	2,00
Loop End		Wait	1,00

Inject A		Measure	2,00
Loop Start	4 Loops	Loop End	
Mix	2,00	Inject D	
Wait	1,00	Loop Start	5 Loops
Measure	2,00	Mix	2,00
Loop End		Wait	1,00
Inject B		Measure	2,00
Loop Start	3 Loops	Loop End	
Mix	1,00		

The Quant-iT PicoGreen dsDNA Assay Kit was used to quantify DNA in each well. 100 µg/ml λ DNA standard was diluted into 10, 5, 2.5, 1.25, 0.625, 0.3125, 0.15625 µg/ml with 1 × TE buffer prepared by dilution of 20 × TE buffer. All diluted λ DNA standard was added in a flat and transparent bottom 96 well plate for the standard curve measurement, 10 µl for one well. 200 µl RIPA lysis buffer was added to each well of XF96 cell culture microplate and pipette up and down several times to lyse cells. 10 µl cell lysate of each well was transferred into the 96 well plate. 90 µl 1 × TE buffer was added to all the wells with 10 µl solution. 100 ul diluted Quant-iT PicoGreen dsDNA reagent (1 : 200 by 1 × TE buffer) was added to all the wells with 100 µl solution. Then the 96 well plate was incubated in a dark place at room temperature for 5 min. The fluorescence density was measured at 488 nm of each well.

DNA concentration c (µg/ml) in each well was calculated based on the standard curve. Then total DNA mass was calculated.

$$m_{DNA}(\mu g) = c(\mu g/\mathrm{ml}) \times 0.1\ ml$$

Seahorse file and DNA mass of each well were imported into seahorse software Wave to be analyzed.

2.2.5 Proliferation assay

Cell Counting Kit – 8 (CCK–8) was used for this assay.

Cells were seeded into 4 wells of the 96 well plate (2000 cells in 200 µl medium per well) under the hood. The plate was kept in cell culture incubator for four days. One well was used for measurement in each day. In each measurement, cells in one well were incubated

with 200 µl medium mixed with 20 µl CCK–8 solution in cell culture incubator for 1 h. The absorption was measured in plate reader under 450 nm (200 µl medium mixed with 20 µl CCK-8 as blank).

2.2.6 qPCR

2.2.6.1 RNA isolation

RNA isolation was performed by using the Qiagen RNeasy Mini Kit. RLT buffer was needed to be added β-mercaptoethanol (1 : 100), buffer RPE working solution was needed to be prepared by adding pure ethanol of 4 times volumes (220 ml pure ethanol is added to 55 ml buffer RPE).

For cells:

Cells were washed with cold PBS on ice several times. 350 µl buffer RLT containing β-mercaptoethanol was added to cells for 6 well plate (adjust the volume for the other plates). Cells were scraped from the plate by cell Scraper on ice and pipette up and down several times for lysing well. After adding 350 µl 70% ethanol, the lysate was transferred to the spin column. Centrifugation for 15 s full speed at room temperature was performed. 700 µl buffer RW1 and then 500 µl buffer RPE working solution was used to wash the spin column by centrifugations for 15 s full speed at room temperature. Then spin column was washed again by 500 µl buffer RPE working solution, centrifugation was performed for full 2 min speed at room temperature. The column was put into the new 2 ml collection tube and centrifuged for 1 min full speed at room temperature. The column then was transferred to a 1.5 ml collection tube. 40 µl RNase free water was added to the column membrane. After 5 min incubation at room temperature, the column was centrifuged for 1 min full speed at room temperature. RNA concentration in the elution was measured the by using nanodrop. RNA solution was stored at −80°C.

For tissues:

1 ml QIAzol lysis buffer was added to the tissue in 2 ml prechilled tube. After adding one steel bead into the tube, the tissue was disrupted for 2 times and each time 2 min at 20

Hz in the lyser. Homogenate was then centrifuged for 5 min at 4°C 10000 × g. The supernatant was transferred to a new tube and mixed with 200 µl chloroform. The tube was shack gently several times and then stood at room temperature for 5 min. After centrifuge for 5 min at 4°C, 12000 × g, the supernatant was transferred into the spin column. RNA was isolated then according to the protocol for cells.

2.2.6.2 The protocol of reverse PCR to generate cDNA

High-capacity cDNA reverse transcription kit is used for reverse PCR.

0.5 - 1 µg RNA was diluted into10 µl final volume in 96 well PCR plate with PCR water on ice. The RT master was prepared on ice by mixing 2 µl 10 × RT buffer, 0.8 µl 25 × dNTP mix buffer (100 mM), 2 µl 10 × RT random primers, 1 µl MultiScribe reverse transcriptase and 4.2 µl Nuclease free water per reaction. 10 µl RT master mix was added to each well with sample in 96 well PCR plate on ice. The plate was sealed with the membrane and centrifuged briefly. The program of thermal cycler was: 10°C 10 min, 37°C 120 min, 85°C 5 min, 4°C ∞. The product cDNA was diluted by adding 180 µl PCR water per well and then stored at −20°C.

2.2.6.3 qPCR test

The CFX384 Touch™ Real-Time PCR Detection System was used for the qPCR test.

3 µl cDNA per well was added into 384 well PCR plate. The SYBR green master mix was prepared by mixing 5 µl iTaq universal SYBR green supermix, 0.03 µl (0.003 nmol) Forward primer, 0.03 µl (0.003 nmol) Reverse primer, 1.94 µl PCR water per reaction. *tbp* gene is chosen as the Housekeeping gene. 7 µl SYBR green master mix was added to each well. Then the plate was sealed with qPCR membrane and centrifuged the plate briefly.

The qPCR program in C1000 touch thermal cycler chassis with CFX384™ Optical reaction module was used:

Step	Temperature	Time	Cycle
1	95°C	30 s	1
2	95°C	5 s	
3	60°C	30 s	40
4	plate read		

5	95°C	10 s	1
6	Melting curve 65°C - 95°C, increment 0.5°C and plate read once per 5 s		
End			

The file was exposed and analyzed by CFX manager software. The exported Cq values were used for calculating the relative expression.

$$\text{Relative expression} = 2^{-(\text{Cq}-\text{Cq}_{tbp})}$$

2.2.6.4 Primers

All the qPCR primers are purchased from Sigma Aldrich and listed below:

Table 2.5 Primers for qPCR

Primer	Sequence
pat2 forward (f)	GTGCCAAGAAGCTGCAGAG
pat2 reverse (r)	TGTTGCCTTTGACCAGATGA
tbp f	ACCCTTCACCAATGACTCCTATG
tbp r	TGACTGCAGCAAATCGCTTGG
pparγ f	TCCTATTGACCCAGAAAGCGA
pparγ r	TGGCATCTCTGTGTCAACCA
ucp1 f	CTGCCAGGACAGTACCCAAG
ucp1 r	TCAGCTGTTCAAAGCACACA
lc3b f	AGAGTGGAAGATGTCCGGCT
lc3b r	TCTCCCCCTTGTATCGCTCT
integrin β1 f	ATCATGCAGGTTGCGGTTTG
integrin β1 r	TGGAAAACACCAGCAGTCGT
integrin β2 f	GATTCTCGGAGTGGAGGCTT
integrin β2 r	TTGGTGCATTCCTGGGACAC
integrin β3 f	GACAAGCCTGTATCGCCGTA
integrin β3 r	GTAGCCAAACATGGGCAAGC
integrin β6 f	GCTGGCAGGCATTGTCATTC
integrin β6 r	TGAGTTGGCCGATAGTTGGA
integrin α5 f	TCCAGTGCACCACCATTCAA
integrin α5 r	TCCTCTCCCTTGGCACTGTA
integrin α1 f	CCACCAAGATGAACGAGCCT
integrin α1 r	GGCTGCCCAGCGATATAGAG
integrin α2 f	ATGGTGGGGACCTCACAAAC
integrin α2 r	GCCATCGGTCACAACTACCA
kindlin-2 f	ACCTGCTCATCAGCTGAACC
kindlin-2 r	ATTCATGCCCTCTGCTACCG
kindlin-3 f	GCAATCCTTGCCCGACTTTG
kindlin-3 r	TCCGGATGAGTCGGTTGTTG
vma21 f	CACGGTTCCTATCGGCTTGT
vma21 r	ACAGCAACAATTGCGGCATA
tmem199 f	AGATCTGCATCAGCACCTGAG
tmem199 r	ATTCCGGGGAGGCTTCACAA
ccdc115 f	GATCAAAGCTGACGCCCAGA
ccdc115 r	ACTCTTTGGTCTTGGTGGGG

2.2.7 Western blot

2.2.7.1 Protein extraction from cells and tissues

For cells:

The phosphatase Inhibitor Cocktail 2, 3 and protease inhibitor cocktail were added to RIPA buffer as volume ratio 1 : 100 on ice. Cells were washed with prechilled PBS and then scraped from the plate by using cell Scraper on ice. After being transferred to a new prechilled tube, cells were centrifuged for 5 min at 4°C 500 × g. 500 µl RIPA buffer containing phosphatase Inhibitor Cocktails and protease inhibitor cocktail was added to the pellet (for one well of a 6 well plate, adjust the volume for the other plates). Homogenization by passing lysate through 30G 1/2" syringe several times on ice was performed. Then the homogenate was centrifuged for 30 min at 4°C 20000 × g. The protein concentration was measured in supernatant by BCA assay kit.

2 mg/ml albumin standard in ampules was diluted into 1, 0.5 and 0.25 mg/ml with RIPA buffer. Then the diluted 1, 0.5 and 0.25 mg/ml albumin standard was added into 5 wells in a flat and transparent bottom 96 well plate for the standard curve. A part of lysate was diluted 1 : 10 with RIPA buffer (adjust the dilution radio when optical density excesses the standard curve) and 10 µl diluted lysate was transferred to the 96 well plate. 90 µl RIPA buffer was further added to each well. BCA working reagent was prepared by mixing BCA reagent A and B as radio 1 : 50. 100 µl BCA working reagent was added to all the wells with the solution in the 96 well plate. The plate was sealed with the membrane and incubated in 37°C incubator for 30 min. The optical density of each well was measured at 562 nm. The concentration was calculated based on the standard curve and dilution radio. The lysate was diluted to the needed concentration with RIPA buffer containing Inhibitor Cocktails and stored –20°C.

For tissues:

The tissue was cut into small pieces in 2 ml tube by using scissor and then homogenized in 1 ml RIPA buffer containing Inhibitor Cocktails by homogenizer. The homogenate was sonicated twice. Centrifugation of the homogenate, protein concentration measurement and storage were performed according to the protocol for cells

2.2.7.2 SDS-PAGE and transfer

For hand cast gel, the resolving gel solution (the volume depends on the chamber size) was prepared according to the following table:

Component	Volume per 5 ml 8% gel	Volume per 5 ml 10% gel	Volume per 5 ml 12% gel
Double distilled water	2.3 ml	1.9 ml	1.6 ml
Acrylamide/Bis solution 30%	1.3 ml	1.7 ml	2ml
1.5 M Tris-HCl pH8.8	1.3 ml	1.3 ml	1.3 ml
10% SDS	50 µl	50 µl	50 µl
10% Ammonium peroxydisulfate	50 µl	50 µl	50 µl
TEMED	3 µl	2 µl	2 µl

The solution was added into chamber carefully and sealed with a little 100% isopropanol. The chamber was stood at room temperature until polymerization.

5 % stacking gel solution (the volume depends on the chamber size) was prepared by mixing 3.4 ml double distilled water, 830 µl 30% Acrylamide/Bis solution, 630 µl 1 M Tris-HCl pH6.8, 50 µl 10% SDS, 50 µl 10% Ammonium peroxydisulfate, 5 µl TEMED per 5 ml. After Pouring out the upper isopropanol the stack gel solution was added carefully. The chamber stood at room temperature until polymerization after the comb was inserted.

The samples were diluted to be the same volume and concentration (as needed) by RIPA buffer containing phosphor phosphatase Inhibitor Cocktails and protease inhibitor cocktail.

The comb was removed from the gel and the gel was then put into the electrophoresis chamber. Next, running buffer was added to the chamber (3 mg/ml Tris, 14.4 mg/ml Glycine and 0.1% SDS in double distilled water). The sample and prestained protein marker were loaded on the gel then. The electrophoresis was performed at 100 V until samples are stacked at the border between stacking gel and resolving gel. Then 120 V volt was set. The electrophoresis was stopped when the dye front of samples reaches the position 1 cm away from the bottom of the gel.

For precast gel, NuPAGE 4-12% Bis-Tris protein gels were used in precast gel chamber. For a better separation on big sized proteins, MOPS (50 mM MOPS, 50 mM Tris

Base, 0.1% SDS and 1 mM EDTA in double distilled water) was used as running buffer. For separating small sized proteins, MES (50 mM MES, 50 mM Tris Base, 0.1% SDS and 1 mM EDTA in double distilled water) was used. The volt was set at 200 V during the whole electrophoresis. The other steps were the same with hand cast gel steps.

Mini Trans-Blot cell (for small sized gel) and Criterion blotter (for big sized gel) were used for transfer.

The transfer buffer (3 mg/ml Tris, 14.4 mg/ml Glycine and 10% methanol in double distilled water) was prepared. One piece of 0.45 µm PVDF membrane and 2 pieces of filter paper (all the sizes of pieces are bigger than the gel) were cut. The PVDF membrane was further activated in 100% methanol and then the membrane, two pieces of filter paper and two pieces of foam pad were incubated in transfer buffer. The opened gel holder cassette was put in the gel/blot assembly tray and let its cathode side touched the bottom of the tray. Enough transfer buffer was added to immerse the cathode side of gel holder cassette. One piece of the foam pad, one piece of soaked filter paper, gel, soaked membrane, one piece of soaked filter paper and one piece of foam pad were put in turn on the cathode side of gel holder cassette. More transfer buffer was added if any layer cannot be immersed and the bubbles were removed among layers by using the roller. The closed cassette was put into the electrodes in the chamber. To cool the chamber, a cooling unit and a magnetic stirrer bar were put into the chamber which was moved into the ice box with a magnetic stirrer below. Enough transfer buffer was added into the chamber to make the buffer to reach the indicated liquid level. After turning on the stirrer at a low speed, the transfer was started to run at 100 V for 90 min.

2.2.7.3 Blue native PAGE and transfer

NativePAGE Novex Bis-Tris gel system was used to perform Blue native PAGE. Cells were seeded into a 6 well plate for this test.

Prepare sample buffer 20 µl for each well by mix 5 µl 4 × NativePAGE sample buffer, 4 µl 5% Digitonin, 10.2 µl double distilled water, 0.2 µl phosphatase Inhibitor Cocktail 1, 2, 3 and protease inhibitor cocktail on ice.

Cells were washed with PBS several times. Cells then were scraped from the plate and transferred into a new prechilled 1.5 ml tube. 20 µl sample buffer was added to lyse the cells by pipetting up and down several times on ice. The homogenate was centrifuged for 30 min at 4°C 20000 × g. The protein concentration in the supernatant was measured by using BCA (see sample preparation). Each sample was diluted to be equal volume and concentration by sample buffer as needed. The NativePAGE 5% G-250 sample additive was added then to each sample at the final concentration0.25%.

The running buffer was prepared. For 1000 ml anode buffer, 50 ml 20 × NativePAGE running buffer and 950 ml Double distilled water was mixed.

For 200 ml cathode buffer:

Reagent	Volume (ml) for dark blue	Volume (ml) for light blue
20 × NativePAGE running buffer	10	10
20 × NativePAGE cathode addictive	10	1
Double distilled water	180	189
Total	200	200

The comb was removed from the NativePAGE 3-12% Bis-Tris protein gel and the wells in the gel were rinsed with cathode dark blue buffer twice. The gel was then transferred into the electrophoresis chamber for precast gel. Some cathode dark blue buffer was loaded on the wells of the gel before loading the samples and NativeMark unstained protein standard (7 µl). The upper buffer chamber was filled with cathode dark blue buffer carefully and for lower buffer chamber anode buffer was added. The electrophoresis was performed at 150 V until the dye front of samples reached the 1/3 position of the gel. Then the upper buffer chamber was evacuated to be filled with cathode light blue buffer. The electrophoresis at 150 V was continued until the dye front of samples reaches the bottom of the gel.

For transfer:

The gel was soaked in transfer buffer (the same with the transfer buffer for SDS PAGE transfer) containing 0.1% SDS for 10 min. The following transfer steps were according to SDS-PAGE transfer protocol except transfer buffer is mixed with SDS at concentration 0.01%. After transfer, the membrane was incubated with 8% acetic acid at room temperature for 15 min and protein ladders were marks by using a pencil. Then the membrane was rinsed with double distilled water and dried at room temperature. After reactivation of the membrane with 100% methanol several times, the membrane was further rinsed with double distilled water.

2.2.7.4 Western blot

TBST (50 mM Tris, 150 mM NaCl and 0.1% Tween 20 in double distilled water) was prepared.

The membrane was incubated on a shaker in turn with 5% skimmed milk in TBST at room temperature for 1 h, primary antibody solution diluted by 5% BSA in TBST as the normal radio 1 : 1000 (adjust the radio depend on different antibodies) at 4°C overnight, TBST at room temperature for 3 times (each time 5 min), HRP linked secondary antibody solution diluted by 5% BSA in TBST as the normal radio 1 : 5000 (adjust the radio depend on different antibodies) at room temperature 1 h and TBST at room temperature for 3 times (each time 5 min). The membrane was put in the development cassette after removing the liquid.

Enhanced chemiluminescence (ECL) solution was prepared by mixing the detection reagent 1 and detection regent 2 in ECL Western blotting-substrate kit as 1 : 1. The ECL solution was then added to the membrane until the whole membrane is covered. The ECL film was used for membrane development in the dark room. Afer film was dried the protein ladders were marked on the film.

The membrane was stripped by incubating the membrane in striping buffer on a shaker at room temperature for 10 min and then rinsed with double distilled water. Another needed blotting was performed according to the same protocol.

The results were quantified by using software ImageJ.

2.2.8 Co-IP

All the cells were seeded into 15 cm plate for Co-IP test.

Extraction of protein was performed according to cell protein extraction part except using IP lysis buffer rather than RIPA buffer (1 ml IP lysis buffer for 15 cm plate). The lysate samples were diluted to be the same protein concentration 1 mg protein of each sample was transfer to a new prechilled tube on ice. Then 50 µg antibody was added. The lysate was overhead shaken at 4°C 5 rpm overnight. 10 µl Dynabeads protein G beads were added to each tube before an overhead shake at 4°C 5 rpm for 1 h. Beads were washed with 500 µl IP lysis buffer containing phosphatase inhibitor cocktails and protease inhibitor for 5 min and the buffer was removed by centrifugation for 3 min at 4°C 1000 × g. Wash was performed for in total three times. Then beads were incubated with 30 µl double distilled water mixed with 10 µl 4 × sample buffer at 70°C for 10 min. The elution was used for WB.

For MS sample preparation, beads were additionally washed twice with buffer containing 25 mM TrisHCl (pH 7.4), 150 mM NaCl, 1 mM EDTA, 5% glycerol, 1% protease inhibitor cocktail, phosphatase Inhibitor Cocktail 2 and phosphatase Inhibitor Cocktail 3.

2.2.9 Fluorescence imaging

2.2.9.1 Immunofluorescence for cells

Cells were seeded into 8 well chamber slide for immunofluorescence.
Cells were washed with cold PBS several times and fixed with cold 100% methanol for 15 min at –20°C or 4% PFA in PBS (pH 7.4) for 10 min at room temperature.

Cells then were incubated in turn with PBS containing 3% BSA and 0.3% Triton X-100 at room temperature for 1 h, primary antibody 1 : 100 diluted in PBS containing 3% BSA and 0.3% Triton X-100 at 4°C overnight (100 µl for one well), PBS for 3 times (5 min each time), fluorescence dye linked secondary antibody (1 : 400 diluted) and DAPI (1 : 5000 diluted) in PBS containing 3% BSA and 0.3% Triton X-100 at room temperature for 1 h (100 µl in total for one well, protect from light) and PBS for 3 times (5 min each time, protect from

light). The chamber was removed then and the slide was mounted by 2 drops of mounting medium (protect from light). The coverslip was put carefully on the slide (avoid bubbles) in the dark. The slide was dried and stored at 4°C in the dark.

2.2.9.2 Immunofluorescence for tissue sections

For Cryo embedding section, the tissue piece was incubated with 4% PFA in PBS (pH 7.4) for 10 min at room temperature for fixation. Steps of staining on the slide were according to the protocol for cells.

For Vibratome section, staining was performed in 12 well plate according to the protocol for cells. The tissue piece was transferred to a slide when mounting.

2.2.9.3 Cell imaging of mitochondria tracker, DsRed-LC3-EGFP, mCherry-LC3B-EGFP, intracellular pH indicator and Mito-Kaima

For Mitochondria tracker, the staining medium was prepared by adding 250 nM MitoTracker in puromycin selective medium and then was added to PAT2 overexpression preadipocytes. Preadipocytes were incubated in the incubator (5% CO_2, 37°C) for 30 min (protect from light) and then washed with PBS (protect from light). After fixation by 4% PFA in PBS (pH 7.4) for 10 min at room temperature (protect from light), preadipocytes were staining according to the protocol of immunofluorescence for cells.

2.2.9.3.1 DsRed-LC3-GFP

pQCXI Neo DsRed-LC3-GFP deposited by David Sabatini lab was purchased from Addgene (Addgene plasmid # 31183). It is a retroviral vector and expresses DsRed-LC3-GFP autophagy reporter (Sheen et al 2011).

Establishment of cell lines.

The transfect solution was prepared by mixing 6 µg plasmid DsRed-LC3-GFP, 3 µg EcoPAK and 40 µl polyfect in a clean tube. The tube was stood at room temperature for 20 min. Then the transfect solution was mixed with 5 ml cell culture normal medium and added to 100% confluence HEK 293T in 10 cm plate. The plate was kept in the incubator (5% CO_2, 37°C) for two days. The medium of HEK 293T cells was transferred to Scr, PAT2 knockdown

and overexpression preadipocytes in a 6 well plate (each well 1.5 ml), keep preadipocytes in another well in puromycin selective medium for each cell line as control. The preadipocytes were kept in the incubator (5% CO_2, 37°C) for two days. Then the 1.5 ml puromycin selective medium containing 500 µg/ml G418 was added to all wells. The infected preadipocytes were split with selective medium containing 500 µg/ml G418 until no control cell survives and then stored when reaching the needed total number.

Cell culture was performed by using puromycin selective medium containing 500 µg/ml G418. Cell image was performed in 8 well chamber slide.

After Wash cells with PBS several times, Cells were fixed with 4% PFA in PBS (pH 7.4) for 1 h and then incubated with DAPI 1 : 5000 diluted PBS for 5 min.

Cells were washed for 3 times with PBS (each time 5 min). The mounting steps were according to immunofluorescence for cells.

2.2.9.3.2 mCherry-LC3B-EGFP

pBABE-puro mCherry-EGFP-LC3B deposited by Jayanta Debnath lab was purchased from Addgene (Addgene plasmid # 22418). It is used for indicating autuphagosome lysosome fusion (N'Diaye et al 2009). This test was performed through transient transfection and life cell imaging.

The preadipocytes were induced by MDI protocol till the 8th day in 8 well life cell image chamber.

The transfection solution was prepared by mixing 120 µl amino acid fee DMEM, 80 µl polyfect and 4 µg pBABE-puro mCherry-EGFP-LC3B plasmid in a tube.
The tube was stood at room temperature for 20 min. Two 100 µl aliquots were made. Then 900 µl amino acid free medium or 900 µl normal medium was added each aliquot. 150 µl amino acid free transfection medium for each well was added to the cells upon amino acid starvation, and 150 µl normal transfection medium for each well to control cells. For control cells, Bafilomycin A1(100 nM) also added. The chamber was kept in the incubator (5% CO_2,

37°C) for one day. The observation was performed under the confocal microscope by using external incubator and gas mixer to keep cells in 5% CO_2, 37°C environment.

2.2.9.3.3 Intracellular pH indicator

pEGFP-LC3 (human) deposited by Toren Finkel lab was a gift from Addgene (Addgene plasmid # 24920). It expresses pEGFP-LC3 fusion protein (Lee et al 2008).

1 µl pHrodo Red AM was mixed with 10 µl Powerload concentrate and two 5.5 µl aliquots were made (protect from light). 500 µl normal medium or amino acid free medium was added to each aliquot.

The preadipocytes were induced by MDI protocol till the 8th day in an 8 well life cell image chamber. The transfection solution contained 120 µl amino acid fee DMEM, 80 µl polyfect and 4 µg pEGFP-LC3 plasmid was stood at room temperature for 20 min. The transfection was performed according to the mCherry-LC3B-EGFP protocol. After 23 h incubaton in the incubator (5% CO_2, 37°C), for amino acid starvation for 1 h cells, the normal transfection medium was replaced by amino acid free transfection medium. After 23.5 h incubation, the medium of all cells upon fed or amino acid starvation was replaced by pHrodo Red AM contained the normal or amino acid free medium respectively. Cells were incubated for another 30 min in the incubator (5% CO_2, 37°C) and then the medium was changed to 150 µl life cell image solution in each well. The observation was performed according to the mCherry-LC3B-EGFP protocol.

2.2.9.3.4 Mito-Keima

mKeima-Red-Mito-7 deposited by Michael Davidson lab was purchased from Addgene (Addgene plasmid # 56018). The plasmid expresses mitochondria localized mKeima proteins which are sensitive to pH and can indicate mitophagy.

Establishment of the cell lines:

The transfection solution was prepared by mixing 360 µl DMEM, 240 µl polyfect and 12 µg mKeima-Red-Mito-7 plasmid in a tube. The tube was stood at room temperature for 20 min. Scr, shPAT2 and PAT2-HA cells were seeded into a 6 well plate (each cell line two

wells). 200 µl transfection solution was added to each well and control cells were kept in another 3 wells in 200 µl puromycin selective medium.

The plate was kept in the incubator (5% CO_2, 37°C) for 4 h.

1.3 ml puromycin selective medium was added to each transfection well and The plate was kept in the incubator (5% CO_2, 37°C) for another one day.

Then the medium in the plate was changed by 1.5 ml puromycin selective medium containing 500 µg/ml G418 for each well. The plate was kept in the incubator (5% CO_2, 37°C) until no control cell survives. Transfected cells were split with puromycin selective medium containing 500 µg/ml G418 and stored when reaching to the needed total number.

Cells were seeded into an 8 well life cell image chamber and then were induced for adipogenesis by MDI protocol. Till the 8th day, cells were treated with amino acid starvation for 1 h or 24 h, other cells were kept in puromycin selective medium. Finally, the medium of all the wells was changed to life cell image solution and observed under the confocal microscope by using external incubator and gas mixer to keep cells in 5% CO2, 37°C environment.

2.2.10 Flow cytometry test in DsRed-LC3-EGFP transfected cells

For cell culture of DsRed-LC3-EGFP transfected cells, puromycin selective medium containing 500 µg/ml G418 was used. Puromycin selective medium was used for Scr cells without DsRed-LC3-EGFP. Cells with fluorescence needed to be protected from light.

Cell preparation:

For sample, adipocytes and preadipocytes controls: Control and DsRed-LC3-EGFP transfected preadipocytes were seed in a 6 well plate and induced for the adipogenic differentiation till the 8th day. 1 h or 24 h amino acid starvation was performed then. Scr preadipocytes were seeded into another well in 6 well plate as preadipocyte control.

For the fluorescence controls: Scr preadipocytes were seeded into two wells of 6 well plate. The GFP/RFP transfection solution was prepared by mixing 120 µl DMEM, 80 µl polyfect and 4 µg GFP/RFP plasmid. After standing for 5 min, the GFP/RFP transfection

solution was added respectively to the 2 wells to cover all the cells. Cells were incubated in the incubator (5% CO2, 37°C) for 4 h. Then 1.3 ml puromycin selective medium was added to each well and cells were further incubated in the incubator (5% CO2, 37°C) for one day.

For the flow cytometry test: All the cells were degisted by 500 µl Trypsin-EDTA (0.05%) phenol red in the incubator (5% CO_2, 37°C) for 1 min and then 500 µl cold PBS was added to each well. Cells were pipette up and down several times carefully and then transferred to 1.5 ml prechilled tubes. Tubes were centrifuged for 5 min at 4°C 500 × g. Cells were resuspended with 500 µl fluorescence-activated cell sorting (FACS) buffer (1 mM EDTA and 1% BSA in PBS) for each tube. The cell suspension was pipette through the 35 µm membrane in the cap and collected the flow through in the tube on ice.

The control Scr preadipocytes and adipocytes were analyzed to exclude the preadipocyte population in the adipocyte. Scr preadipocytes with GFP/RFP were analyzed to set the compensation of channels for GFP and DsRed. Samples were analyzed and the files were exposed to be analyzed in the software FlowJo. Autophagy indexes were calculated according to the reported method (Sheen et al 2011).

$$\text{Autophagy index } = 100 - 100 \times \frac{\text{FL(GFP)}}{\text{FL(DsRed)}}$$

2.2.11 Electron microscope samples preparation

Each coverslip was bended on one side and put into each well of 24 well plate by a sterilized forceps under the cell culture hood. 1 ml collagen was added to each well. The plate was kept in the incubator (5% CO_2, 37°C) for 2 h and then collagen solution was removed. Then preadipocytes were seeded into each well and induced for adipogenic differentiation till the 8th day. The adipocytes were treated with/without amino acid starvation (1 h or 24 h). Cells were washed by prechilled PBS several times and then fixed by 700 µl 4% PFA in PBS (pH 7.4) mixed with glutaraldehyde (at final concentration 2%) for each well overnight at 4°C. The coverslips were transferred into 5 ml tubes with 3 ml PBS containing 0.01% sodium azide and then delivered out.

2.2.12 *In vitro* quenching experiment

This test was performed in a dark place:

2.2 mg/ml FITC-Dextran 70000 in puromycin selective medium was prepared under the cell culture hood.

Adipocytes (Scr, PAT2 knockdown and overexpression cells in 10 cm plates, each cell line 2 plates) were incubated with 10 ml FITC-Dextran 70000 contained medium overnight in incubator (5% CO_2, 37°C). The medium of one plate of each cell line was changed by 10 ml normal puromycin selective medium and for another plate 10 ml amino acid free DMEM. Cells were incubated for 1 h in the incubator (5% CO_2, 37°C) and then washed by prechilled PBS several times.

500 µl fractionation buffer (125 mM KCl, 1 mM EDTA, 50 mM sucrose, 20 mM HEPES pH 7.4, 1 : 100 diluted phosphatase inhibitor cocktails and protease inhibitor cocktail in double distilled water) was added to each plate. Cells then were scraped from the plates on ice and centrifuged for 5 min at 4°C 1200 × g. The pellet was resuspended with 700 µl fractionation buffer and homogenized with Potter-Elvehjehm grinder. The homogenate was centrifuged for 10 min at 4°C 2000 × g. The supernatant was further centrifuged for 15 min at 4°C 16100 × g. The pellet was resuspended with 100 µl fractionation buffer. The protein concentration in the resuspension was measured by using BCA kit (see sample preparation part of western blot). The suspension was added to wells in a flat glass bottom 96 well plate, 4 µg suspension for 1 well, add in total 2 wells.

100 µl prewarmed fractionation buffer was added to each well and Concanamycin A was added to one well at 1 µM final concentration as negative control. 10 mM ATP solution and 20 mM $MgCl_2$ in fractionation buffer was put in port A and B respectively in Pheastar plate reader. The plate with samples was put in the 37°C prewarmed Pheastar plate reader. The intensities of fluorescence in the two wells alternately were recorded at 488 nm for 150 cycles (Port A and B were set to add both 12.5 µl liquid to each well after 30 cycles). A blue native PAGE western blot analysis was performed by using the rest of homogenate (see blue

native PAGE and western blot part) to quantify intact V-TAPase bands. The values from Pheastar plate reader were normalized by the quantity of the intact V-ATPase bands and the average fluorescence level in flat phase (former 30 cycles). Then reciprocal values of the normalized values were calculated for values in the quenching phase (later 120 cycles). Slop values were calculated by linear regression of reciprocal values on time (s) in later 120 cycles.

2.2.13 Mouse line genotyping

Ear clips in 1.5 ml tubes were stored at –20°C. 100 µl 50 mM NaOH was used to lyse ear clips for each tube by incubation at 95°C 1000 rpm shake for 30 min. Then 10 µl 1 M Tris pH 8 was added to each tube. For one reaction, 0.5 µl ear clips lysate, 0.5 µl primer mix (0.01 nmol for each primer) and 10 µl Platinum Blue MM was mixed in a PCR tube. PCR tubes were put into thermos cycler and the needed program was run.

Preparation of 100 ml 2% agarose gel (adjust amount of reagents if volume changes): 2 g agarose was added to 100 ml TE buffer and then the mix was heated up in microwave oven till agarose dissolve. 3 µl DNA/RNA Dye was added when agarose solution was cooled a little bit. The mold with the needed comb was set to the needed size and filled by the agarose solution. The casting gates and comb were removed until gel solidifies. The gel together with the mold was put into the electrophoresis chamber. The PCR products and DNA ladder were loaded. And the electrophoresis was run at 150 V for 20 min for small sized 2% gel (adjust volt for different gel concentrations and sizes). Images were acquired by a BioImaging gel documentation system.

2.2.13.1 PAT2 whole body knockout mouse line

2.2.13.1.1 PAT2 knockout

Primers:

Primer	Sequence
pat2 5' L ko L wt	CCAAATCCCTCCTTCCTCTC
pat2 5' R ko	GTTTTCCCAGTCACGACGTT
pat2 5' R wt	GGTGTATGTGCAGGTGCAAG

Knockout band's size is 331 bp and wildtype band's size is 153 bp.

PCR program:

PCR Settings	Temperature	Time	# of cycles
1 Denaturation (Melting)	94°C	2 min	1
	94°C	20 s	
2 Amplification (Melting, Annealing, Polymerisation)	65°C; -0.5°C per cycle	15 s	10
	68°C	10 s	
	94°C	15 s	
2 Amplification (Melting, Annealing, Polymerisation)	60°C	15 s	28
	72°C	10 s	
3 Polymerization	72°C	5 min	1
4 Cooling	12°C	infinite	1

2.2.13.1.2 Rosa26 Cre

Primers:

Primer	Sequence
pCre1	ATGCCCAAGAAGAAGAGGAAGGT
pCre2	GAAATCAGTGCGTTCGAACGCTAGA

Size of Rosa26 Cre band is 447 bp and wildtype show no band.

PCR program:

PCR Settings	Temperature	Time	# of cycles
1 Denaturation (Melting)	94°C	5 min	1
	94°C	30 s	
2 Amplification (Melting, Annealing, Polymerisation)	58°C	40 s	35
	72°C	90 s	
3 Polymerization	72°C	2 min	1
4 Cooling	12°C	infinite	1

2.2.13.1.3 *neo* deletion

Primers:

Primer	Sequence
EP 418	AGCCATACCACATTTGTAGAGG
EP 423	CAGCCCAATTCCGATCATATTC
EP 420	ATTGCATCGCATTGTCTGAGTAG
EP 1337	GTTGTGGTTTGTCCAAACTCATC

neo deletion shows 351 bp and 101 bp two bands, *neo* shows 459 bp (very light) and 275 bp two bands.

PCR program:

PCR Settings	Temperature	Time	# of cycles
1 Denaturation (Melting)	94°C	2 min	1
	94°C	20 s	
2 Amplification (Melting, Annealing, Polymerisation)	65°C; -0.5°C per cycle	15 s	10
	68°C	10 s	
	94°C	15 s	
2 Amplification (Melting, Annealing, Polymerisation)	60°C	15 s	28
	72°C	10 s	
3 Polymerization	72°C	5 min	1
4 Cooling	12°C	infinite	1

2.2.13.2 Kindlin-2 adipose tissue specific knockout mouse line

2.2.13.2.1 Kindlin-2 flox

Primers:

Primer	Sequence
Fermt2 5'	TACAGGTGGCTGACAAGATCC
Fermt2 3'	GTGAGGCTCACCTTTCAGAGG

Size of wildtype band is 743 bp and Kindlin-2 flox is 820 bp.

PCR program:

PCR Settings	Temperature	Time	# of cycles
1 Denaturation (Melting)	95°C	5 min	1
	94°C	30 s	
2 Amplification (Melting, Annealing, Polymerisation)	65°C	45 s	39
	72°C	45 s	
3 Polymerization	72°C	10 min	1
4 Cooling	12°C	infinite	1

2.2.13.2.2 Adiponectin Cre

Primers:

Primer	Sequence
Transgene Reverse	ACGGACAGAAGCATTTTCCA
Transgene Forward	GGATGTGCCATGTGAGTCTG
Internal Positive Control Forward	CTAGGCCACAGAATTGAAAGATCT
Internal Positive Control Reverse	GTAGGTGGAAATTCTAGCATCATCC

Size of control band is 324 bp and Adiponectin Cre is 200 bp.

PCR program:

PCR Settings	Temperature	Time	# of cycles
1 Denaturation (Melting)	94°C	2 min	1

	94°C	20 s	
2 Amplification (Melting, Annealing, Polymerisation)	65°C; -0.5°C per cycle	15 s	10
	68°C	10 s	
	94°C	15 s	
2 Amplification (Melting, Annealing, Polymerisation)	60°C	15 s	28
	72°C	10 s	
3 Polymerization	72°C	5 min	1
4 Cooling	12°C	infinite	1

2.2.13.2.3 Flop

Primers:

Primer	Sequence
flp- as	CTCGAGGATAACTTGTTTATTGC
flp-s	CTAATGTTGTGGGAAATTGGAGC

Size of the positive band is 550 bp.

PCR program:

PCR Settings	Temperature	Time	# of cycles
1 Denaturation (Melting)	94°C	4 min	1
	94°C	30 s	
2 Amplification (Melting, Annealing, Polymerisation)	59°C	30 s	35
	72°C	60 s	
3 Polymerization	72°C	5 min	1
4 Cooling	12°C	infinite	1

2.2.14 Animal measurement

2.2.14.1 Random fast experiment

For wildtype mice, the diet was removed in the afternoon. The test was performed in the morning for random fast 18 h. Diets were kept in the cages of control mice.

2.2.14.2 High fat diet (HFD) test

All the mice were weighed before the test. Mice for HFD were fed 5 g per mouse every week. Mice for chow diet (CD) were fed as normal. The weights of both HFD and CD mice were recorded every week.

2.2.14.3 Glucose tolerance test (GTT) and Insulin tolerance test (ITT)

Each mouse was transferred to a single empty cage with water but without diet for fast 3 h.

For GTT, 20% glucose injection solution was injected intraperitoneally for each mouse base on the weight according to the radio 2 g glucose per 1 kg weight. For ITT, 0.075 munit/ µl insulin injection solution was intraperitoneally injected for each mouse base on the weight according to the radio 10 µl insulin injection solution per 1 g per weight.

The blood glucose concentration of each mouse was measured before injection and after injection 15 min, 30 min, 60 min, 90 min, 120 min by using the glucose meter.

Then Mice were transferred back to the original cages with diet.

For ITT, once blood glucose was measured to be below 40 mg/dl, the mouse needed to be Intraperitoneally injected with 20% glucose as the radio 2 g glucose per 1 kg weight.

2.2.14.4 ECHO-MRI

A calibration was performed if ECHO-MRI was not calibrated. The standard sample was put in ECHO-MRI and the system test was run.

The mouse was transferred to a suitable clean holder with a suitable caster at a suitable height to make the mouse at the bottom of the holder. After putting the holder into ECHO-MRI, weight and ear tag number of the mouse were input. The data were acquired after scanning. The mouse was transferred back to the original cage. Next scanning was performed if needed.

2.2.14.5 Evans blue intravenous injection

5 ml 0.5% Evans blue solution was prepared by dissolving 0.025 g Evans blue in 5 ml saline (adjust the volumes if final volume is different) and then filtering the solution by using 0.22 µm filter under cell culture hood. 2 ml anesthetic solution was prepared by mixing 400 µl ketamine, 150 µl xylazine and 1450 µl saline (adjust the volumes if the total volume is different).

The anesthetic solution was intraperitoneally injected for the mouse according to the radio 10 µl per 1 g weight. The mouse after injection was put in an empty cage until the mouse showed no reflection. The mouse was then transferred to a warm pad to warm the tail

up. 200 µl Evans blue was injected into the vein in the tail by using 30G x 1/2" insulin syringe. The needed tissues were sampled after several minutes and images were acquired.

2.2.15 Histology

2.2.15.1 Embedding

For wax embedding:

Tissues in cassettes were incubated by 4% PFA in PBS for fixation overnight at 4°C and then washed by PBS. The tissues were further incubated in turn by 70% ethanol to incubate all the cassettes overnight at 4°C, 80% ethanol for 1 h at room temperature, 90% ethanol for 1 h at room temperature, 100% ethanol for two times (each time 1 h) at room temperature, xylene for two times (each time for 10 min) at room temperature melted paraffin for two times (each time for 1 h) at 60°C and melted paraffin overnight at 60°C. Tissues were embedded in paraffin by using paraffin embedding station. Cooled blocks were stored at room temperature.

For cryostat embedding:

The tissues were put in the appropriately sized mold containing a little unsolidified OTC on dry ice. Enough OTC was added to immerse the tissue (avoid bubbles). Until OTC solidifies completely on dry ice blocks of tissues were stored at −80°C.

For vibratome embedding:

5% low melting point agarose in PBS was melted completely at 70°C. Tissues fixed by 4% PFA in PBS 1 h at room temperature was washed by PBS for three times. Then tissues were transferred to molds with suitable sizes. Melted 5% low melting point agarose was carefully added to immerse the tissues. The section was carried out until agarose completely solidifies. Tissues were stored in PBS at 4°C with 0.01% sodium azide after removing agarose.

2.2.15.2 Staining of paraffin section

2.2.15.2.1 H&E staining

For hydration, sections were incubated in turn by xylene for two times (each time for 5 min) at room temperature, 100% ethanol for 3 min at room temperature, 90% ethanol for 3 min at room temperature, 70% ethanol for 3 min at room temperature and double distilled water for 3 min at room temperature. For staining, sections were incubated by Mayer hematoxylin solution (1 : 5 dilution for stock solution) for 1 min at room temperature. Sections then were washed carefully by double distilled water and rinsed by running tap water for 2 min. Next, sections were incubated in turn by 96% ethanol for 3 min at room temperature, 100% ethanol for 3 min at room temperature and Chromotrope II (Eosin) solution containing 100 mg Chromotrope II (Eosin), 100 ml 95% ethanol and 100 µl acetic acid (adjust volume as needed) for 3 min at room temperature. For dehydration, sections were incubated in turn by 96% ethanol for 3 min at room temperature, 100% ethanol for 3 min at room temperature, xylene for 5 min at room temperature and xylene for two times (each time for 5 min) at room temperature. Sections were mounted by Roti-Mount and coverslips were used to cover for all slides.

2.2.15.2.2 Masson staining

The hydration was performed according to the H&E staining.

Sections were re-fixed by Bouin's solution containing 75 ml picric acid (saturated), 25 ml 37-40% formaldehyde and 5 ml acetic acid (adjust volume as needed) for 1 h at 56°C. Next, sections were rinsed with running tap water for 5 min.

Then sections were incubated in turn in the following solution. After every incubation except Phosphomolybdic-phosphotungstic acid solution incubation sections were washed by double distilled water. The solution includes:

Weigert's solution containing 0.5 g hematoxylin, 50 ml 95% ethanol, 2 ml 29% ferric chloride in water, 47.5 ml double distilled water and 0.5ml hydrochloric acid (adjust volume as needed) for 10 min at room temperature.

Biebrich scarlet-acid fuchsin solution containing 90 ml 1% biebrich scarlet, aqueous,10 ml 1% acid fuchsin, aqueous and 1 ml acetic acid (adjust volume as needed) for 10 min at room temperature.

Phosphomolybdic-phosphotungstic acid solution containing 50 ml 5% Phosphomolybdic acid and 50 ml 5% Phosphotungstic acid (adjust volume as needed) for 10 min at room temperature.

Aniline blue solution containing 2.5 g aniline blue, 2 ml acetic acid and 100 ml double distilled water (adjust volume as needed) for 10 min at room temperature.

1% acetic acid solution for 10 min at room temperature.

The dehydration was performed according to the H&E staining.

2.2.15.2.3 Picrocirius red staining

The hydration was performed according to the H&E staining.

Sections were incubated in Weigert's solution (same composition as for Masson staining) for 8 min at room temperature and then rinsed by running tap water for 10 min. Next, sections were incubated in the picro-sirius red solution containing 0.1 g sirius red (direct red 80) and 100 ml picric acid (saturated) (adjust volume as needed) for 1 h at room temperature. Then sections were washed with 0.5% acetic acid twice.

The dehydration was performed according to the H&E staining.

2.2.15.2.4 Azan staining

The dehydration was performed according to the H&E staining.

Sections were re-fix section in Bouin's solution (same composition as for Masson staining) for 1 h at 56°C and then rinsed by running tap water for 5 min. Then sections were incubated in solution A containing 2 g azocamine, 1 ml acetic acid and 100 ml double distilled water (adjust volume as needed) for 1 h at 50°C. Brief washing by double distilled water was performed. Then sections were incubated in solution B containing 0.1 ml aniline and 100ml 95% ethanol (adjust volume as needed) at room temperature for several minutes still nucleuses were observed to be differentiated (before observation under microscope dig

sections in 0.1% hydrochloric acid in 100% ethanol (solution C)). Sections were washed with double distilled water. Then sections were incubated in 5% phosphomolybdic solution (solution D) for 2 h at room temperature. Next, sections were incubated in solution E containing 2 g orange G, aniline blue (methyl blue), 7.5 ml acetic acid and 100 ml double distilled water (adjust volume as needed) for 2 h at room temperature. Washing by double distilled water was performed. The dehydration was performed according to the H&E staining.

2.2.16 Statistic analysis

All the calculations were performed using Excel and all the statistic analyses were performed by using software prism. Error bars show SEM. One way ANOVA and two way ANOVA with tukey post hoc were used to analyzed single variation and multi variation respectively. For comparison between two groups, t test was used. For all the statistics, * means $p < 0.05$, ** means $p < 0.01$, *** means $p < 0.001$ and **** means $p < 0.0001$.

3 Results

3.1 Kindlin-2

3.1.1 Kindlins and integrins expression levels in mice upon HFD

Kindlin mediated integrin activation plays a critical role in cell adhesion, cell spreading, migration and other cellular functions (Rognoni et al 2016). As a broadly expressed Kindlin, Kindlin-2 is the only Kindlin with a high expression level in adipose tissue (Ussar et al 2006). The ablation of Kindlin-2 in fats was reported to cause lipodystrophy and metabolic disorders (Gao et al 2019). However, still little is known about the related physiological functions of Kindlin-2 in adipose tissues.

In order to primarily figure this out, mice were fed HFD to check if expression of Kindlin-2 and its potential interacting integrins were altered compared with the CD diet mice. Wildtype mice were treated with HFD (5 mice) and CD (5 mice) from the 8th to the 18th week. Body weight of each mouse was recorded every week. On the 18th week, blood

glucose of CD mice was slightly lower than HFD mice, average body weights of HFD and CD showed the significant difference (**Figure 3.1 A**), which indicated that the HFD model worked.

Following, inguinal adipose tissue (iWAT), BAT, SCF and PGF were taken for RNA isolation. By qPCR analysis for the expression levels of *Kindlin-2, Kindlin3,* and several integrin genes which can interact directly or indirectly with Kindlin-2, including *integrin β1, integrin β2, integrin β3, integrin β6, integrin α1, integrin α2* and *integrin α5.* The results indicate that Kindlin-2 is the predominant Kindlin in all 4 types of adipose tissue (**Figure 3.1 B**), which matches the published data (Ussar et al 2006). The integrin β1 is the major integrin protein in these adipose tissues among the integrins tested and the raise of *integrin β1* expression upon HFD BAT compared to CD BAT was significant (**Figure 3.1 B**).

Together, these results reveal that some ECM components can be regulated by HFD in brown adipose tissue, such as integrin β1.

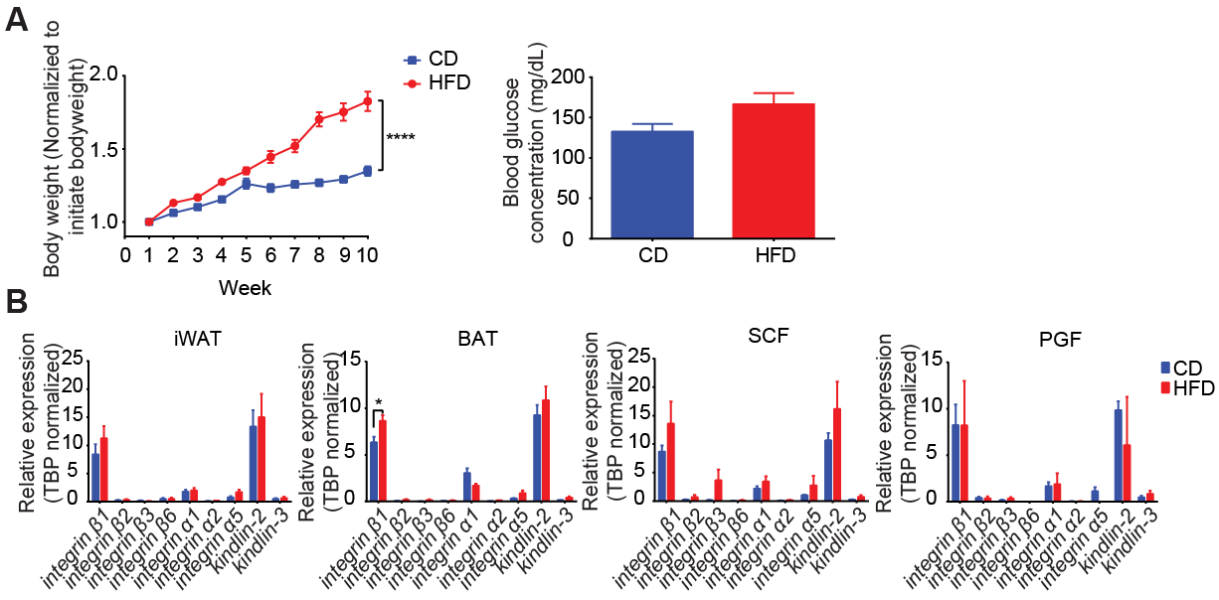

Figure 3.1 Expression variations of Kindlins and integrins in fats of mice upon HFD or CD. (A) Body weight variations and blood glucose concentration (10 weeks old) of mice upon HFD or CD. RM two-way ANOVA with Tukey's post hoc test for the left panel, non-paired t-test for the right panel, n=5. **(B)** Semi-quantification qPCR of Kindlins and integrins expression in fats of mice upon HFD or CD. RM two-way ANOVA with Tukey's post hoc test, n=5.

3.1.2 Verification of Kindlin-2 knockout in adipose tissues and Kindlin-2 knockout does not block adipogenesis

Because of the lethality of Kindlin-2 whole body knockout (Montanez et al 2008), in order to investigate the role of Kindlin-2 in adipose tissue, conditional Kindlin-2 knockout mice were generated. To achieve specific knockout in adipose tissue, Kindlin-2$^{fl/fl}$ was crossbred with Adiponectin-Cre mice expressing Cre recombinase under the Adiponectin promoter, which ensures Kindlin-2 knockout only exits in adipose tissue.

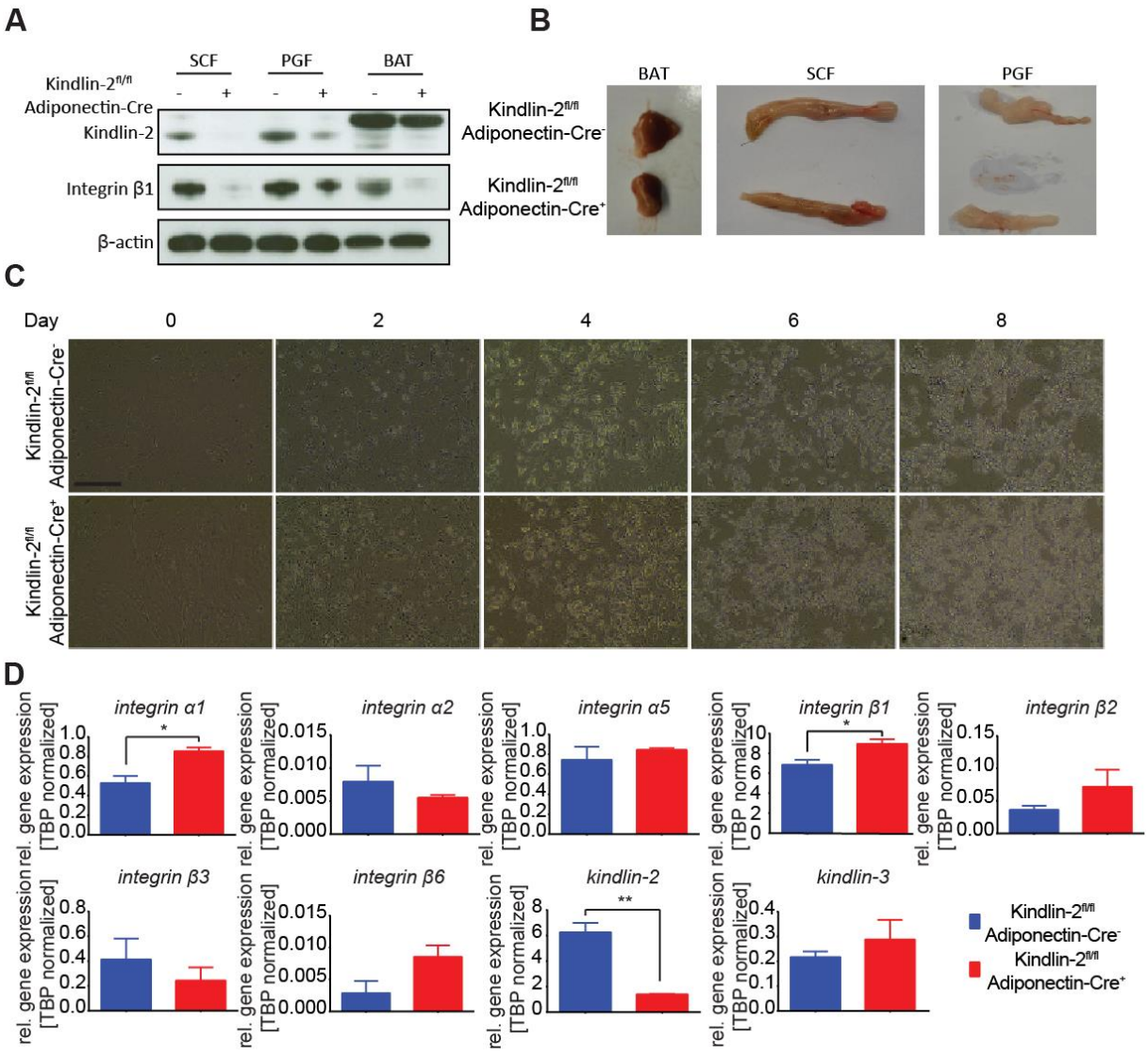

Figure 3.2 Kindlin-2 adipose tissue conditional knockout leads to fats shrink but does not block adipogenesis. (A) Western blot analysis of Kindlin-2 and integrin β1 in fats of Kindlin-2 conditional knockout and wild type mice. **(B)** Fats in Kindlin-2 conditional knockout mice and wild type. **(C)** Adipogenesis induction (0 – 8 day) of preadipocytes isolated from BAT of Kindlin-2 conditional knockout mice and wild type. The bar shows 100 µm. **(D)** Semi-quantification qPCR of Kindlins and integrins expression in adipocytes at day 8 in (C). Non-paired t-test, n=3.

To verify Kindlin-2 knockout in adipose tissue, SCF, PGF and BAT were taken from the Kindlin-$2^{fl/fl}$ Adiponectin-Cre^{+} and Kindlin-$2^{fl/fl}$ Adiponectin-Cre^{-} mice in the same cohort for protein isolation. Western blot analysis for these protein samples showed comparing with wildtype samples, Kindlin-2 levels in Kindlin-$2^{fl/fl}$ Adiponectin-Cre^{+} samples decreased in all 3 adipose tissues (**Figure 3.2 A**). As the main type of integrin in adipose tissue, integrin β1 protein level showed a similar reduction in knockout mice than wildtype mice (**Figure 3.2 A**). Interestingly, the decrease of integrin β1 was even bigger than Kindlin-2 in BAT. Another, sizes of SCF, PGF and BAT showed decreases due to Kindlin-2 knockout (**Figure 3.2 B**).

BAT is a special tissue with enriched blood vessels (Cinti 2009), which make it hard to isolate pure proteins from brown adipocytes. To exclude this interference, the pre-brown adipocytes were isolated from BAT and then induced for adipogenesis in primary culture. As the results showed, no matter isolated from knockout mice or wildtype mice, the pre-brown adipocytes were able to differentiate into mature adipocytes on the 8th day (**Figure 3.2 C**). The differentiated adipocytes were harvested for RNA isolation and then RT-PCR analysis. A significant decrease of Kindlin-2 RNA level was shown in cells from Kindlin-$2^{fl/fl}$ Adiponectin-Cre^{+} mice **(Figure 3.2 D**). Additionally, *integrin α1* and *integrin β1* in this test showed significant increase in knockout mice **(Figure 3.2 D**). It is noticeable that *integrin β1* performed an opposite variation in RNA and protein level, which implicates Kindlin-2 may regulate translation or protein degradation of integrin β1.

The research of Monrtanez et al. suggests Kindlin-$2^{-/-}$ embryonic stem cell (ESC) line has a severe adhesion disorder comparing with wild type cell line (Montanez et al 2008). However, the pre-brown adipocytes isolated from Kindlin-$2^{fl/fl}$ Adiponectin-Cre^{+} mice could adhere normally at least on morphology during the whole adipogenesis although induction had triggered the expression of Cre recombinase to delete Kindlin-2 (**Figure 3.2 C**). Additionally, at the 8th day these cells were also able to differentiate into mature adipocytes as wildtype cells, which illustrates the adipogenesis was not impaired due to Kindlin-2

knockout, it also means that the important integrin signaling of adipogenesis was not blocked by Kindlin-2 knockout. , such as integrin *α*5 and integrin *α*6 (Liu et al 2005).

If severe cell adhesion disorder appears in adipose tissue *in vivo,* the adipose tissue will demonstrate development deficiency or even disappear. However, Kindlin-2 knockout mice only reflected a slightly decrease in size of BAT, SCF and PGF compared to wildtype mice (**Figure 3.2 B**).

These protein and RNA data illustrate the Kindlin-2 knockout in adipose tissue is reliable. Besides, the data also show the particular characteristic of Kindlin-2 in adipose tissue. This also hints that the function of Kindlin-2 and its activated integrin signaling may perform some unique functions in adipose tissue. Absence of Kindlin-2 impairs intercellular structure in adipose tissue on morphology

As the *in vivo* and *in vitro* data indicate, adipose tissue development can be completed without Kindlin-2. Whether the interior structure and morphology of adipose tissue can be affected by Kindlin-2 knockout was tested by performing stainings.

3.1.2.1 H&E staining

To investigate the morphology of adipose tissue, one of the most general ways is the H&E staining. The BAT, SCF and PGF were taken from 8 weeks old CD fed Kindlin-2$^{fl/fl}$ Adiponectin-Cre^{-}, Kindlin-2$^{fl/fl}$ Adiponectin-Cre^{+} and Kindlin-2$^{fl/-}$ Adiponectin-Cre^{+} mice. After paraffin embedding and section, 2 µm sections were used for H&E staining.

The H&E staining of these 3 kinds of tissue showed different changes due to Kindlin-2 knockout. For BAT, it was easy to recognize that the average size of the lipid droplets was smaller in knockout mice than in the other two wildtype mice (**Figure 3.3 A**). Another, thicker and darker red staining appeared in the intercellular space in knockout mice, which implicates the abnormal structures among adipocytes in BAT . These two aspects were even more obvious when observing the 4x magnification of the original images (**Figure 3.3 A**). For these two WATs, SCF and PGF, the phenomenon of different lipid droplets sizes did not appear between knockout mice and any one of the wildtype mice (**Figure 3.3 A**). But the

potential red stainings of ECM in SCF and PGF of knockout mice were still a little darker than wildtype mice in PGF (**Figure 3.3 A**).

Considering Kindlin-2 is the activator for integrins the disorders in knockout mice appearing in ECM seem to be reasonable. Furthermore, ECM disorders may also cause changes in the functions of adipose tissue or other adipose tissue related physiological functions when comparing knockout and wildtype mice.

As the results above showed, Kindlin-2 knockout induced alteration in WAT was very limited in H&E stainings. Because WAT is characterzed by very large lipid droplets which squeeze the space of cytosol and ECM, it is possible to make the alterations induced by Kindlin-2 knockout difficult to be recognized in H&E staining of WAT 2 µm section. So whether WAT is affected by Kindlin-2 knockout should be evaluated by further analyses.

3.1.2.2 Special stainings

Based on the observations of H&E staining results, morphological disorders appear in the intercellular space in the BAT of Kindlin-2 knockout mice. However, what is affected by Kindlin-2 knockout in the intercellular space was still not figured out.

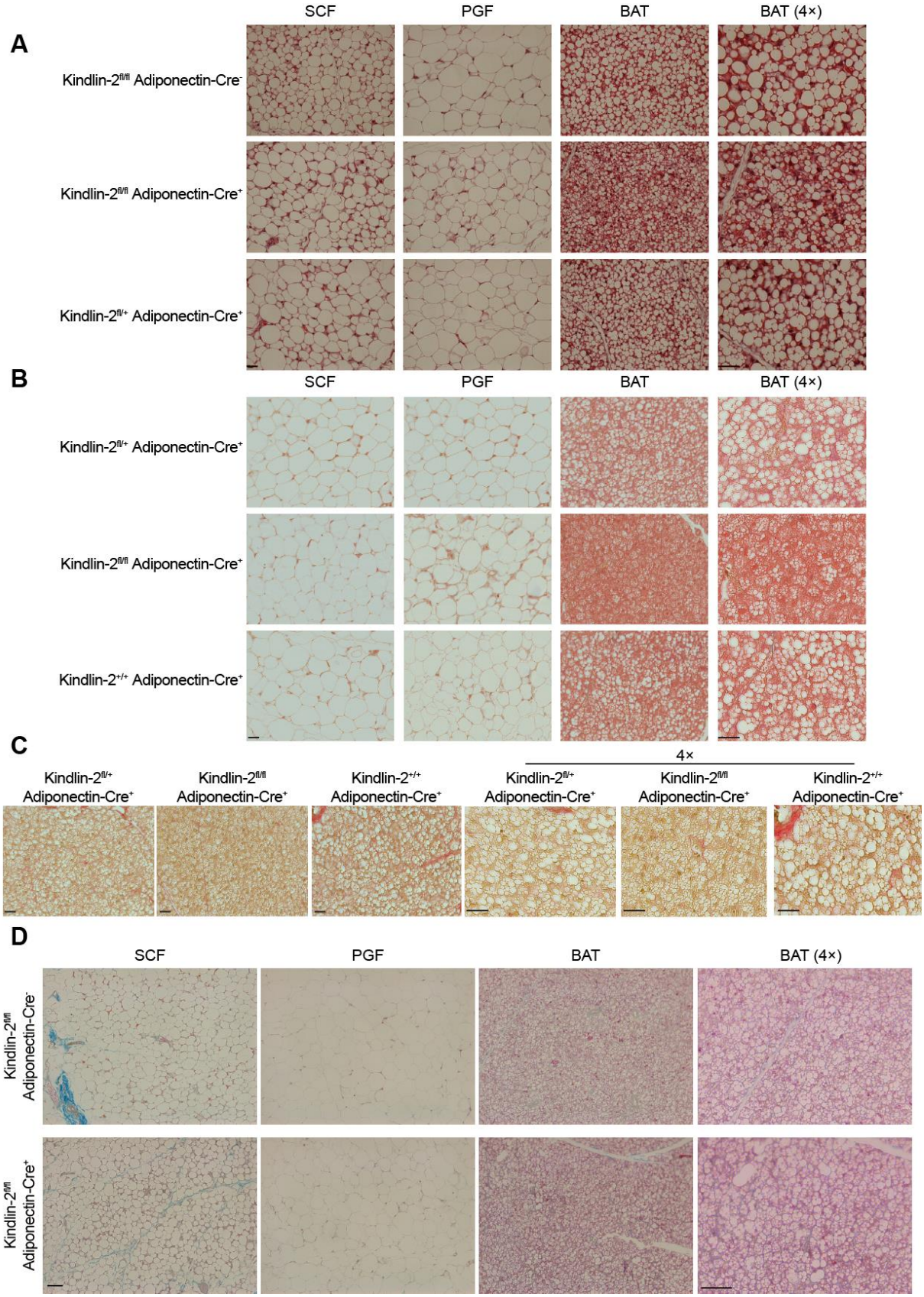

Figure 3.3 Kindlin-2 knockout affects the morphology of adipose tissues. (A) H&E staining, **(B)** Masson staining, **(C)** Picro sirius staining and **(D)** AZAN staining of adipose tissues from 8 weeks old Kindlin-2 knockout and wild type mice. Bars show 200 µm.

Some special stainings can distinguish the different components in the tissue based on their characteristic features. As a good way to distinguish collagen (blue stained) as the representation of connective tissue from the cytoplasm (red stained), the Masson's trichrome stain was performed. The same sections of 3 kinds of tissues in 3 mice were stained. For WAT, SCF and PGF lacked blue stains (**Figure 3.3 B**), which may be because of the limitation of WAT section as mentioned previously. For BAT, the blue stains were observed in the intercellular space (especially peri blood vessel area) together with red stains in wildtype samples. But in Kindlin-2 knockout samples the intercellular space showed a thick and dark red stained but nearly no blue stained structure (**Figure 3.3 B**). Because the red staining overlays the brown collagen stain, it is hard to give a conclusion that Kindlin-2 knockout decrease collagen (ECM). But these results still support the hypothesis that Kindlin-2 knockout caused ECM disorders, which lead to intercellular morphology alterations in BAT.

To confirm this phenomenon, another special staining for visualizing collagen, picro sirius red staining was used. In this staining, collagen was stained to be red, cytoplasm shows pale yellow. Sections from the same samples of BAT as the previous two stainings were stained. It can be found that in all samples the red stains (collagen) existed in the intercellular space, particularly some very dark stains were observed around the big blood vessels (**Figure 3.3 C**). However, the cover effect still exists to make the red stains difficult to be distinguished These similar results confirm the disorder of BAT in Kindlin-2 knockout mice, but still, face the problem of the potential sheltered collagen stains.

The collagen stains in these two kinds of stainings were not strong enough and not easy to detect. So it is hard to give a conclusion Kindlin-2 knockout leads to ECM components decline which causes the weak stainings. So it is still necessary to find another method for collagen staining which fits adipose tissue more. AZAN trichrome stain was chosen and performed for the following test. In AZAN staining, collagen was stained to be blue, cytoplasm was stained to be a variety of colors mixed with orange, red and blue, which makes collagen contrast more obvious. Still, SCF, PGF and BAT were taken from Kindlin-

2fl/fl Adiponectin-Cre- and Kindlin-2fl/fl Adiponectin-Cre^{+} mice. The 2 μm sections from these samples embedded with paraffin were stained according to the AZAN staining protocol. The results showed in all 3 tissues slightly enhanced collagen stains in knockout mice compared with wildtype samples (**Figure 3.3 D**). The increase of both the two components resulted in a strongly stained structure between adipocytes in knockout mice, and this phenomenon was much more obvious in BAT (**Figure 3.3 D**). Furthermore, collagen in wildtype mice showed a better-distributed blue staining than in knockout mouse (**Figure 3.3 D**).

All the staining analyses indicate that the absence of Kindlin-2 in adipose tissue leads to morphological hyperplasia of intercellular structures. Particularly, the AZAN staining suggests enhanced collagen deposition in Kindlin-2 knockout mice.

3.1.3 Kindlin-2$^{fl/fl}$ AdiponectinCre^{+} mice show less fat mass than Kindlin-2$^{fl/fl}$ AdiponectinCre^{-}

The previous data demonstrate the Kindlin-2 knockout mice in BAT show disorders on morphology rather than in WATs SCF and PGF. However, only staining results are not sufficient to conclude that the morphology of WATs is not affected by Kindlin-2 knockout. So next, analyses for whole tissues were performed to check if Kindlin-2 knockout can alter WAT besides BAT.

3.1.3.1 Fat mass in CD mice

Fat mass variation alters body weight (Hall et al 2011). And measuring body weight is much easier than measuring isolated fat mass, especially for continuous measurement. So firstly the body weight curve was recorded for Kindlin-2$^{fl/fl}$ AdiponectinCre^{-} mice and Kindlin-2$^{fl/fl}$ AdiponectinCre^{+} mice. The curves for males were from the 7th week to the 17th week, for females were from the 9th week the 17th week. Analysis of two-way ANOVA showed no significant difference for females between wildtype and knockout mice, but significant higher body weights of wildtype mice than knockout mice were showed at the 15th, 16th and 17th weeks old (**Figure 3.4 A**).

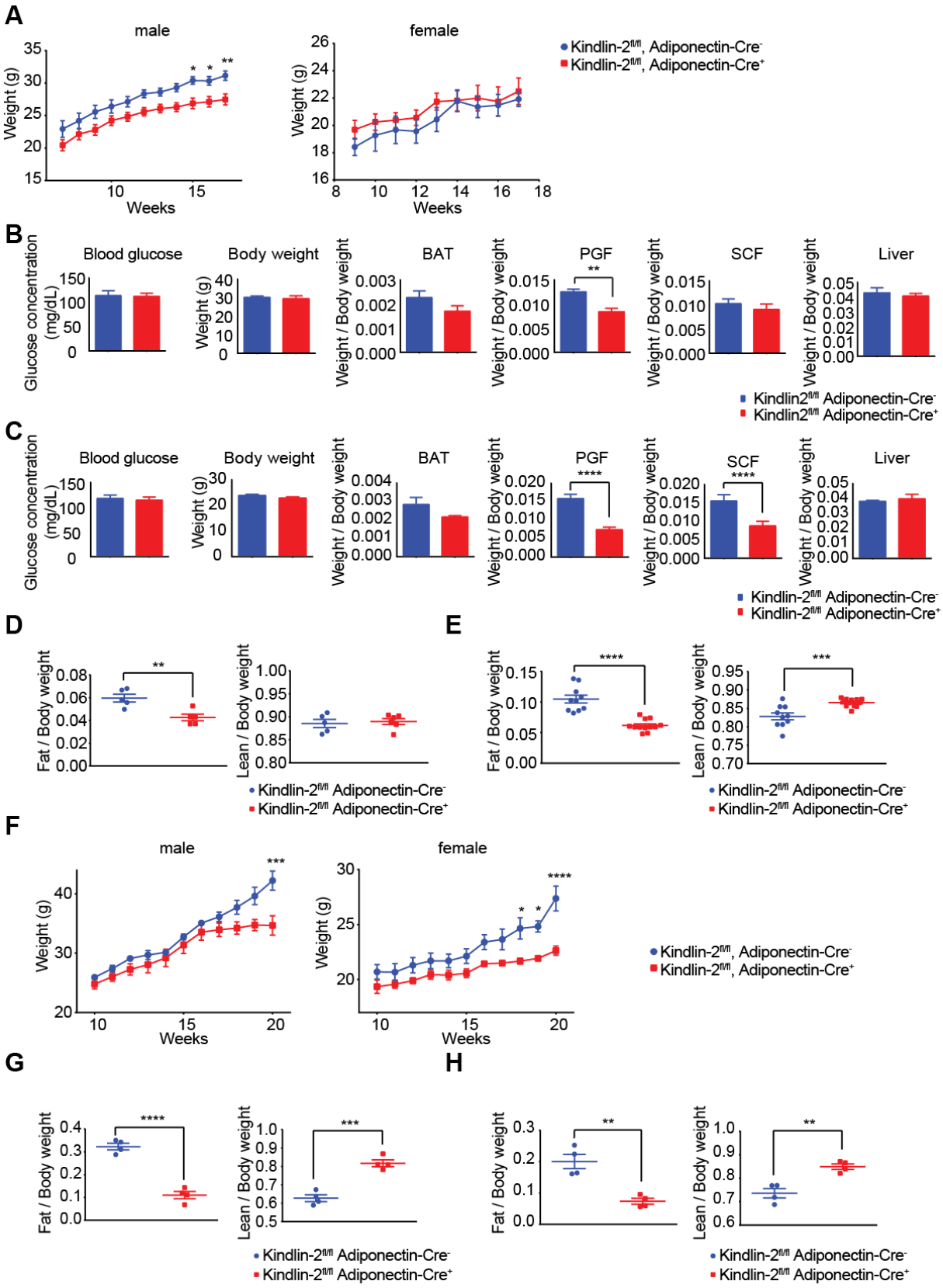

Figure 3.4 Fat mass declines in Kindlin-2 knockout mice. **(A)** Body weights variations of Kindlin-2 conditional knockout and wild type mice. n=3-4 for male, n=3-5 for female. Blood glucose, body weights and body weight normalized weights of tissues from 18 weeks old male **(B)** and female **(C)** Kindlin-2 conditional knockout and wild type mice. n=6 for male, n=12-15 for female. Body weight normalized masses of fat and lean measured by ECHO-MRI from 18 weeks old male **(D)** and female

(E) Kindlin-2 conditional knockout and wild type mice. n=5-6 for male, n=10-12 for female. **(F)** Body weights variations of Kindlin-2 conditional knockout and wild type mice upon HFD. n=5 for male, n=4 for female. Body weight normalized masses of fat and lean measured by ECHO-MRI from 18 weeks old male **(G)** and female **(H)** Kindlin-2 conditional knockout and wild type mice upon HFD. n=4-6 for male, n=4 for female. RM two-way ANOVA with Tukey's post hoc test for (A) and (F), non-paired t-test for (B), (C), (D), (E), (G) and (H).

In order to figure out whether the less bodyweight is caused by less fat mass for male mice and whether adipose tissue in female changes due to Kindlin-2 knockout, several kinds of tissues were taken and weighed. The data of isolated tissues from 12 males (including 6 Kindlin-$2^{fl/fl}$ AdiponectinCre^{+} mice and 6 Kindlin-$2^{fl/fl}$ AdiponectinCre^{-} mice) and 27 females (including 15 Kindlin-$2^{fl/fl}$ AdiponectinCre^{+} mice and 12 Kindlin-$2^{fl/fl}$ AdiponectinCre^{-} mice) at age 18 weeks were counted. Considering the individual difference, all the tissue weight data were normalized by whole body weight. For male mice, the average values of SCF, PGF and BAT in knockout mice were all lower than wildtype mice. PGF shows a significant difference (**Figure 3.4 B**). The female mice data showed similar decreases appearing in all the 3 kinds of fat, but both SCF and PGF showed significant declines in knockout mice (**Figure 3.4 C**).

Interestingly, the blood glucose levels did not show a difference between knockout mice and wildtype mice regardless of gender (**Figure 3.4 B and C**). In addition, liver mass also did not show a significant difference between knockout mice and wildtype mice (**Figure 3.4 B and C**).

Due to the limitation of accuracy for isolating fat, it is unavoidable to lose some part of the adipose tissue. In order to acquire more accurate data for fat mass, knockout mice and wildtype mice were analyzed by EchoMRI. All the EchoMRI values of fat and lean mass for male and female mice were normalized by whole body weights and all the mice were 18 weeks old. Similar to the previous data, fat in knockout mice was shown to be significantly lower than wildtype mice for both male (**Figure 3.4 D**) and female mice (**Figure 3.4 E**). The difference between male and females appeared in the lean mass part, wildtype lean mass was significantly lower than knockout for female mice, but this difference did not exist for male mice (**Figure 3.4 D and E**). This may explain why for female knockout mice there is no difference shown on the body weight curve, but fat mass actually shrinks.

3.1.3.2 Fat mass in HFD mice

HFD is a model that progressively increases body weight (Winzell & Ahren 2004). So feeding the knockout and wildtype mice with HFD was also performed to check if the decline on fat mass for knockout mice will be magnified.

The body weight curves for male and female mice fed with HFD were similar with the CD diet experiment, for both male and female mice, wildtype mice showed higher body weight gain than knockout mice (**Figure 3.4 F**). But the body weight disparity was magnified to around 10 g for 18 weeks old male, 5 g for 18 weeks old female mice (**Figure 3.4 F**). The EchoMRI data also revealed the magnified differences on values of fat and lean mass for male mice (**Figure 3.4 G**) and for female mice (**Figure 3.4 H**). Remarkably, for male mice, the lean mass showed significantly higher in knockout mice than wildtype mice (**Figure 3.4 G and H**).

3.1.4 Kindlin-2 knockout induces the disordered angiogenesis in fats

The previous results have revealed a series of phenomena for Kindlin-2 knockout in adipose tissues, such as hyperplasia of ECM, deterioration of fat mass. Next, the adipose tissues related functions were tested to figure out whether these Kindlin-2 knockout induced changes of adipose tissues can affect some normal physiological activities.

3.1.4.1 GTT and ITT

The systemic glucose metabolism and insulin sensitivity are two important functions contributed by adipose tissues (Attie & Scherer 2009). In order to investigate whether glucose metabolism and insulin sensitivity are affected by Kindlin-2 knockout in adipose tissues, intraperitoneal GTT and ITT were performed to Kindlin-2 knockout and wildtype mice of 18 weeks old.

The GTT results showed the blood glucose levels for all the mice demonstrated a rapid rise at 15min after intraperitoneal glucose injection and a slow decline to the initial level (**Figure 3.5 A**). Two-way ANOVA and multiple comparison tests showed no significant difference between knockout and wildtype mice at each time point for both male and female

mice. However, knockout mice showed a more rapid glucose deposit than wildtype mice, which could be found from the different speeds of blood glucose declines. According to multiple comparisons of two-way ANOVA between each two time points for knockout or wildtype mice, due to glucose injection, glucose levels at 15 min are significantly higher than 0 min. Then it can be found after 15 min the earliest time point which showed significant decrease for male knockout mice was 30 min, but for male wildtype mice was 60 min (**Figure 3.5 A**). Similarly, for female mice the earliest significant decrease after glucose level peak was 30 min for knockout mice, 60min for wildtype mice (**Figure 3.5 A**). These results implicate Kindlin-2 knockout does not alter glucose tolerance, although there is an obvious deterioration of fat mass. Another possibility is a potential self-balance mechanism *in vivo* may have compensated the influence of fat loss on blood glucose. Nevertheless, the differences shown on glucose deposit still reveal some possible effects of Kindlin-2 knockout on systemic glucose metabolism.

As another important part, ITT was performed to study whether the insulin sensitivity was altered by Kindlin-2 knockout. For all mice, the blood glucose variations during ITT showed declines after the insulin intraperitoneal injection and a slow rebound subsequently (**Figure 3.5 B**). Similar to GTT, there was no significant difference in the average values of blood glucose shown between knockout and wildtype at the same time point for male or female mice. Besides, the speed of insulin induced blood glucose decrease can also reflect insulin sensitivity. The data were analyzed by multiple comparisons of two-way ANOVA to find out the earliest time point of significant decline of the blood glucose after the injection compared with the peak level. The results show the earliest significant decreases of blood glucose for knockout and wildtype male were both at 60 min, for knockout and wildtype female were both 15 min (**Figure 3.5 B**). Male mice show lower insulin sensitivity than female mice, but insulin sensitivities for knockout and wildtype are similar.

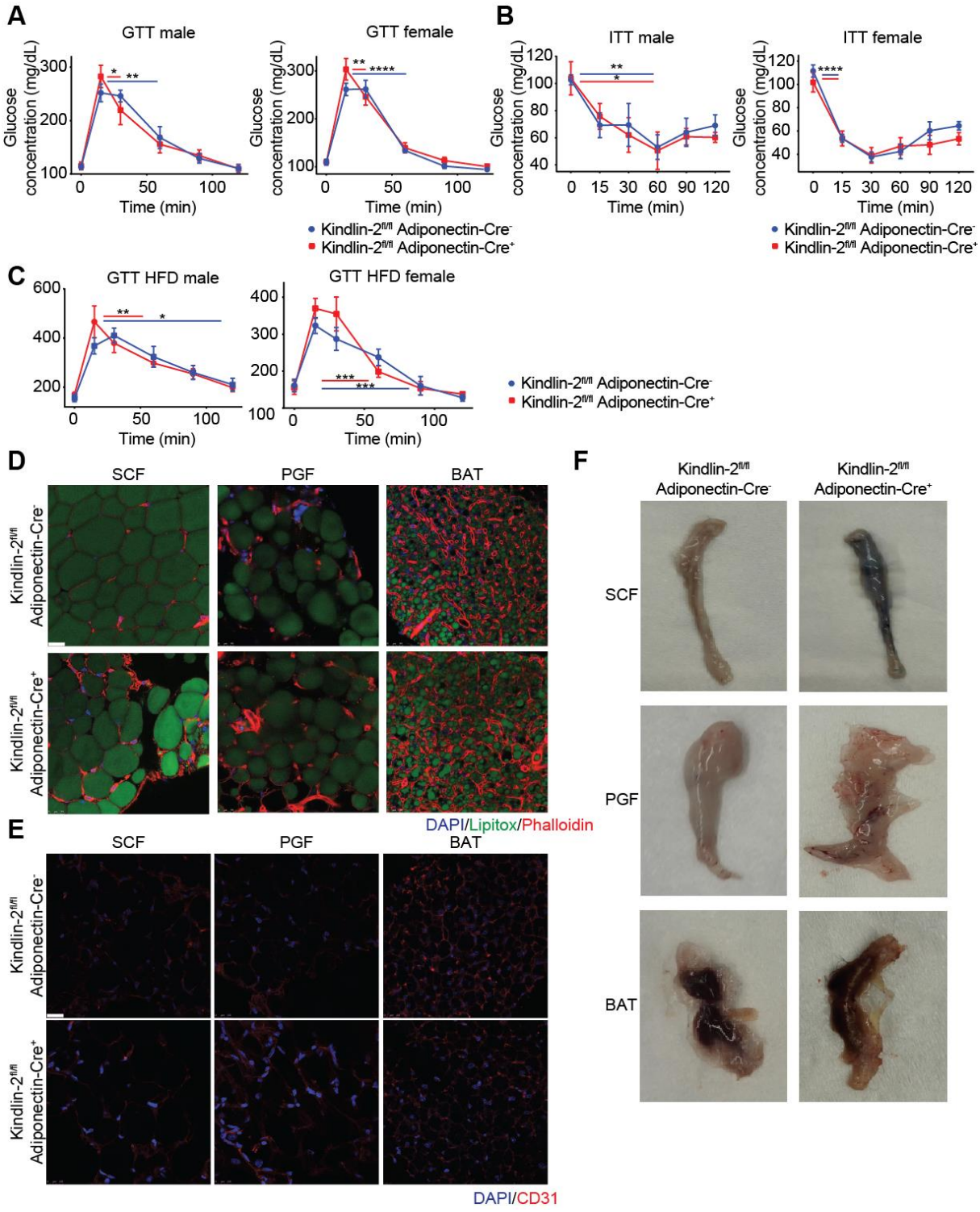

Figure 3.5 Angiogenesis disorders are shown in Kindlin-2 knockout fats. (A) GTT test for 18 weeks old Kindlin-2 conditional knockout and wild type mice. n=4-5 for male, n=10-11 for female. **(B)** ITT test for 18 weeks old Kindlin-2 conditional knockout and wild type mice. n=4-5 for male and female. **(C)** GTT test for 18 weeks old Kindlin-2 conditional knockout and wild type mice upon HFD. n=4 for male and female. **(D)** Fluorescence staining for lipid droplets (Lipitox) and F-actin (Phalloidin) in SCF, PGF and BAT from 18 weeks old Kindlin-2 conditional knockout and wild type mice. The bar shows 25 µm. **(E)** Immunostaining for blood vessels marker CD31 in SCF, PGF and BAT from 18 weeks old Kindlin-2 conditional knockout and wild type mice. The bar shows 15 µm. **(F)** SCF, PGF and BAT in evans blue test by intravenous injection. RM two-way ANOVA with Tukey's post hoc test for (A), (B) and (C).

The GTT for HFD mice was also performed. By two-way ANOVA analysis, for male and female HFD mice, no significant difference was shown between wildtype and knockout at each time point. Surprisingly, the glucose disposal in CD mice showed a delay compared with HFD mice. Based on the multiple comparisons, for HFD male mice, the earliest time point of the significant decline for knockout mice was delayed to 60 min and for wildtype mice was delayed to astonishing 120 min (**Figure 3.5 C**). For HFD female mice, knockout mice showed the significant decline at 60 min, wildtype showed at 90 min (**Figure 3.5 C**). All the mice showed delayed glucose declines comparing with CD mice (**Figure 3.5 A and C**).

For the reason why knockout mice show quicker glucose deposit no matter for CD or HFD is still hard to be answered, it implicates Kindlin-2 may be involved in some related complex regulations, such as insulin secretion and signaling.

3.1.4.2 Kindlin-2 knockout impaired the angiogenesis

On the aspect of morphology, as described previously, what is the hyperplasia structure appearing in the intercellular space is still a question.

Because H&E staining and other special stainings can only roughly distinguish different components, a more specific staining, phalloidin staining, was performed. Phalloidin can specifically bind and stabilize filamentous actin (F-actin), which is an important component of the cytoskeleton. Based on the pattern of phalloidin staining, alterations in F-actin related structure can be observed.

150 µm vibratome sections of SCF, PGF and BAT were used for this staining. The tissues were taken from 18 weeks old wildtype and knockout mice, respectively. As the references, DAPI and Lipitox were co-stained for indicating nucleus and lipid droplets. The phalloidin stains showed a thin linear pattern in most regions among adipocytes (**Figure 3.5 D**). Another strong accumulated thick linear structure which sometimes showed a hollow pattern could also be observed among adipocytes (**Figure 3.5 D**), this structure should be the section of the big blood vessels. It was easy to find much more thick structures in

knockout mice in SCF and PGF (**Figure 3.5 D**). Additional, phalloidin staining in knockout mice also exhibited a disordered and irregular pattern in BAT. A lot of tubular structures between adipocytes indicated a high vascularisation in wildtype mice. However, in knockout mice, almost all the tubular structures were replaced by some circular structure among adipocytes (**Figure 3.5 D**). All of these results indicate a different blood vessels distribution in Kindlin-2 knockout mice and the angiogenesis in adipose tissue may be severely impaired by Kindlin-2 knockout.

To confirm this conclusion, immunostaining of CD31 was performed. CD31 is the endothelial cell marker (Newman 1997), so CD31 staining can specifically show the distribution of blood vessels in the section. The SCF, PGF and BAT were taken from 18 weeks old wildtype and knockout mice for 30 µm cryosection. DAPI and anti CD31 antibody were co-stained. The different blood vessels pattern can be visualized by CD31 staining. No obvious difference was showed in SCF and PGF for knockout mice (**Figure 3.5 E**). In BAT, the linear stains of CD31 in wildtype was stronger than in knockout mice, similar to the phalloidin staining, blood vessels showed round structures among adipocytes in knockout mice (**Figure 3.5 E**).

So the results from these two stainings match with each other. If Kindlin-2 knockout can impaire angiogenesis, the knockout mice may suffer from an impaired circulatory system. To verify this, the evans blue test was performed. This test can check the permeability of the blood vessel. The wildtype and knockout mice at 18 weeks old were intravenously injected with evans blue. Evans blue can bind to proteins but is impermeable to the blood vessel, so if blood vessel is leaky adipose tissue will also be stained by blue dye. The results showed in SCF from knockout mice it was very obvious to find the blue dye leaked and distributed in the most part of the tissue, but in SCF from wildtype mice there was only a little blue shown in lymph node where vessels come through (**Figure 3.5 F**). Similar to SCF, in wildtype PGF almost no blue dye was observed, in knockout PGF it was easy to find many hemorrhage sites showing blue dye mixed with blood (**Figure 3.5 F**). Due to the dark

initial color, the difference in BAT was not obvious to be observed, but the big hemorrhage site could still be found between the two pieces of BAT in knockout mice (**Figure 3.5 F**).

3.2 PAT2

3.2.1 Establishment of PAT2 knockdown and overexpression preadipocyte cell lines

In order to investigate the function of PAT2 in brown adipocytes, PAT2 overexpression and knockdown cell lines were established. For PAT2 knockdown cell line, there are 6 kinds of PAT2 shRNA purchased, include 381, 443, 444, 445, 446 and 447, the Scramble plasmid was also included as a negative control. For overexpression, the PAT2 coding sequence with 3' HA tag sequence was inserted into pCDH plasmid with a cytomegalovirus (CMV) promoter. Then each of these plasmids was transfected with virus packaging plasmids into 293T cells to package lentiviruses. Then the home-made pre brown adipocyte cell line was infected with each lentivirus.

A qPCR was performed to verify the reduced PAT2 expression in the cells infected with shRNA viruses. As PAT2 is highly expressed in adipocytes rather than preadipocyte, preadipocytes (including control cell line and knockdown cell line) were induced into adipocytes according to adipogenesis induction protocol for 8 days. On days 0, 2, 4, 6 and 8, cells were harvested for RNA extraction and qPCR analysis. As the results showed, the control cell line (Scr) showed an increase of PAT2 during the differentiation. All the candidates of PAT knockdown cell lines showed lower expression levels, thereinto, 446 cell line showed a stable low expression at each time point **(Figure 3.6 A)**. So finally, 446 was chosen as the knockdown cell line for the following experiments. The PAT2 overexpression cell line showed strong expression of PAT2 during differentiation, significant differences were shown among Scr, PAT2 knockdown cell line (shPAT2) and PAT2 overexpression cell line (PAT2-HA) **(Figure 3.6 A)**.

Because there is not a reliable commercial antibody for PAT2 detection, it is difficult to evaluate the protein levels in these three kinds of cell lines by WB. However, the HA tag

sequence following the PAT2 coding sequence in the overexpression plasmid provides a way for detecting PAT2-HA in PAT2 overexpression cells. As expected, the PAT2-HA western blot results showed no bands in all the Scr and shPAT2 samples and bands in PAT2-HA samples. Compared to preadipocytes, PAT2-HA in adipocytes showed dramatically higher HA levels **(Figure 3.6 B)**. This phenomenon hints to a possible post-translation regulation of PAT2.

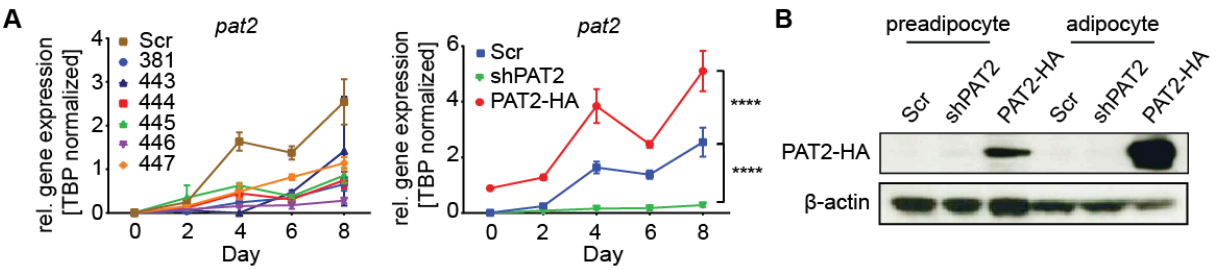

Figure 3.6 Establishment of PAT2 knockdown and overexpression preadipocyte cell lines. (A) Semi-quantification qPCR analysis for PAT2 expression during adipogenesis. The left panel shows Scr and shPAT2 cell lines, right panel shows Scr, shPAT2 (446) and PAT2-HA cell lines. RM two-way ANOVA with Tukey's post hoc test for the right panel, n=3. **(B)** WB analysis for PAT2-HA in Scr, shPAT2 and PAT2-HA preadipocytes and adipocytes.

3.2.2 PAT2 is not necessary for the adipogenesis of brown adipocytes

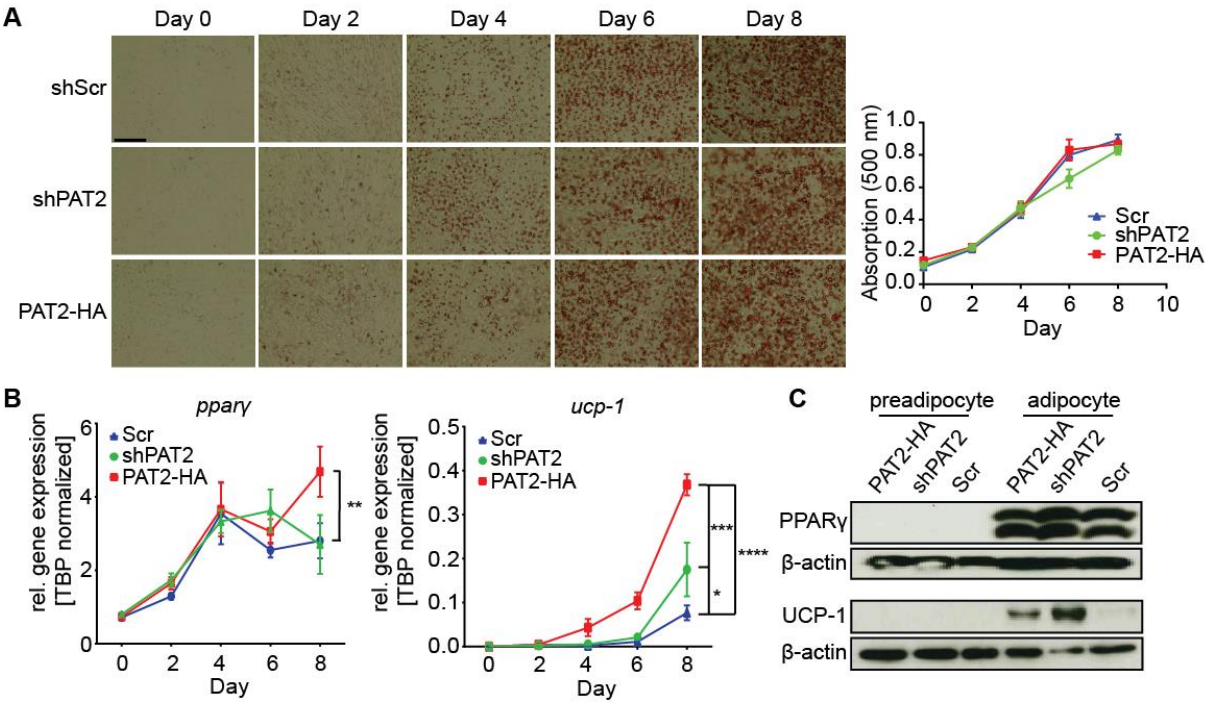

Figure 3.7 PAT2 is not necessary for adipogenesis of brown adipocytes. (A) Lipid accumulation during brown adipocyte differentiation visualized by Oil Red O staining. The scale shows 100 µm.

PPARg and UCP-1 mRNA **(B)** and protein **(C)** levels during differentiation. RM Two-way ANOVA with Tukey's posthoc test, n=3 for qPCR.

PAT2 shows a specific high expression level in BAT, whether PAT2 plays a necessary role in adipogenesis is the first question needed to be figure out. If PAT2 is the necessity for adipogenesis, PAT2 knockdown cells may not differentiate into mature adipocytes. Oil Red O staining

To evaluate adipogenesis, a convenient way is the Oil Red O staining.

The Scr, shPAT2 and PAT2-HA cells on differentiation day 0, 2, 4, 6 and 8 were fixed and stained by Oil Red O. The images of the Oil Red O staining under bright field clearly showed a similar rise in the number and size of lipid droplets from day 0 to day 8 for all cell lines **(Figure 3.7 A)**. Additional, quantification by measuring the absorption of Oil Red O dissolved in lipid showed no significant difference among the three cell lines on day 8 **(Figure 3.7 A)**. It means lipid accumulation in differentiated adipocytes is not altered by PAT2 knockdown or overexpression. Interestingly, the only difference is shown on day 6; shPAT2 cells show significantly lower absorption than PAT2-HA and Scr cells **(Figure 3.7 A)**. It may indicate that in shPAT2 cells lipogenesis is a little slower than Scr and PAT2-HA cells, as in these two kinds of cells absorption start to be stable on day 6. The Oil Red O results illustrate PAT2 knockdown or PAT2 overexpression do not affect the differentiation of preadipocytes.

3.2.2.1 qPCR and Western blot results of differentiation markers

In order to confirm the result for adipogenesis, some differentiation markers were also tested in PAT2 knockdown and overexpression cells, including the key adipogenesis marker PPARγ and brown adipocyte marker UCP-1. Similarly, all kinds of cells were harvested every two days for RNA extraction, cDNA generation and quantification. As the result showed, after an increase at day 4 in all the cell lines PPARγ demonstrated a fluctuation phase. On day 8, PAT2-HA cells show a significantly higher expression level of PPARγ than other cells **(Figure 3.7 B)**. Interestingly, on day 6 shPAT2 cells showed the lowest expression level

(Figure 3.7 B), which may explain the low lipid deposit in Oil Red O staining at day 6. As a brown adipocyte marker, UCP-1 also demonstrated a rise during the brown adipocyte differentiation. The difference is that UCP-1 in PAT2-HA cells is much higher than in Scr and shPAT2 cells since day 4. On day 8, PAT2-HA showed a significantly higher expression than other cell lines. The expression level of UCP-1 in PAT2-HA cells reached 7-8 times of the levels in Scr cells, shPAT2 also showed a significantly stronger expression than Scr cells **(Figure 3.7 B)**.

To evaluate the differentiation marker, only the gene expression data are not enough. The protein levels of PPARγ and UCP-1 in Scr, shPAT2, PAT2-HA preadipocytes (day 0) and adipocytes (day 8) were tested by WB. The results illustrated PPARγ in three kinds of adipocytes reached a similar level. Compared to preadipocytes, UCP-1 also showed an increase in adipocytes **(Figure 3.7 C)**. Noticeably, PAT2-HA cells showed a much higher UCP-1 protein level which matches the qPCR data, but PAT2 knockdown cells showed even higher UCP-1 than PAT2-HA cells **(Figure 3.7 C)**. As a defining feature of brown adipocytes, the thermogenesis of mitochondria is performed by UCP-1 (Golozoubova et al 2001, Matthias et al 2000, Nedergaard et al 2001), suggesting that there is a possible regulation of PAT2 on mitochondrial function.

All of these results illustrate PAT2 is not necessary for adipogenesis of brown adipocyte.

3.2.3 PAT2's different localization in preadipocytes and adipocytes and the dynamics of its localization

The reason why PAT2 is regarded as a brown adipocyte marker and its function is attractive is not only for the specific high expression level but also its potential plasma membrane localization (Ussar et al 2014). So to figure out the intracellular localization of PAT2 is an important aspect for studying the function of PAT2.

3.2.3.1 Localization of PAT2 in preadipocytes and adipocytes

The PAT2 overexpression cell line highly expresses PAT2-HA. Detecting PAT2-HA by anti HA tag antibody can demonstrate the subcellular localization of PAT2 in PAT2-HA adipocytes.

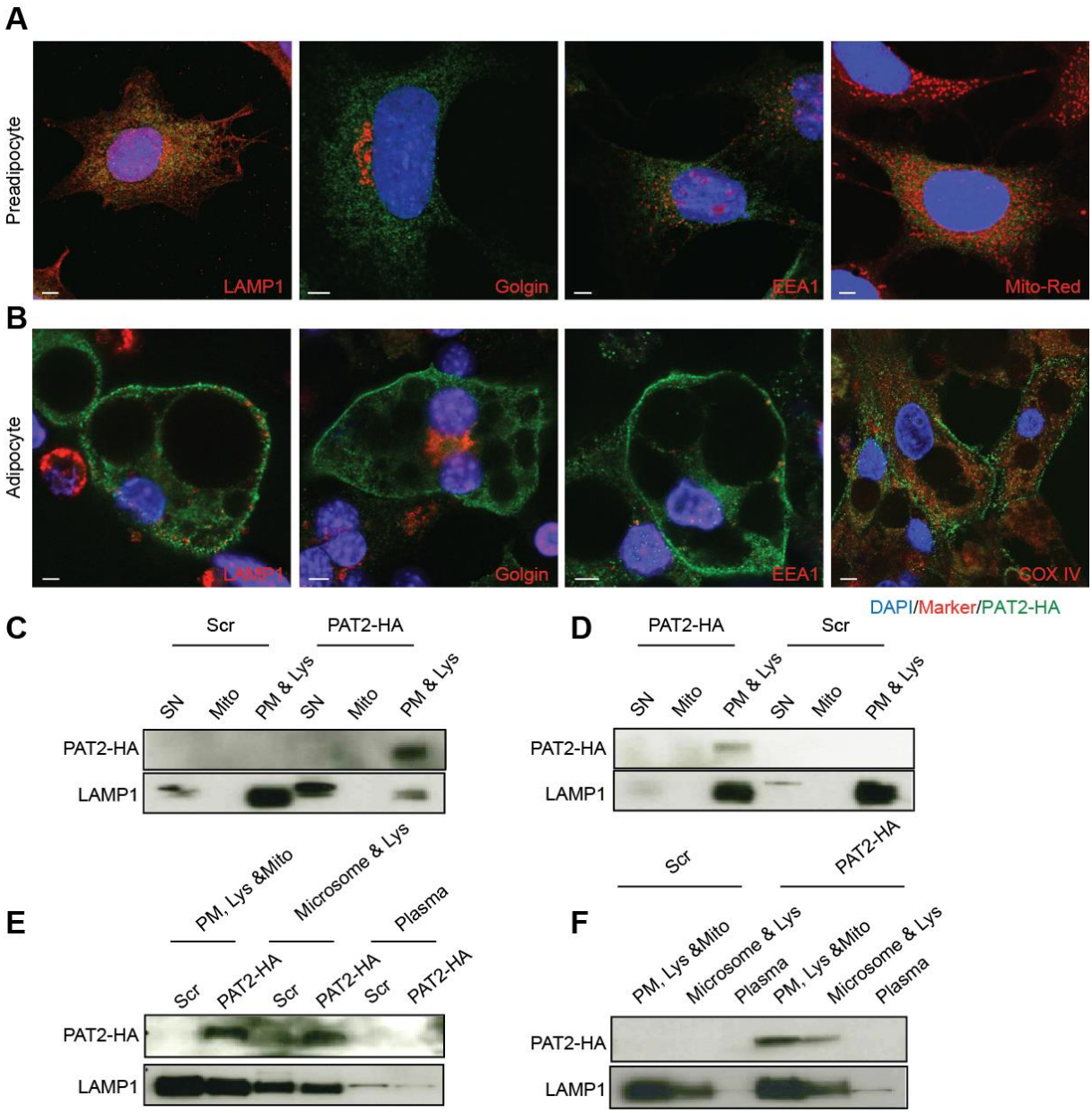

Figure 3.8 PAT2 is localized to the lysosome in preadipocyte and the cell surface in adipocyte. Co-immunostaining of PAT2-HA and different organelle markers in **(A)** preadipocytes and **(B)** adipocytes. Scale bars show 5 μm. Fractionation with Ficoll 400 gradient centrifugation assays for **(C)** preadipocytes and **(D)** adipocytes. Sucrose fractionation assays for **(E)** preadipocytes and **(F)** adipocytes. SN: Supernatant; Mito: mitochondria; PM: plasma membrane; Lys: lysosome

PAT2 is possibly localized to the plasma membrane, membrane protein after synthesis is secreted from Golgi apparatus to membrane, it is also possible for membrane

protein to be transported to the lysosome via endocytosis (Tooze et al 2014). So LAMP1 (lysosome marker), Golgin (Golgi apparatus marker) and EEA1 (endosome marker) were chosen for showing the subcellular components, considering the potential regulation on UCP-1 shown above, mitochondria red tracker and COX IV were also chosen for detecting mitochondria in preadipocytes and adipocytes, respectively.

Anti-HA antibody and antibodies for each marker were co-stained in PAT2 overexpression cells. The results clearly showed in preadipocyte PAT2-HA localized to the lysosome, but in adipocytes the signal of PAT2-HA was mainly shown on the cell surface rather than colocalizing with any intracellular organelle marker **(Figure 3.8 A and B)**.

To confirm the results of immunostaining, the membrane component was isolated from cells by gradient Ficoll 400 centrifugation. Depending on different density, subcellular components were separated into membrane (including plasma membrane and lysosome), mitochondria and supernatant fraction. All the separated components were collected for WB analysis. Similarly, PAT2 was detected by anti HA antibody, at the same time LAMP1 was detected for indicating lysosome fractions. Scr cells were included as a negative control. PAT2-HA in preadipocytes demonstrated a membrane localization. LAMP1 is shown in plasma membrane and lysosome fraction in Scr cells as expected, but in PAT2-HA cells there is also a big part of LAMP1shown in the supernatant fraction **(Figure 3.8 C)**. For adipocytes data, PAT2 demonstrated the same membrane localization. The LAMP1 in both Scr and PAT2-HA adipocytes mostly showed to be in the membrane fractions **(Figure 3.8 D)**. Actually, as a lysosome membrane marker, all LAMP1 should be detected in the membrane sample as shown in adipocyte data. This phenomenon may suggest that the maturation of the lysosome is interfered by overexpressed PAT2 in PAT2-HA preadipocyte rather than in Scr preadipocyte with very low PAT2 expression **(Figure 3.6 A)**. The interference may result in preventing the synthesized LAMP1 from localizing to the lysosome.

Due to the similar density of the lysosome and plasma membrane, the Ficoll 400 gradient centrifugation cannot distinguish lysosome and plasma membrane. Light lysosome

may also be mixed in the supernatant. Another different sucrose fractionation was also performed. For sucrose fractionation, the heavy plasma membrane and mature lysosome still are pelleted in the same fraction, but some lighter lysosome is together with the microsome and other lighter membrane like endosomes. Lysosome derives from the endosome, endosome has a lower density than lysosome (Authier & Chauvet 1999). So the lysosome with lower density is always in the lysosome. The sucrose fractionation results showed in preadipocytes LAMP1 in the microsome and lysosome fraction, the lighter fraction, occupied a higher proportion of total LAMP1 than in adipocytes **(Figure 3.8 E and F)**. This seemingly matches the hypothesis mentioned above. Upon PAT2 overexpression LAMP1 is trapped and cannot be delivered to the lysosome. For PAT2, similarly, as the negative control, there was no PAT-HA band in Scr cells. In overexpression cells, PAT2 was distributed in the heavy fraction (plasma membrane, lysosome and Mitochondria) and the light fraction (microsome and lysosome) in both preadipocyte and adipocyte samples. The difference is PAT2 in light fraction occupied a lower proportion of total PAT2-HA in adipocytes than preadipocytes **(Figure 3.8 E and F)**. Because the endosome was in the light fraction, this phenomenon may indicate that in adipocytes less PAT2 is transported from the plasma membrane to the lysosome than in preadipocytes. This hypothesis may explain why most of PAT2 are kept on the cell surface in adipocyte rather than on lysosome in preadipocyte, but to confirm it more evidence is still needed.

3.2.3.2 Transportation and degradation of PAT2 in pre- and mature brown adipocyte

Besides the completely different localizations, PAT2-HA in preadipocyte and adipocyte also showed an enormous difference in protein levels **(Figure 3.6 B)**. Normally, CMV promotor used in PAT2 overexpression plasmid is a strong promoter which drives a constitutive and stable expression. However, the protein level of PAT2-HA in adipocytes was much higher than in preadipocytes. Based on evaluating qPCR data, it can be found that mRNA level is at least not the main reason for the low protein level in preadipocytes **(Figure**

3.6 A). The PAT2 primers used in qPCR are designed for evaluating all PAT2 mRNA including PAT2-HA expressed by the overexpression plasmid and endogenous PAT2. The difference of PAT2 levels in Scr and overexpression cells shows PAT2-HA mRNA levels. We can find the expression curves of PAT2 in Scr and overexpression cells were almost parallel except the big deviations appearing at day 4 and day 8 with the big standard error of mean. However, even the biggest difference between PAT2 RNA levels in Scr and overexpression cells at day 8 (adipocyte) is just 2-3 times of the smallest difference at day 0 (preadipocyte). So mRNA data indicate pre translational regulation is not the main reason for the enormous protein levels difference.

Another possible reason is the strong degradation of PAT2-HA proteins in preadipocytes. As a plasma membrane localized protein, PAT2 should be synthesized and delivered to the plasma membrane by the Golgi apparatus. As for degradation, membrane proteins at the cell surface should be transported to the lysosome for hydrolysis. This is supported by mass spectrometry (MS) data **(Figure 3.9 A)**.

The Scr and PAT2-HA adipocytes were harvested to get the lysates. Then Co-IP was performed by utilizing anti HA antibody. The elution of Scr and overexpression samples were analyzed by MS to figure out which protein docking on the same kind of membrane with PAT2. As protein hydrolysis is always connected to amino acid starvation, PAT2-HA adipocytes upon amino acid starvation 24 hours were analyzed. To clarify where PAT2 was, specific membrane markers were also needed. Specific Rabs are associated physically with the specific membrane of vesicles or organelles (Hutagalung & Novick 2011). So the Rabs acquired in Co-IP samples can indicate the location of PAT2-HA.

The Rabs values from MS data were normalized by Scr sample values. Normalized values above 2 were regarded as the reliable values, so in adipocytes Rab10, Rab1b and Rab5a were found to physically associate with PAT2-HA **(Figure 3.9 A)**. Rab10 mainly regulates biosynthesis from *trans*-Golgi network to plasma membrane, Rab1b is mainly for ER and Golgi traffic (Hutagalung & Novick 2011). These two Rabs showed the route of

PAT2-HA synthesis and delivery to the plasma membrane. Specially, Rab5a is a Rab which mediates the formation of early endosome (Chavrier et al 1990). This implicates that for PAT2-HA at least the way from the plasma membrane to the lysosome via endocytosis exists. Additional, 24 hours amino acid starvation caused weaker associations of these 3 Rabs with PAT2-HA. Thereinto, Rab10 showed the biggest decrease in values, which may mean upon 24 hours amino acid starvation the secretion of PAT2-HA is inhibited.

The Rabs data in MS provided a possibility PAT2-HA can be transported from the plasma membrane through endocytosis. To verify whether most of PAT2-HA was degraded in lysosome/late endosome in preadipocytes, lysosomal/late endosomal degradation inhibition test was performed. Bafilomycin A1, the V-ATPase specific inhibitor, can inhibit the acidification of endosomes and lysosomes. The acid environment is necessary for hydrolases to degrade the target protein. So if most of PAT2-HA is degraded in preadipocyte, the Bafilomycin A1 treated preadipocytes will show a much higher level of PAT2-HA than untreated cells. Considering other several important signaling pathways related to adipocyte and nutrition regulation, insulin, mTORC1 inhibitor Rapamycin and β3 agonist CL316243 were also included in this experiment. The 1 hour treated and untreated PAT2-HA preadipocytes together with negative control Scr preadipocytes were harvested for WB. As expected, Bafilomycin A1 (100nM) triggered the accumulation of LC3 A/B II showed Bafilmycin A1 worked well and has inhibited autophagy. For PAT2-HA, insulin (100nM) and Rapamycin (10μM) only slightly increased PAT2-HA level. Conversely, PAT2-HA showed a slight decrease in CL316243 (500nM) treated cells. Obviously, Bafilomycin A1 boosted PAT2-HA level to be extremely high in preadipocytes **(Figure 3.9 B)**. This phenomenon indicates the main reason for low PAT2-HA level in preadipocyte is the strong degradation of synthesized PAT2-HA.

This result makes it interesting to figure out how PAT2-HA level can be boosted in only 1 hour. PAT2-HA immunostaining was performed for the same kind of cells to reveal the PAT2-HA localization under treatments. Several combinations of Bafilomycin A1, insulin and

Rapamycin were tested to see if different results were shown. As controls, Scr preadipocytes almost showed no PAT2-HA signal, and for PAT2-HA preadipocytes only weak signals were observed, which matches the WB results of low level PAT2-HA in preadipocytes. For Bafilomycin A1 treated PAT2-HA preadipocytes, strong green signals demonstrated a porous and multi-vesicle structure **(Figure 3.9 C)**. Actually, multi-vesicle is the characteristic appearance of the multivesicular body or multivesicular endosome, which fuses with the lysosome to degrade protein (Piper & Katzmann 2007). This matches my hypothesis that in preadipocytes PAT2-HA transported from the cell surface cannot be degraded as Bafilomycin A1 inhibits acidification of lysosome and late endosome. A large amount of PAT2-HA then accumulates on the unmatured multivesicular bodies/endosomes. Similar to the WB results, insulin or Rapamycin treated cells showed a slight increase in PAT2-HA signals, compared with untreated cells. Signals were mainly localized on a nuclear periphery area. Following, cells treated with double combinations of Bafilomycin A1, insulin and Rapamycin showed insulin and Rapamycin increased PAT2-HA levels in cells to be higher than the levels in individual treated cells. Furthermore, Bafilomycin A1 together with insulin or Rapamycin treated cells showed a similar staining pattern with only Bafilomycin A1 treated cells **(Figure 3.9 C)**. It suggests that endocytosis to the lysosome is the principal delivery for PAT2-HA protein in preadipocytes. Interestingly, more PAT2-HA stains were showed in preadipocytes treated with combination of insulin, rapamycin and Bafilomycin A1 **(Figure 3.9 C)**.

The results above roughly depicted the route of PAT2-HA from synthesis to degradation in preadipocyte. But the route from synthesis to the cell surface is inferred based on Rabs data in adipocyte rather than in preadipocytes where the route from cell surface to lysosome was found. That is to say, in preadipocytes PAT2-HA may be secreted via a different path to endosome directly without any opportunity of staying on cell surface. So the key to figure out this question is to verify whether PAT2-HA temporarily stays on the cell surface in preadipocytes from synthesis to degradation.

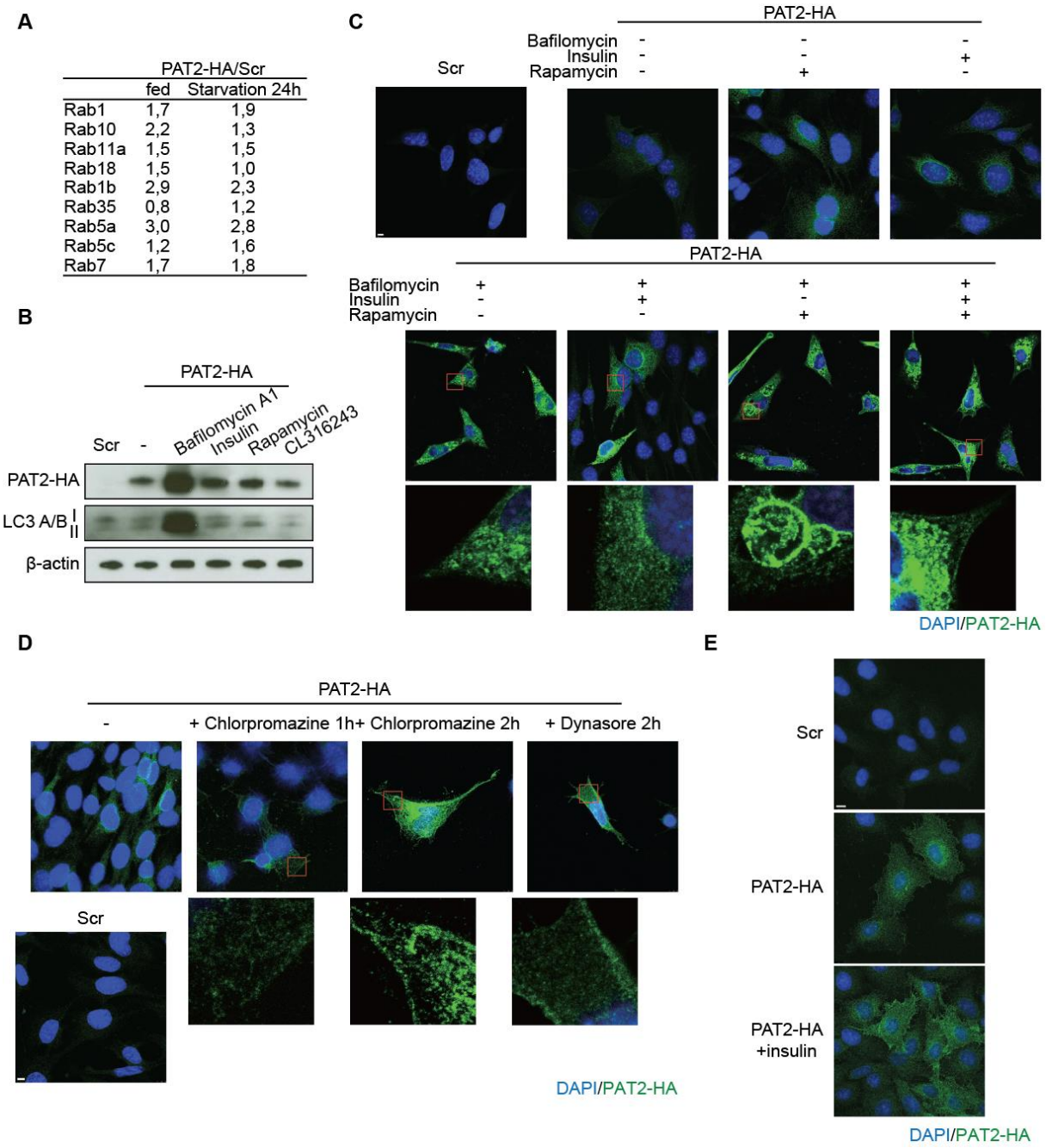

Figure 3.9 Transportation and degradation of PAT2 in preadipocyte and adipocyte. (A) MS quantification analysis of Rabs in PAT2-HA cells Co-IP sample by using anti HA tag antibody upon normal condition or amino acid starvation 24h, values were normalized by Scr values. **(B)** WB test for Scr and PAT2-HA cells treated with Bafilomycin A1 (100nM), insulin (100nM), Rapamycin (10μM) or CL316243 (500nM) for 1h. **(C)** Immunostaining of PAT2-HA in PAT2-HA preadipocytes treated with Bafilomycin A1 (100nM), insulin (100nM), Rapamycin (10μM) or CL316243 (500nM) or their combination for 1h. Scr preadipocytes were regarded as the negative control. The scale shows 5 μm. **(D)** Immunofluorescence staining of the PAT2-HA in PAT2-HA transfected preadipocytes treated with the endocytosis inhibitors, Chlorpromazine (100uM) and Dynasore (400uM). Scr preadipocytes were regarded as the negative control. The scale shows 7.5 μm. **(E)** Immunofluorescence staining of the PAT2-HA in PAT2-HA transfected rat fibroblast treated with/without insulin (100nM 1h) treatment. Scr rat fibroblast was regarded as the negative control. The scale shows 8 μm.

If endocytosis is inhibited PAT2-HA could in this case not be transported to early endosomes and will be trapped on the cell surface. However, to find a specific endocytosis inhibitor is difficult. Many endocytosis inhibitors found can also inhibit other vesicle traffics or functions (Dutta & Donaldson 2012). Finally, methyl-β-cyclodextrin, filipin, chlorpromazine and dynasore were selected as the candidates. In the pre-experiment, methyl-β-cyclodextrin and filipin showed strong toxicity to PAT2-HA preadipocyte, so chlorpromazine (100uM 1h or 2h) and dynasore (400uM 2h) were used for the following PAT2-HA immunostaining. For chlorpromazine, in 1hour treated cell a light membrane-liked staining was shown. If the treatment is extended to 2 hours, an obvious cell surface staining was observed together with some strong stained intercellular structures **(Figure 3.9 D)**. It means some other vesicle traffic, like PAT2-HA secretion, was possibly also inhibited. For cells treated with dynasore for 2 hours, a cell surface staining was also observed. Still, many intracellular stains may also mean not only endocytosis was inhibited **(Figure 3.9 D)**.

All in all, in adipocyte and preadipocyte PAT2 docks on the cell surface after it is synthesized, PAT2 can also be transported to the lysosome via endocytosis.

Based on the previous data, the difference between PAT2 in adipocytes and in preadipocytes illustrates that PAT2 is maintained on the cell surface in adipocytes, but in preadipocyte, overexpressed PAT2-HA is degraded in lysosome/late endosome rather than maintained on the cell surface. There should be a mechanism in adipocyte but not in preadipocyte which can keep PAT2 on the cell surface.

PAT2-HA overexpression plasmid was also transfected in rat fibroblasts. Immunostaining of PAT2-HA showed cell surface and perinuclear accumulation together with massive distribution in the other parts, the insulin enhancement on PAT2-HA signals was also observed **(Figure 3.9 E)**. These results implicate plasma membrane distribution may be the feature of PAT2 and rat cell cannot degrade PAT2-HA as much as mouse brown preadipocytes.

3.2.3.3 PAT2 translocates to the lysosome in adipocytes upon amino acid starvation and mTORC1 inhibition

If the translocation of PAT2 from cell surface to lysosome also exists in adipocytes, there should be a mechanism, which regulates the balance of how much PAT2 should be maintained at the cell surface and how much should be transported to the lysosome. Actually, mTORC1 activation has been reported as the dominating factor in a similar case. mTORC1 inhibition triggers transportation of proteins on the early endosome to the lysosome rather than back to the cell surface (Dauner et al 2017). mTOR signaling is the hub of nutrition sensing in the cell, particularly for amino acid sensing. Many kinds of amino acids, which can be sensed by mTOR have been reported, even intracellular or extracellular amino acid variation can be responded by mTOR (Goberdhan et al 2016). Actually, PAT2 is fundamentally an amino acid transporter (Fredriksson et al 2008). So it is very possible that mTORC1 regulates the translocation of the amino acid transporter PAT2 as a way to maintain amino acid homeostasis.

Amino acid starvation inhibits mTOR (Hara et al 1998). So treating cells with amino acid free DMEM is an easy way to check the possible PAT2 translocation upon mTOR inhibition.

The data from MS analysis of the HA Co-IP showed lysosome markers LAMP1 and LAMP2 both associated with PAT2 and the associations were enhanced upon amino acid starvation for 24 hours **(Figure 3.10 A)**. This phenomenon illustrates that amino acid starvation triggers PAT2 translocation to the lysosome in adipocytes. In order to get a visualized result, co-immunostaining of PAT2-HA and LAMP1 in PAT2 overexpression adipocytes was performed. For normal culture conditions, green signals (PAT2-HA) showed a plasma membrane localization. A quick shift was shown within 1 hour of amino acid withdrawal. PAT2-HA colocalized with red signals (LAMP1). Importantly, re-stimulation of amino acid for 10 or 20 min, after starvation 1 hour, was sufficient to drive PAT2 back to cell surface **(Figure 3.10 B)**. This result indicates a similar conclusion as the MS analysis and implicates that this translocation of PAT2 can be very fast.

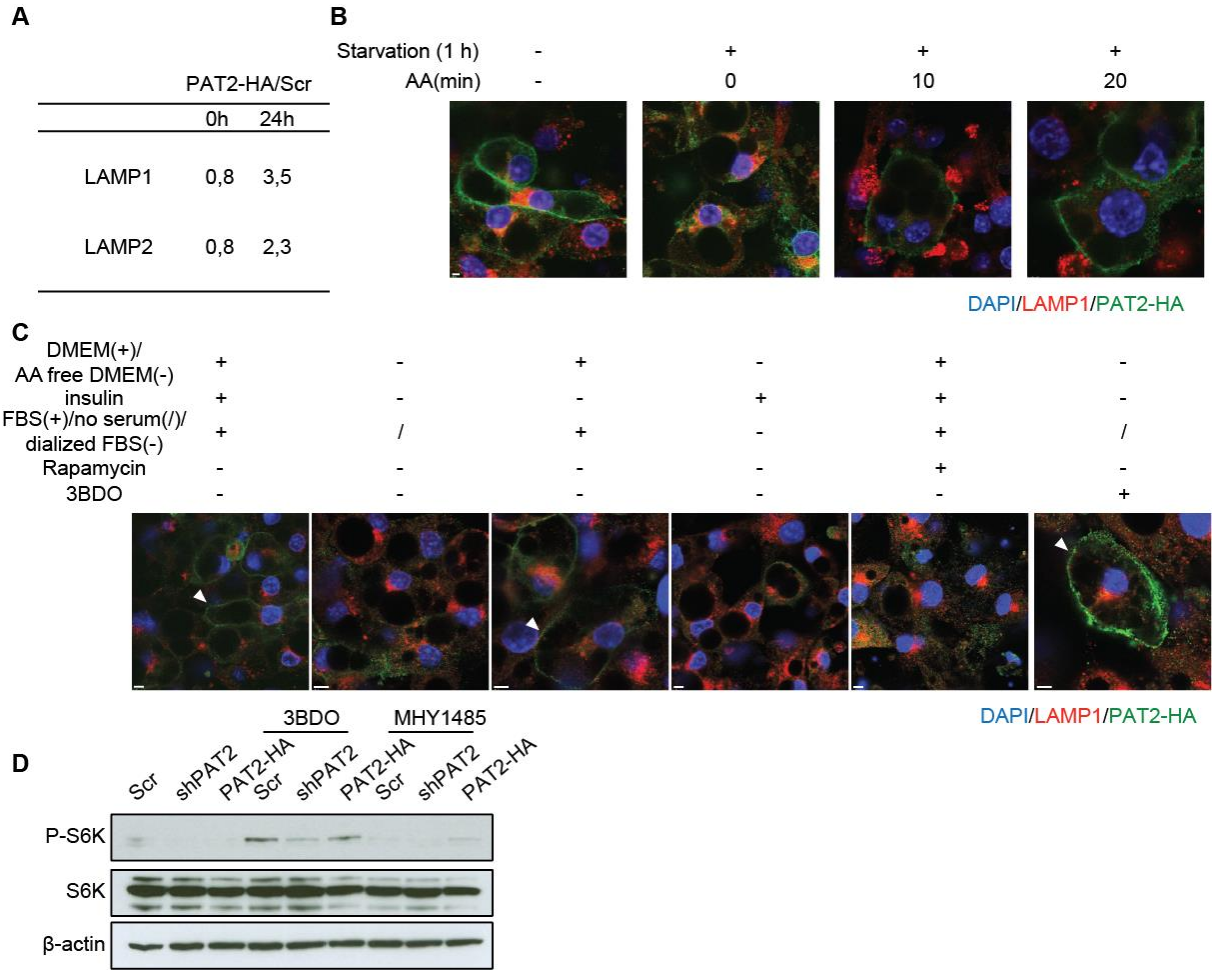

Figure 3.10 Amino acid starvation induces PAT2 translocation through mTORC1inhibition. (A) Lysosomal markers LAMP1/2 values in MS analysis of PAT2-HA co-immunoprecipitations upon fed or amino acid starvation 24h, values were normalized by Scr values. (B) Immunostaining of PAT2-HA and LAMP1 in adipocytes upon fed or amino acid starvation 1h with/without following amino acid restimulation for 10 or 20 minutes. The scale shows 2.5 µm. (C) Immunostaining of PAT2-HA and LAMP1 upon different treatments 1h. Arrows show plasma membrane staining. Scales show 5 µm. (D) Western blot test for P-S6K and S6K in Scr, shPAT2 and PAT2-HA adipocytes upon 1h amino acid starvation with/without 3BDO (60 µM) or MHY1485 (10 µM).

Precisely, the amino acid starvation model is not completely equal to mTORC1 inhibition and cells treated with amino acid free DMEM also suffer from fetal bovine serum (FBS) depletion and differences in glucose concentration. So the same co-immunostainings were performed on PAT2-HA adipocytes upon different treatments to confirm mTORC1 inhibition triggers the translocation. The results showed the same translocation of PAT2 upon amino acid free DMEM treated cells compared with fed cells. The 10% dialyzed FBS rather than FBS, together with amino acid free DMEM also triggered similar PAT2 translocation after one hour incubation in PAT2-HA adipocyte **(Figure 3.10 C)**. Insulin was also omitted in

amino acid free DMEM and potentially affects PAT2-HA level **(Figure 3.9 B)**. But insulin removal did not induce translocation of PAT2 to the lysosome. Actually, the mTORC1 inhibitor Rapamycin was found to trigger PAT2 translocation in 1 hour without any nutrition depletion in the medium **(Figure 3.10 C)**. Besides, mTORC1 agonist 3BDO rather than MHY1485 continuously activated mTOCR1 upon amino acid starvation **(Figure 3.10 D)** and was found to prevent amino acid induced PAT2 translocation **(Figure 3.10 C)**.

All the results above suggest that mTORC1 regulates PAT2 localization and protein content.

3.2.4 PAT2 interacts directly with mTORC1 in preadipocytes

mTORC1 can be recruited to the lysosome and then activated by amino acid stimulation (Betz & Hall 2013). In overexpression preadipocytes, PAT2-HA also showed a colocalization with the lysosome **(Figure 3.8 A)**. So in PAT2 overexpression preadipocytes, PAT2 could interact with mTORC1 directly.

A Co-IP was performed by using anti HA antibody. PAT2 overexpression preadipocytes were harvested to get lysate as input. Input and elution were analyzed by WB. Scr preadipocytes samples were included as a negative control. Besides PAT2-HA, two kinds of protein in mTORC1, mTOR and RagC were also tested. The results showed in IP elution an enrichment of PAT2-HA which means Co-IP system works well. The mTOR and RagC were both detected in PAT2 overexpression IP elution sample, at the same time no signal is shown in Scr IP sample **(Figure 3.11 A)**. The results indicate PAT2 associated with mTORC1 physically in preadipocytes.

mTOR signaling promotes proliferation (Laplante & Sabatini 2012). So an easy way to test if PAT2 overexpression induced mTOCR1 activation is to test the proliferation of Scr, shPAT2 and PAT2-HA preadipocytes. Proliferation tests showed PAT2-HA preadipocytes grew much faster than Scr and shPAT2 preadipocytes **(Figure 3.11 B)**. These results indicate a potentially enhanced mTORC1activation in PAT2 overexpression preadipocytes.

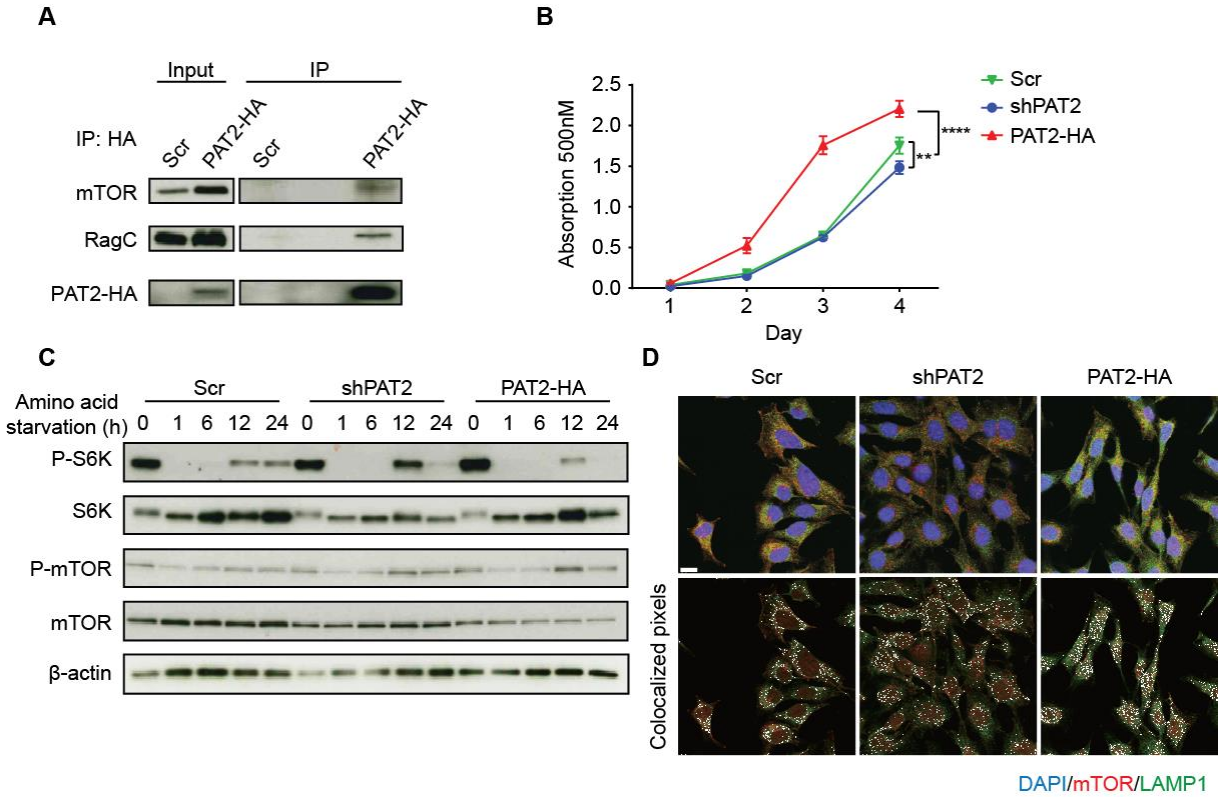

Figure 3.11 PAT2 interacts with mTORC1 and promotes mTOCR1 activation. (A) Co-immunoprecipitation of PAT2-HA with components of mTORC1 in preadipocytes. **(B)** The relative proliferation rate of subconfluent Scr, shPAT2 and PAT2-HA brown preadipocytes. RM Two-way ANOVA with Tukey's posthoc test; n=3. **(C)** WB analysis of S6K and mTOR phosphorylation in Scr, shPAT2 and PAT2-HA preadipocytes upon amino acid starvation 0, 1, 6, 12 and 24 hours. **(D)** Co-immunostaining of mTOR and LAMP1 in Scr, shPAT2 and PAT2-HA preadipocytes. Colocalized pixels are shown in white. The scale shows 7.5 µm.

Actually, PAT1, another amino acid transporter in the SLC36 family, shares 69% amino acid sequence with PAT2 (Bermingham & Pennington 2004b). Overexpressing PAT1 has been reported to promote proliferation in HEK 293 cells but not to alter basal mTOR activation. So PAT1 is inferred to regulate amino acid sensitivity of mTOR (Heublein et al 2010).

Now in my results, PAT2 overexpression preadipocytes demonstrated a similar phenomenon. To verify whether PAT2 also only regulates amino acid sensitivity like PAT1, Scr, shPAT2 and PAT2-HA preadipocytes were treated with amino acid free DMEM, cells were harvested at 0, 1, 6, 12 and 24 hours. Cell lysates were analyzed by WB. In order to detect activation of mTORC1, S6K and mTOR were tested as indicators.

First, in PAT2-HA preadipocytes the initial phosphorylation of S6K the mTORC1 downstream transcription factor showed a stronger band in PAT2 overexpression cells than Scr and knockdown cells **(Figure 3.11 C)**. The results indicate that the basal activation of mTOR in preadipocytes can be enhanced by PAT2 overexpression, which is different with PAT1 in HEK 293 cells. Second, because amino acid starvation inhibited mTORC1 and triggered autophagy to generate amino acids to reactivate mTORC1, phosphorylation of mTOR and S6K in Scr shPAT2 and PAT2-HA preadipocytes all showed a reduction followed by a rebound, but the re-phosphorylation bands in different cells were not equal **(Figure 3.11 C)**. The mTOR results show that PAT2 may not affect the upstream signaling of mTOR in preadipocytes, as mTOR phosphorylation was similar in all cell lines. The S6K re-phosphorylation bands were different in different cell lines, especial for PAT2-HA the re-phosphoralytion band was very weak **(Figure 3.11 C)**. The possible explanation is the PAT2 overexpression may impair autophagy in preadipocytes, another possibility is that the amino acid sensitivity of mTOR is regulated by overexpression of PAT2.

In fact, Scr and shPAT2 preadipocytes both do not express PAT2, so they should perform the same way in the tests. However, Scr cells showed a little faster growth on day 4 than PAT2 knockdown cells **(Figure 3.11 B)**. And differences of the re-phosphorylation between Scr and shPAT2 cells were also observed. I infer it is caused by either a random variation or starvation induced expression of PAT2 in Scr preadipocytes. Another reason may be that Scr preadipocytes express PAT2 when reaching 100% confluence on day 4..

To confirm the results about PAT2 regulated activation of mTOR, immunostainings for visualizing relative localizations of mTOR and lysosome were performed, because activated mTORC1is recruited to the lysosome (Betz & Hall 2013). mTOR and LAMP1 were co-stained in Scr, shPAT2 and PAT2-HA preadipocytes upon amino acid starvation 0, 1 and 24 hours. The colocalized pixels showed that at baseline PAT2 overexpression enhanced the colocalization, which matches the WB results **(Figure 3.11 D)**.

As a conclusion, PAT2 can interact with mTORC1and at the same time promotes mTORC1 activation in preadipocytes. But whether PAT2 can regulate amino acid sensitivity of mTORC1 like PAT1 still needs further verification.

3.2.5 Impaired autophagy in shPAT2 and PAT2-HA adipocytes upon amino acid starvation

In the last chapter, based on the overexpressed PAT2 in preadipocytes, several potential functions of PAT2 were revealed. Next, the more important part is the biological function of PAT2 in adipocytes, after all, adipocyte rather than preadipocyte shows expression of PAT2 endogenously.

3.2.5.1 S6K cannot be reactivated in shPAT2 and PAT2-HA adipocytes upon amino acid starvation 24h

PAT2 localized to cell surface rather than to the lysosome in adipocytes **(Figure 3.8 B)**. So it is impossible for PAT2 to interact with mTORC1 directly in the adipocyte. But PAT2 may still regulate mTORC1 indirectly.

In order to check whether PAT2 can regulate mTORC1 in adipocytes, a similar amino acid starvation experiment was performed. In this experiment, Scr, shPAT2 and PAT2-HA adipocytes were harvested after 0, 1, 6, 12 and 24 hours amino acid starvation, additionally cells upon amino acid restimulation for 10 and 20 minutes after 24 hours starvation were included to check the amino acid sensitivity of mTOR phosphorylation. The results showed in shPAT2 or PAT2-HA adipocytes phosphorylation of mTOR still was not altered and demonstrated a similar decrease and restimulation as in preadipocytes. mTOR was phosphorylated upon stimulating with amino acid in all cell lines **(Figure 3.12 A)**. It indicates PAT2 in adipocytes was not on the upstream of mTOR as in preadipocytes.

For testing phosphorylation of S6K, which is downstream of mTORC1, the same protocol of mTOR phosphorylation was utilized but excluding the two time points of amino acid restimulation. Experiments on amino acid restimulation to S6K in adipocytes will be described later on. The WB and quantitation results showed, comparing with preadipocytes that the basal phosphorylation levels of S6K in Scr, shPAT2 and PAT2-HA adipocytes were

similar **(Figure 3.12 B and C)**. This phenomenon is reasonable as alteration of PAT2 on the cell surface probably cannot regulate the phosphorylation of mTOR on the lysosomal surface. For amino acid starvation, S6K re-phosphorylation bands were shown in Scr, surprisingly, very light re-phosphorylated bands were shown in shPAT2 and PAT2-HA adipocytes. **(Figure 3.12 B and C)**. This phenomenon indicates impaired autophagy in shPAT2 and PAT2-HA adipocytes.

Before checking the role of PAT2 in autophagy, another clue for amino acid sensitivity needs to be pointed out. For the bands of phosphorylated S6K, except a very light band shown in shPAT2 adipocytes, Scr and PAT2-HA adipocytes both showed blunted S6K phosphorylation **(Figure 3.12 B)**. These results indicate that one hour amino acid starvation shut down most of the mTOR activation in all three cell lines. The induction of autophagy was also observed at the same time as LC3 A/B II, the active LC3 type for autophagosome formation, was enhanced after one hour starvation compared to basal levels in each cell line **(Figure 3.12 B)**. These data mean that the mechanism responding to amino acid starvation to trigger autophagy is not impaired no matter in shPAT2 or PAT2-HA adipocytes, but this conclusion does not mean Scr, shPAT2 and PAT2-HA adipocytes have the same amino acid sensitivity. Actually, the light band in shPAT2 cells after 1 hour may mean a slight reduced amino acid sensitivity of mTORC1. An explanation for the slight sensitivity decline could be that the difference is too small. Short term starvation may magnify the difference and this part will be discussed in the individual later chapter. Here, we do not need to consider it when studying autophagy because autophagy had been triggered successfully in all cells by only one hour starvation.

Besides, for LC3 A/B, a stronger degradation of LC3 was observed in shPAT2 and PAT2-HA adipocytes. Especially in PAT2-HA cells, LC3 bands did not appear until 24 hours of starvation **(Figure 3.12 B)**. This implicates a problem of insufficient generated amino acid or defective amino acid sensing. As for shPAT2 cells, a different trend was shown compared to Scr cells. LC3 A/B bands appeared after starvation for 12 hours but were not maintained

after 24 hours. It may mean that shPAT2 adipocytes cannot maintain continuous autophagy and/or amino acid sensitivity is blunted.

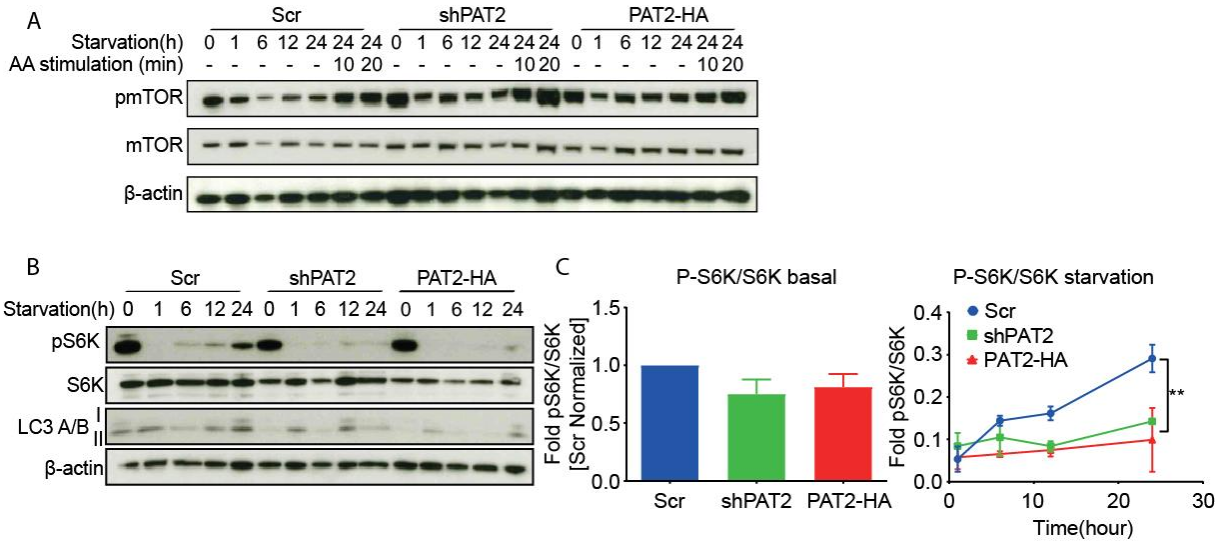

Figure 3.12 Autophagy is impaired in shPAT2 and PAT2-HA adipocytes. (A) Western blot analysis for mTOR phosphorylation in Scr, shPAT2 and PAT2-HA adipocytes upon amino acids starvation with/without following amino acid restimulation for the indicated times. **(B)** Western blot analysis for S6K phosphorylation and LC3 conversion in Scr, shPAT2 and PAT2-HA adipocytes upon amino acids starvation for the indicated times. **(C)** Quantification of p-S6K at baseline (left panel) and during starvation (right panel). n=3, RM two-way ANOVA with Tukey's post hoc test.

3.2.5.2 Abnormal fusion between lysosome and autophagosome in shPAT2 and PAT2-HA adipocytes

During autophagy autophagosomes carry cargo to fuse with the lysosome. Lysosome proteases then degrade the content (Bento et al 2016). So in order to confirm the impaired autophagy results and to figure out how PAT2 regulates autophagy, a co-immunostaining of autophagosome marker LC3 A/B and lysosome marker LAMP1 was performed. LC3, the active type LC3 type II localizing to autophagosome, shows as puncta in staining, but LC3 type I shows as a blurry staining as it spreads in the cytoplasm (Klionsky et al 2016).

The results showed that fusion between the lysosome and the autophagosome was enhanced from starvation 1 hour to 24 hours in Scr cells as amino acid starvation triggered autophagy **(Figure 3.13 A and B)**. However, in shPAT2 and PAT2-HA cells the colocalization was weakened no matter upon starvation 1 hour or 24 hours **(Figure 3.13 A and B)**. This phenomenon confirms the results of the WB that both PAT2 knockdown and overexpression can impair autophagy in adipocytes.

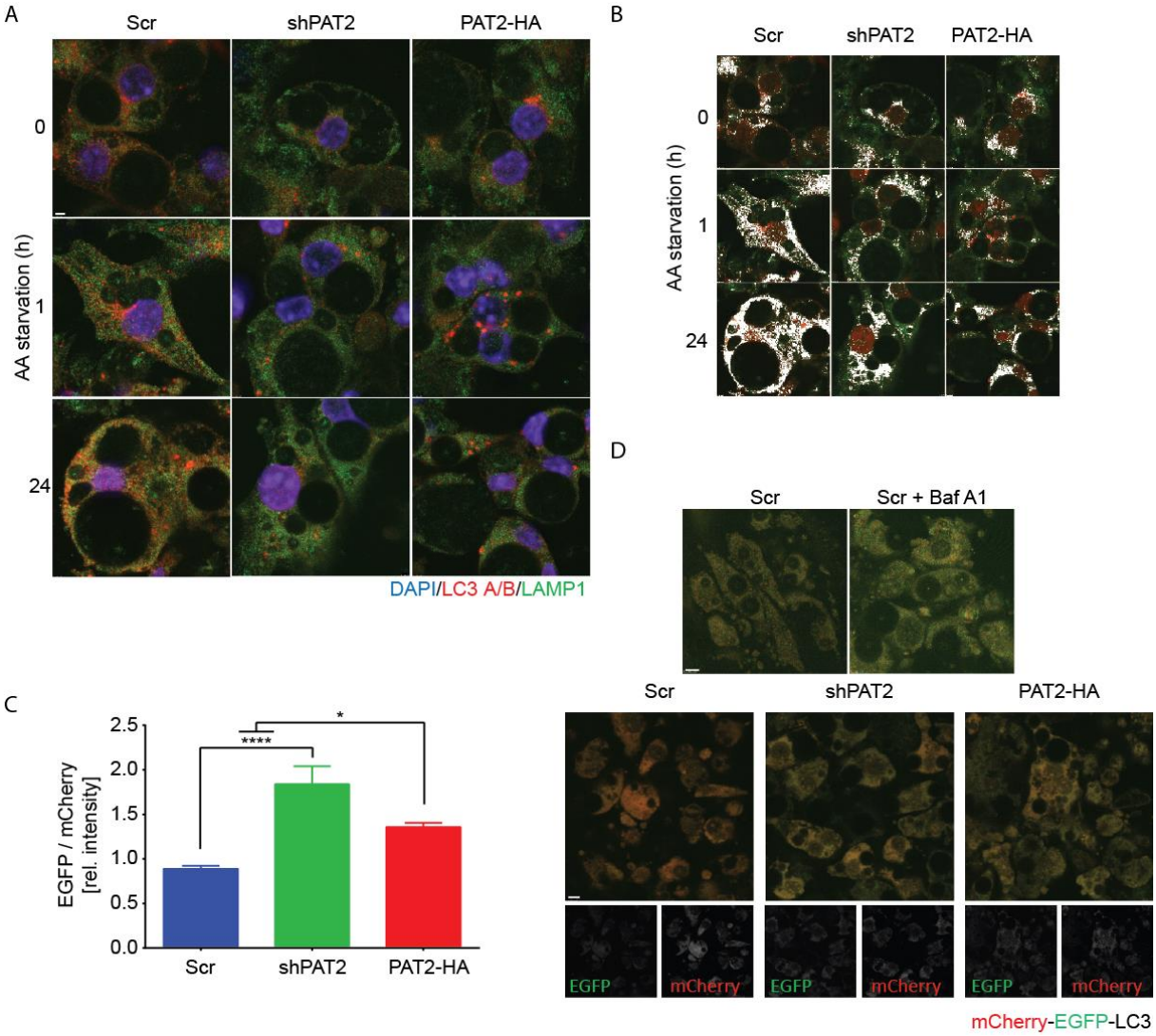

Figure 3.13 PAT2 knockdown or overexpression impairs fusion of lysosome and autophagosome. (A) Immunostaining of LAMP1 and LC3 A/B in Scr, shPAT2 and PAT2-HA adipocytes upon amino acid starvation for the indicated time. The scale shows 2.5 µm. **(B)** The colocalized pixels in (A) were shown in white. **(C)** Quantification of EGFP quenching in cells transiently transfected with mCherry-EGFP-LC3 upon one hour amino acid starvation. n = 28 - 33 cells, one-way ANOVA with Tukey's post hoc test. **(D)** Visualization of autophagosome and lysosome fusion by assessing quenching of EGFP in cells transiently transfected with mCherry-EGFP-LC3 upon 24 hours amino acid starvation. Control cells were additionally treated with Bafilomycin A1 (Baf A1, 100nM). Scale in upper panel shows 7.5 µm and in lower panel shows 5 µm.

To confirm the conclusion that PAT2 knockdown or overexpression impairs fusion, a tandem reporter was used for detecting autophagosome-lysosome fusion. The reporter protein consists of a series connection of mCherry and EGFP at the N terminus of LC3. After transfection the reporter protein was expressed in the adipocyte to integrate into autophagosomes. The mCharry-EGFP-LC3 reporter is exposed to the acid lumen of the lysosome after the autophagosome fuses with the lysosome. Due to the acid sensitivity,

EGFP will be quenched, however, the red signal of mCherry is maintained. Based on this, the lower ratio of EGFP/mCherry means stronger fusion. Scr, shPAT2 and PAT2-HA adipocytes were transiently transfected with the reporter plasmid and then cells were treated with amino acid free DMEM for 24 hours. Comparing with shPAT2 and PAT2-HA cells, a weaker green signal in Scr cells was observed. Additional, shPAT2 cells showed weaker quenching than PAT2-HA cells **(Figure 3.13 C and D)**. As negative control, V-ATPase inhibitor Bafilomycin A1 treated Scr adipocytes were used and showed the strongest green signal as expected **(Figure 3.13 D)**.

The results of mCherry-EGFP-LC3 match the conclusion of the immune stainings **(Figure 3.13 A and B).** PAT2 knockdown and overexpression both impair fusion. Besides, the different EGFP quenching levels shown in shPAT2 and PAT2-HA indicate possible differences between these two cell lines. A possibility is the pH of the lysosomal lumen. Because fusion was not completely blocked in shPAT2 and PAT2-HA adipocytes **(Figure 3.13 A and B)**, the quenching of mCherry-EGFP-LC3 depends on the lysosomal pH.

3.2.5.3 Formation of autophagosome is independent of PAT2

An interesting point was that in shPAT2 or PAT2-HA cells fusion between lysosome and autophagosome was weakened but did not completely disappear **(Figure 3.13 A and B)**. So PAT2 knockdown or overexpression may affect the process of fusion itself or may reduce the number of autophagosomes.

In order to check the formation of autophagosomes, firstly, the expression levels of LC3B in Scr, shPAT2 and PAT2-HA adipocytes upon 0, 1 and 24 hours were tested by qPCR. The results showed no significant difference in LC3B levels among the three kinds of adipocytes at each time point **(Figure 3.14 A)**. It indicates that PAT2 knockdown or overexpression does not alter LC3B expression.

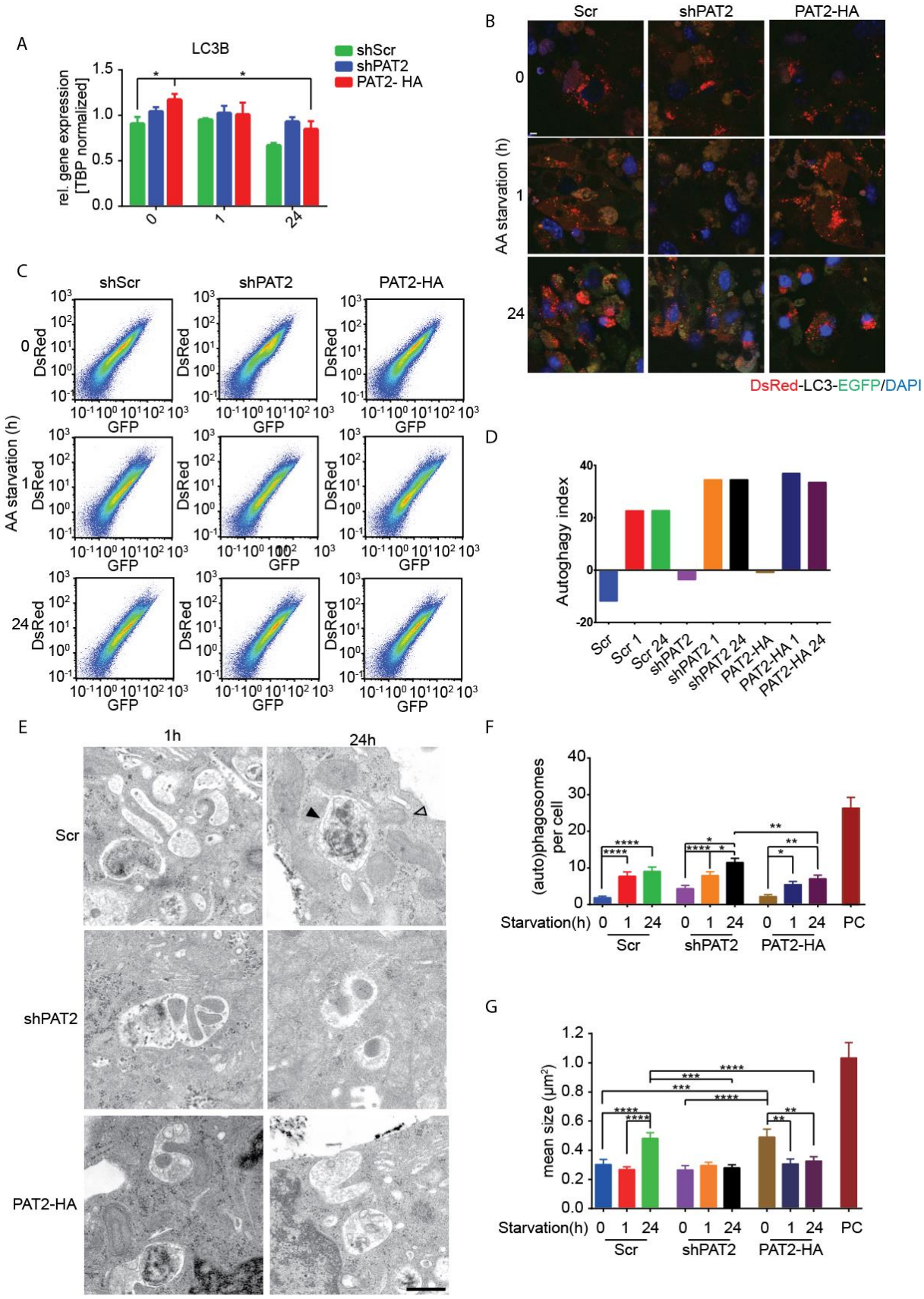

Figure 3.14 PAT2 knockdown or overexpression does not impair autophagosome formation. **(A)** qPCR test of LC3B expression during amino acid depletion for 1 or 24 hours in Scr, shPAT2 and PAT2-HA adipocytes. RM two-way ANOVA with Tukey's post hoc test, n=3. LC3 I to LC3 II conversion

assessed upon stable transfection of a DsRed-LC3-EGFP fusion construct in Scr, shPAT2 and PAT2-HA adipocytes upon starvation (1 and 24 hours) or normal conditions. Fluorescence images for adipocytes shown in **(B)**, flow cytometry analyses shown in **(C)**, Autophagy indexes calculated based on (C) shown in **(D)**, Autophagy index = 100-100*(FL(GFP)/FL(DsRed)). **(E)** Representative electron microscopy images for Scr, shPAT2 and PAT2-HA cells upon amino acid starvation for one and 24 hours. Black arrow indicates autophagosomes, open arrow indicates lysosome, scale bar shows 500 nm. Quantification of average autophagosome size (n=74-161) **(F)** and number (n=30-31) **(G)** per cell in Scr, shPAT2 and PAT2-HA adipocytes in regular culture conditions and upon one or 24 hours amino acid starvation. Positive control (PC) was performed as Bafilomycin A1 (100nM) treatment for one and 24 hours. RM two-way ANOVA with Tukey's post hoc test; PC was excluded from statistic.

The formation of autophagosomes includes two main phases; nucleation and elongation. The ATG8/LC3- and ATG12- conjugation system is required for elongation (Kroemer & Levine 2008, Nakatogawa et al 2009). LC3 I is conversed to LC3 II in this system through cleavage at the C terminus of LC3 I. The conversion of LC3 can be examined by monitoring autophagy activity (Sheen et al 2011).

To evaluate this, a dual-color fluorescence reporter DsRed-LC3-EGFP was stably transfected into Scr, shPAT2 and PAT2-HA adipocytes. Then cells were treated with amino acid free DMEM for 0, 1 and 24 hours. Fixed cells were observed under the microscope to acquire images. Theoretically, EGFP linked to the C terminus of LC3 is cut off and then degraded due to LC3 conversion to type II, but DsRed at N terminal is kept, so based on how strong the red signal is and how weak the green signal is, LC3 conversion representing the activity of autophagy can be monitored. The images showed very weak green signal in all the three kinds of cells upon starvation for 0 or 1 hour **(Figure 3.14 B)**. These results indicate on one hand brown adipocyte may have a high basal level of autophagy, on the other hand PAT2 knockdown or overexpression does not regulate C terminal cleavage of LC3. Upon starvation for 24 hours, green signal becomes stronger **(Figure 3.14 B)**. This may be caused by the high expression of endogenous LC3 induced by amino acid starvation, which makes excessive DsRed-LC3-EGFP accumulated in the cell.

In order to quantify the LC3 conversion, the cells with the same treatments were analyzed by flow cytometry. The results were shown in rectangular coordinates with the GFP fluorescence on the X-axis and DsRed on the Y-axis. Assuming a diagonal y = x separating quadrant into two areas, cells distributed in the left up area had high autophagy activity, cells

on the diagonal meant no LC3 conversion. Theoretically, because of the degradation of EGFP, there should be no cell localizing in the right down area, but actually, there were many cells shown in this area due to a number of interferences, such as transfection efficiency of different cells, compensation setting, etc. But LC3 conversion can still be evaluated relatively by comparing the distribution of each sample. The results showed all the cell distributions demonstrated a shift upon amino acid starvationMost of the cells localized in parallel with the diagonal of the quadrant. For Scr, shPAT2 and PAT2-HA adipocytes, from 0 to 24 hours amino acid starvation all cells showed ashift, cells move from right down area to left up area of the diagonal of cell population **(Figure 3.14 C)**. This phenomenon meant LC3 conversion is enhanced in all kinds of cells due to amino acid starvation. Additional, for all cells the cell population moved along the X-axis to right after amino acid starvation **(Figure 3.14 C)**. It matches the results shown in cell imaging, which means green signal becomes stronger. Based on the formula reported by the provider of this plasmid (Sheen et al 2011), autophagy indexes were calculated by utilizing flow cytometry data. For all cells autophagy activity is enhanced by amino acid starvation, the difference was Scr showed the lowest basal level **(Figure 3.14 D)**.

In order to figure out how lysosome autophagosome fusion exactly operates in shPAT2 and PAT2-HA adipocytes, Scr, shPAT2 and PAT2-HA adipocytes were fixed for electron microscope observation upon amino acid starvation for one hour or 24 hours.

Fusion is a temporary process, so individual lysosome or autophagosome-like vesicles are the most structures which can be observed. Lysosome can be recognized as dark vesicle based on proton accumulation. An autophagosome with cargo at different phases shows different characters such as single or double layer membrane. The empty early autophagosome is difficult to be distinguished from other vesicles. There was still fusion captured in Scr adipocytes; a big autophagosome with cargo (arrow) was fusing with lysosome (open arrow) **(Figure 3.14 E)**. For shPAT2 or PAT2-HA cells, surprisingly many fusions were observed as dark vesicle (lysosome) engulfed by autophagosome. The images

clearly showed in shPAT2 and PAT-HA adipocytes the darkvesicles were engulfed in light vesicles **(Figure 3.14 E)**. But obviously this kind of fusion is not actually fusing lysosome and autophagosome. Actually, the fact that many fusion moments can be observed may mean fusion was stuck and this status. If it is right, this phenomenon indicates not all the colocalization in immunostaining **(Figure 3.13 B)** represents actual fusing. On the opposite to the fusion, the autophagosome formation was not impaired as the cargoes loaded autophagosomes were found to exist in all the adipocytes upon amino acid starvation **(Figure 3.14 E)**. An increase in number of autophagosomes per cell was found in all the cell lines **(Figure 3.14 F)**, which means autophagosome formation was not impaired due to PAT2 knockdown or overexpression. Additionally, Scr showed an expanded autophagosome size, inversely a decline was shown inPAT2-HA, size in shPAT2 did not show significant variation **(Figure 3.14 G)**. Actually, the abnormalities in autophagosome size had been reported upon V-ATPase depended acidification defects (Mauvezin et al 2015). But it still needs more researches to find out whether it is the same reason leading to different size variations.

These results showed that PAT2 knockdown or overexpression both weaken the lysosome autophagosome fusion but do not impair autophagosome formation.

3.2.6 PAT2 alters V-ATPase depended acidification by modulating assembly and proton pumping of V-ATPase

The data above showed that PAT2 knockdown or overexpression does not affect autophagosome formation. The **(Figure 3.13 C)** and **(Figure 3.14 G)** had suggested impaired acidification in shPAT2 or PAT2-HA adipocytes. So the endosomal/lysosomal acidification may be the target of PAT2. Lysosome derives from endosome and endosome is formed through endocytosis. V-ATPase on the membrane of early endosome starts to acidify the lumen through pumping protons in. Autophagosome can fuse with lysosome to form autophagolysosome and also can fuse with late endosome to form amphisomes for cargo degradation during autophagy (Gordon & Seglen 1988, Marshansky & Futai 2008). It has been reported that dysfunctional acidification impair fusion and autophagy (Kawai et al 2007,

Yamamoto et al 1998). As its full name suggests the Proton coupled amino acid transporter 2, PAT2 can transport amino acids and protons (Boll et al 2002). So it is reasonable to hypothesize that PAT2 may regulate acidification to affect autophagy.

3.2.6.1 PAT2 is necessary and enhancive for V-ATPase depended acidification

If PAT2 plays a role in acidification, differences of acid vesicles will be shown among Scr, shPAT2 and PAT2-HA adipocytes, such as the number of acid vesicles and pH of vesicles.

In order to monitor intracellular acid vesicles, an intracellular pH indicator was used. The intracellular pH indicator is a fluorescent probe which can permeate the membrane and indicate intracellular pH in live cells. Its fluorescence is inversely proportional to environmental pH. In this experiment, Scr, shPAT2 and PAT2-HA adipocytes upon amino acid starvation 0, 1 and 24 hours were incubated with the intracellular pH indicator. As a reference, EGFP-LC3 plasmid was transiently transfected at the same time to indicate autophagosomes. The fluorescence images of Scr adipocytes showed few and weak red vesicles at 0 hours, but after starvation, acid vesicles became much stronger. The red fluorescence was found to be further enhanced upon starvation for 24 hours **(Figure 3.15 A and B)**. The increasing red signal indicates enhanced acidification, these phenomena showed that acidification was triggered by amino acid starvation. For shPAT2 adipocytes, all the acid vesicles with fluorescence showed weak red signal, vesicles in adipocytes upon starvation became only slightly stronger than adipocytes at 0 hours **(Figure 3.15 A and B)**. This result indicates that acidification is impaired by PAT2 knockdown in adipocyte. As for PAT2-HA adipocytes, enhancement of red fluorescence was also observed similar to Scr cells, but at each time point, acid vesicles in PAT2-HA cells showed stronger red signal than in Scr cells. Especially many acid vesicles were present in PAT2-HA cells at 0 hours **(Figure 3.15 A and B)**. Based on the fluorescence, pH in these vesicles in PAT2-HA cells were much

lower than the stained vesicles in Scr and shPAT2 cells at each point. In another word, PAT2-HA showed excessive enhanced acidification.

Additionally, the colocalized pixels of the pH indicator and EGFP-LC3 showed that most of the red stained vesicles were colocalized with LC3, which proves these vesicles are lysosome or late endosome as autophagosome can be recruited to them **(Figure 3.15 B)**. Due to the pH sensitivity, EGFP starts to be quenched when pH is lower than 7 (Patterson et al 1997). So these colocalized pixels do not represent fused autophagolysosome, they probably indicate that the closed autophagosome and lysosome/late endosome as shown in EM images **(Figure 3.14 E)**.

These results suggest that amino acid starvation induced acidification in the adipocyte is PAT2 depended.

V-ATPase is the main proton pump for acidification in the cell (McGuire et al 2017). PAT2 can also transport protons together with amino acids (Chen et al 2003). So there are two possibilities for the altered acidification: 1) PAT2 itself pumps protons for acidification in brown adipocytes, so overexpression enhances acidification and knockdown impairs it. 2) Proton pumping is still V-ATPase depended, but PAT2 is necessary for V-ATPase acidification in brown adipocytes. In order to test this, Scr, shPAT2 and PAT2-HA adipocytes, upon amino acid starvation for 24 hours, were treated with/without V-ATPase inhibitor Bafilomycin A1. The results showed that when compared with control cells all the cells treated with Bafilomycin A1 showed no acid vesicles in the cells **(Figure 3.15 C)**. This phenomenon clearly indicates that PAT2 regulates acidification via the V-ATPase.

3.2.6.2 PAT2 directly interacts with V1B2 subunit

As the results above showed that regulation of PAT2 to acidification is V-ATPase depended, the next question is to figure out how PAT2 affects V-ATPase.

In order to check if PAT2 knockdown or overexpression can alter the amount of V-ATPase, several subunits of the V-ATPase were studied by western blot. V-ATPase is a complex which consisting of a V1 and V0 domain, with each domain comprised of many

subunits (Cotter et al 2015). V1B2 subunit was chosen to be tested by WB to show whether its protein level can be affected by PAT2 knockdown and overexpression. The results showed that in all cells V1D2 expression was enhanced by amino acid starvation, but there was no big difference among cell lines, especially after starvation **(Figure 3.15 D)**. Compared to the tremendous differences in acidification, it is clear that regulation of PAT2 to V-ATPase activity does not mainly depend on altering protein expression.

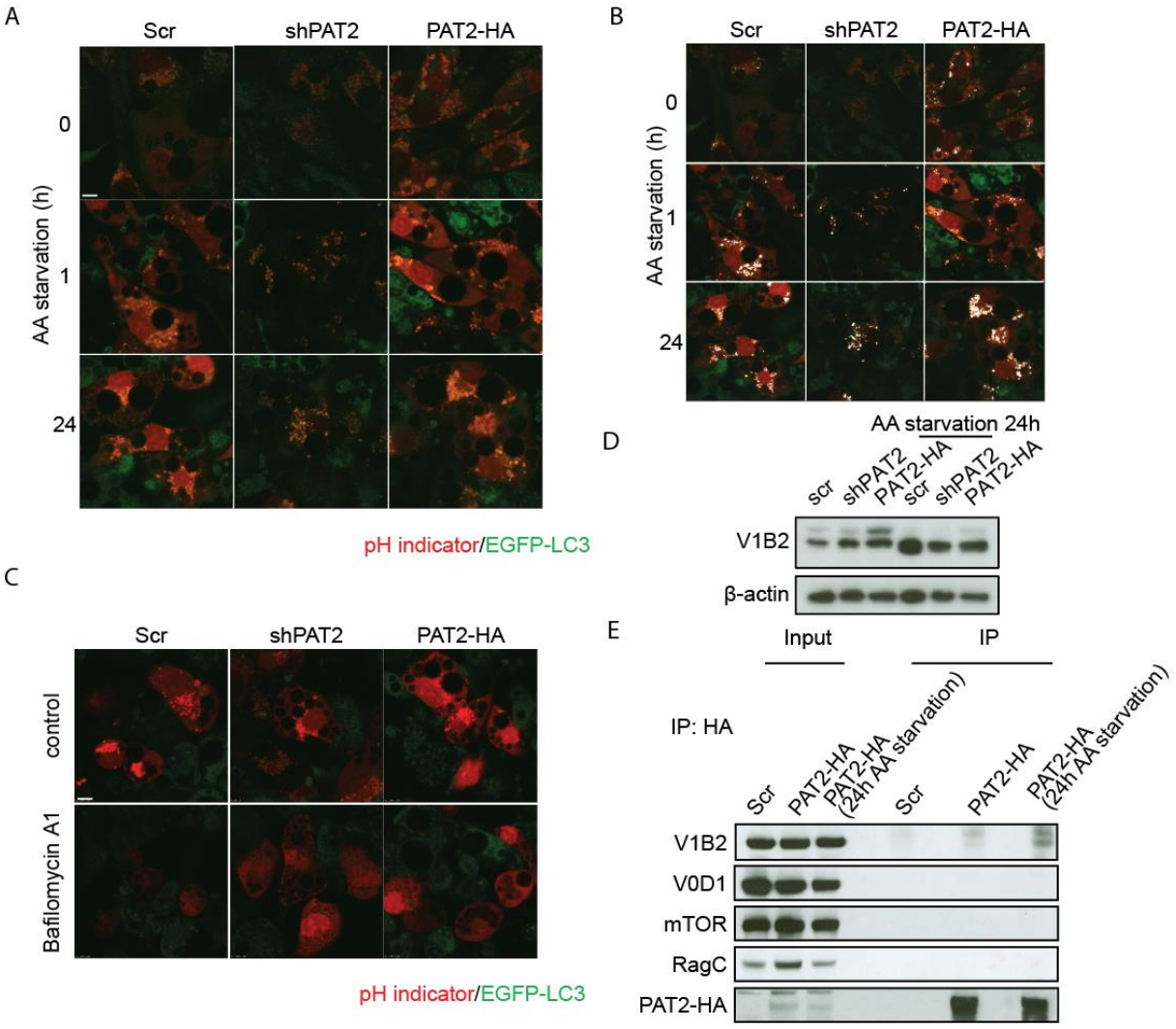

Figure 3.15 PAT2 alters acidification through V-ATPase. (A) Fluorescence staining of intracellular pH indicator in Scr, shPAT2 and PAT2-HA brown adipocytes transiently transfected with EGFP-LC3 upon control medium or amino acid starvation for one or 24 hours. The bar shows 7.5 nm. **(B)** Colocalised pixels of (A) shown in white. **(C)** Fluorescence staining of intracellular pH indicator in Scr, shPAT2 and PAT2-HA brown adipocytes transiently transfected with EGFP-LC3 upon normal medium condition or amino acid starvation with Bafilomycin A1 (100 nM) for 24 hours. The bar shows 7.5 nm. **(D**) WB test for V1B2 in Scr, shPAT2 and PAT2-HAadipocytes upon normal medium condition or amino acid starvation 24 hours. **(E)** Co-immunoprecipitation of PAT2-HA with subunits of V-ATPase and components of mTORC1 in differentiated brown adipocytes.

Then another possible way for PAT2 is to regulate the activity of V-ATPase directly or indirectly. So a Co-IP was performed by using anti HA antibody for immunoprecipitating overexpressed PAT2-HA and associated proteins, to test whether PAT2 can directly interact with V-ATPase. PAT2-HA adipocytes upon amino acid starvation 24 hours and normal culture conditions were harvested, Scr adipocytes were included as the negative control. Because unassembled cytosolic V1 and integral V0 are separated in the cell (Cotter et al 2015), V1B2 and V0D1were chosen for detecting if V1 and V0 domains were eluted. As a reference, mTOR and RagC were also tested. The results showed no band in Scr elution sample as expectation. And because mTORC1 was still inactivated in PAT2-HA adipocytes upon starvation 24 hours **(Figure 3.12 B and C)**, mTOR and RagC were still away from the lysosome membrane where PAT2 localized to upon amino acid starvation. Upon normal medium condition activated mTORC1 localizes to lysosome but PAT2 is kept on cell surface **(Figure 3.8 B)**. The results of Co-IP test matched the previous data; no bands of mTOR and RagC were detected in neither starvation nor control elution sample. Importantly, amino acid starvation enhanced the interaction of PAT2 and the V1 domain, but no interaction with V0D1 was detected **(Figure 3.15 E)**. Thus, PAT2 can directly interact with V1 domain of V-ATPase rather than V0 domain.

PAT2 did not alter V1B2 subunit protein levels and interacted with the V1 domain. Thus, it could be possible for PAT2 to regulate V-ATPase activity during autophagy.

3.2.6.3 PAT2 is necessary for the assembly of the V-ATPase

V-ATPase assembly can be regulated by various stimuli (Cotter et al 2015). PAT2 may modulate V-ATPase assembly to alter V-ATPase activity.

The BN-PAGE is a good way of detecting protein complexes. By adjusting concentration of weak detergent, cells can be lysed without severe damaging interactions among subunits. Therefore, big complexes can be detected by WB. Still, V1B2 and V0D1

were chosen for detecting V1 and V0 domain. Scr, shPAT2 and PAT2-HA adipocytes upon normal medium condition or amino acid starvation 1 hour were harvested for testing.

Coomassie bright blue staining of the BN-PAGE gel demonstrated equal loading for each sample. For V1B2, complexes/proteins with 3 different sizes were detected, one size was a little bigger than 720 kD (around 800 kD), another one was around 350 kD, the smallest one was blurry and bigger than 66 kD. As for V0D1, the bands which are bigger than 720 kD (around 800 kD) were also observed. Besides, another two closed bands at size around 480 kD were also detected. Interestingly, the bands with the biggest size in V1B2 and V0D1 blotting localize at the same position of the same gel **(Figure 3.16 A)**. The molecular weight of the peripheral complex V1 domain is 570 kD, the molecular weight of the integral V0 complex is 260 kD (Forgac 1999). So the bands at this size can be regarded as the intact V-ATPase. Then by comparing bands at around 800 kD, V-ATPase assembly can be evaluated. In both Scr and PAT2-HA adipocytes V-ATPase assembly was enhanced by amino acid starvation. But for shPAT2 cells no matter upon normal culture conditions or starvation, only a very low level of intact V-ATPase was detected. At the same time, the bands at around 350 kD (possible to be V0 domain or a V-ATPase component) were the strongest in PAT2-HA cells **(Figure 3.16 A)**. Considering V1B2 protein levels were not tremendously altered, the results indicate that PAT2 knockdown impairs V-ATPase assembly. Furthermore, shPAT2 brown adipocytes also loose V-ATPase assembly in response to amino acid starvation.

By utilizing anti HA antibody, PAT2-HA in PAT2-HA adipocytes was also detected. PAT2 localized at the same size as V1B2 350 kD, another part localized at around 180 kD **(Figure 3.16 A)**. This result illustrates that PAT2 interacts with the V1 domain but not the V0 domain, which matches the Co-IP data **(Figure 3.15 E)**. Besides, PAT2 may not directly interact with the intact V-ATPase.

To confirm the conclusion that PAT2 is necessary and promotive for V-ATPase assembly, another fractionation experiment was performed. In this experiment, lysates of

Scr, shPAT2 and PAT2-HA adipocytes using either normal culture condition or amino acid starvation for one hour were separated into cytosol and membrane fraction. As disassociated V1 domain spreads in the cytosol but V0 domain anchors at the membrane, V-ATPase assembly can be detected if the V1 domain shifts from the cytosol to the membrane fraction. The results showed that the cytosolic protein α-tubulin was only detected in the cytosol fractions, similarly membrane protein Na^+K^+ ATPase α1 was only in membrane fractions. V0D1 was mainly in membrane fractions as expected. For the V1 domain, V1B2 blotting showed most V1 domains were in cytosol fractions, but membrane localized V1 domains increased after one hour amino acid starvation in Scr and PAT2-HA adipocytes. For shPAT2 adipocytes, this enhancement of the V1domain in membrane sample did not occur **(Figure 3.16 B)**. So the fractionation results support the same conclusion; PAT2 is necessary for the amino acid starvation induced enhancement of V-ATPase assembly.

V-ATPase is required for ysosomal amino acid sensing of mTORC1 (Zoncu et al 2011). And restimulated with amino acids to the medium will rapidly spread to lysosome lumen and can be sensed by V-ATPase (Zoncu et al 2011). So if the conclusion above is right, shPAT2 adipocytes with less V-ATPase should show low sensitivity to amino acid restimulation, in the opposite, PAT2-HA adipocytes should be more sensitive. By depriving amino acid for one hour, Scr, shPAT2 and PAT2-HA adipocytes were stimulated with amino acid mix for 10 minutes. Phosphorylation of S6K was detected for indicating mTORC1 activity. The results showed in all the cells mTORC1 activity was shut down after one hour starvation. After 10 minutes amino acid restimulation, PAT2-HA adipocytes showed the strongest P-S6K band, shPAT2 cells showed the weakest band **(Figure 3.16 C)**. These results match the previous expectation.

Considering that mTORC1 inhibition determines PAT2 translocation in response to amino acid starvation **(Figure 3.10 C)**, another experiment was performed to test whether V-ATPase assembly was also induced by mTORC1 inhibition during starvation. The similar BN-PAGE was performed for analyzing V1B2 and V0D1 in Scr and PAT2-HA adipocytes

with/without mTORC1 inhibitor rapamycin treatment. By evaluating the bands at around 800 kD, it was easy to find that in rapamycin treated cells intact V-ATPase did not increase but slightly decreased **(Figure 3.16 D)**. These results indicate mTOCR1 inhibition cannot induce the enhancement of V-ATPase assembly.

To test if mTORC1inhibition is necessary for V-ATPase assembly, Scr, Scr following amino acid starvation one hour with/without 3BDO treatment and Scr following one hour rapamycin treatment adipocytes were harvested for BN-PAGE analysis. The bands at around 800 kD in amino acid depletion treated Scr cells were stronger than in Scr cells upon normal condition **(Figure 3.16 E)**. It matches the previous data. For 1hour starved cells treated with 3BDO, the band at about 800 kD disappeared in V1B2 blotting. In V0D1 blotting, we can find a blurry massive band was stuck in the upper part of the gel **(Figure 3.16 E)**. These results showed that the active mTORC1 together with amino acid starvation may cause abnormal structures of the V0 domain on the membrane, which led to almost no bands at around 800 kD. However, a technical problem cannot be excluded, albeit the experiment was repeated several times with the same result.

As a conclusion, PAT2 is necessary for amino acid starvation induced V-ATPase assembly. Interestingly, brown adipose tissue still expresses other V-ATPase assembly regulators reported in other cells **(Figure 3.16 F)**. It hints that the PAT2 dependent V-ATPase assembly regulation is a specific modification to the broadly existed V-ATPase assembly mechanisms. Considering the strong expression of PAT2 in brown adipocytes and V-ATPase as an amino acid sensor, it is possible for brown adipocyte to show a different sensitivity to amino acid.

3.2.6.4 PAT2 promotes proton pumping of V-ATPase

V-ATPase activity can also be directly regulated (Cotter et al 2015). As a proton pump, it is possible that the efficiency of V-ATPase proton pumping is affected by PAT2. To check it, an *in vivo* quenching experiment was performed.

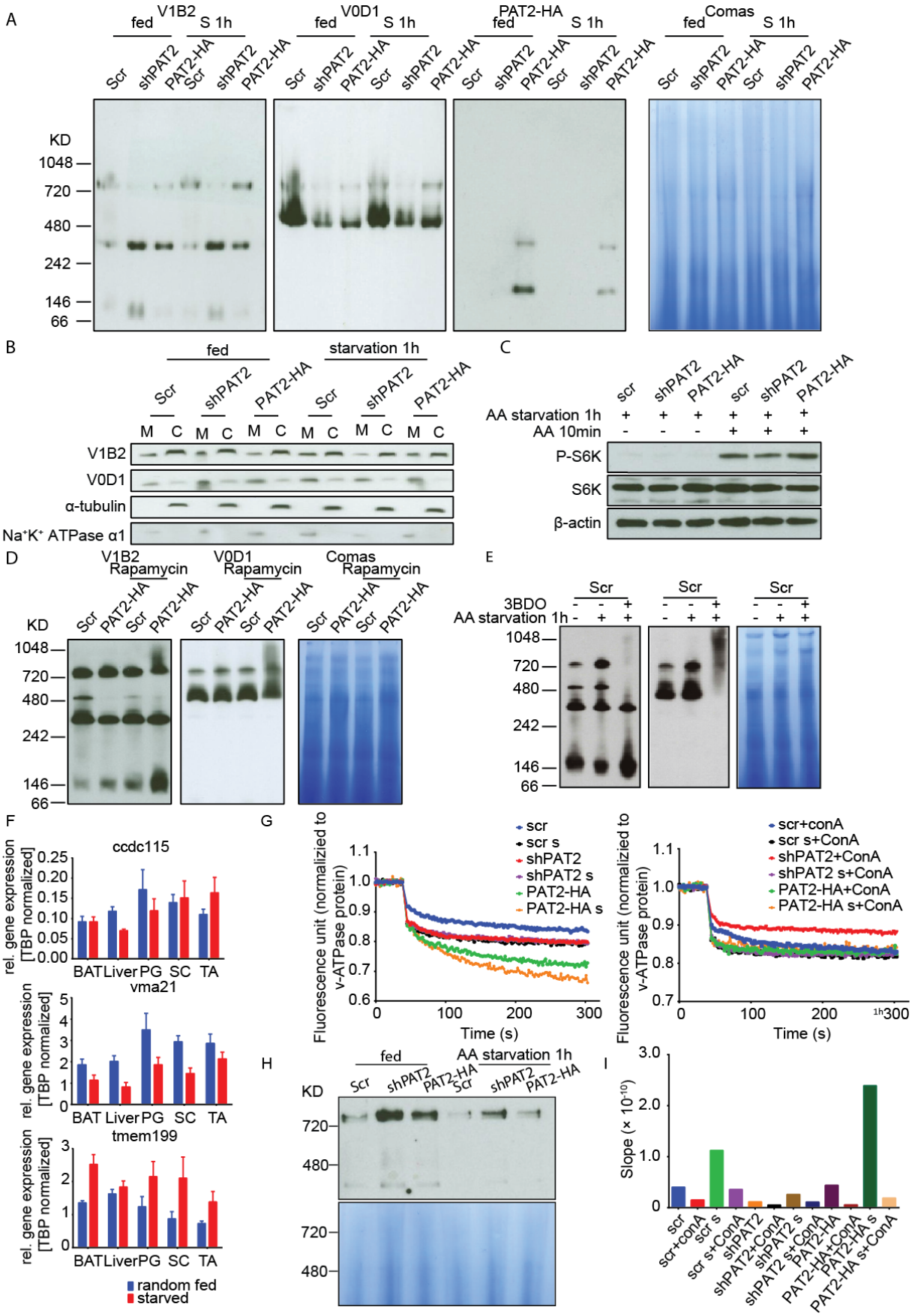
A
fed V1B2 S 1h
fed V0D1 S 1h
fed PAT2-HA S 1h
fed Comas S 1h
Scr shPAT2 PAT2-HA
KD
1048
720
480
242
146
66
B
fed
starvation 1h
M C
V1B2
V0D1
α-tubulin
Na+K+ ATPase α1
C
AA starvation 1h
AA 10min
P-S6K
S6K
β-actin
D
V1B2 Rapamycin
V0D1 Rapamycin
Comas Rapamycin
E
3BDO
AA starvation 1h
F
ccdc115
vma21
tmem199
rel. gene expression [TBP normalized]
BAT Liver PG SC TA
random fed
starved
G
Fluorescence unit (normalized to v-ATPase protein)
Time (s)
scr
scr s
shPAT2
shPAT2 s
PAT2-HA
PAT2-HA s
scr+conA
scr s+ConA
shPAT2+ConA
shPAT2 s+ConA
PAT2-HA+ConA
PAT2-HA s+ConA
H
fed
AA starvation 1h
I
Slope (× 10-10)

Figure 3.16 PAT2 promotes V-ATPase assembly and proton pumping. (A) BN-PAGE analysis for Scr, shPAT2 and PAT2-HA adipocytes upon the control medium condition and amino acid starvation one hour. **(B)** WB analysis for the cytosol (C) and membrane (M) proteins isolated by fractionation from Scr, shPAT2 and PAT2-HA adipocytes upon the control medium condition and amino acid starvation one hour. **(C)** WB analysis for Scr, shPAT2 and PAT2-HA adipocytes upon one hour amino acid starvation with/without following amino acid 10 min restimulation. **(D)** BN-PAGE analysis for Scr and PAT2-HA adipocytes upon the normal medium condition with/without one hour rapamycin treatment (10μM). **(E)** BN-PAGE analysis for Scr and PAT2-HA adipocytes upon the normal medium condition with/without one hour 3BDO treatment (60μM). **(F)** qPCR test for V-ATPase assembly regulator in BAT, Liver, PG, SC and TA from wild type mice upon random fed or starvation. n=4. **(G)** Quenching test for the Scr, shPAT2 and PAT2-HA adipocytes upon control medium condition and amino acid starvation one hour, each sample treated with Concanamycin A as the negative control. BN-PAGE analysis **(H)** and regression analysis **(I)** for the samples and curves of (G).

Medium containing dextran-FITC was used for incubating cells. As a branched glucan complex, dextran-FITC was endocytosed by the cell and then loaded to thelysosome. Following the fractionation protocol, lysosome/late endosome containing dextran-FITC were isolated. Due to the acid sensitivity of FITC, its fluorescence was quenched once V-ATPase was triggered to acidify the vesicles by ATP and Mg^{+} addition. By evaluating the curve of FITC fluorescence, proton pumping efficiency of V-ATPase can be measured. In this experiment, Scr, shPAT2 and PAT2-HA adipocytes upon normal medium condition or amino acid starvation one hour were tested. As a negative control, a specific inhibitor of V-ATPase, concanamycin A was added to the same system to exclude possible non V-ATPase triggered quenching.

The results clearly showed no quenching appeared for FITC in concanamycin A treatment samples. But for samples without concanamycin A treatment, fluorescence of FITC demonstrated a decrease after ATP and Mg^{+} addition **(Figure 3.16 G)**. It indicates in this experiment that FITC quenching is triggered by V-ATPase depended acidification. All the fluorescence values were normalized by the amount of intact V-ATPase which was quantified by BN-PAGE according to the same protocol above **(Figure 3.16 H)**. To make it easy to compare, values were also normalized by the average value before ATP and Mg^{+} addition. In these results, PAT2-HA samples showed the highest pumping efficiency upon normal culture conditions. Upon starvation the efficiency was further increased. For Scr samples, a lower efficiency upon normal medium and an enhanced acidification efficiency upon starvation

were observed. As for shPAT2 samples, proton pumping was always at a very low level **(Figure 3.16 G)**.

Based on the Stern-Volmer relationship, quenching curve was a hyperbola. In order to compare pumping efficiencies quantitatively, the hyperbola equation was transformed into a linear function of fluorescence reciprocal with a variation of time. The slope was proportional to proton pumping velocity. Slopes were calculated by linear regression. Proton pumping efficiencies among samples can be compared by comparing slopes. The calculation results showed the same conclusion PAT2 promoted the proton pumping of V-ATPase. PAT2knockdown caused V-ATPase only maintained a low level of pumping efficiency and also lost the enhancement responding to amino acid starvation **(Figure 3.16 I)**.

3.2.7 Different amino acid sensitivities of the different tissues, shPAT2, PAT2-HA and control brown adipocytes

The PATs have been reported to as amino acid sensors (Goberdhan et al 2016, Heublein et al 2010). The previous data have implicated the potential function of PAT2 for amino acid sensitivity modulation. Then experiments were performed to confirm this.

3.2.7.1 PAT2 increases amino acid sensitivity *in vitro*

Different amino acid sensitivity can show different threshold and responding velocity to amino acid depletion. For threshold, cells with high amino acid sensitivity may trigger mTORC1 inhibition when extracellular amino acid concentration slightly decrease. On the contrary, low sensitivity cells may ignore the small fluctuation of amino acid concentration. As for responding velocity, to the same variation in amino acid concentration, cells with different sensitivities spend different time for inhibition of mTOCR1. The phosphorylation of S6K was chosen as the indicator for mTORC1activity in these experiments.

Scr,shPAT2 and PAT2-HA preadipocytes were treated with amino acid free DMEM supplemented with different amino acid concentrations for one hour. The range was 0, 1/3, 2/3 and 1 time of the normal amino acid concentration in DMEM. The results showed the Scr and shPAT2 preadipocytes have similar amino acid sensitivity. But PAT2-HA preadipocytes

obviously showed more sensitive to amino acid deprivation. Especially when comparing 2/3 concentration samples, PAT2-HA sample showed much weaker S6K phosphorylation than the other two kinds of cells **(Figure 3.17 A)**. The similar sensitivity of Scr and shPAT2 cells shown is reasonable as Scr preadipocytes do not express PAT2 which is nearly equal to shPAT2 cells. The high sensitivity in PAT2 overexpression cells illustrates PAT2 can promote amino acid sensitivity.

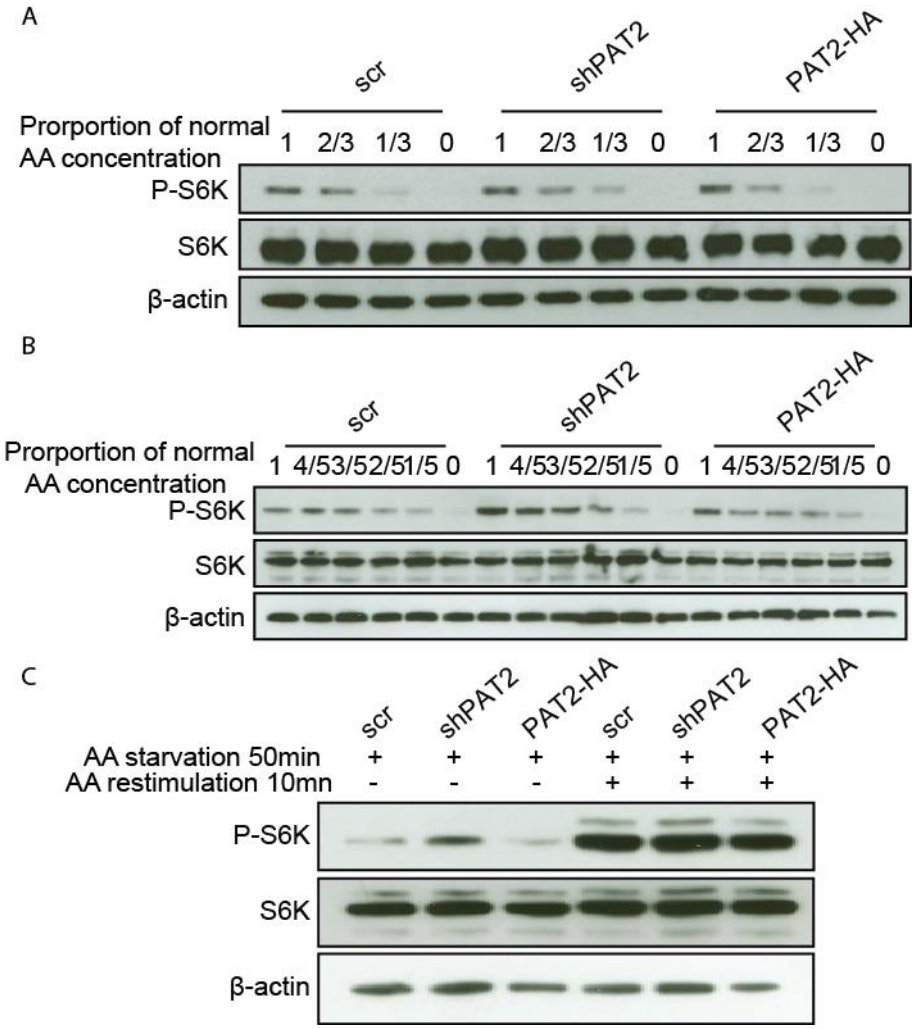

Figure 3.17 PAT2 enhances amino acid sensitivity of brown adipocyte in vitro. (A) WB analysis for P-S6K in Scr, shPAT2 and PAT2-HA preadipocytes treated with different concentration of amino acid for one hour. **(B)** WB analysis for P-S6K in Scr, shPAT2 and PAT2-HA adipocytes treated with different concentration of amino acid for one hour. **(C)** WB analysis for P-S6K in Scr, shPAT2 and PAT2-HA adipocytes treated with amino acid starvation for 50 min and following 10 min amino acid restimulation.

Then a similar experiment for adipocytes was performed. In this The results showed that in 4/5 of the normal amino acid concentration for one hour, PAT2-HA cells demonstrated

a dramatic decrease of S6K phosphorylation, which did not appear in Scr and shPAT2 samples. Besides, shPAT2 adipocytes still kept a quite high activity of mTORC1 after starvation for one hour, but the other two kinds of cells had decreased it to a lower level **(Figure 3.17 B)**. It indicates that PAT2 overexpression makes brown adipocytes more sensitive to amino acids, and PAT2 knockdown makes cells more insensitive. These results match the data of preadipocytes.

Next, to check the response velocity, Scr, shPAT2 and PAT2-HA adipocytes were treated with amino acid free DMEM for a short time, 50 minutes, with/without a 10 minutes restimulation of amino acid. The results showed after 50 minuts starvation, a quite strong band for S6K phosphorylation was still present in shPAT2 adipocytes, but in PAT2-HA cells mTORC1 activity had been nearly shut down, Scr cells showed an intermediate sensitivity **(Figure 3.17 C)**. And all the restimulation samples showed mTORC1 reactivated normally. This phenomenon indicates a similar sensitivity when PAT2 is away from cell surface. So from the aspect of responding time, I also conclude that PAT2 enhances amino acid sensitivity in brown adipocytes.

3.2.7.2 BAT shows higher amino acid sensitivity during fast *in vivo*

PAT2 showed a specific high expression level in BAT compared to other tissues (Ussar et al 2014). To test if BAT is especially sensitive to starvation induced induction of autophagy, BAT and two WATs, PGF and SCF, were taken from wild type mice upon random feeding or overnight fasting. As a reference, the liver and TA were also included. By qPCR analysis, there was no significant difference in LC3B expression between random fed and starvation samples in all tissues. But, PAT2 and UCP-1 in BAT showed a quick decrease after fasting overnight. Two WATs, SCF and PGF, also expressed PAT2 normally, but the expression did not show a decrease after fasting overnight in these two tissues **(Figure 3.18 A)**. This means it is very possible for PAT2 to play a role in nutrient depletion related mechanisms.

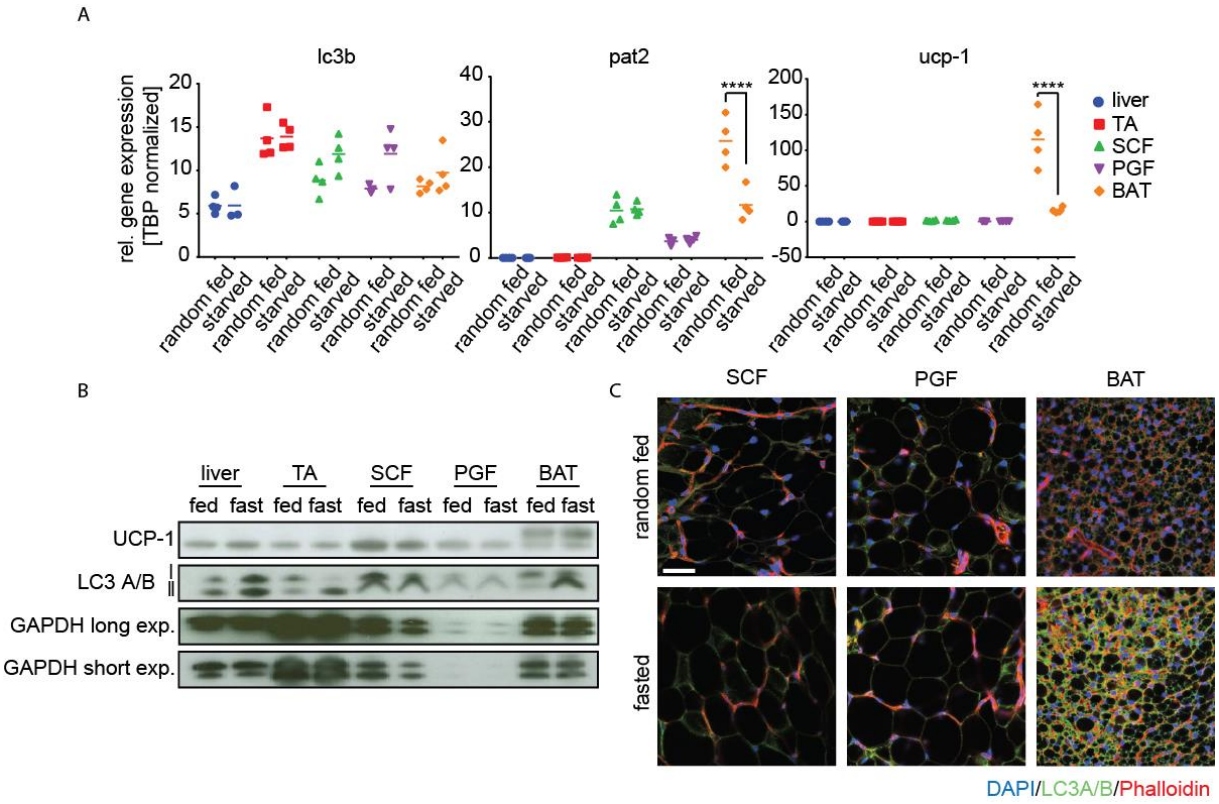

Figure 3.18 BAT is sensitive to amino acid starvation during fasting in vivo. (A) RT-PCR analysis of LC3B, PAT2 and UCP-1 expression in the Liver, TA, SC, PG and BAT from random fed and overnight starved mice. n=4. **(B)** Western blot test of LC3B and UCP-1in the Liver, TA, SC, PG and BAT from random fed and overnight starved mice. **(C)** Coimmunofluorescence of LC3A/B, Phalloidin and DAPI for SC, PG and BAT from random fed and overnight starved mice. The bar shows 10 μm.

Then the same tissues were analyzed by WB. UCP-1 and LC3 A/B were detected. For Ucp-1, the protein levels slightly increased after fasting overnight **(Figure 3.18 B)**, which is different from the qPCR data. This indicates a potential post-transcriptional regulation of UCP-1 in brown adipose tissue. As for LC3 A/B, a typical conversion of type I to type II was clearly shown in TA and BAT after fasting overnight **(Figure 3.18 B)**. It indicates overnight fasting is sufficient to trigger autophagy in BAT and TA. Comparing with the WAT, BAT showed higher sensitivity to starvation than WAT. To confirm this conclusion, BAT, SCF and PGF were isolated from mice upon random fed or fasting overnight for staining. Frozen sections were used for co-immune staining of LC3 A/B, DAPI and phalloidin. Similarly, puncta staining indicating LC3 type II was much more in fasting sample than random fed

sample in BAT, but in SCF and PGF there was no obvious difference **(Figure 3.18 C)**. These results above indicate that BAT is faster to trigger autophagy than WAT.

3.2.8 PAT2 is related to mitochondrial turnover

BAT is different from WAT for its high mitochondrial uncoupling protein level which makes BAT be a thermogenic tissue (Cedikova et al 2016). PAT2 is also specifically and highly expressed in BAT and showed similar decrease in BAT in fasted mice **(Figure 3.18 A)**. Whether PAT2 can regulate mitochondria especially when amino acids are depleted was also checked.

3.2.8.1 PAT2 can interact with mitochondrial proteins

The MS analysis mentioned in 3.2.3 was performed by utilizing anti HA tag antibody for detected PAT2-HA and its physically associated proteins in PAT2-HA adipocytes upon the normal condition and amino acid starvation 24 hours.

The MS data showed subunits from all 5 complexes, complex I, II, III, IV and F-ATPase in mitochondria were detected. These complexes comprise the electron transport chain for oxidative phosphorylation (Sirey & Ponting 2016). Scr sample normalized MS data showed that almost all the subunits were detected and demonstrated an enhanced physical association with PAT2 after amino acid starvation. Especially, Ndufb5 from complex I, sdha and sdhb from complex II, uqcrc2 from complex III, cox7a2 from complex IV, atp5a1, atp5d, atp5e atp5f1, atp5h and atp5k from F-ATPase showed values above 2 after normalization with Scr values **(Figure 3.19 A)**. These values indicate interactions with PAT2. These results implicate amino acid starvation may not only translocate PAT2 to the lysosome but also to mitochondria. It is reasonable for PAT2 translocation to mitochondria as the pathways for membrane delivery from plasma membrane (Westermann 2015) or autophagosome (Hailey et al 2010) to mitochondria have been reported. Besides, there were also several subunits whose values were above 2 upon normal medium condition **(Figure 3.19 A)**. It may be caused by the spill-out effect of PAT2 overexpression . But it is also probably that a small part of PAT2 localizes to mitochondria.

Co-staining of PAT2-HA and COX IV antibody showed that normally PAT2 accumulated on the cell surface and COX IV was in the cytoplasm. After one hour of amino acid starvation, PAT2 stared to be translocated and some colocalizations with COX IV appeared. Upon starvation for 24 hours, a part of PAT2 returned to the cell surface and the rest remained in the cytoplasm and also colocalized with COX IV **(Figure 3.19 B)**. So as a conclusion, PAT2 can be translocated to mitochondria upon amino acid starvation.

A

	PAT2-HA (scr normalized) fed	starvation 24h
Complex I		
Ndufa4	0,6	1,1
Ndufa9	0,8	0,7
Ndufb5	0,3	0,3
Ndufs1	1,7	4,5
Ndufs2	2,2	0,3
Complex II		
Sdha	2,1	2,9
Sdhb	2,2	2,6
Complex III		
Uqcrc2	1,6	3,1
Complex IV		
Cox15	0,6	0,8
Cox6c	0,8	1,0
Cox7a2	0,9	2,1
Cox7c	0,9	1,5
F-ATPase		
Atp5a1	2,1	2,2
Atp5b	1,7	1,9
Atp5c1	1,8	1,8
Atp5d	0,8	3,5
Atp5e	1,3	4,1
Atp5f1	1,6	2,0
Atp5h	1,4	4,4
Atp5j2	0,0	1,0
Atp5k	0,9	11,3
Atp5o	1,3	1,6

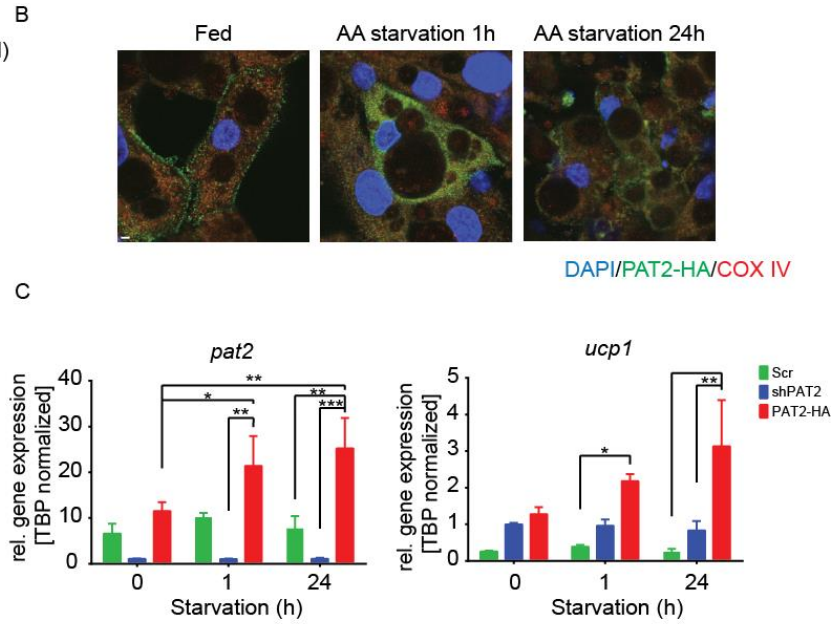

Figure 3.19 PAT2 can interact with mitochondrial proteins. (A) MS quantification analysis of mitochondrial proteins in PAT2-HA cells Co-IP sample by using anti HA tag antibody upon normal condition or amino acid starvation 24h, values were normalized by Scr values. **(B)** coimmunostaining of PAT2-HA and COX IV in PAT2-HA adipocytes upon normal condition and amino acid starvation one and 24 hours. The scale shows 3 µm. **(C)** qPCR analysis for PAT2 and UCP-1 in Scr, shPAT2 and PAT2-HA adipocytes upon normal condition, amino acid starvation 1 and 24 hours. RM two-way ANOVA with Tukey's post hoc test, n=3.

Additionally, Scr, shPAT2 and PAT2-HA adipocytes upon amino acid starvation 0, 1 and 24 hours were harvested for RNA isolation and qPCR analysis. For PAT2, Scr values showed an increase triggered by amino acid deprivation one hour and a decrease after 24 hours. PAT2-HA cells showed also the increase in PAT2 expression upon amino acid starvation. In Scr cells UCP-1 expression level showed a slight increase after one hour starvation and then a decrease. PAT2-HA cells demonstrated a significant increase of PAT2 expression and the expression level is higher than Scr cells. shPAT2 cells did not show

obvious variation **(Figure 3.19 C)**. These results indicate again that PAT2 and UCP-1 expressions perform a similar way in responding to amino acid starvation.

3.2.8.2 PAT2 plays a complicate role in mitophagy

Next, whether mitochondria can be regulated by PAT2 was tried to be verified.

To evaluate the function of mitochondria, the seahorse mito stress test was performed. Oligomycin (F-ATPase inhibitor), FCCP (Uncoupling reagent), antimycin A and rotenone (electron transport chain inhibitor), 2-DG (Glucose analogs, glycolysis inhibitor) were injected into the medium serially. Oxygen consumption rate was measured during the whole test **(Figure 3.20 A)**. The mitochondria related parameters were calculated (Details see material and methods). The Scr, shPAT2 and PAT2-HA adipocytes upon 0, 1 and 24 hours amino acid starvation were tested.

The results showed that the nonmitochondrial respiration (non mito respiration), coupling efficiency (%), maximal respiration, spare respiration capacity and spare respiration capacity (%) were similar between the cell lines during amino acid starvation. The non mito respiration showed no significant variation after starvation, coupling efficiency (%) showed a decrease in average value after starvation 24 hours. The maximal respiration increased after 1hour and declined after 24 hours. The latter two parameters showed a similar but more obvious trend. The other parameters, basal respiration (basal), proton leak and ATP production demonstrated a comparable stable variation for Scr and a similar rapid decrease in shPAT2 and PAT2-HA cells **(Figure 3.20 B)**.

The variation trend of proton leak is different withUCP-1 mRNA alteration during starvation, it is possible for PAT2 to regulate the turnover of mitochondria upon amino acid starvation but not actual oxidative phosphorylation. The previous data showed that both PAT2 knockdown and overexpression impair autophagy. Mitochondria may be degraded upon amino acid depletion through a kind of autophagy, mitophagy. Dysfunctional mitochondria which are not degraded but accumulate in shPAT2 and PAT2 adipocytes may result in high level of UCP-1 but not high level of proton leak.

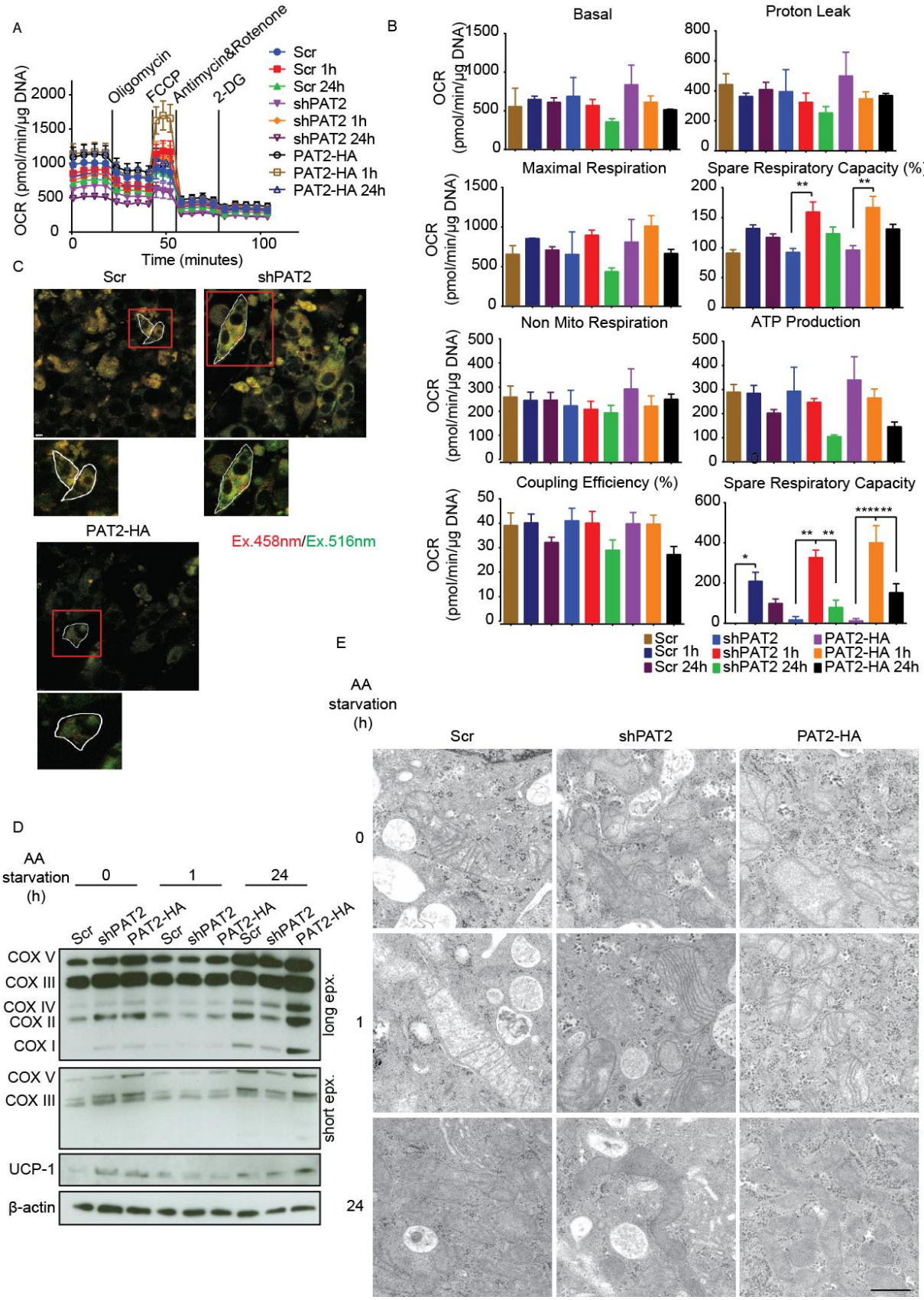

Figure 3.20 PAT2 regulates mitochondrion. (A) Seahorse test for Scr, shPAT2 and PAT2-HA adipocytes upon the normal condition, amino acid starvation one and 24 hours. **(B)** Respiration parameters calculated based on 3 independent experiments with 3-6 independent duplication. RM

two-way ANOVA with Tukey's post hoc test. **(C)** Scr, shPAT2 and PAT2-HA adipocytes transfected with Mito-Keima plasmid upon amino acid starvation 24 hours. Images were acquired under 458 nm and 516 nm excitation. The scale shows 5 μm. **(D)** Western blot analysis for COXs and UCP-1 in Scr, shPAT2 and PAT2-HA adipocytes upon normal condition, amino acid starvation one and 24 hours. **(E)** Representative electron microscopy images for Scr, shPAT2 and PAT2-HA cells upon normal condition, amino acid starvation one and 24 hours. The scale shows 500 nm.

So to figure out whether mitophagy can be regulated by PAT2, a Mito-mKeima plasmid was stably transfected into adipocytes to monitor mitophagy in adipocytes. The plasmid overexpresses a fusion protein containing mKeima and a mitochondria destined signal peptide in the cell. mKeima is a pH sensitive fluorescence protein whose excitation wavelength is 440 nm in neutral environment, but when in acidic environment its wavelength becomes longer to 550 nm. So mitochondria localized mKeima normally can be excited by 440 nm laser. For mitophagy, mKeima together with mitochondria were exposed to acidic lysosome lumen, at this time mKeima emits fluorescence upon 550 nm excitation. Then mitophagy can be distinguished by the wavelength shift.

Before acquiring images, the transfected Scr, shPAT2 and PAT-HA adipocytes were treated with amino acid free DMEM for 24 hours. The images were acquired by using a similar excitation wavelength 458 nm and 516 nm. The results showed a high level of mitophagy in Scr adipocytes because of the strongest acidic mKeima signal. In shPAT2 and PAT2-HA cells, the neutral mKeima signal is stronger, especially PAT2-HA only showed very few mitophagy dots **(Figure 3.20 C)**. These results indicate that PAT2 knockdown or overexpression impairs amino acid depletion induced mitophagy.

Western blots for COX I, II, III, IV and V showed that under normal culture condition shPAT2 and PAT2-HA cells have more mitochondrial complex subunits than Scr cells. Upon amino acid starvation for one hour COXs in shPAT2 and PAT2-HA cells decreased. After 24 hours, COXs rebounded, especially for PAT2-HA cells. Scr and shPAT2 cells after starvation 24 hours showed similar COXs except COX II which in Scr is higher than in shPAT2 cells **(Figure 3.20 D)**. The declines of COXs suggested the possible clearance of accumulated mitochondrial proteins in shPAT2 and PAT2. Furthermore, the strong increase of COXs inPAT2-HA cells after 24h may be caused by the mitochondrial regeneration **(Figure 3.20 E)**

and weak mitophagy **(Figure 3.20 C)**. For shPAT2 cells, a possible explaination for no COXs rebound after 24h is the impaired mitochondrial regeneration.

It has been reported that the fusion of mitochondria into tubular structure is to protect mitochondria from being degraded during nutrition depletion induced mitophagy (Gomes et al 2011, Rambold et al 2011). Actually, this tubular structure can be observed in EM images of Scr after starvation. For shPAT2 cells, only rare tubular mitochondria were observed after starvation 24 hours. For PAT2-HA adipocytes, many small mitochondria appeared after amino acid starvation 24 hours which were probably to be the new mitochondria generation. On the contrary, less small mitochondria but tubular mitochondria were found in shPAT2 cells **(Figure 3.20 E)**. These results from another aspect support the hypothesis of impaired mitochondria generation in shPAT2.

3.2.9 PAT2 knockout mice show embryonic lethality

In order to figure out the function of PAT2 *in vivo*, a PAT2 whole body knockout mouse line was generated (The details about genome structure are described in material and method).

Chimeric PAT2 knockout mice were bred with wildtype mice and in total 15 wildtype mice and 16 heterozygote mice were obtained from 5 matings as F1 generation. These F1 $PAT^{+/-}$ mice were bred with wild type mice one more time to make the knockout stable.

A

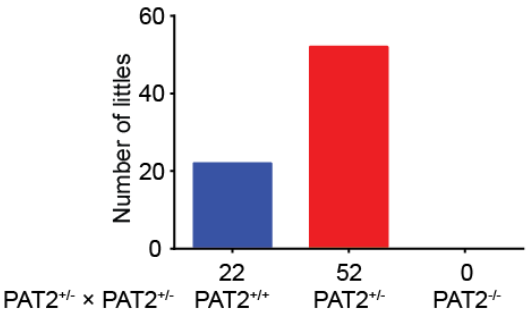

B

Male genotype	Female genotype	Litter genotype $PAT2^{+/+}$	Litter genotype $PAT2^{+/-}$
$PAT2^{+/-}$	$PAT2^{+/+}$	8	4
		3	1
		3	1
		4	7
In total		18	13
$PAT2^{+/+}$	$PAT2^{+/-}$	3	2
		0	3
In total		3	5

Figure 3.21 PAT2 knockout mice show embryonic lethality. (A) Genotype distribution from PAT2 heterozygous matings, in total 74 mice from 9 litters. **(B)** Genotype distribution from PAT2 heterozygous mating with wild type mice.

After this, heterozygotes PAT2$^{+/-}$ mice were bred with heterozygotes PAT2$^{+/-}$ mice to get homozygote PAT2 $^{-/-}$ mice. 9 mating totally produced 22 wild type mice and 52 PAT2$^{+/-}$ heterozygote mice, but no PAT2$^{-/-}$ homozygotes mice **(Figure 3.21 A)**. Base on Mendel's law, the ratio of wildtype, heterozygote and homozygote should be 1:2:1 theoretically. In this breeding, radio between wildtype and heterozygote mice is nearly 1:2. So PAT2 knockout seems to be lethal for mice.

Additional, based on the mating between wildtype and heterozygote mice, no matter if male wildtype mated with female heterozygote or male heterozygote mated with female wildtype, wildtype and heterozygote litters can be born. **(Figure 3.21 B)**. It suggests PAT2 knockout sperm or oocyte can be generated in heterozygote mice.

4 Discussion

4.1 Kindlin-2

Integrin mediated "inside-out" and "outside-in" signaling regulates multiple intracellular and extracellular events (Hu & Luo 2013). Kindlins as the intracellular activators for integrins play an important role in the "inside-out" signal transduction (Hu & Luo 2013). Although various functions of Kindlins have been revealed (Larjava et al 2008, Ma et al 2008, Meves et al 2009, Montanez et al 2008, Moser et al 2008, Plow et al 2014, Shi et al 2007, Ye et al 2011), still very little is known about the role of Kindlins in adipose tissue. The major type of Kindlins in adipose tissues is Kindlin-2 (Malinin et al 2010). To find out whether Kindlin-2 and its related integrins are implicated in adipose tissue activities, the gene expression levels in adipose tissues from mice fed with HFD and CD were tested. The data show the expression of *integrin β1* was significantly increased by HFD feed (**Figure 3.1 B**).

Analyzing the adipose tissue conditional knockout mice demonstrated a different way of Kindlin-2 in adipocyte compared to other cell types. The absence of Kindlin-2 leads to a serious adhesion disorder as for ESC (Montanez et al 2008). Loss of Kindlin-2 did not severely impair the survival and adipogenesis of adipocytes (**Figure 3.2 C**). Actually, the

presence of a considerable fat mass in Kindlin-2 knockout mice also supports this conclusion (**Figure 3.1 B**). Although Kindlin-2 overexpression was reported to inhibit adipogenesis of induced pluripotent cell-derived mesenchymal stromal cells (Moslem et al 2017), morphologically SCF, PGF and BAT in knockout mice were much smaller due to Kindlin 2 ablation (**Figure 3.1 B**). HFD increased the differences to wildtype mice (**Figure 3.4 G and H**). The Kindlin-2 knockout leads to lipodystrophybut does not impair differentiation of adipocytes.

The ablation of many proteins in fats can lead to lipodystrophy, including mTOR (Lee et al 2016b, Shan et al 2016), PPARγ (Wang et al 2013a), insulin receptor (Qiang et al 2016, Softic et al 2016), AKT (Shearin et al 2016) and Lamin A/C (Wojtanik et al 2009). But whether Kindlin-2 knockout induced lipodystrophy is a novel mechanism still needs more researches. As there is almost no report about whether ECM can affect lipid intake, the possibility that less lipid intake causes Kindlin-2 knockout induced lipodystrophy cannot be excluded. Integrins have been reported to affect adipogenesis (Chen et al 2014, Liu et al 2005). The results showed the related integrins were affected by Kindlin-2 knockout. The genes *integrin β1*and *integrin* α*1* showed increased expression, but integrin β1 protein was dramatically decreased (**Figure 3.2 A and D**). it is reasonable for Kindlin-2 knockout to weaken adipose tissue development via integrins decrease. But to prove this still needs further researches. Another possible explanation for the lipoatrophy is the disordered angiogenesis which regulates many processes including adipogenesis (Carmeliet 2003).

Kindlin-2 knockout induced disordered angiogenesis is another important phenomenon. It has been reported that fat accumulation leads to increased blood vessels size but fewer capillaries though affecting ECM (Spencer et al 2011). The reverse regulation that angiogenesis affects adipogenesis has also been reported (Neels et al 2004). It is possible that Kindlin-2 knockout affected ECM decreases fat mass by regulating angiogenesis. Actually, many ECM components play a crucial role in angiogenesis as described in the introduction. Integrins have been reported to take part in many steps of

angiogenesis, such as regulating endothelial cells (Akiyama et al 1989, Giancotti & Ruoslahti 1999, Meredith & Schwartz 1997, Wary et al 1996) and modulating morphogenesis (Liu & Senger 2004, Sweeney et al 2003, Whelan & Senger 2003). It is predictable that Kindlin-2 knockout causes ECM and blood vessels impairment as the data have shown Kindlin-2 knockout in adipose tissues severely declined integrin β1 level **(Figure 3.2 A)**. And indeed, anomalies were found in the intercellular space, such as the potential enlargement of collagen shown in AZAN trichrome staining **(Figure 3.3 D)**, which may be the compensative enlargement to integrin decrease as β integrins were reported to bind to collagen as collagen receptor (Leitinger 2011, Zeltz et al 2014). Another anomaly is the morphological hyperplasia observed in adipose tissues especially BAT of knockout mice by H&E, Mason, picro sirius red or AZAN trichrome staining **(Figure 3.3)**. The more circular structures in knockout mice rather than tubular structures in wildtype mice in phalloidin staining further suggest less blood vesselsin BAT**Figure 3.5 D)**. The more direct support is the CD31 immunostaining, where blood vessels in Kindlin-2 knockout BAT distributed irregularly between adipocytes **(Figure 3.5 E)**. The abnormal vessels were further indicated to be leaky **(Figure 3.5 F)**. The Kindlin-2 knockout adipose tissues with less mass and leaked blood vessels did not show different values of blood glucose and insulin sensitivity (**Figure 3.5 A and B**). Surprisingly, knockout mice showed faster glucose deposit than wildtype mice, HFD delayed glucose deposit for knockout and wildtype mice (**Figure 3.5**). HFD can induce insulin resistance (Akiyama et al 1996, Hancock et al 2008, Pedersen et al 1991, Storlien et al 1986) , which can explain why the delay of glucose deposit happens for the mice fed with HFD. So a possible reason is that Kindlin-2 knockout induced insulin secretion alteration, which could explain the quicker glucose deposit in knockout mice with no significant insulin sensitivity change. If the hypothesis about the increased insulin level in Kindlin-2 knockout mice is true, lipolysis may not be the reason for lipodystrophy as insulin inhibits lipolysis in adipocytes (Chakrabarti et al 2013). However, it may also be possible that Kindlin-2 is implicated in the other complicate metabolism mechanisms. For example, VEGF signaling is one of the candidates. VEGF itself

is a necessary factor for angiogenesis in adipose tissue (Melincovici et al 2018, Roy et al 2006). VEGF signaling is reported to be related to thermogenesis and energy expenditure. During white adipocyte browning VEGF receptor 2 promotes thermogenesis but VEGF receptor 1 function is opposite to this (Xue et al 2009). In BAT, VEGF enhances thermogenesis and energy expenditure (Elias et al 2012). Interestingly, similar disordered intercellular space in BAT appears in VEGF transgenic mice (Elias et al 2012). If Kindlin-2 knockout affects angiogenesis through increasing VEGF levels, the enhanced energy expenditure may explain the quick glucose deposit. But to verify this still requires further researches.

The role of Kindlin-2 in adipose tissue may be very complicated and also very important for clearly understanding adipose tissues, to figure out these more deep researches are needed.

4.2 PAT2

Because of the cell surface localization and specific high expression level in brown adipocyte, PAT2 is identified as a brown adipocyte marker (Ussar et al 2014). However, its role in brown adipocytes and why it is maintained at such a high level in brown adipocyte were unknown. Actually, before the brown adipocyte marker identification, PAT2 was always understood as an amino acid transporter, which performs the function of amino acid transmembrane transportation (Chen et al 2003, Edwards et al 2011, Foltz et al 2004a, Foltz et al 2004b, Kennedy et al 2005). And BAT is regarded as the tissue which performs strong amino acid metabolism (Lopez-Soriano & Alemany 1986, Lopez-Soriano & Alemany 1987). Interestingly, some particular characters of PAT2 have been revealed in the previous publications, including localization differences to PAT1, strong affinity but low capacity for amino acid transportation (Rubio-Aliaga et al 2004) and its pH dependent action (Chen et al 2003). These characters make PAT2 to be different to the other PATs, although all PATs share 48% sequence (Boll et al 2004) and 72% identity is shared for PAT2 with the most

similar PAT1 (Edwards et al 2011). Noticeable, more and more amino acid transporters are found to play a role in signal transduction and regulation.

Actually, many characteristics of PAT2 suggest the possible roles of PAT2 in regulation crosstalk. For example, the transportation capacity of PAT2 are much less than PAT1, but brown adipocytes still keep numerous PAT2 rather than PAT1, it is hard for this phenomenon to exist during the evolution if PAT2 performs only as a transporter.

As a brown adipocyte marker, PAT2 was speculated to be necessary to maintain the brown adipocytes characters. However, the results clearly show the absence of PAT2 does not impair brown adipocyte adipogenesis not matter on the morphogenesis, the lipid accumulation (**Figure 3.7 A**) or the expression adipogenic gene PPARγ (**Figure 3.7 B and C**). Besides, the data confirm the cell surface localization of PAT2 in previous publications (Rubio-Aliaga et al 2004, Ussar et al 2014) and also indicate in preadipocyte PAT2 can also localize to lysosome as PAT1 (**Figure 3.8**) even it is regarded to lack lysosome motif (Bermingham et al 2002).

Two phenomena implicate PAT2 is related to protein and amino acid homeostasis in the adipocyte. The PAT2 overexpression in preadipocytes was found to be strongly weakened compared with adipocytes (**Figure 3.6**). As preadipocyte did not express PAT2 normally (**Figure 3.6 A**) and undegraded PAT2-HA localized to lysosome (**Figure 3.8 A)**, it was reasonable to postulate the redundant PAT2 was degraded in lysosome. Results supported this hypothesis as the inhibition of endosome/lysosome acidification by autophagy inhibitor Bafilomycin A1 prevented degradation of PAT2 in preadipocyte (**Figure 3.9 B)**. The related data revealed PAT2 in preadipocyte was possible to be transported to lysosome via cell surface (**Figure 3.9 C and D)**. Another phenomenon was the upregulated UCP-1 induced by both PAT2 knockdown or overexpression (**Figure 3.7 B and C**). However, the increased UCP-1 levels did not lead to the enhanced proton leak, especially in PAT2 knockdown cells (**Figure 3.20**). It can be explained as the accumulation of abundant dysfunctional mitochondria which cannot be degraded normally.

These two aspects were both related to intracellular protein degradation. In fact, some publications have shown PAT2 may be implicated in mTOR signaling the hub pathway for amino acid homeostasis regulation (Goberdhan et al 2005b, Heublein et al 2010). Results also showed lysosome localized PAT2 in preadipocyte can directly interact with mTORC1 and can promote its activation (**Figure 3.11**). Nevertheless, adipocytes express PAT2 highly rather than preadipocytes. In adipocytes, cell surface localized PAT2 seems to be impossible to interact with mTORC1 or be involved in lysosome related protein degradation. Surprisingly, an important translocation of PAT2 from cell surface to lysosome was shown and the triggers are amino acid starvation or mTORC1 inhibitor Rapamycin (**Figure 3.10**). Amino acid depletion and Rapamycin can both induce autophagy for protein degradation through deactivating mTORC1 (Wolfson & Sabatini 2017). The translocation strongly hints the potential role of PAT2 in autophagy.

The further results indicate PAT2 knockdown and overexpression both impaired the processing of autophagy (**Figure 3.12**). But the formation of autophagosome was found to be not affected by PAT2 knockdown or overexpression (**Figure 3.14**). The further results revealed weakened autophagosome-lysosome fusion **(Figure 3.13 A and B)** in shPAT2 and PAT2-HA adipocytes.

Actually, PAT2 has been reported at a very early time as a proton coupled transporter and its transportation efficiency is dependent on environmental pH (Edwards et al 2011). The well-accepted vesicles transportation from cytoplasm to the lysosome is through endocytosis which is also the path of endosome/lysosome acidification (Mindell 2012). PAT2 translocating to lysosome in responding to amino acid starvation implicates the potential relationship with this mechanism. And indeed the abnormal endosome/lysosome acidification was found in shPAT2 and PAT2-HA adipocytes **(Figure 3.15 A and B)**.

Further, I found the promotion of PAT2 is V-ATPase dependent (**Figure 3.15 C**), PAT2 also showed the interaction directly with V1 subunit rather than V0 subunit (**Figure 3.15 E**). The regulations of PAT2 to V-ATPase at least were observed as assembly

promotion (**Figure3.16 A and B**) and proton pumping enhancement (**Figure3.16 G, H and I**). Importantly, the regulation of PAT2 to V-ATPase assembly is independent of mTORC1 activation (**Figure 3.16 D**).

Till now the potential brown adipocyte specific mechanism upon amino acid starvation shows its outline. The mTORC1 gathers the amino acid depletion signaling from upstream amino acid sensing system and induces autophagy and also triggers PAT2 translocation from the cell surface to lysosome during which PAT2 assists V-ATPase assembly and proton pumping for lysosome acidification **(Figure 4.1)**.

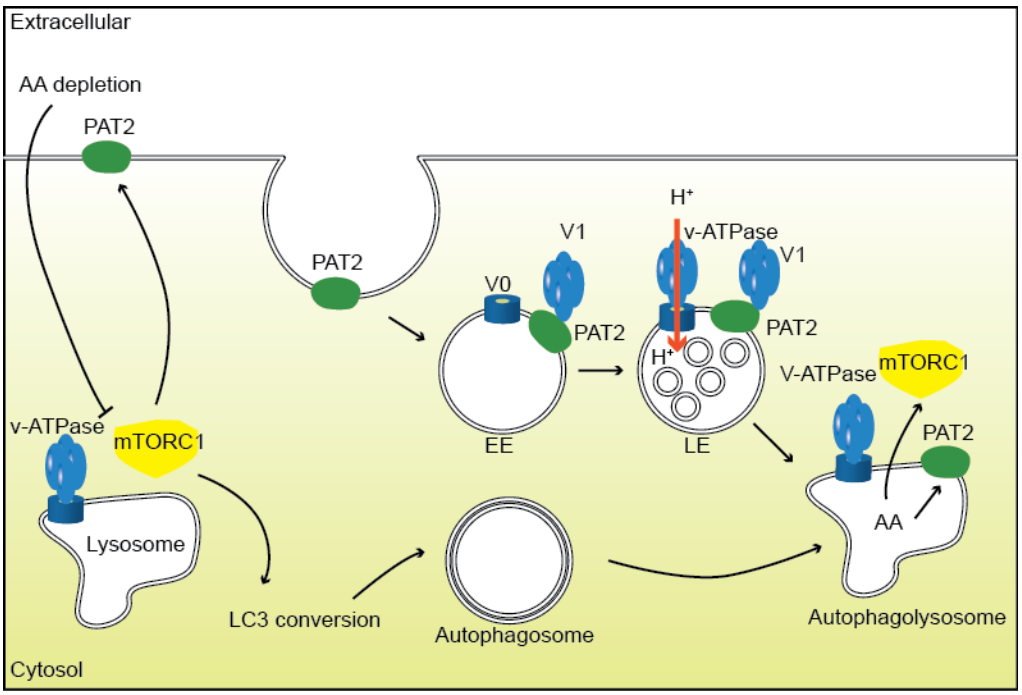

Figure 4.1 PAT2 promotes acidification through V-ATPase regulation upon amino acid starvation.

Interestingly, this additional acidification promotion event in many other cells with low PAT2 expression may even not exist. It implicates the physiological meaning of the high expression of PAT2 in brown adipocyte may be the increased sensitivity to amino acid starvation. Surprisingly, comparing with the WATs expressing less PAT2 BAT showed quicker autophagy induction upon random fast *in vivo* (**Figure 3.18 B and C**). Actually, *in vitro* brown adipocytes also showed the positive correlation between amino acid sensitivity and PAT2 level although the differences were comparably slight (**Figure 3.17**). However, the

differences between WAT and BAT are numerous, whether the enhanced sensitivity of BAT is assigned by PAT2 still needs more researches to figure it out. And a more complicated but meaningful question is why BAT needs to be sensitive to amino acids. The answer will be important for deeply understand adipose tissue and its role in amino acid homeostasis.

Although BAT deficiency is not embryonic lethal (Lowell et al 1993), the data showed the lethality of whole body PAT2 knockout **(Figure 3.21)**. Actually, PAT2 ablation has been reported for its lethality (Klein et al 2010, Vanslambrouck et al 2010). It may implicate the functions of PAT2 may not only in fat but also in other tissues, PAT2 may start to play its important role in the embryonic phase.

There are also some open questions which are worth to be discussed.

It is clear that insulin recruits GLUT4 on the cell surface in 3T3-L1 adipocyte (Calderhead et al 1990) and at the same time reduces intercellular GLUT4 storage (Cushman & Wardzala 1980, Suzuki & Kono 1980). Besides, it is also clear that Rab10 can promote insulin regulated translocation of GLUT4 to cell surface (Babbey et al 2006, Leaf & Blum 1998, Sano et al 2008, Schuck et al 2007). Actually, Rab10 was physically associated with PAT2-HA in MS data **(Figure 3.9 A)** and insulin was observed to alternate PAT2 expression and subcellular localization **(Figure 3.7 B and C)**. It is reasonable to explain the increase upon insulin treatment because insulin activates mTORC1 which can be weakened by S6K in the downstream as feedback (Blagosklonny 2013) and activated mTORC1 weaken protein degradation (Zhao et al 2015). But the regulation of insulin to PAT2-HA may not be simple. The published databases have reported the insulin regulated phosphorylation sites of PAT2 in 3T3-L1 cells (Parker et al 2015). However, insulin seems to be not a predominant element for PAT2, at least amino acid depletion induced PAT2 translocation was independent of insulin in my data **(Figure 3.10 C)**. But to figure out how insulin regulates PAT2 still needs more researches. Another, rapamycin triggered PAT2-HA perinuclear accumulation and slightly increased PAT2-HA protein level in preadipocytes **(Figure 3.9 B and C)**. In the published data, rapamycin can increase lysosomal protein degradation mildly

(Zhao et al 2015), but rapamycin induced autophagy at least shows some degree of selectivity (Berger et al 2006, Mochida et al 2015). So the increase of PAT2 upon rapamycin treatment implicates the possible role of PAT2 in mechanism in response to mTORC1 inhibition or amino acid depletion in preadipocyte. However, about the exact effects of rapamycin and insulin to PAT2 still need more deep researches.

Another important question is how autophagosome and lysosome fusion is regulated by PAT2. It has been reported that impaired acidification does not intercept fusion (Mauvezin et al 2015). Actually, my data also supported this conclusion, abnormal acidification in shPAT2 and PAT2-HA adipocytes weaken but does not completely impair fusion **(Figure 3.13)**. The mCherry-EGFP-LC3 test supported this conclusion from another aspect, different acidification in shPAT2 and PAT2-HA led to different EGFP, if fusion was completely intercepted there should be no significant difference on EGFP quenching between these two cell lines. The EM images revealed more details as an abnormal engulfing-liked fusion was observed in shPAT2 and PAT2-HA adipocytes **(Figure 3.14 E)**. At the same time, the different variations after amino acid starvation in shPAT2 and PAT2-HA adipocytes implicate the mechanisms of abnormal fusion differ in these two cell lines **(Figure 3.14 G)**. However, what exactly the different mechanisms are is still hard to be answered.

Another interesting phenomenon is PAT2 promoted V-ATPase assembly was found to be independent with mTORC1 activation. The similar result has been reported as amino acid starvation induced V-ATPase assembly is not regulated by mTORC1 (Stransky & Forgac 2015). As discussed previously, many other cells with low or no PAT2 expression can trigger acidification and autophagy normally. Then the role of PAT2 in adipocyte in this mechanism seems to be an additional gain or loss regulation. This regulation mode may be the key to explain the different amino acid sensitivity of different fat.

When PAT2 localized to the lysosome, its promotion to mTORC1 activation was observed no matter in adipocytes **(Figure 3.16 C)** or preadipocytes **(Figure 3.11 C)**. But when PAT2 localized to cell surface, different activation of mTORC1 was also found **(Figure**

3.17 B). As the different localization prevent direct interact, it is reasonable to postulate the potential regulation is via other pathways. This speculation may also work for PAT2 knockdown and overexpression induced amino acid sensitivity variations as lysosome localized PAT2 may also directly interact with mTOR in the plasma. About the exact interact site of mTORC1 to PAT2, the mTORC1 agonist 3BDO experiment revealed a clue as its activation was weakened in shPAT2 adipocytes **(Figure 3.10 D)**. This phenomenon implicates PAT2 is needed for 3BDO to activate mTORC1 in adipocytes. The target of 3BDO in mTORC1 was reported to be FK506-binding protein 1A (FKBP1A) (Ge et al 2014). It is very possible for PAT2 to interact with FKBP1A and then regulate mTORC1 activation. About details of PAT2 mTORC1, still very less is known.

Amino acid homeostasis and its regulation in mitochondria are still not clear, only few amino acid transporters have been reported to function in mitochondria (Palmieri 2014). The data showed the closed relation between PAT2 and mitochondria and depicted the possible functions of PAT2 to mitochondria **(Figure 3.7 B and C, 3.19 and 3.20)**. But it is still difficult to explain seahorse data showed different variation with COXs in WB. Besides, the mitochondria showed huge differences in morphology among Scr, shPAT2 and PAT2-HA adipocytes upon the normal condition or amino acid starvation **(Figure 3.20 E)**. It means regulation of PAT2 to mitochondria may not only restrict into amino acid starvation responding. To figure out the complex role of PAT2 in mitochondria still needs more deep researches.

Finally, the ultimate question is why brown adipocyte or BAT maintains specific strong expression of PAT2. It is hard to give a precise answer now. But it should be something about amino acid related mechanisms. Adipose tissues in the past are regarded no matter the energy conservative tissues or the endocrine organs, very little is known about its role in amino acid homeostasis. If PAT2 make BAT more sensitive to amino acid, BAT will be the amino acid sensor tissue *in vivo*. As the main substrates of PAT2 are not the necessary amino acids, it is reasonable for BAT to quickly trigger the related metabolism and signaling

pathways in response to amino acid variation sensitively, like amino acid synthesis and mTORC1 inhibition. Because BAT itself is not a big tissue *in vivo*, it is also possible for BAT to regulate other tissues through endocrine, like regulating the biggest amino acid storage tissue muscle. As an amio acid sensing organ, BAT is also a good target for therapy of amino acid related metabolic syndrome.

As an essential protein, the functions of PAT2 are also very complicated. But the meaning to reveal its role may not only benefit amino acid metabolism regulation researches but also it may help to understand other physiological processes deeply.

5 Conclusion

Kindlin-2 knockout in adipose tissues causes lipoatrophy and angiogenesis disorders.

PAT2 is translocated from cell surface to lysosome by mTORC1 inhibition and PAT2 promotes intracellular acidification through modulating V-ATPase upon amino acid starvation in brown adipocytes. PAT2 knockdown or overexpression affects mitochondria, autophagy and amino acid sensitivity in brown adipocytes. PAT2 is necessary for mouse embryo development.

6 Reference

Aamodt JM, Grainger DW. 2016. Extracellular matrix-based biomaterial scaffolds and the host response. *Biomaterials* 86: 68-82

Akiyama SK, Yamada SS, Chen WT, Yamada KM. 1989. Analysis of fibronectin receptor function with monoclonal antibodies: roles in cell adhesion, migration, matrix assembly, and cytoskeletal organization. *J Cell Biol* 109: 863-75

Akiyama T, Tachibana I, Shirohara H, Watanabe N, Otsuki M. 1996. High-fat hypercaloric diet induces obesity, glucose intolerance and hyperlipidemia in normal adult male Wistar rat. *Diabetes Res Clin Pract* 31: 27-35

Alzamora R, Al-Bataineh MM, Liu W, Gong F, Li H, et al. 2013. AMP-activated protein kinase regulates the vacuolar H+-ATPase via direct phosphorylation of the A subunit (ATP6V1A) in the kidney. *American journal of physiology. Renal physiology* 305: F943-56

Ananieva EA, Powell JD, Hutson SM. 2016. Leucine Metabolism in T Cell Activation: mTOR Signaling and Beyond. *Adv Nutr* 7: 798S-805S

Aoudjit F, Vuori K. 2001. Matrix attachment regulates Fas-induced apoptosis in endothelial cells: a role for c-flip and implications for anoikis. *J Cell Biol* 152: 633-43

Aplin AC, Fogel E, Zorzi P, Nicosia RF. 2008. The aortic ring model of angiogenesis. *Methods Enzymol* 443: 119-36

Aplin AE, Short SM, Juliano RL. 1999. Anchorage-dependent regulation of the mitogen-activated protein kinase cascade by growth factors is supported by a variety of integrin alpha chains. *J Biol Chem* 274: 31223-8

Armstrong LC, Bornstein P. 2003. Thrombospondins 1 and 2 function as inhibitors of angiogenesis. *Matrix Biol* 22: 63-71
Arriza JL, Kavanaugh MP, Fairman WA, Wu YN, Murdoch GH, et al. 1993. Cloning and expression of a human neutral amino acid transporter with structural similarity to the glutamate transporter gene family. *J Biol Chem* 268: 15329-32
Ashrafi G, Schwarz TL. 2013. The pathways of mitophagy for quality control and clearance of mitochondria. *Cell Death Differ* 20: 31-42
Assoian RK. 1997. Anchorage-dependent cell cycle progression. *J Cell Biol* 136: 1-4
Assoian RK, Schwartz MA. 2001. Coordinate signaling by integrins and receptor tyrosine kinases in the regulation of G1 phase cell-cycle progression. *Curr Opin Genet Dev* 11: 48-53
Astrof S, Crowley D, Hynes RO. 2007. Multiple cardiovascular defects caused by the absence of alternatively spliced segments of fibronectin. *Dev Biol* 311: 11-24
Astrof S, Hynes RO. 2009. Fibronectins in vascular morphogenesis. *Angiogenesis* 12: 165-75
Atit R, Sgaier SK, Mohamed OA, Taketo MM, Dufort D, et al. 2006. Beta-catenin activation is necessary and sufficient to specify the dorsal dermal fate in the mouse. *Dev Biol* 296: 164-76
Attie AD, Scherer PE. 2009. Adipocyte metabolism and obesity. *J Lipid Res* 50 Suppl: S395-9
Ausprunk DH, Folkman J. 1977. Migration and proliferation of endothelial cells in preformed and newly formed blood vessels during tumor angiogenesis. *Microvasc Res* 14: 53-65
Authier F, Chauvet G. 1999. In vitro endosome-lysosome transfer of dephosphorylated EGF receptor and Shc in rat liver. *FEBS Lett* 461: 25-31
Avruch J, Long X, Ortiz-Vega S, Rapley J, Papageorgiou A, Dai N. 2009. Amino acid regulation of TOR complex 1. *Am J Physiol Endocrinol Metab* 296: E592-602
Babbey CM, Ahktar N, Wang E, Chen CC, Grant BD, Dunn KW. 2006. Rab10 regulates membrane transport through early endosomes of polarized Madin-Darby canine kidney cells. *Mol Biol Cell* 17: 3156-75
Balasubramanian MN, Butterworth EA, Kilberg MS. 2013. Asparagine synthetase: regulation by cell stress and involvement in tumor biology. *Am J Physiol Endocrinol Metab* 304: E789-99
Balderhaar HJ, Ungermann C. 2013. CORVET and HOPS tethering complexes - coordinators of endosome and lysosome fusion. *J Cell Sci* 126: 1307-16
Bar-Peled L, Sabatini DM. 2014. Regulation of mTORC1 by amino acids. *Trends Cell Biol* 24: 400-6
Barak Y, Nelson MC, Ong ES, Jones YZ, Ruiz-Lozano P, et al. 1999. PPAR gamma is required for placental, cardiac, and adipose tissue development. *Mol Cell* 4: 585-95
Barbatelli G, Morroni M, Vinesi P, Cinti S, Michetti F. 1993. S-100 protein in rat brown adipose tissue under different functional conditions: a morphological, immunocytochemical, and immunochemical study. *Exp Cell Res* 208: 226-31
Barbatelli G, Murano I, Madsen L, Hao Q, Jimenez M, et al. 2010. The emergence of cold-induced brown adipocytes in mouse white fat depots is determined predominantly by white to brown adipocyte transdifferentiation. *Am J Physiol Endocrinol Metab* 298: E1244-53
Barbera MJ, Schluter A, Pedraza N, Iglesias R, Villarroya F, Giralt M. 2001. Peroxisome proliferator-activated receptor alpha activates transcription of the brown fat uncoupling protein-1 gene. A link between regulation of the thermogenic and lipid oxidation pathways in the brown fat cell. *J Biol Chem* 276: 1486-93
Barretina J, Caponigro G, Stransky N, Venkatesan K, Margolin AA, et al. 2012. The Cancer Cell Line Encyclopedia enables predictive modelling of anticancer drug sensitivity. *Nature* 483: 603-7
Bayless KJ, Davis GE. 2002. The Cdc42 and Rac1 GTPases are required for capillary lumen formation in three-dimensional extracellular matrices. *J Cell Sci* 115: 1123-36
Bayless KJ, Salazar R, Davis GE. 2000. RGD-dependent vacuolation and lumen formation observed during endothelial cell morphogenesis in three-dimensional fibrin matrices involves the alpha(v)beta(3) and alpha(5)beta(1) integrins. *Am J Pathol* 156: 1673-83
Benjamin LE, Golijanin D, Itin A, Pode D, Keshet E. 1999. Selective ablation of immature blood vessels in established human tumors follows vascular endothelial growth factor withdrawal. *J Clin Invest* 103: 159-65
Bento CF, Renna M, Ghislat G, Puri C, Ashkenazi A, et al. 2016. Mammalian Autophagy: How Does It Work? *Annu Rev Biochem* 85: 685-713
Berger Z, Ravikumar B, Menzies FM, Oroz LG, Underwood BR, et al. 2006. Rapamycin alleviates toxicity of different aggregate-prone proteins. *Hum Mol Genet* 15: 433-42

Bergstrom J, Furst P, Noree LO, Vinnars E. 1974. Intracellular free amino acid concentration in human muscle tissue. *J Appl Physiol* 36: 693-7
Bermingham JR, Jr., Pennington J. 2004a. Organization and expression of the SLC36 cluster of amino acid transporter genes. *Mamm Genome* 15: 114-25
Bermingham JR, Jr., Shumas S, Whisenhunt T, Sirkowski EE, O'Connell S, et al. 2002. Identification of genes that are downregulated in the absence of the POU domain transcription factor pou3f1 (Oct-6, Tst-1, SCIP) in sciatic nerve. *The Journal of neuroscience : the official journal of the Society for Neuroscience* 22: 10217-31
Bermingham JR, Pennington J. 2004b. Organization and expression of the SLC36 cluster of amino acid transporter genes. *Mammalian Genome* 15: 114-25
Berrier AL, Yamada KM. 2007. Cell-matrix adhesion. *J Cell Physiol* 213: 565-73
Betz C, Hall MN. 2013. Where is mTOR and what is it doing there? *J Cell Biol* 203: 563-74
Bhutia YD, Ganapathy V. 2016. Glutamine transporters in mammalian cells and their functions in physiology and cancer. *Biochim Biophys Acta* 1863: 2531-9
Biazik J, Yla-Anttila P, Vihinen H, Jokitalo E, Eskelinen EL. 2015. Ultrastructural relationship of the phagophore with surrounding organelles. *Autophagy* 11: 439-51
Billon N, Dani C. 2012. Developmental origins of the adipocyte lineage: new insights from genetics and genomics studies. *Stem Cell Rev* 8: 55-66
Birbrair A, Zhang T, Wang ZM, Messi ML, Enikolopov GN, et al. 2013. Role of pericytes in skeletal muscle regeneration and fat accumulation. *Stem Cells Dev* 22: 2298-314
Bix G, Iozzo RV. 2008. Novel interactions of perlecan: unraveling perlecan's role in angiogenesis. *Microsc Res Tech* 71: 339-48
Blagosklonny MV. 2013. TOR-centric view on insulin resistance and diabetic complications: perspective for endocrinologists and gerontologists. *Cell death & disease* 4: e964
Bledzka K, Bialkowska K, Sossey-Alaoui K, Vaynberg J, Pluskota E, et al. 2016. Kindlin-2 directly binds actin and regulates integrin outside-in signaling. *J Cell Biol* 213: 97-108
Bledzka K, Liu J, Xu Z, Perera HD, Yadav SP, et al. 2012. Spatial coordination of kindlin-2 with talin head domain in interaction with integrin beta cytoplasmic tails. *J Biol Chem* 287: 24585-94
Boll M, Daniel H, Gasnier B. 2004. The SLC36 family: proton-coupled transporters for the absorption of selected amino acids from extracellular and intracellular proteolysis. *Pflugers Arch* 447: 776-9
Boll M, Foltz M, Rubio-Aliaga I, Daniel H. 2003. A cluster of proton/amino acid transporter genes in the human and mouse genomes. *Genomics* 82: 47-56
Boll M, Foltz M, Rubio-Aliaga I, Kottra G, Daniel H. 2002. Functional characterization of two novel mammalian electrogenic proton-dependent amino acid cotransporters. *J Biol Chem* 277: 22966-73
Bond S, Forgac M. 2008. The Ras/cAMP/protein kinase A pathway regulates glucose-dependent assembly of the vacuolar (H+)-ATPase in yeast. *J Biol Chem* 283: 36513-21
Bottcher RT, Stremmel C, Meves A, Meyer H, Widmaier M, et al. 2012. Sorting nexin 17 prevents lysosomal degradation of beta1 integrins by binding to the beta1-integrin tail. *Nat Cell Biol* 14: 584-92
Brandstaetter H, Kishi-Itakura C, Tumbarello DA, Manstein DJ, Buss F. 2014. Loss of functional MYO1C/myosin 1c, a motor protein involved in lipid raft trafficking, disrupts autophagosome-lysosome fusion. *Autophagy* 10: 2310-23
Breton S, Brown D. 2007. New insights into the regulation of V-ATPase-dependent proton secretion. *American journal of physiology. Renal physiology* 292: F1-10
Breton S, Brown D. 2013. Regulation of luminal acidification by the V-ATPase. *Physiology (Bethesda)* 28: 318-29
Broer A, Rahimi F, Broer S. 2016. Deletion of Amino Acid Transporter ASCT2 (SLC1A5) Reveals an Essential Role for Transporters SNAT1 (SLC38A1) and SNAT2 (SLC38A2) to Sustain Glutaminolysis in Cancer Cells. *J Biol Chem* 291: 13194-205
Broer A, Wagner CA, Lang F, Broer S. 2000. The heterodimeric amino acid transporter 4F2hc/y+LAT2 mediates arginine efflux in exchange with glutamine. *Biochem J* 349 Pt 3: 787-95
Broer S. 2014. The SLC38 family of sodium-amino acid co-transporters. *Pflugers Arch* 466: 155-72
Broer S, Bailey CG, Kowalczuk S, Ng C, Vanslambrouck JM, et al. 2008. Iminoglycinuria and hyperglycinuria are discrete human phenotypes resulting from complex mutations in proline and glycine transporters. *J Clin Invest* 118: 3881-92
Broer S, Broer A. 2017. Amino acid homeostasis and signalling in mammalian cells and organisms. *Biochem J* 474: 1935-63

Broer S, Palacin M. 2011. The role of amino acid transporters in inherited and acquired diseases. *Biochem J* 436: 193-211

Brosnan JT, Brosnan ME. 2006. Branched-chain amino acids: enzyme and substrate regulation. *J Nutr* 136: 207S-11S

Brown D, Paunescu TG, Breton S, Marshansky V. 2009. Regulation of the V-ATPase in kidney epithelial cells: dual role in acid-base homeostasis and vesicle trafficking. *J Exp Biol* 212: 1762-72

Bruce Alberts AJ, Julian Lewis, Martin Raff, Keith Roberts, and Peter Walter. 2002. Cell fractionation by centrifugation. In *Molecular Biology of the Cell, 4th edition*. New York: Garland Science

Brugarolas J, Lei K, Hurley RL, Manning BD, Reiling JH, et al. 2004. Regulation of mTOR function in response to hypoxia by REDD1 and the TSC1/TSC2 tumor suppressor complex. *Genes Dev* 18: 2893-904

Bryan BA, D'Amore PA. 2007. What tangled webs they weave: Rho-GTPase control of angiogenesis. *Cell Mol Life Sci* 64: 2053-65

Budanov AV, Karin M. 2008. p53 target genes sestrin1 and sestrin2 connect genotoxic stress and mTOR signaling. *Cell* 134: 451-60

Bukowiecki L, Lupien J, Follea N, Paradis A, Richard D, LeBlanc J. 1980. Mechanism of enhanced lipolysis in adipose tissue of exercise-trained rats. *Am J Physiol* 239: E422-9

Calderhead DM, Kitagawa K, Tanner LI, Holman GD, Lienhard GE. 1990. Insulin regulation of the two glucose transporters in 3T3-L1 adipocytes. *J Biol Chem* 265: 13801-8

Cannon B, Jacobsson A, Rehnmark S, Nedergaard J. 1996. Signal transduction in brown adipose tissue recruitment: noradrenaline and beyond. *Int J Obes Relat Metab Disord* 20 Suppl 3: S36-42

Cannon B, Nedergaard J. 2004. Brown adipose tissue: function and physiological significance. *Physiol Rev* 84: 277-359

Cannon B, Nedergaard J. 2011. Nonshivering thermogenesis and its adequate measurement in metabolic studies. *J Exp Biol* 214: 242-53

Cao X, Yang Q, Qin J, Zhao S, Li X, et al. 2012. V-ATPase promotes transforming growth factor-beta-induced epithelial-mesenchymal transition of rat proximal tubular epithelial cells. *American journal of physiology. Renal physiology* 302: F1121-32

Cao Y. 2007. Angiogenesis modulates adipogenesis and obesity. *J Clin Invest* 117: 2362-8

Carlson TR, Feng Y, Maisonpierre PC, Mrksich M, Morla AO. 2001. Direct cell adhesion to the angiopoietins mediated by integrins. *J Biol Chem* 276: 26516-25

Carmeliet P. 2003. Angiogenesis in health and disease. *Nat Med* 9: 653-60

Cascone I, Napione L, Maniero F, Serini G, Bussolino F. 2005. Stable interaction between alpha5beta1 integrin and Tie2 tyrosine kinase receptor regulates endothelial cell response to Ang-1. *J Cell Biol* 170: 993-1004

Cebollero E, van der Vaart A, Zhao M, Rieter E, Klionsky DJ, et al. 2012. Phosphatidylinositol-3-phosphate clearance plays a key role in autophagosome completion. *Curr Biol* 22: 1545-53

Cedikova M, Kripnerova M, Dvorakova J, Pitule P, Grundmanova M, et al. 2016. Mitochondria in White, Brown, and Beige Adipocytes. *Stem Cells Int* 2016: 6067349

Chakrabarti P, Kim JY, Singh M, Shin YK, Kim J, et al. 2013. Insulin inhibits lipolysis in adipocytes via the evolutionarily conserved mTORC1-Egr1-ATGL-mediated pathway. *Mol Cell Biol* 33: 3659-66

Chan CY, Parra KJ. 2014. Yeast phosphofructokinase-1 subunit Pfk2p is necessary for pH homeostasis and glucose-dependent vacuolar ATPase reassembly. *J Biol Chem* 289: 19448-57

Chang SH, Kanasaki K, Gocheva V, Blum G, Harper J, et al. 2009. VEGF-A induces angiogenesis by perturbing the cathepsin-cysteine protease inhibitor balance in venules, causing basement membrane degradation and mother vessel formation. *Cancer Res* 69: 4537-44

Chantranupong L, Scaria SM, Saxton RA, Gygi MP, Shen K, et al. 2016. The CASTOR Proteins Are Arginine Sensors for the mTORC1 Pathway. *Cell* 165: 153-64

Chau YY, Bandiera R, Serrels A, Martinez-Estrada OM, Qing W, et al. 2014. Visceral and subcutaneous fat have different origins and evidence supports a mesothelial source. *Nat Cell Biol* 16: 367-75

Chavrier P, Parton RG, Hauri HP, Simons K, Zerial M. 1990. Localization of low molecular weight GTP binding proteins to exocytic and endocytic compartments. *Cell* 62: 317-29

Chen D, Fan W, Lu Y, Ding X, Chen S, Zhong Q. 2012. A mammalian autophagosome maturation mechanism mediated by TECPR1 and the Atg12-Atg5 conjugate. *Mol Cell* 45: 629-41

Chen Q, Shou P, Zhang L, Xu C, Zheng C, et al. 2014. An osteopontin-integrin interaction plays a critical role in directing adipogenesis and osteogenesis by mesenchymal stem cells. *Stem Cells* 32: 327-37

Chen TT, Luque A, Lee S, Anderson SM, Segura T, Iruela-Arispe ML. 2010. Anchorage of VEGF to the extracellular matrix conveys differential signaling responses to endothelial cells. *J Cell Biol* 188: 595-609

Chen Z, Kennedy DJ, Wake KA, Zhuang L, Ganapathy V, Thwaites DT. 2003. Structure, tissue expression pattern, and function of the amino acid transporter rat PAT2. *Biochem Biophys Res Commun* 304: 747-54

Choi CK, Vicente-Manzanares M, Zareno J, Whitmore LA, Mogilner A, Horwitz AR. 2008. Actin and alpha-actinin orchestrate the assembly and maturation of nascent adhesions in a myosin II motor-independent manner. *Nat Cell Biol* 10: 1039-50

Christensen HN. 1966. Methods for distinguishing amino acid transport systems of a given cell or tissue. *Fed Proc* 25: 850-3

Chun TH, Sabeh F, Ota I, Murphy H, McDonagh KT, et al. 2004. MT1-MMP-dependent neovessel formation within the confines of the three-dimensional extracellular matrix. *J Cell Biol* 167: 757-67

Cinti S. 2005. The adipose organ. *Prostaglandins Leukot Essent Fatty Acids* 73: 9-15

Cinti S. 2009. Transdifferentiation properties of adipocytes in the adipose organ. *Am J Physiol Endocrinol Metab* 297: E977-86

Closs EI, Simon A, Vekony N, Rotmann A. 2004. Plasma membrane transporters for arginine. *J Nutr* 134: 2752S-59S; discussion 65S-67S

Cohen-Kaplan V, Livneh I, Avni N, Cohen-Rosenzweig C, Ciechanover A. 2016. The ubiquitin-proteasome system and autophagy: Coordinated and independent activities. *Int J Biochem Cell Biol* 79: 403-18

Cooper AJ. 1990. Ammonia metabolism in normal and portacaval-shunted rats. *Adv Exp Med Biol* 272: 23-46

Corcelle-Termeau E, Vindelov SD, Hamalisto S, Mograbi B, Keldsbo A, et al. 2016. Excess sphingomyelin disturbs ATG9A trafficking and autophagosome closure. *Autophagy* 12: 833-49

Cotter K, Stransky L, McGuire C, Forgac M. 2015. Recent Insights into the Structure, Regulation, and Function of the V-ATPases. *Trends Biochem Sci* 40: 611-22

Couchman JR. 2010. Transmembrane signaling proteoglycans. *Annu Rev Cell Dev Biol* 26: 89-114

Cousin B, Cinti S, Morroni M, Raimbault S, Ricquier D, et al. 1992. Occurrence of brown adipocytes in rat white adipose tissue: molecular and morphological characterization. *J Cell Sci* 103 (Pt 4): 931-42

Cruciat CM, Ohkawara B, Acebron SP, Karaulanov E, Reinhard C, et al. 2010. Requirement of prorenin receptor and vacuolar H+-ATPase-mediated acidification for Wnt signaling. *Science* 327: 459-63

Cui D, Xiong X, Zhao Y. 2016. Cullin-RING ligases in regulation of autophagy. *Cell Div* 11: 8

Cushman SW, Wardzala LJ. 1980. Potential mechanism of insulin action on glucose transport in the isolated rat adipose cell. Apparent translocation of intracellular transport systems to the plasma membrane. *J Biol Chem* 255: 4758-62

D'Aniello C, Fico A, Casalino L, Guardiola O, Di Napoli G, et al. 2015. A novel autoregulatory loop between the Gcn2-Atf4 pathway and (L)-Proline [corrected] metabolism controls stem cell identity. *Cell Death Differ* 22: 1094-105

Dang CV. 2011. Therapeutic targeting of Myc-reprogrammed cancer cell metabolism. *Cold Spring Harb Symp Quant Biol* 76: 369-74

Dauner K, Eid W, Raghupathy R, Presley J, Zha X. 2017. mTORC1 Activity is Required to Maintain Canonical Endocytic Recycling Pathway against Lysosomal Delivery. *J Biol Chem*

Davis GE, Bayless KJ. 2003. An integrin and Rho GTPase-dependent pinocytic vacuole mechanism controls capillary lumen formation in collagen and fibrin matrices. *Microcirculation* 10: 27-44

Davis GE, Camarillo CW. 1995. Regulation of endothelial cell morphogenesis by integrins, mechanical forces, and matrix guidance pathways. *Exp Cell Res* 216: 113-23

Davis GE, Camarillo CW. 1996. An alpha 2 beta 1 integrin-dependent pinocytic mechanism involving intracellular vacuole formation and coalescence regulates capillary lumen and tube formation in three-dimensional collagen matrix. *Exp Cell Res* 224: 39-51

Davis GE, Koh W, Stratman AN. 2007. Mechanisms controlling human endothelial lumen formation and tube assembly in three-dimensional extracellular matrices. *Birth Defects Res C Embryo Today* 81: 270-85

Davis S, Wang J, Ferro-Novick S. 2017. Crosstalk between the Secretory and Autophagy Pathways Regulates Autophagosome Formation. *Dev Cell* 41: 23-32

de Lartigue J, Polson H, Feldman M, Shokat K, Tooze SA, et al. 2009. PIKfyve regulation of endosome-linked pathways. *Traffic* 10: 883-93

De Wever O, Demetter P, Mareel M, Bracke M. 2008. Stromal myofibroblasts are drivers of invasive cancer growth. *Int J Cancer* 123: 2229-38

DeBerardinis RJ, Mancuso A, Daikhin E, Nissim I, Yudkoff M, et al. 2007. Beyond aerobic glycolysis: transformed cells can engage in glutamine metabolism that exceeds the requirement for protein and nucleotide synthesis. *Proc Natl Acad Sci U S A* 104: 19345-50
Dechant R, Binda M, Lee SS, Pelet S, Winderickx J, Peter M. 2010. Cytosolic pH is a second messenger for glucose and regulates the PKA pathway through V-ATPase. *Embo j* 29: 2515-26
Dejana E, Languino LR, Polentarutti N, Balconi G, Ryckewaert JJ, et al. 1985. Interaction between fibrinogen and cultured endothelial cells. Induction of migration and specific binding. *J Clin Invest* 75: 11-8
Dennis MD, Jefferson LS, Kimball SR. 2012. Role of p70S6K1-mediated phosphorylation of eIF4B and PDCD4 proteins in the regulation of protein synthesis. *J Biol Chem* 287: 42890-9
Deter RL, De Duve C. 1967. Influence of glucagon, an inducer of cellular autophagy, on some physical properties of rat liver lysosomes. *J Cell Biol* 33: 437-49
Diakov TT, Kane PM. 2010. Regulation of vacuolar proton-translocating ATPase activity and assembly by extracellular pH. *J Biol Chem* 285: 23771-8
Diao J, Liu R, Rong Y, Zhao M, Zhang J, et al. 2015. ATG14 promotes membrane tethering and fusion of autophagosomes to endolysosomes. *Nature* 520: 563-6
Dibble CC, Manning BD. 2013. Signal integration by mTORC1 coordinates nutrient input with biosynthetic output. *Nat Cell Biol* 15: 555-64
Dooley HC, Razi M, Polson HE, Girardin SE, Wilson MI, Tooze SA. 2014. WIPI2 links LC3 conjugation with PI3P, autophagosome formation, and pathogen clearance by recruiting Atg12-5-16L1. *Mol Cell* 55: 238-52
Dowling JJ, Gibbs E, Russell M, Goldman D, Minarcik J, et al. 2008. Kindlin-2 is an essential component of intercalated discs and is required for vertebrate cardiac structure and function. *Circ Res* 102: 423-31
Dulbecco R, Freeman G. 1959. Plaque production by the polyoma virus. *Virology* 8: 396-7
Dunlop EA, Tee AR. 2014. mTOR and autophagy: a dynamic relationship governed by nutrients and energy. *Semin Cell Dev Biol* 36: 121-9
Dupont N, Chauhan S, Arko-Mensah J, Castillo EF, Masedunskas A, et al. 2014. Neutral lipid stores and lipase PNPLA5 contribute to autophagosome biogenesis. *Curr Biol* 24: 609-20
Durbeej M. 2010. Laminins. *Cell Tissue Res* 339: 259-68
Dutta D, Donaldson JG. 2012. Search for inhibitors of endocytosis: Intended specificity and unintended consequences. *Cell Logist* 2: 203-08
Eagle H. 1955a. The minimum vitamin requirements of the L and HeLa cells in tissue culture, the production of specific vitamin deficiencies, and their cure. *J Exp Med* 102: 595-600
Eagle H. 1955b. Nutrition needs of mammalian cells in tissue culture. *Science* 122: 501-14
Eagle H. 1955c. The specific amino acid requirements of a mammalian cell (strain L) in tissue culture. *J Biol Chem* 214: 839-52
Edwards N, Anderson CM, Gatfield KM, Jevons MP, Ganapathy V, Thwaites DT. 2011. Amino acid derivatives are substrates or non-transported inhibitors of the amino acid transporter PAT2 (slc36a2). *Biochim Biophys Acta* 1808: 260-70
Efeyan A, Sabatini DM. 2010. mTOR and cancer: many loops in one pathway. *Curr Opin Cell Biol* 22: 169-76
Egginton S, Gerritsen M. 2003. Lumen formation: in vivo versus in vitro observations. *Microcirculation* 10: 45-61
Elias I, Franckhauser S, Ferre T, Vila L, Tafuro S, et al. 2012. Adipose tissue overexpression of vascular endothelial growth factor protects against diet-induced obesity and insulin resistance. *Diabetes* 61: 1801-13
Enerback S. 2009. The origins of brown adipose tissue. *N Engl J Med* 360: 2021-3
Eng CH, Yu K, Lucas J, White E, Abraham RT. 2010. Ammonia derived from glutaminolysis is a diffusible regulator of autophagy. *Sci Signal* 3: ra31
Fang F, Orend G, Watanabe N, Hunter T, Ruoslahti E. 1996. Dependence of cyclin E-CDK2 kinase activity on cell anchorage. *Science* 271: 499-502
Farmer SR. 2008. Brown fat and skeletal muscle: unlikely cousins? *Cell* 134: 726-7
Fass E, Shvets E, Degani I, Hirschberg K, Elazar Z. 2006. Microtubules support production of starvation-induced autophagosomes but not their targeting and fusion with lysosomes. *J Biol Chem* 281: 36303-16
Feng C, Li YF, Yau YH, Lee HS, Tang XY, et al. 2012. Kindlin-3 mediates integrin alphaLbeta2 outside-in signaling, and it interacts with scaffold protein receptor for activated-C kinase 1 (RACK1). *J Biol Chem* 287: 10714-26
Feng Y, Forgac M. 1992a. Cysteine 254 of the 73-kDa A subunit is responsible for inhibition of the coated vesicle (H+)-ATPase upon modification by sulfhydryl reagents. *J Biol Chem* 267: 5817-22
Feng Y, Forgac M. 1992b. A novel mechanism for regulation of vacuolar acidification. *J Biol Chem* 267: 19769-72

Feng Y, Forgac M. 1994. Inhibition of vacuolar H(+)-ATPase by disulfide bond formation between cysteine 254 and cysteine 532 in subunit A. *J Biol Chem* 269: 13224-30
Finley D. 2009. Recognition and processing of ubiquitin-protein conjugates by the proteasome. *Annu Rev Biochem* 78: 477-513
Finnigan GC, Cronan GE, Park HJ, Srinivasan S, Quiocho FA, Stevens TH. 2012. Sorting of the yeast vacuolar-type, proton-translocating ATPase enzyme complex (V-ATPase): identification of a necessary and sufficient Golgi/endosomal retention signal in Stv1p. *J Biol Chem* 287: 19487-500
Fischer B, Dimopoulou A, Egerer J, Gardeitchik T, Kidd A, et al. 2012. Further characterization of ATP6V0A2-related autosomal recessive cutis laxa. *Hum Genet* 131: 1761-73
Folkman J, Haudenschild C. 1980. Angiogenesis in vitro. *Nature* 288: 551-6
Foltz M, Boll M, Raschka L, Kottra G, Daniel H. 2004a. A novel bifunctionality: PAT1 and PAT2 mediate electrogenic proton/amino acid and electroneutral proton/fatty acid symport. *FASEB J* 18: 1758-60
Foltz M, Oechsler C, Boll M, Kottra G, Daniel H. 2004b. Substrate specificity and transport mode of the proton-dependent amino acid transporter mPAT2. *Eur J Biochem* 271: 3340-7
Forgac M. 1999. Structure and properties of the vacuolar (H+)-ATPases. *J Biol Chem* 274: 12951-4
Forgac M. 2007. Vacuolar ATPases: rotary proton pumps in physiology and pathophysiology. *Nat Rev Mol Cell Biol* 8: 917-29
Fouser L, Iruela-Arispe L, Bornstein P, Sage EH. 1991. Transcriptional activity of the alpha 1(I)-collagen promoter is correlated with the formation of capillary-like structures by endothelial cells in vitro. *J Biol Chem* 266: 18345-51
Francis SE, Goh KL, Hodivala-Dilke K, Bader BL, Stark M, et al. 2002. Central roles of alpha5beta1 integrin and fibronectin in vascular development in mouse embryos and embryoid bodies. *Arterioscler Thromb Vasc Biol* 22: 927-33
Frantz C, Stewart KM, Weaver VM. 2010. The extracellular matrix at a glance. *J Cell Sci* 123: 4195-200
Fredriksson R, Nordstrom KJ, Stephansson O, Hagglund MG, Schioth HB. 2008. The solute carrier (SLC) complement of the human genome: phylogenetic classification reveals four major families. *FEBS Lett* 582: 3811-6
Gaccioli F, Huang CC, Wang C, Bevilacqua E, Franchi-Gazzola R, et al. 2006. Amino acid starvation induces the SNAT2 neutral amino acid transporter by a mechanism that involves eukaryotic initiation factor 2alpha phosphorylation and cap-independent translation. *J Biol Chem* 281: 17929-40
Galluzzi L, Baehrecke EH, Ballabio A, Boya P, Bravo-San Pedro JM, et al. 2017. Molecular definitions of autophagy and related processes. *EMBO J* 36: 1811-36
Gao C, Cao W, Bao L, Zuo W, Xie G, et al. 2010. Autophagy negatively regulates Wnt signalling by promoting Dishevelled degradation. *Nat Cell Biol* 12: 781-90
Gao H, Guo Y, Yan Q, Yang W, Li R, et al. 2019. Lipoatrophy and metabolic disturbance in mice with adipose-specific deletion of kindlin-2. *JCI Insight* 4
Gao P, Tchernyshyov I, Chang TC, Lee YS, Kita K, et al. 2009. c-Myc suppression of miR-23a/b enhances mitochondrial glutaminase expression and glutamine metabolism. *Nature* 458: 762-5
Gatica D, Lahiri V, Klionsky DJ. 2018. Cargo recognition and degradation by selective autophagy. *Nat Cell Biol* 20: 233-42
Ge D, Han L, Huang S, Peng N, Wang P, et al. 2014. Identification of a novel MTOR activator and discovery of a competing endogenous RNA regulating autophagy in vascular endothelial cells. *Autophagy* 10: 957-71
Ge L, Melville D, Zhang M, Schekman R. 2013. The ER-Golgi intermediate compartment is a key membrane source for the LC3 lipidation step of autophagosome biogenesis. *Elife* 2: e00947
Geiger B, Bershadsky A, Pankov R, Yamada KM. 2001. Transmembrane crosstalk between the extracellular matrix--cytoskeleton crosstalk. *Nat Rev Mol Cell Biol* 2: 793-805
George EL, Baldwin HS, Hynes RO. 1997. Fibronectins are essential for heart and blood vessel morphogenesis but are dispensable for initial specification of precursor cells. *Blood* 90: 3073-81
George EL, Georges-Labouesse EN, Patel-King RS, Rayburn H, Hynes RO. 1993. Defects in mesoderm, neural tube and vascular development in mouse embryos lacking fibronectin. *Development* 119: 1079-91
Gerhardt H, Golding M, Fruttiger M, Ruhrberg C, Lundkvist A, et al. 2003. VEGF guides angiogenic sprouting utilizing endothelial tip cell filopodia. *J Cell Biol* 161: 1163-77
Gesta S, Tseng YH, Kahn CR. 2007. Developmental origin of fat: tracking obesity to its source. *Cell* 131: 242-56
Giancotti FG, Ruoslahti E. 1999. Integrin signaling. *Science* 285: 1028-32
Ginsberg MH, Partridge A, Shattil SJ. 2005. Integrin regulation. *Curr Opin Cell Biol* 17: 509-16

Giralt M, Villarroya F. 2013. White, brown, beige/brite: different adipose cells for different functions? *Endocrinology* 154: 2992-3000
Glick D, Barth S, Macleod KF. 2010. Autophagy: cellular and molecular mechanisms. *J Pathol* 221: 3-12
Glickman MH, Ciechanover A. 2002. The ubiquitin-proteasome proteolytic pathway: destruction for the sake of construction. *Physiol Rev* 82: 373-428
Goberdhan DC, Meredith D, Boyd CA, Wilson C. 2005a. PAT-related amino acid transporters regulate growth via a novel mechanism that does not require bulk transport of amino acids. *Development* 132: 2365-75
Goberdhan DC, Wilson C, Harris AL. 2016. Amino Acid Sensing by mTORC1: Intracellular Transporters Mark the Spot. *Cell Metab* 23: 580-9
Goberdhan DCI, Meredith D, Boyd CAR, Wilson C. 2005b. PAT-related amino acid transporters regulate growth via a novel mechanism that does not require bulk transport of amino acids. *Development* 132: 2365-75
Goldberg AL, Cascio P, Saric T, Rock KL. 2002. The importance of the proteasome and subsequent proteolytic steps in the generation of antigenic peptides. *Mol Immunol* 39: 147-64
Golozoubova V, Hohtola E, Matthias A, Jacobsson A, Cannon B, Nedergaard J. 2001. Only UCP1 can mediate adaptive nonshivering thermogenesis in the cold. *FASEB J* 15: 2048-50
Gomes LC, Di Benedetto G, Scorrano L. 2011. During autophagy mitochondria elongate, are spared from degradation and sustain cell viability. *Nat Cell Biol* 13: 589-98
Gordon PB, Seglen PO. 1988. Prelysosomal convergence of autophagic and endocytic pathways. *Biochem Biophys Res Commun* 151: 40-7
Gozgit JM, Pentecost BT, Marconi SA, Otis CN, Wu C, Arcaro KF. 2006. Use of an aggressive MCF-7 cell line variant, TMX2-28, to study cell invasion in breast cancer. *Mol Cancer Res* 4: 905-13
Grant DS, Kleinman HK. 1997. Regulation of capillary formation by laminin and other components of the extracellular matrix. *EXS* 79: 317-33
Guo B, Liang Q, Li L, Hu Z, Wu F, et al. 2014. O-GlcNAc-modification of SNAP-29 regulates autophagosome maturation. *Nat Cell Biol* 16: 1215-26
Gutierrez MG, Munafo DB, Beron W, Colombo MI. 2004. Rab7 is required for the normal progression of the autophagic pathway in mammalian cells. *J Cell Sci* 117: 2687-97
Hailey DW, Rambold AS, Satpute-Krishnan P, Mitra K, Sougrat R, et al. 2010. Mitochondria supply membranes for autophagosome biogenesis during starvation. *Cell* 141: 656-67
Hall KD, Sacks G, Chandramohan D, Chow CC, Wang YC, et al. 2011. Quantification of the effect of energy imbalance on bodyweight. *The Lancet* 378: 826-37
Hallmann R, Horn N, Selg M, Wendler O, Pausch F, Sorokin LM. 2005. Expression and function of laminins in the embryonic and mature vasculature. *Physiol Rev* 85: 979-1000
Hamasaki M, Furuta N, Matsuda A, Nezu A, Yamamoto A, et al. 2013. Autophagosomes form at ER-mitochondria contact sites. *Nature* 495: 389-93
Han J, Back SH, Hur J, Lin YH, Gildersleeve R, et al. 2013. ER-stress-induced transcriptional regulation increases protein synthesis leading to cell death. *Nat Cell Biol* 15: 481-90
Han J, Lee JE, Jin J, Lim JS, Oh N, et al. 2011. The spatiotemporal development of adipose tissue. *Development* 138: 5027-37
Han JM, Jeong SJ, Park MC, Kim G, Kwon NH, et al. 2012. Leucyl-tRNA synthetase is an intracellular leucine sensor for the mTORC1-signaling pathway. *Cell* 149: 410-24
Hancock CR, Han DH, Chen M, Terada S, Yasuda T, et al. 2008. High-fat diets cause insulin resistance despite an increase in muscle mitochondria. *Proc Natl Acad Sci U S A* 105: 7815-20
Hara K, Yonezawa K, Weng QP, Kozlowski MT, Belham C, Avruch J. 1998. Amino acid sufficiency and mTOR regulate p70 S6 kinase and eIF-4E BP1 through a common effector mechanism. *J Biol Chem* 273: 14484-94
Harburger DS, Bouaouina M, Calderwood DA. 2009. Kindlin-1 and -2 directly bind the C-terminal region of beta integrin cytoplasmic tails and exert integrin-specific activation effects. *J Biol Chem* 284: 11485-97
Harper AE, Miller RH, Block KP. 1984. Branched-chain amino acid metabolism. *Annu Rev Nutr* 4: 409-54
Hascall VC, Majors AK, De La Motte CA, Evanko SP, Wang A, et al. 2004. Intracellular hyaluronan: a new frontier for inflammation? *Biochim Biophys Acta* 1673: 3-12
Hatzoglou M, Fernandez J, Yaman I, Closs E. 2004. Regulation of cationic amino acid transport: the story of the CAT-1 transporter. *Annu Rev Nutr* 24: 377-99
Hayashi K, Madri JA, Yurchenco PD. 1992. Endothelial cells interact with the core protein of basement membrane perlecan through beta 1 and beta 3 integrins: an adhesion modulated by glycosaminoglycan. *J Cell Biol* 119: 945-59

He Y, Esser P, Schacht V, Bruckner-Tuderman L, Has C. 2011. Role of kindlin-2 in fibroblast functions: implications for wound healing. *J Invest Dermatol* 131: 245-56
Hediger MA, Clemencon B, Burrier RE, Bruford EA. 2013. The ABCs of membrane transporters in health and disease (SLC series): introduction. *Mol Aspects Med* 34: 95-107
Hegedus K, Takats S, Boda A, Jipa A, Nagy P, et al. 2016. The Ccz1-Mon1-Rab7 module and Rab5 control distinct steps of autophagy. *Mol Biol Cell* 27: 3132-42
Heldin P, Pertoft H. 1993. Synthesis and assembly of the hyaluronan-containing coats around normal human mesothelial cells. *Exp Cell Res* 208: 422-9
Heublein S, Kazi S, Ogmundsdottir MH, Attwood EV, Kala S, et al. 2010. Proton-assisted amino-acid transporters are conserved regulators of proliferation and amino-acid-dependent mTORC1 activation. *Oncogene* 29: 4068-79
Heuser J. 1989. Changes in lysosome shape and distribution correlated with changes in cytoplasmic pH. *J Cell Biol* 108: 855-64
Himms-Hagen J. 1989. Role of thermogenesis in the regulation of energy balance in relation to obesity. *Can J Physiol Pharmacol* 67: 394-401
Himms-Hagen J, Melnyk A, Zingaretti MC, Ceresi E, Barbatelli G, Cinti S. 2000. Multilocular fat cells in WAT of CL-316243-treated rats derive directly from white adipocytes. *Am J Physiol Cell Physiol* 279: C670-81
Hinnebusch AG. 1994. The eIF-2 alpha kinases: regulators of protein synthesis in starvation and stress. *Semin Cell Biol* 5: 417-26
Hinnebusch AG, Ivanov IP, Sonenberg N. 2016. Translational control by 5'-untranslated regions of eukaryotic mRNAs. *Science* 352: 1413-6
Ho A, Cho CS, Namkoong S, Cho US, Lee JH. 2016. Biochemical Basis of Sestrin Physiological Activities. *Trends Biochem Sci* 41: 621-32
Hoffmann EK, Lambert IH. 1983. Amino acid transport and cell volume regulation in Ehrlich ascites tumour cells. *J Physiol* 338: 613-25
Holliday LS. 2014. Vacuolar H+-ATPase: An Essential Multitasking Enzyme in Physiology and Pathophysiology. *New Journal of Science*
Honda S, Shirotani-Ikejima H, Tadokoro S, Tomiyama Y, Miyata T. 2013. The integrin-linked kinase-PINCH-parvin complex supports integrin alphaIIbbeta3 activation. *PLoS One* 8: e85498
Hondares E, Rosell M, Diaz-Delfin J, Olmos Y, Monsalve M, et al. 2011. Peroxisome proliferator-activated receptor alpha (PPARalpha) induces PPARgamma coactivator 1alpha (PGC-1alpha) gene expression and contributes to thermogenic activation of brown fat: involvement of PRDM16. *J Biol Chem* 286: 43112-22
Honek J, Lim S, Fischer C, Iwamoto H, Seki T, Cao Y. 2014. Brown adipose tissue, thermogenesis, angiogenesis: pathophysiological aspects. *Horm Mol Biol Clin Investig* 19: 5-11
Horton ER, Byron A, Askari JA, Ng DHJ, Millon-Fremillon A, et al. 2015. Definition of a consensus integrin adhesome and its dynamics during adhesion complex assembly and disassembly. *Nat Cell Biol* 17: 1577-87
Hosokawa N, Hara T, Kaizuka T, Kishi C, Takamura A, et al. 2009. Nutrient-dependent mTORC1 association with the ULK1-Atg13-FIP200 complex required for autophagy. *Mol Biol Cell* 20: 1981-91
Hu P, Luo BH. 2013. Integrin bi-directional signaling across the plasma membrane. *J Cell Physiol* 228: 306-12
Humphries JD, Byron A, Humphries MJ. 2006. Integrin ligands at a glance. *J Cell Sci* 119: 3901-3
Hung YH, Chen LM, Yang JY, Yang WY. 2013. Spatiotemporally controlled induction of autophagy-mediated lysosome turnover. *Nat Commun* 4: 2111
Hutagalung AH, Novick PJ. 2011. Role of Rab GTPases in membrane traffic and cell physiology. *Physiol Rev* 91: 119-49
Hutchins MU, Veenhuis M, Klionsky DJ. 1999. Peroxisome degradation in Saccharomyces cerevisiae is dependent on machinery of macroautophagy and the Cvt pathway. *J Cell Sci* 112 (Pt 22): 4079-87
Hutson SM, Sweatt AJ, Lanoue KF. 2005. Branched-chain [corrected] amino acid metabolism: implications for establishing safe intakes. *J Nutr* 135: 1557s-64s
Hynes RO. 2002. Integrins: bidirectional, allosteric signaling machines. *Cell* 110: 673-87
Hynes RO. 2009. The extracellular matrix: not just pretty fibrils. *Science* 326: 1216-9
Ichihara A. 2012. (Pro)renin receptor and vacuolar H(+)-ATPase. *The Keio journal of medicine* 61: 73-8
Ikeda K, Maretich P, Kajimura S. 2018. The Common and Distinct Features of Brown and Beige Adipocytes. *Trends Endocrinol Metab* 29: 191-200

Ilan N, Mahooti S, Madri JA. 1998. Distinct signal transduction pathways are utilized during the tube formation and survival phases of in vitro angiogenesis. *J Cell Sci* 111 (Pt 24): 3621-31
Ingber D, Folkman J. 1988. Inhibition of angiogenesis through modulation of collagen metabolism. *Lab Invest* 59: 44-51
Inoki K, Zhu T, Guan KL. 2003. TSC2 mediates cellular energy response to control cell growth and survival. *Cell* 115: 577-90
Iorio V, Troughton LD, Hamill KJ. 2015. Laminins: Roles and Utility in Wound Repair. *Adv Wound Care (New Rochelle)* 4: 250-63
Iozzo RV, Schaefer L. 2015. Proteoglycan form and function: A comprehensive nomenclature of proteoglycans. *Matrix Biol* 42: 11-55
Iruela-Arispe ML, Davis GE. 2009. Cellular and molecular mechanisms of vascular lumen formation. *Dev Cell* 16: 222-31
Iruela-Arispe ML, Diglio CA, Sage EH. 1991. Modulation of extracellular matrix proteins by endothelial cells undergoing angiogenesis in vitro. *Arterioscler Thromb* 11: 805-15
Ishibashi J, Seale P. 2010. Medicine. Beige can be slimming. *Science* 328: 1113-4
Itakura E, Kishi-Itakura C, Mizushima N. 2012. The hairpin-type tail-anchored SNARE syntaxin 17 targets to autophagosomes for fusion with endosomes/lysosomes. *Cell* 151: 1256-69
Itoh T, Kanno E, Uemura T, Waguri S, Fukuda M. 2011. OATL1, a novel autophagosome-resident Rab33B-GAP, regulates autophagosomal maturation. *J Cell Biol* 192: 839-53
Jahreiss L, Menzies FM, Rubinsztein DC. 2008. The itinerary of autophagosomes: from peripheral formation to kiss-and-run fusion with lysosomes. *Traffic* 9: 574-87
Jaiswal MK, Agrawal V, Katara GK, Pamarthy S, Kulshrestha A, et al. 2015. Male fertility and apoptosis in normal spermatogenesis are regulated by vacuolar-ATPase isoform a2. *Journal of reproductive immunology* 112: 38-45
Jarvelainen H, Sainio A, Koulu M, Wight TN, Penttinen R. 2009. Extracellular matrix molecules: potential targets in pharmacotherapy. *Pharmacol Rev* 61: 198-223
Jewell JL, Kim YC, Russell RC, Yu FX, Park HW, et al. 2015. Metabolism. Differential regulation of mTORC1 by leucine and glutamine. *Science* 347: 194-8
Jewell JL, Russell RC, Guan KL. 2013. Amino acid signalling upstream of mTOR. *Nat Rev Mol Cell Biol* 14: 133-9
Jiang Y, Berry DC, Tang W, Graff JM. 2014. Independent stem cell lineages regulate adipose organogenesis and adipose homeostasis. *Cell Rep* 9: 1007-22
Jiménez G L-RE, Griñán-Lisón C, Antich C, Marchal J.A. 2016. Brown Adipose Tissue and Obesity In *Obesity*, ed. A S., I S., pp. 13-28. Cham: Springer
Jin M, Liu X, Klionsky DJ. 2013. SnapShot: Selective autophagy. *Cell* 152: 368-68 e2
Jobard F, Bouadjar B, Caux F, Hadj-Rabia S, Has C, et al. 2003. Identification of mutations in a new gene encoding a FERM family protein with a pleckstrin homology domain in Kindler syndrome. *Hum Mol Genet* 12: 925-35
Jung J, Genau HM, Behrends C. 2015. Amino Acid-Dependent mTORC1 Regulation by the Lysosomal Membrane Protein SLC38A9. *Mol Cell Biol* 35: 2479-94
Jung YS, Jun S, Kim MJ, Lee SH, Suh HN, et al. 2018. TMEM9 promotes intestinal tumorigenesis through vacuolar-ATPase-activated Wnt/beta-catenin signalling. *Nat Cell Biol* 20: 1421-33
Kajimura S, Seale P, Kubota K, Lunsford E, Frangioni JV, et al. 2009. Initiation of myoblast to brown fat switch by a PRDM16-C/EBP-beta transcriptional complex. *Nature* 460: 1154-8
Kamei M, Saunders WB, Bayless KJ, Dye L, Davis GE, Weinstein BM. 2006. Endothelial tubes assemble from intracellular vacuoles in vivo. *Nature* 442: 453-6
Kanai Y, Segawa H, Miyamoto K, Uchino H, Takeda E, Endou H. 1998. Expression cloning and characterization of a transporter for large neutral amino acids activated by the heavy chain of 4F2 antigen (CD98). *J Biol Chem* 273: 23629-32
Kane PM. 2012. Targeting reversible disassembly as a mechanism of controlling V-ATPase activity. *Curr Protein Pept Sci* 13: 117-23
Kanematsu A, Yamamoto S, Ozeki M, Noguchi T, Kanatani I, et al. 2004. Collagenous matrices as release carriers of exogenous growth factors. *Biomaterials* 25: 4513-20
Karanasios E, Walker SA, Okkenhaug H, Manifava M, Hummel E, et al. 2016. Autophagy initiation by ULK complex assembly on ER tubulovesicular regions marked by ATG9 vesicles. *Nat Commun* 7: 12420
Karet FE. 2005. Physiological and metabolic implications of V-ATPase isoforms in the kidney. *Journal of bioenergetics and biomembranes* 37: 425-9

Kartner N, Manolson MF. 2014. Novel techniques in the development of osteoporosis drug therapy: the osteoclast ruffled-border vacuolar H(+)-ATPase as an emerging target. *Expert opinion on drug discovery* 9: 505-22
Kato K, Shiozawa T, Mitsushita J, Toda A, Horiuchi A, et al. 2004. Expression of the mitogen-inducible gene-2 (mig-2) is elevated in human uterine leiomyomas but not in leiomyosarcomas. *Hum Pathol* 35: 55-60
Kaushik S, Bandyopadhyay U, Sridhar S, Kiffin R, Martinez-Vicente M, et al. 2011. Chaperone-mediated autophagy at a glance. *J Cell Sci* 124: 495-9
Kavanaugh MP. 1993. Voltage dependence of facilitated arginine flux mediated by the system y+ basic amino acid transporter. *Biochemistry* 32: 5781-5
Kawai A, Uchiyama H, Takano S, Nakamura N, Ohkuma S. 2007. Autophagosome-lysosome fusion depends on the pH in acidic compartments in CHO cells. *Autophagy* 3: 154-7
Kennedy DJ, Gatfield KM, Winpenny JP, Ganapathy V, Thwaites DT. 2005. Substrate specificity and functional characterisation of the H+/amino acid transporter rat PAT2 (Slc36a2). *British journal of pharmacology* 144: 28-41
Kershaw EE, Flier JS. 2004. Adipose tissue as an endocrine organ. *J Clin Endocrinol Metab* 89: 2548-56
Khunweeraphong N, Nagamori S, Wiriyasermkul P, Nishinaka Y, Wongthai P, et al. 2012. Establishment of stable cell lines with high expression of heterodimers of human 4F2hc and human amino acid transporter LAT1 or LAT2 and delineation of their differential interaction with alpha-alkyl moieties. *J Pharmacol Sci* 119: 368-80
Kilberg MS, Balasubramanian M, Fu L, Shan J. 2012. The transcription factor network associated with the amino acid response in mammalian cells. *Adv Nutr* 3: 295-306
Kilberg MS, Shan J, Su N. 2009. ATF4-dependent transcription mediates signaling of amino acid limitation. *Trends Endocrinol Metab* 20: 436-43
Kilberg MS, Terada N, Shan J. 2016. Influence of Amino Acid Metabolism on Embryonic Stem Cell Function and Differentiation. *Adv Nutr* 7: 780S-9S
Kim J, Kundu M, Viollet B, Guan KL. 2011. AMPK and mTOR regulate autophagy through direct phosphorylation of Ulk1. *Nat Cell Biol* 13: 132-41
Kim YC, Guan KL. 2015. mTOR: a pharmacologic target for autophagy regulation. *J Clin Invest* 125: 25-32
Kimball SR. 2001. Regulation of translation initiation by amino acids in eukaryotic cells. *Prog Mol Subcell Biol* 26: 155-84
Kimball SR, Gordon BS, Moyer JE, Dennis MD, Jefferson LS. 2016. Leucine induced dephosphorylation of Sestrin2 promotes mTORC1 activation. *Cellular signalling* 28: 896-906
Kimball SR, Jefferson LS. 2005. Role of amino acids in the translational control of protein synthesis in mammals. *Semin Cell Dev Biol* 16: 21-7
Kimball SR, Jefferson LS. 2010. Control of translation initiation through integration of signals generated by hormones, nutrients, and exercise. *J Biol Chem* 285: 29027-32
Kimura N, Tokunaga C, Dalal S, Richardson C, Yoshino K, et al. 2003. A possible linkage between AMP-activated protein kinase (AMPK) and mammalian target of rapamycin (mTOR) signalling pathway. *Genes to cells : devoted to molecular & cellular mechanisms* 8: 65-79
Kimura S, Noda T, Yoshimori T. 2008. Dynein-dependent movement of autophagosomes mediates efficient encounters with lysosomes. *Cell Struct Funct* 33: 109-22
Kinashi T. 2005. Intracellular signalling controlling integrin activation in lymphocytes. *Nat Rev Immunol* 5: 546-59
Kirkin V, McEwan DG, Novak I, Dikic I. 2009. A role for ubiquitin in selective autophagy. *Mol Cell* 34: 259-69
Kissing S, Hermsen C, Repnik U, Nesset CK, von Bargen K, et al. 2015. Vacuolar ATPase in phagosome-lysosome fusion. *J Biol Chem* 290: 14166-80
Klein C, Scoggin KE, Ealy AD, Troedsson MH. 2010. Transcriptional profiling of equine endometrium during the time of maternal recognition of pregnancy. *Biol Reprod* 83: 102-13
Klionsky DJ, Abdelmohsen K, Abe A, Abedin MJ, Abeliovich H, et al. 2016. Guidelines for the use and interpretation of assays for monitoring autophagy (3rd edition). *Autophagy* 12: 1-222
Klionsky DJ, Eskelinen EL, Deretic V. 2014. Autophagosomes, phagosomes, autolysosomes, phagolysosomes, autophagolysosomes... wait, I'm confused. *Autophagy* 10: 549-51
Knudson CB, Knudson W. 1993. Hyaluronan-binding proteins in development, tissue homeostasis, and disease. *FASEB J* 7: 1233-41
Koh W, Stratman AN, Sacharidou A, Davis GE. 2008. In vitro three dimensional collagen matrix models of endothelial lumen formation during vasculogenesis and angiogenesis. *Methods Enzymol* 443: 83-101

Krall AS, Xu S, Graeber TG, Braas D, Christofk HR. 2016. Asparagine promotes cancer cell proliferation through use as an amino acid exchange factor. *Nat Commun* 7: 11457
Kroemer G, Levine B. 2008. Autophagic cell death: the story of a misnomer. *Nat Rev Mol Cell Biol* 9: 1004-10
Kuijpers TW, van de Vijver E, Weterman MA, de Boer M, Tool AT, et al. 2009. LAD-1/variant syndrome is caused by mutations in FERMT3. *Blood* 113: 4740-6
Kumanomidou T, Mizushima T, Komatsu M, Suzuki A, Tanida I, et al. 2006. The crystal structure of human Atg4b, a processing and de-conjugating enzyme for autophagosome-forming modifiers. *J Mol Biol* 355: 612-8
Lafourcade C, Sobo K, Kieffer-Jaquinod S, Garin J, van der Goot FG. 2008. Regulation of the V-ATPase along the endocytic pathway occurs through reversible subunit association and membrane localization. *PLoS One* 3: e2758
Lamb CA, Nuhlen S, Judith D, Frith D, Snijders AP, et al. 2016. TBC1D14 regulates autophagy via the TRAPP complex and ATG9 traffic. *Embo j* 35: 281-301
Lange C, Prenninger S, Knuckles P, Taylor V, Levin M, Calegari F. 2011. The H(+) vacuolar ATPase maintains neural stem cells in the developing mouse cortex. *Stem Cells Dev* 20: 843-50
Laplante M, Sabatini DM. 2012. mTOR signaling in growth control and disease. *Cell* 149: 274-93
Larjava H, Plow EF, Wu C. 2008. Kindlins: essential regulators of integrin signalling and cell-matrix adhesion. *EMBO Rep* 9: 1203-8
Laurent TC, Fraser JR. 1992. Hyaluronan. *FASEB J* 6: 2397-404
Leaf DS, Blum LD. 1998. Analysis of rab10 localization in sea urchin embryonic cells by three-dimensional reconstruction. *Exp Cell Res* 243: 39-49
Lee IH, Cao L, Mostoslavsky R, Lombard DB, Liu J, et al. 2008. A role for the NAD-dependent deacetylase Sirt1 in the regulation of autophagy. *Proc Natl Acad Sci U S A* 105: 3374-9
Lee JH, Cho US, Karin M. 2016a. Sestrin regulation of TORC1: Is Sestrin a leucine sensor? *Sci Signal* 9: re5
Lee JH, Yu WH, Kumar A, Lee S, Mohan PS, et al. 2010. Lysosomal proteolysis and autophagy require presenilin 1 and are disrupted by Alzheimer-related PS1 mutations. *Cell* 141: 1146-58
Lee M, Kim JH, Yoon I, Lee C, Fallahi Sichani M, et al. 2018. Coordination of the leucine-sensing Rag GTPase cycle by leucyl-tRNA synthetase in the mTORC1 signaling pathway. *Proc Natl Acad Sci U S A* 115: E5279-E88
Lee PL, Tang Y, Li H, Guertin DA. 2016b. Raptor/mTORC1 loss in adipocytes causes progressive lipodystrophy and fatty liver disease. *Mol Metab* 5: 422-32
Lee YH, Petkova AP, Mottillo EP, Granneman JG. 2012. In vivo identification of bipotential adipocyte progenitors recruited by beta3-adrenoceptor activation and high-fat feeding. *Cell Metab* 15: 480-91
Legate KR, Wickstrom SA, Fassler R. 2009. Genetic and cell biological analysis of integrin outside-in signaling. *Genes Dev* 23: 397-418
Leitinger B. 2011. Transmembrane collagen receptors. *Annu Rev Cell Dev Biol* 27: 265-90
Lemus L, Goder V. 2016. A SNARE and specific COPII requirements define ER-derived vesicles for the biogenesis of autophagosomes. *Autophagy* 12: 1049-50
Li Y, Erickson JW, Stalnecker CA, Katt WP, Huang Q, et al. 2016. Mechanistic Basis of Glutaminase Activation: A KEY ENZYME THAT PROMOTES GLUTAMINE METABOLISM IN CANCER CELLS. *J Biol Chem* 291: 20900-10
Li Y, Li L, Brown TJ, Heldin P. 2007. Silencing of hyaluronan synthase 2 suppresses the malignant phenotype of invasive breast cancer cells. *Int J Cancer* 120: 2557-67
Lim S, Honek J, Xue Y, Seki T, Cao Z, et al. 2012. Cold-induced activation of brown adipose tissue and adipose angiogenesis in mice. *Nat Protoc* 7: 606-15
Lin M, Li SC, Kane PM, Hofken T. 2012. Regulation of vacuolar H+-ATPase activity by the Cdc42 effector Ste20 in Saccharomyces cerevisiae. *Eukaryotic cell* 11: 442-51
Liu J, DeYoung SM, Zhang M, Zhang M, Cheng A, Saltiel AR. 2005. Changes in integrin expression during adipocyte differentiation. *Cell Metab* 2: 165-77
Liu J, Fukuda K, Xu Z, Ma YQ, Hirbawi J, et al. 2011. Structural basis of phosphoinositide binding to kindlin-2 protein pleckstrin homology domain in regulating integrin activation. *J Biol Chem* 286: 43334-42
Liu Y, Senger DR. 2004. Matrix-specific activation of Src and Rho initiates capillary morphogenesis of endothelial cells. *FASEB J* 18: 457-68
Liu Y, Zhu Y, Ye S, Zhang R. 2012. Crystal structure of kindlin-2 PH domain reveals a conformational transition for its membrane anchoring and regulation of integrin activation. *Protein Cell* 3: 434-40

Lopez-Soriano FJ, Alemany M. 1986. Activities of enzymes of amino acid metabolism in rat brown adipose tissue. *Biochem Int* 12: 471-8
Lopez-Soriano FJ, Alemany M. 1987. Effect of cold-temperature exposure and acclimation on amino acid pool changes and enzyme activities of rat brown adipose tissue. *Biochim Biophys Acta* 925: 265-71
Lowell BB, V SS, Hamann A, Lawitts JA, Himms-Hagen J, et al. 1993. Development of obesity in transgenic mice after genetic ablation of brown adipose tissue. *Nature* 366: 740-2
Lu G, Sun H, She P, Youn JY, Warburton S, et al. 2009. Protein phosphatase 2Cm is a critical regulator of branched-chain amino acid catabolism in mice and cultured cells. *J Clin Invest* 119: 1678-87
Lu M, Ammar D, Ives H, Albrecht F, Gluck SL. 2007. Physical interaction between aldolase and vacuolar H+-ATPase is essential for the assembly and activity of the proton pump. *J Biol Chem* 282: 24495-503
Lubarsky B, Krasnow MA. 2003. Tube morphogenesis: making and shaping biological tubes. *Cell* 112: 19-28
Luo BH, Carman CV, Springer TA. 2007. Structural basis of integrin regulation and signaling. *Annu Rev Immunol* 25: 619-47
Lurick A, Gao J, Kuhlee A, Yavavli E, Langemeyer L, et al. 2017. Multivalent Rab interactions determine tether-mediated membrane fusion. *Mol Biol Cell* 28: 322-32
Ma YQ, Qin J, Wu C, Plow EF. 2008. Kindlin-2 (Mig-2): a co-activator of beta3 integrins. *J Cell Biol* 181: 439-46
Mack HI, Zheng B, Asara JM, Thomas SM. 2012. AMPK-dependent phosphorylation of ULK1 regulates ATG9 localization. *Autophagy* 8: 1197-214
Malinin NL, Plow EF, Byzova TV. 2010. Kindlins in FERM adhesion. *Blood* 115: 4011-7
Margosio B, Marchetti D, Vergani V, Giavazzi R, Rusnati M, et al. 2003. Thrombospondin 1 as a scavenger for matrix-associated fibroblast growth factor 2. *Blood* 102: 4399-406
Mari M, Griffith J, Rieter E, Krishnappa L, Klionsky DJ, Reggiori F. 2010. An Atg9-containing compartment that functions in the early steps of autophagosome biogenesis. *J Cell Biol* 190: 1005-22
Marjuki H, Gornitzky A, Marathe BM, Ilyushina NA, Aldridge JR, et al. 2011. Influenza A virus-induced early activation of ERK and PI3K mediates V-ATPase-dependent intracellular pH change required for fusion. *Cellular microbiology* 13: 587-601
Marshansky V, Futai M. 2008. The V-type H+-ATPase in vesicular trafficking: targeting, regulation and function. *Curr Opin Cell Biol* 20: 415-26
Marshansky V, Rubinstein JL, Gruber G. 2014. Eukaryotic V-ATPase: novel structural findings and functional insights. *Biochim Biophys Acta* 1837: 857-79
Mas-Vidal A, Minones-Suarez L, Toral JF, Mallo S, Perez-Oliva N. 2010. A novel mutation in the FERMT1 gene in a Spanish family with Kindler's syndrome. *J Eur Acad Dermatol Venereol* 24: 978-9
Mastroberardino L, Spindler B, Pfeiffer R, Skelly PJ, Loffing J, et al. 1998. Amino-acid transport by heterodimers of 4F2hc/CD98 and members of a permease family. *Nature* 395: 288-91
Matthias A, Ohlson KB, Fredriksson JM, Jacobsson A, Nedergaard J, Cannon B. 2000. Thermogenic responses in brown fat cells are fully UCP1-dependent. UCP2 or UCP3 do not substitute for UCP1 in adrenergically or fatty scid-induced thermogenesis. *J Biol Chem* 275: 25073-81
Mattson MP. 2010. Perspective: Does brown fat protect against diseases of aging? *Ageing Res Rev* 9: 69-76
Mauro VP, Chappell SA. 2014. A critical analysis of codon optimization in human therapeutics. *Trends Mol Med* 20: 604-13
Mauvezin C, Nagy P, Juhasz G, Neufeld TP. 2015. Autophagosome-lysosome fusion is independent of V-ATPase-mediated acidification. *Nat Commun* 6: 7007
Mauvezin C, Neufeld TP. 2015. Bafilomycin A1 disrupts autophagic flux by inhibiting both V-ATPase-dependent acidification and Ca-P60A/SERCA-dependent autophagosome-lysosome fusion. *Autophagy* 11: 1437-8
Maxfield FR, McGraw TE. 2004. Endocytic recycling. *Nat Rev Mol Cell Biol* 5: 121-32
McConnell M, Feng S, Chen W, Zhu G, Shen D, et al. 2017. Osteoclast proton pump regulator Atp6v1c1 enhances breast cancer growth by activating the mTORC1 pathway and bone metastasis by increasing V-ATPase activity. *Oncotarget* 8: 47675-90
McEwan DG, Popovic D, Gubas A, Terawaki S, Suzuki H, et al. 2015. PLEKHM1 regulates autophagosome-lysosome fusion through HOPS complex and LC3/GABARAP proteins. *Mol Cell* 57: 39-54
McGuire C, Stransky L, Cotter K, Forgac M. 2017. Regulation of V-ATPase activity. *Front Biosci (Landmark Ed)* 22: 609-22
McGuire CM, Forgac M. 2018. Glucose starvation increases V-ATPase assembly and activity in mammalian cells through AMP kinase and phosphatidylinositide 3-kinase/Akt signaling. *J Biol Chem* 293: 9113-23
McKeel DW, Jarett L. 1970. Preparation and characterization of a plasma membrane fraction from isolated fat cells. *J Cell Biol* 44: 417-32

Melincovici CS, Bosca AB, Susman S, Marginean M, Mihu C, et al. 2018. Vascular endothelial growth factor (VEGF) - key factor in normal and pathological angiogenesis. *Rom J Morphol Embryol* 59: 455-67
Meredith JE, Jr., Schwartz MA. 1997. Integrins, adhesion and apoptosis. *Trends Cell Biol* 7: 146-50
Merkulova M, Paunescu TG, Azroyan A, Marshansky V, Breton S, Brown D. 2015. Mapping the H(+) (V)-ATPase interactome: identification of proteins involved in trafficking, folding, assembly and phosphorylation. *Scientific reports* 5: 14827
Metcalf DG, Moore DT, Wu Y, Kielec JM, Molnar K, et al. 2010. NMR analysis of the alphaIIb beta3 cytoplasmic interaction suggests a mechanism for integrin regulation. *Proc Natl Acad Sci U S A* 107: 22481-6
Meves A, Stremmel C, Gottschalk K, Fassler R. 2009. The Kindlin protein family: new members to the club of focal adhesion proteins. *Trends Cell Biol* 19: 504-13
Meyer GT, Matthias LJ, Noack L, Vadas MA, Gamble JR. 1997. Lumen formation during angiogenesis in vitro involves phagocytic activity, formation and secretion of vacuoles, cell death, and capillary tube remodelling by different populations of endothelial cells. *Anat Rec* 249: 327-40
Miles AL, Burr SP, Grice GL, Nathan JA. 2017. The vacuolar-ATPase complex and assembly factors, TMEM199 and CCDC115, control HIF1alpha prolyl hydroxylation by regulating cellular iron levels. *Elife* 6
Milkereit R, Persaud A, Vanoaica L, Guetg A, Verrey F, Rotin D. 2015. LAPTM4b recruits the LAT1-4F2hc Leu transporter to lysosomes and promotes mTORC1 activation. *Nat Commun* 6: 7250
Mindell JA. 2012. Lysosomal acidification mechanisms. *Annual review of physiology* 74: 69-86
Mitsi M, Forsten-Williams K, Gopalakrishnan M, Nugent MA. 2008. A catalytic role of heparin within the extracellular matrix. *J Biol Chem* 283: 34796-807
Mochida K, Oikawa Y, Kimura Y, Kirisako H, Hirano H, et al. 2015. Receptor-mediated selective autophagy degrades the endoplasmic reticulum and the nucleus. *Nature* 522: 359-62
Montanez E, Ussar S, Schifferer M, Bosl M, Zent R, et al. 2008. Kindlin-2 controls bidirectional signaling of integrins. *Genes Dev* 22: 1325-30
Monteiro MC, Wdziekonski B, Villageois P, Vernochet C, Iehle C, et al. 2009. Commitment of mouse embryonic stem cells to the adipocyte lineage requires retinoic acid receptor beta and active GSK3. *Stem Cells Dev* 18: 457-63
Moreau K, Fleming A, Imarisio S, Lopez Ramirez A, Mercer JL, et al. 2014. PICALM modulates autophagy activity and tau accumulation. *Nat Commun* 5: 4998
Moreau K, Ravikumar B, Puri C, Rubinsztein DC. 2012. Arf6 promotes autophagosome formation via effects on phosphatidylinositol 4,5-bisphosphate and phospholipase D. *J Cell Biol* 196: 483-96
Moreau K, Ravikumar B, Renna M, Puri C, Rubinsztein DC. 2011. Autophagosome precursor maturation requires homotypic fusion. *Cell* 146: 303-17
Morgan MR, Humphries MJ, Bass MD. 2007. Synergistic control of cell adhesion by integrins and syndecans. *Nat Rev Mol Cell Biol* 8: 957-69
Morse EM, Brahme NN, Calderwood DA. 2014. Integrin cytoplasmic tail interactions. *Biochemistry* 53: 810-20
Mory A, Feigelson SW, Yarali N, Kilic SS, Bayhan GI, et al. 2008. Kindlin-3: a new gene involved in the pathogenesis of LAD-III. *Blood* 112: 2591
Moser M, Bauer M, Schmid S, Ruppert R, Schmidt S, et al. 2009. Kindlin-3 is required for beta2 integrin-mediated leukocyte adhesion to endothelial cells. *Nat Med* 15: 300-5
Moser M, Nieswandt B, Ussar S, Pozgajova M, Fassler R. 2008. Kindlin-3 is essential for integrin activation and platelet aggregation. *Nat Med* 14: 325-30
Moslem M, Eggenschwiler R, Wichmann C, Buhmann R, Cantz T, Henschler R. 2017. Kindlin-2 Modulates the Survival, Differentiation, and Migration of Induced Pluripotent Cell-Derived Mesenchymal Stromal Cells. *Stem Cells Int* 2017: 7316354
Murano I, Barbatelli G, Giordano A, Cinti S. 2009. Noradrenergic parenchymal nerve fiber branching after cold acclimatisation correlates with brown adipocyte density in mouse adipose organ. *J Anat* 214: 171-8
Murano I, Barbatelli G, Parisani V, Latini C, Muzzonigro G, et al. 2008. Dead adipocytes, detected as crown-like structures, are prevalent in visceral fat depots of genetically obese mice. *J Lipid Res* 49: 1562-8
N'Diaye EN, Kajihara KK, Hsieh I, Morisaki H, Debnath J, Brown EJ. 2009. PLIC proteins or ubiquilins regulate autophagy-dependent cell survival during nutrient starvation. *EMBO Rep* 10: 173-9
Nakamura S, Hasegawa J, Yoshimori T. 2016. Regulation of lysosomal phosphoinositide balance by INPP5E is essential for autophagosome-lysosome fusion. *Autophagy* 12: 2500-01
Nakamura S, Yoshimori T. 2017. New insights into autophagosome-lysosome fusion. *J Cell Sci* 130: 1209-16
Nakatogawa H, Mochida K. 2015. Reticulophagy and nucleophagy: New findings and unsolved issues. *Autophagy* 11: 2377-8

Nakatogawa H, Suzuki K, Kamada Y, Ohsumi Y. 2009. Dynamics and diversity in autophagy mechanisms: lessons from yeast. *Nat Rev Mol Cell Biol* 10: 458-67
Nakatsu MN, Hughes CC. 2008. An optimized three-dimensional in vitro model for the analysis of angiogenesis. *Methods Enzymol* 443: 65-82
Nedergaard J, Golozoubova V, Matthias A, Asadi A, Jacobsson A, Cannon B. 2001. UCP1: the only protein able to mediate adaptive non-shivering thermogenesis and metabolic inefficiency. *Biochim Biophys Acta* 1504: 82-106
Neels JG, Thinnes T, Loskutoff DJ. 2004. Angiogenesis in an in vivo model of adipose tissue development. *FASEB J* 18: 983-5
Newman PJ. 1997. The biology of PECAM-1. *J Clin Invest* 99: 3-8
Newsholme EA, Crabtree B, Ardawi MS. 1985. Glutamine metabolism in lymphocytes: its biochemical, physiological and clinical importance. *Q J Exp Physiol* 70: 473-89
Nicosia RF, Madri JA. 1987. The microvascular extracellular matrix. Developmental changes during angiogenesis in the aortic ring-plasma clot model. *Am J Pathol* 128: 78-90
Nishimura M, Naito S. 2005. Tissue-specific mRNA expression profiles of human ATP-binding cassette and solute carrier transporter superfamilies. *Drug Metab Pharmacokinet* 20: 452-77
Norgett EE, Golder ZJ, Lorente-Canovas B, Ingham N, Steel KP, Karet Frankl FE. 2012. Atp6v0a4 knockout mouse is a model of distal renal tubular acidosis with hearing loss, with additional extrarenal phenotype. *Proc Natl Acad Sci U S A* 109: 13775-80
O'Callaghan KM, Ayllon V, O'Keeffe J, Wang Y, Cox OT, et al. 2010. Heme-binding protein HRG-1 is induced by insulin-like growth factor I and associates with the vacuolar H+-ATPase to control endosomal pH and receptor trafficking. *J Biol Chem* 285: 381-91
Ohashi Y, Munro S. 2010. Membrane delivery to the yeast autophagosome from the Golgi-endosomal system. *Mol Biol Cell* 21: 3998-4008
Ohno H, Shinoda K, Spiegelman BM, Kajimura S. 2012. PPARgamma agonists induce a white-to-brown fat conversion through stabilization of PRDM16 protein. *Cell Metab* 15: 395-404
Olsvik HL, Lamark T, Takagi K, Larsen KB, Evjen G, et al. 2015. FYCO1 Contains a C-terminally Extended, LC3A/B-preferring LC3-interacting Region (LIR) Motif Required for Efficient Maturation of Autophagosomes during Basal Autophagy. *J Biol Chem* 290: 29361-74
Orsi A, Razi M, Dooley HC, Robinson D, Weston AE, et al. 2012. Dynamic and transient interactions of Atg9 with autophagosomes, but not membrane integration, are required for autophagy. *Mol Biol Cell* 23: 1860-73
Palacin M, Estevez R, Bertran J, Zorzano A. 1998. Molecular biology of mammalian plasma membrane amino acid transporters. *Physiol Rev* 78: 969-1054
Palmieri F. 2014. Mitochondrial transporters of the SLC25 family and associated diseases: a review. *J Inherit Metab Dis* 37: 565-75
Pamarthy S, Kulshrestha A, Katara GK, Beaman KD. 2018. The curious case of vacuolar ATPase: regulation of signaling pathways. *Mol Cancer* 17: 41
Pamarthy S, Mao L, Katara GK, Fleetwood S, Kulshreshta A, et al. 2016. The V-ATPase a2 isoform controls mammary gland development through Notch and TGF-beta signaling. *Cell death & disease* 7: e2443
Pankiv S, Alemu EA, Brech A, Bruun JA, Lamark T, et al. 2010. FYCO1 is a Rab7 effector that binds to LC3 and PI3P to mediate microtubule plus end-directed vesicle transport. *J Cell Biol* 188: 253-69
Parker BL, Yang G, Humphrey SJ, Chaudhuri R, Ma X, et al. 2015. Targeted phosphoproteomics of insulin signaling using data-independent acquisition mass spectrometry. *Sci Signal* 8: rs6
Patterson GH, Knobel SM, Sharif WD, Kain SR, Piston DW. 1997. Use of the green fluorescent protein and its mutants in quantitative fluorescence microscopy. *Biophys J* 73: 2782-90
Paunescu TG, Jones AC, Tyszkowski R, Brown D. 2008. V-ATPase expression in the mouse olfactory epithelium. *Am J Physiol Cell Physiol* 295: C923-30
Paunescu TG, Rodriguez S, Benz E, McKee M, Tyszkowski R, et al. 2012. Loss of the V-ATPase B1 subunit isoform expressed in non-neuronal cells of the mouse olfactory epithelium impairs olfactory function. *PLoS One* 7: e45395
Pedersen O, Kahn CR, Flier JS, Kahn BB. 1991. High fat feeding causes insulin resistance and a marked decrease in the expression of glucose transporters (Glut 4) in fat cells of rats. *Endocrinology* 129: 771-7
Pena-Llopis S, Vega-Rubin-de-Celis S, Schwartz JC, Wolff NC, Tran TA, et al. 2011. Regulation of TFEB and V-ATPases by mTORC1. *Embo j* 30: 3242-58

Perera HD, Ma YQ, Yang J, Hirbawi J, Plow EF, Qin J. 2011. Membrane binding of the N-terminal ubiquitin-like domain of kindlin-2 is crucial for its regulation of integrin activation. *Structure* 19: 1664-71
Perland E, Fredriksson R. 2017. Classification Systems of Secondary Active Transporters. *Trends Pharmacol Sci* 38: 305-15
Perruzzi CA, de Fougerolles AR, Koteliansky VE, Whelan MC, Westlin WF, Senger DR. 2003. Functional overlap and cooperativity among alphav and beta1 integrin subfamilies during skin angiogenesis. *J Invest Dermatol* 120: 1100-9
Petit CS, Roczniak-Ferguson A, Ferguson SM. 2013. Recruitment of folliculin to lysosomes supports the amino acid-dependent activation of Rag GTPases. *J Cell Biol* 202: 1107-22
Petrovic N, Walden TB, Shabalina IG, Timmons JA, Cannon B, Nedergaard J. 2010. Chronic peroxisome proliferator-activated receptor gamma (PPARgamma) activation of epididymally derived white adipocyte cultures reveals a population of thermogenically competent, UCP1-containing adipocytes molecularly distinct from classic brown adipocytes. *J Biol Chem* 285: 7153-64
Phang JM, Liu W, Hancock CN, Fischer JW. 2015. Proline metabolism and cancer: emerging links to glutamine and collagen. *Curr Opin Clin Nutr Metab Care* 18: 71-7
Pillai SM, Meredith D. 2011. SLC36A4 (hPAT4) is a high affinity amino acid transporter when expressed in Xenopus laevis oocytes. *J Biol Chem* 286: 2455-60
Piper MDW, Soultoukis GA, Blanc E, Mesaros A, Herbert SL, et al. 2017. Matching Dietary Amino Acid Balance to the In Silico-Translated Exome Optimizes Growth and Reproduction without Cost to Lifespan. *Cell Metab* 25: 610-21
Piper RC, Katzmann DJ. 2007. Biogenesis and function of multivesicular bodies. *Annu Rev Cell Dev Biol* 23: 519-47
Plow EF, Meller J, Byzova TV. 2014. Integrin function in vascular biology: a view from 2013. *Curr Opin Hematol* 21: 241-7
Pochini L, Scalise M, Galluccio M, Indiveri C. 2014. Membrane transporters for the special amino acid glutamine: structure/function relationships and relevance to human health. *Front Chem* 2: 61
Popovic D, Dikic I. 2014. TBC1D5 and the AP2 complex regulate ATG9 trafficking and initiation of autophagy. *EMBO Rep* 15: 392-401
Pramme-Steinwachs I, Jastroch M, Ussar S. 2017. Extracellular calcium modulates brown adipocyte differentiation and identity. *Scientific reports* 7: 8888
Pramod AB, Foster J, Carvelli L, Henry LK. 2013. SLC6 transporters: structure, function, regulation, disease association and therapeutics. *Mol Aspects Med* 34: 197-219
Puigserver P, Wu Z, Park CW, Graves R, Wright M, Spiegelman BM. 1998. A cold-inducible coactivator of nuclear receptors linked to adaptive thermogenesis. *Cell* 92: 829-39
Puri C, Renna M, Bento CF, Moreau K, Rubinsztein DC. 2013. Diverse autophagosome membrane sources coalesce in recycling endosomes. *Cell* 154: 1285-99
Qadota H, Moerman DG, Benian GM. 2012. A molecular mechanism for the requirement of PAT-4 (integrin-linked kinase (ILK)) for the localization of UNC-112 (Kindlin) to integrin adhesion sites. *J Biol Chem* 287: 28537-51
Qiang G, Whang Kong H, Xu S, Pham HA, Parlee SD, et al. 2016. Lipodystrophy and severe metabolic dysfunction in mice with adipose tissue-specific insulin receptor ablation. *Mol Metab* 5: 480-90
Qin A, Cheng TS, Pavlos NJ, Lin Z, Dai KR, Zheng MH. 2012. V-ATPases in osteoclasts: structure, function and potential inhibitors of bone resorption. *Int J Biochem Cell Biol* 44: 1422-35
Qu H, Tu Y, Shi X, Larjava H, Saleem MA, et al. 2011. Kindlin-2 regulates podocyte adhesion and fibronectin matrix deposition through interactions with phosphoinositides and integrins. *J Cell Sci* 124: 879-91
Rabinowitz JD, White E. 2010. Autophagy and metabolism. *Science* 330: 1344-8
Ramachandran N, Munteanu I, Wang P, Ruggieri A, Rilstone JJ, et al. 2013. VMA21 deficiency prevents vacuolar ATPase assembly and causes autophagic vacuolar myopathy. *Acta Neuropathol* 125: 439-57
Rambold AS, Kostelecky B, Elia N, Lippincott-Schwartz J. 2011. Tubular network formation protects mitochondria from autophagosomal degradation during nutrient starvation. *Proc Natl Acad Sci U S A* 108: 10190-5
Ramirez F, Dietz HC. 2007. Fibrillin-rich microfibrils: Structural determinants of morphogenetic and homeostatic events. *J Cell Physiol* 213: 326-30
Ramirez F, Dietz HC. 2009. Extracellular microfibrils in vertebrate development and disease processes. *J Biol Chem* 284: 14677-81

Ravikumar B, Acevedo-Arozena A, Imarisio S, Berger Z, Vacher C, et al. 2005. Dynein mutations impair autophagic clearance of aggregate-prone proteins. *Nat Genet* 37: 771-6
Ravikumar B, Moreau K, Jahreiss L, Puri C, Rubinsztein DC. 2010. Plasma membrane contributes to the formation of pre-autophagosomal structures. *Nat Cell Biol* 12: 747-57
Rebsamen M, Pochini L, Stasyk T, de Araujo ME, Galluccio M, et al. 2015. SLC38A9 is a component of the lysosomal amino acid sensing machinery that controls mTORC1. *Nature* 519: 477-81
Reiling JH, Hafen E. 2004. The hypoxia-induced paralogs Scylla and Charybdis inhibit growth by down-regulating S6K activity upstream of TSC in Drosophila. *Genes Dev* 18: 2879-92
Rieder SE, Emr SD. 1997. A novel RING finger protein complex essential for a late step in protein transport to the yeast vacuole. *Mol Biol Cell* 8: 2307-27
Rivera OC, Hennigar SR, Kelleher SL. 2018. ZnT2 is critical for lysosome acidification and biogenesis during mammary gland involution. *Am J Physiol Regul Integr Comp Physiol* 315: R323-R35
Rognoni E, Ruppert R, Fassler R. 2016. The kindlin family: functions, signaling properties and implications for human disease. *J Cell Sci* 129: 17-27
Rognoni E, Widmaier M, Jakobson M, Ruppert R, Ussar S, et al. 2014. Kindlin-1 controls Wnt and TGF-beta availability to regulate cutaneous stem cell proliferation. *Nat Med* 20: 350-9
Roovers K, Assoian RK. 2000. Integrating the MAP kinase signal into the G1 phase cell cycle machinery. *Bioessays* 22: 818-26
Rosen ED, Sarraf P, Troy AE, Bradwin G, Moore K, et al. 1999. PPAR gamma is required for the differentiation of adipose tissue in vivo and in vitro. *Mol Cell* 4: 611-7
Rosen ED, Spiegelman BM. 2014. What we talk about when we talk about fat. *Cell* 156: 20-44
Rosenwald M, Perdikari A, Rulicke T, Wolfrum C. 2013. Bi-directional interconversion of brite and white adipocytes. *Nat Cell Biol* 15: 659-67
Rousselle A, Sihn G, Rotteveel M, Bader M. 2014. (Pro)renin receptor and V-ATPase: from Drosophila to humans. *Clinical science (London, England : 1979)* 126: 529-36
Rowe RG, Weiss SJ. 2008. Breaching the basement membrane: who, when and how? *Trends Cell Biol* 18: 560-74
Roy H, Bhardwaj S, Yla-Herttuala S. 2006. Biology of vascular endothelial growth factors. *FEBS Lett* 580: 2879-87
Rozario T, DeSimone DW. 2010. The extracellular matrix in development and morphogenesis: a dynamic view. *Dev Biol* 341: 126-40
Rubio-Aliaga I, Boll M, Vogt Weisenhorn DM, Foltz M, Kottra G, Daniel H. 2004. The proton/amino acid cotransporter PAT2 is expressed in neurons with a different subcellular localization than its paralog PAT1. *J Biol Chem* 279: 2754-60
Saely CH, Geiger K, Drexel H. 2012. Brown versus white adipose tissue: a mini-review. *Gerontology* 58: 15-23
Saftig P, Klumperman J. 2009. Lysosome biogenesis and lysosomal membrane proteins: trafficking meets function. *Nat Rev Mol Cell Biol* 10: 623-35
Saharinen P, Eklund L, Miettinen J, Wirkkala R, Anisimov A, et al. 2008. Angiopoietins assemble distinct Tie2 signalling complexes in endothelial cell-cell and cell-matrix contacts. *Nat Cell Biol* 10: 527-37
Sainson RC, Aoto J, Nakatsu MN, Holderfield M, Conn E, et al. 2005. Cell-autonomous notch signaling regulates endothelial cell branching and proliferation during vascular tubulogenesis. *FASEB J* 19: 1027-9
Sancak Y, Bar-Peled L, Zoncu R, Markhard AL, Nada S, Sabatini DM. 2010. Ragulator-Rag complex targets mTORC1 to the lysosomal surface and is necessary for its activation by amino acids. *Cell* 141: 290-303
Sanchez-Gurmaches J, Guertin DA. 2014. Adipocytes arise from multiple lineages that are heterogeneously and dynamically distributed. *Nat Commun* 5: 4099
Sanchez-Gurmaches J, Hung CM, Sparks CA, Tang Y, Li H, Guertin DA. 2012. PTEN loss in the Myf5 lineage redistributes body fat and reveals subsets of white adipocytes that arise from Myf5 precursors. *Cell Metab* 16: 348-62
Sano H, Roach WG, Peck GR, Fukuda M, Lienhard GE. 2008. Rab10 in insulin-stimulated GLUT4 translocation. *Biochem J* 411: 89-95
Satoo K, Noda NN, Kumeta H, Fujioka Y, Mizushima N, et al. 2009. The structure of Atg4B-LC3 complex reveals the mechanism of LC3 processing and delipidation during autophagy. *EMBO J* 28: 1341-50
Saunders WB, Bohnsack BL, Faske JB, Anthis NJ, Bayless KJ, et al. 2006. Coregulation of vascular tube stabilization by endothelial cell TIMP-2 and pericyte TIMP-3. *J Cell Biol* 175: 179-91
Sautin YY, Lu M, Gaugler A, Zhang L, Gluck SL. 2005. Phosphatidylinositol 3-kinase-mediated effects of glucose on vacuolar H+-ATPase assembly, translocation, and acidification of intracellular compartments in renal epithelial cells. *Mol Cell Biol* 25: 575-89

Schaefer L, Schaefer RM. 2010. Proteoglycans: from structural compounds to signaling molecules. *Cell Tissue Res* 339: 237-46
Schaller MD. 2001. Paxillin: a focal adhesion-associated adaptor protein. *Oncogene* 20: 6459-72
Schioth HB, Roshanbin S, Hagglund MG, Fredriksson R. 2013. Evolutionary origin of amino acid transporter families SLC32, SLC36 and SLC38 and physiological, pathological and therapeutic aspects. *Mol Aspects Med* 34: 571-85
Schuck S, Gerl MJ, Ang A, Manninen A, Keller P, et al. 2007. Rab10 is involved in basolateral transport in polarized Madin-Darby canine kidney cells. *Traffic* 8: 47-60
Schulz TJ, Tseng YH. 2013. Brown adipose tissue: development, metabolism and beyond. *Biochem J* 453: 167-78
Scott CC, Gruenberg J. 2011. Ion flux and the function of endosomes and lysosomes: pH is just the start: the flux of ions across endosomal membranes influences endosome function not only through regulation of the luminal pH. *Bioessays* 33: 103-10
Seale P, Bjork B, Yang W, Kajimura S, Chin S, et al. 2008. PRDM16 controls a brown fat/skeletal muscle switch. *Nature* 454: 961-7
Seale P, Kajimura S, Yang W, Chin S, Rohas LM, et al. 2007. Transcriptional control of brown fat determination by PRDM16. *Cell Metab* 6: 38-54
Seals DF, Eitzen G, Margolis N, Wickner WT, Price A. 2000. A Ypt/Rab effector complex containing the Sec1 homolog Vps33p is required for homotypic vacuole fusion. *Proc Natl Acad Sci U S A* 97: 9402-7
Segawa H, Fukasawa Y, Miyamoto K, Takeda E, Endou H, Kanai Y. 1999. Identification and functional characterization of a Na+-independent neutral amino acid transporter with broad substrate selectivity. *J Biol Chem* 274: 19745-51
Seger R, Krebs EG. 1995. The MAPK signaling cascade. *FASEB J* 9: 726-35
Senger DR. 1996. Molecular framework for angiogenesis: a complex web of interactions between extravasated plasma proteins and endothelial cell proteins induced by angiogenic cytokines. *Am J Pathol* 149: 1-7
Senger DR, Davis GE. 2011. Angiogenesis. *Cold Spring Harb Perspect Biol* 3: a005090
Senger DR, Perruzzi CA. 1996. Cell migration promoted by a potent GRGDS-containing thrombin-cleavage fragment of osteopontin. *Biochim Biophys Acta* 1314: 13-24
Senger DR, Perruzzi CA, Streit M, Koteliansky VE, de Fougerolles AR, Detmar M. 2002. The alpha(1)beta(1) and alpha(2)beta(1) integrins provide critical support for vascular endothelial growth factor signaling, endothelial cell migration, and tumor angiogenesis. *Am J Pathol* 160: 195-204
Sengupta S, Peterson TR, Sabatini DM. 2010. Regulation of the mTOR complex 1 pathway by nutrients, growth factors, and stress. *Mol Cell* 40: 310-22
Sethi N, Yan Y, Quek D, Schupbach T, Kang Y. 2010. Rabconnectin-3 is a functional regulator of mammalian Notch signaling. *J Biol Chem* 285: 34757-64
Shackelford DB, Shaw RJ. 2009. The LKB1-AMPK pathway: metabolism and growth control in tumour suppression. *Nat Rev Cancer* 9: 563-75
Shan T, Zhang P, Jiang Q, Xiong Y, Wang Y, Kuang S. 2016. Adipocyte-specific deletion of mTOR inhibits adipose tissue development and causes insulin resistance in mice. *Diabetologia* 59: 1995-2004
Shattil SJ, Kim C, Ginsberg MH. 2010. The final steps of integrin activation: the end game. *Nat Rev Mol Cell Biol* 11: 288-300
Shearin AL, Monks BR, Seale P, Birnbaum MJ. 2016. Lack of AKT in adipocytes causes severe lipodystrophy. *Mol Metab* 5: 472-79
Sheen JH, Zoncu R, Kim D, Sabatini DM. 2011. Defective regulation of autophagy upon leucine deprivation reveals a targetable liability of human melanoma cells in vitro and in vivo. *Cancer Cell* 19: 613-28
Shi X, Ma YQ, Tu Y, Chen K, Wu S, et al. 2007. The MIG-2/integrin interaction strengthens cell-matrix adhesion and modulates cell motility. *J Biol Chem* 282: 20455-66
Shine L, Kilty C, Gross J, Kennedy B. 2014. Vacuolar ATPases and their role in vision. *Adv Exp Med Biol* 801: 97-103
Shirahama-Noda K, Kira S, Yoshimori T, Noda T. 2013. TRAPPIII is responsible for vesicular transport from early endosomes to Golgi, facilitating Atg9 cycling in autophagy. *J Cell Sci* 126: 4963-73
Short SM, Talbott GA, Juliano RL. 1998. Integrin-mediated signaling events in human endothelial cells. *Mol Biol Cell* 9: 1969-80
Sirey TM, Ponting CP. 2016. Insights into the post-transcriptional regulation of the mitochondrial electron transport chain. *Biochem Soc Trans* 44: 1491-98
Smardon AM, Diab HI, Tarsio M, Diakov TT, Nasab ND, et al. 2014. The RAVE complex is an isoform-specific V-ATPase assembly factor in yeast. *Mol Biol Cell* 25: 356-67

Smith AN, Skaug J, Choate KA, Nayir A, Bakkaloglu A, et al. 2000. Mutations in ATP6N1B, encoding a new kidney vacuolar proton pump 116-kD subunit, cause recessive distal renal tubular acidosis with preserved hearing. *Nat Genet* 26: 71-5

Softic S, Boucher J, Solheim MH, Fujisaka S, Haering MF, et al. 2016. Lipodystrophy Due to Adipose Tissue-Specific Insulin Receptor Knockout Results in Progressive NAFLD. *Diabetes* 65: 2187-200

Solinger JA, Spang A. 2013. Tethering complexes in the endocytic pathway: CORVET and HOPS. *Febs j* 280: 2743-57

Somanath PR, Ciocea A, Byzova TV. 2009. Integrin and growth factor receptor alliance in angiogenesis. *Cell Biochem Biophys* 53: 53-64

Somers J, Poyry T, Willis AE. 2013. A perspective on mammalian upstream open reading frame function. *Int J Biochem Cell Biol* 45: 1690-700

Son SM, Park SJ, Lee H, Siddiqi F, Lee JE, et al. 2018. Leucine Signals to mTORC1 via Its Metabolite Acetyl-Coenzyme A. *Cell Metab*

Sorkin A, von Zastrow M. 2009. Endocytosis and signalling: intertwining molecular networks. *Nat Rev Mol Cell Biol* 10: 609-22

Spencer M, Unal R, Zhu B, Rasouli N, McGehee RE, Jr., et al. 2011. Adipose tissue extracellular matrix and vascular abnormalities in obesity and insulin resistance. *J Clin Endocrinol Metab* 96: E1990-8

Storlien LH, James DE, Burleigh KM, Chisholm DJ, Kraegen EW. 1986. Fat feeding causes widespread in vivo insulin resistance, decreased energy expenditure, and obesity in rats. *Am J Physiol* 251: E576-83

Stransky LA, Forgac M. 2015. Amino Acid Availability Modulates Vacuolar H+-ATPase Assembly. *J Biol Chem* 290: 27360-9

Stratman AN, Malotte KM, Mahan RD, Davis MJ, Davis GE. 2009a. Pericyte recruitment during vasculogenic tube assembly stimulates endothelial basement membrane matrix formation. *Blood* 114: 5091-101

Stratman AN, Saunders WB, Sacharidou A, Koh W, Fisher KE, et al. 2009b. Endothelial cell lumen and vascular guidance tunnel formation requires MT1-MMP-dependent proteolysis in 3-dimensional collagen matrices. *Blood* 114: 237-47

Stratman AN, Schwindt AE, Malotte KM, Davis GE. 2010. Endothelial-derived PDGF-BB and HB-EGF coordinately regulate pericyte recruitment during vasculogenic tube assembly and stabilization. *Blood* 116: 4720-30

Sun-Wada GH, Wada Y. 2013. Vacuolar-type proton pump ATPases: acidification and pathological relationships. *Histology and histopathology* 28: 805-15

Sun-Wada GH, Wada Y. 2015. Role of vacuolar-type proton ATPase in signal transduction. *Biochim Biophys Acta* 1847: 1166-72

Sundberg BE, Waag E, Jacobsson JA, Stephansson O, Rumaks J, et al. 2008. The evolutionary history and tissue mapping of amino acid transporters belonging to solute carrier families SLC32, SLC36, and SLC38. *J Mol Neurosci* 35: 179-93

Sundberg C, Nagy JA, Brown LF, Feng D, Eckelhoefer IA, et al. 2001. Glomeruloid microvascular proliferation follows adenoviral vascular permeability factor/vascular endothelial growth factor-164 gene delivery. *Am J Pathol* 158: 1145-60

Suraweera A, Munch C, Hanssum A, Bertolotti A. 2012. Failure of amino acid homeostasis causes cell death following proteasome inhibition. *Mol Cell* 48: 242-53

Suryawan A, Nguyen HV, Almonaci RD, Davis TA. 2013. Abundance of amino acid transporters involved in mTORC1 activation in skeletal muscle of neonatal pigs is developmentally regulated. *Amino Acids* 45: 523-30

Suzuki K, Kono T. 1980. Evidence that insulin causes translocation of glucose transport activity to the plasma membrane from an intracellular storage site. *Proc Natl Acad Sci U S A* 77: 2542-5

Svensson L, Howarth K, McDowall A, Patzak I, Evans R, et al. 2009. Leukocyte adhesion deficiency-III is caused by mutations in KINDLIN3 affecting integrin activation. *Nat Med* 15: 306-12

Sweeney SM, DiLullo G, Slater SJ, Martinez J, Iozzo RV, et al. 2003. Angiogenesis in collagen I requires alpha2beta1 ligation of a GFP*GER sequence and possibly p38 MAPK activation and focal adhesion disassembly. *J Biol Chem* 278: 30516-24

Tadokoro S, Shattil SJ, Eto K, Tai V, Liddington RC, et al. 2003. Talin binding to integrin beta tails: a final common step in integrin activation. *Science* 302: 103-6

Takahashi Y, Tsotakos N, Liu Y, Young MM, Serfass J, et al. 2016. The Bif-1-Dynamin 2 membrane fission machinery regulates Atg9-containing vesicle generation at the Rab11-positive reservoirs. *Oncotarget* 7: 20855-68

Tan BS, Lonic A, Morris MB, Rathjen PD, Rathjen J. 2011. The amino acid transporter SNAT2 mediates L-proline-induced differentiation of ES cells. *Am J Physiol Cell Physiol* 300: C1270-9
Tan VP, Miyamoto S. 2016. Nutrient-sensing mTORC1: Integration of metabolic and autophagic signals. *Journal of molecular and cellular cardiology* 95: 31-41
Tchkonia T, Giorgadze N, Pirtskhalava T, Tchoukalova Y, Karagiannides I, et al. 2002. Fat depot origin affects adipogenesis in primary cultured and cloned human preadipocytes. *Am J Physiol Regul Integr Comp Physiol* 282: R1286-96
Tee AR, Manning BD, Roux PP, Cantley LC, Blenis J. 2003. Tuberous sclerosis complex gene products, Tuberin and Hamartin, control mTOR signaling by acting as a GTPase-activating protein complex toward Rheb. *Curr Biol* 13: 1259-68
Terawaki S, Camosseto V, Prete F, Wenger T, Papadopoulos A, et al. 2015. RUN and FYVE domain-containing protein 4 enhances autophagy and lysosome tethering in response to Interleukin-4. *J Cell Biol* 210: 1133-52
Theocharis AD, Skandalis SS, Gialeli C, Karamanos NK. 2016. Extracellular matrix structure. *Adv Drug Deliv Rev* 97: 4-27
Thwaites DT, Anderson CM. 2011. The SLC36 family of proton-coupled amino acid transporters and their potential role in drug transport. *British journal of pharmacology* 164: 1802-16
Timmons JA, Wennmalm K, Larsson O, Walden TB, Lassmann T, et al. 2007. Myogenic gene expression signature establishes that brown and white adipocytes originate from distinct cell lineages. *Proc Natl Acad Sci U S A* 104: 4401-6
Tooze SA, Abada A, Elazar Z. 2014. Endocytosis and autophagy: exploitation or cooperation? *Cold Spring Harb Perspect Biol* 6: a018358
Tseng YH, Kokkotou E, Schulz TJ, Huang TL, Winnay JN, et al. 2008. New role of bone morphogenetic protein 7 in brown adipogenesis and energy expenditure. *Nature* 454: 1000-4
Tsuboyama K, Koyama-Honda I, Sakamaki Y, Koike M, Morishita H, Mizushima N. 2016. The ATG conjugation systems are important for degradation of the inner autophagosomal membrane. *Science* 354: 1036-41
Tsun ZY, Bar-Peled L, Chantranupong L, Zoncu R, Wang T, et al. 2013. The folliculin tumor suppressor is a GAP for the RagC/D GTPases that signal amino acid levels to mTORC1. *Mol Cell* 52: 495-505
Tu Y, Huang Y, Zhang Y, Hua Y, Wu C. 2001. A new focal adhesion protein that interacts with integrin-linked kinase and regulates cell adhesion and spreading. *J Cell Biol* 153: 585-98
Tu Y, Wu S, Shi X, Chen K, Wu C. 2003. Migfilin and Mig-2 link focal adhesions to filamin and the actin cytoskeleton and function in cell shape modulation. *Cell* 113: 37-47
Tumbarello DA, Waxse BJ, Arden SD, Bright NA, Kendrick-Jones J, Buss F. 2012. Autophagy receptors link myosin VI to autophagosomes to mediate Tom1-dependent autophagosome maturation and fusion with the lysosome. *Nat Cell Biol* 14: 1024-35
Uldry M, Yang W, St-Pierre J, Lin J, Seale P, Spiegelman BM. 2006. Complementary action of the PGC-1 coactivators in mitochondrial biogenesis and brown fat differentiation. *Cell Metab* 3: 333-41
Ussar S, Lee KY, Dankel SN, Boucher J, Haering MF, et al. 2014. ASC-1, PAT2, and P2RX5 are cell surface markers for white, beige, and brown adipocytes. *Sci Transl Med* 6: 247ra103
Ussar S, Wang HV, Linder S, Fassler R, Moser M. 2006. The Kindlins: subcellular localization and expression during murine development. *Exp Cell Res* 312: 3142-51
Utsunomiya-Tate N, Endou H, Kanai Y. 1996. Cloning and functional characterization of a system ASC-like Na+-dependent neutral amino acid transporter. *J Biol Chem* 271: 14883-90
Valapala M, Hose S, Gongora C, Dong L, Wawrousek EF, et al. 2013. Impaired endolysosomal function disrupts Notch signalling in optic nerve astrocytes. *Nat Commun* 4: 1629
van Hinsbergh VW, Collen A, Koolwijk P. 2001. Role of fibrin matrix in angiogenesis. *Ann N Y Acad Sci* 936: 426-37
Vanslambrouck JM, Broer A, Thavyogarajah T, Holst J, Bailey CG, et al. 2010. Renal imino acid and glycine transport system ontogeny and involvement in developmental iminoglycinuria. *Biochem J* 428: 397-407
Vattem KM, Wek RC. 2004. Reinitiation involving upstream ORFs regulates ATF4 mRNA translation in mammalian cells. *Proc Natl Acad Sci U S A* 101: 11269-74
Vernon RB, Sage EH. 1995. Between molecules and morphology. Extracellular matrix and creation of vascular form. *Am J Pathol* 147: 873-83
Vicente-Manzanares M, Sanchez-Madrid F. 2004. Role of the cytoskeleton during leukocyte responses. *Nat Rev Immunol* 4: 110-22

Vinals F, Pouyssegur J. 1999. Confluence of vascular endothelial cells induces cell cycle exit by inhibiting p42/p44 mitogen-activated protein kinase activity. *Mol Cell Biol* 19: 2763-72
Wagenseil JE, Mecham RP. 2007. New insights into elastic fiber assembly. *Birth Defects Res C Embryo Today* 81: 229-40
Wagenseil JE, Mecham RP. 2009. Vascular extracellular matrix and arterial mechanics. *Physiol Rev* 89: 957-89
Wang F, Mullican SE, DiSpirito JR, Peed LC, Lazar MA. 2013a. Lipoatrophy and severe metabolic disturbance in mice with fat-specific deletion of PPARgamma. *Proc Natl Acad Sci U S A* 110: 18656-61
Wang H, Sun HQ, Zhu X, Zhang L, Albanesi J, et al. 2015a. GABARAPs regulate PI4P-dependent autophagosome:lysosome fusion. *Proc Natl Acad Sci U S A* 112: 7015-20
Wang QA, Tao C, Gupta RK, Scherer PE. 2013b. Tracking adipogenesis during white adipose tissue development, expansion and regeneration. *Nat Med* 19: 1338-44
Wang S, Tsun ZY, Wolfson RL, Shen K, Wyant GA, et al. 2015b. Metabolism. Lysosomal amino acid transporter SLC38A9 signals arginine sufficiency to mTORC1. *Science* 347: 188-94
Wang Z, Miao G, Xue X, Guo X, Yuan C, et al. 2016. The Vici Syndrome Protein EPG5 Is a Rab7 Effector that Determines the Fusion Specificity of Autophagosomes with Late Endosomes/Lysosomes. *Mol Cell* 63: 781-95
Wary KK, Mainiero F, Isakoff SJ, Marcantonio EE, Giancotti FG. 1996. The adaptor protein Shc couples a class of integrins to the control of cell cycle progression. *Cell* 87: 733-43
Webber JL, Tooze SA. 2010. Coordinated regulation of autophagy by p38alpha MAPK through mAtg9 and p38IP. *EMBO J* 29: 27-40
Weerasekara VK, Panek DJ, Broadbent DG, Mortenson JB, Mathis AD, et al. 2014. Metabolic-stress-induced rearrangement of the 14-3-3zeta interactome promotes autophagy via a ULK1- and AMPK-regulated 14-3-3zeta interaction with phosphorylated Atg9. *Mol Cell Biol* 34: 4379-88
Westermann B. 2015. The mitochondria-plasma membrane contact site. *Curr Opin Cell Biol* 35: 1-6
Whelan MC, Senger DR. 2003. Collagen I initiates endothelial cell morphogenesis by inducing actin polymerization through suppression of cyclic AMP and protein kinase A. *J Biol Chem* 278: 327-34
White SJ, McLean WH. 2005. Kindler surprise: mutations in a novel actin-associated protein cause Kindler syndrome. *J Dermatol Sci* 38: 169-75
Wijdeven RH, Janssen H, Nahidiazar L, Janssen L, Jalink K, et al. 2016. Cholesterol and ORP1L-mediated ER contact sites control autophagosome transport and fusion with the endocytic pathway. *Nat Commun* 7: 11808
Winzell MS, Ahren B. 2004. The high-fat diet-fed mouse: a model for studying mechanisms and treatment of impaired glucose tolerance and type 2 diabetes. *Diabetes* 53 Suppl 3: S215-9
Wise DR, DeBerardinis RJ, Mancuso A, Sayed N, Zhang XY, et al. 2008. Myc regulates a transcriptional program that stimulates mitochondrial glutaminolysis and leads to glutamine addiction. *Proc Natl Acad Sci U S A* 105: 18782-7
Wise DR, Thompson CB. 2010. Glutamine addiction: a new therapeutic target in cancer. *Trends Biochem Sci* 35: 427-33
Wise SG, Weiss AS. 2009. Tropoelastin. *Int J Biochem Cell Biol* 41: 494-7
Wojtanik KM, Edgemon K, Viswanadha S, Lindsey B, Haluzik M, et al. 2009. The role of LMNA in adipose: a novel mouse model of lipodystrophy based on the Dunnigan-type familial partial lipodystrophy mutation. *J Lipid Res* 50: 1068-79
Wolfson RL, Chantranupong L, Saxton RA, Shen K, Scaria SM, et al. 2016. Sestrin2 is a leucine sensor for the mTORC1 pathway. *Science* 351: 43-8
Wolfson RL, Sabatini DM. 2017. The Dawn of the Age of Amino Acid Sensors for the mTORC1 Pathway. *Cell Metab* 26: 301-09
Woods A, Couchman JR. 1998. Syndecans: synergistic activators of cell adhesion. *Trends Cell Biol* 8: 189-92
Wu J, Bostrom P, Sparks LM, Ye L, Choi JH, et al. 2012. Beige adipocytes are a distinct type of thermogenic fat cell in mouse and human. *Cell* 150: 366-76
Wurmser AE, Sato TK, Emr SD. 2000. New component of the vacuolar class C-Vps complex couples nucleotide exchange on the Ypt7 GTPase to SNARE-dependent docking and fusion. *J Cell Biol* 151: 551-62
Xu L, Shen X, Bryan A, Banga S, Swanson MS, Luo ZQ. 2010. Inhibition of host vacuolar H+-ATPase activity by a Legionella pneumophila effector. *PLoS pathogens* 6: e1000822
Xu Y, Parmar A, Roux E, Balbis A, Dumas V, et al. 2012. Epidermal growth factor-induced vacuolar (H+)-atpase assembly: a role in signaling via mTORC1 activation. *J Biol Chem* 287: 26409-22

Xue Y, Petrovic N, Cao R, Larsson O, Lim S, et al. 2009. Hypoxia-independent angiogenesis in adipose tissues during cold acclimation. *Cell Metab* 9: 99-109
Xue ZH, Feng C, Liu WL, Tan SM. 2013. A role of kindlin-3 in integrin alphaMbeta2 outside-in signaling and the Syk-Vav1-Rac1/Cdc42 signaling axis. *PLoS One* 8: e56911
Yamamoto A, Tagawa Y, Yoshimori T, Moriyama Y, Masaki R, Tashiro Y. 1998. Bafilomycin A1 prevents maturation of autophagic vacuoles by inhibiting fusion between autophagosomes and lysosomes in rat hepatoma cell line, H-4-II-E cells. *Cell Struct Funct* 23: 33-42
Yamamoto H, Kakuta S, Watanabe TM, Kitamura A, Sekito T, et al. 2012. Atg9 vesicles are an important membrane source during early steps of autophagosome formation. *J Cell Biol* 198: 219-33
Yang HS, Jansen AP, Komar AA, Zheng X, Merrick WC, et al. 2003. The transformation suppressor Pdcd4 is a novel eukaryotic translation initiation factor 4A binding protein that inhibits translation. *Mol Cell Biol* 23: 26-37
Yang S, Graham J, Kahn JW, Schwartz EA, Gerritsen ME. 1999. Functional roles for PECAM-1 (CD31) and VE-cadherin (CD144) in tube assembly and lumen formation in three-dimensional collagen gels. *Am J Pathol* 155: 887-95
Yang Z, Klionsky DJ. 2010. Mammalian autophagy: core molecular machinery and signaling regulation. *Curr Opin Cell Biol* 22: 124-31
Ye F, Kim C, Ginsberg MH. 2011. Molecular mechanism of inside-out integrin regulation. *J Thromb Haemost* 9 Suppl 1: 20-25
Yla-Anttila P, Vihinen H, Jokitalo E, Eskelinen EL. 2009. 3D tomography reveals connections between the phagophore and endoplasmic reticulum. *Autophagy* 5: 1180-5
Young P, Arch JR, Ashwell M. 1984. Brown adipose tissue in the parametrial fat pad of the mouse. *FEBS Lett* 167: 10-4
Young SK, Wek RC. 2016. Upstream Open Reading Frames Differentially Regulate Gene-specific Translation in the Integrated Stress Response. *J Biol Chem* 291: 16927-35
Yu L, Chen Y, Tooze SA. 2018. Autophagy pathway: Cellular and molecular mechanisms. *Autophagy* 14: 207-15
Yu L, McPhee CK, Zheng L, Mardones GA, Rong Y, et al. 2010. Termination of autophagy and reformation of lysosomes regulated by mTOR. *Nature* 465: 942-6
Zaidel-Bar R, Geiger B. 2010. The switchable integrin adhesome. *J Cell Sci* 123: 1385-8
Zaidel-Bar R, Itzkovitz S, Ma'ayan A, Iyengar R, Geiger B. 2007. Functional atlas of the integrin adhesome. *Nat Cell Biol* 9: 858-67
Zamir E, Geiger B. 2001. Molecular complexity and dynamics of cell-matrix adhesions. *J Cell Sci* 114: 3583-90
Zebisch K, Brandsch M. 2013. Transport of L-proline by the proton-coupled amino acid transporter PAT2 in differentiated 3T3-L1 cells. *Amino Acids* 44: 373-81
Zeltz C, Orgel J, Gullberg D. 2014. Molecular composition and function of integrin-based collagen glues-introducing COLINBRIs. *Biochim Biophys Acta* 1840: 2533-48
Zhang H, Bosch-Marce M, Shimoda LA, Tan YS, Baek JH, et al. 2008. Mitochondrial autophagy is an HIF-1-dependent adaptive metabolic response to hypoxia. *J Biol Chem* 283: 10892-903
Zhang Y, Manning BD. 2015. mTORC1 signaling activates NRF1 to increase cellular proteasome levels. *Cell Cycle* 14: 2011-7
Zhang Y, Nicholatos J, Dreier JR, Ricoult SJ, Widenmaier SB, et al. 2014. Coordinated regulation of protein synthesis and degradation by mTORC1. *Nature* 513: 440-3
Zhao J, Brault JJ, Schild A, Cao P, Sandri M, et al. 2007. FoxO3 coordinately activates protein degradation by the autophagic/lysosomal and proteasomal pathways in atrophying muscle cells. *Cell Metab* 6: 472-83
Zhao J, Zhai B, Gygi SP, Goldberg AL. 2015. mTOR inhibition activates overall protein degradation by the ubiquitin proteasome system as well as by autophagy. *Proc Natl Acad Sci U S A* 112: 15790-7
Zheng L, Zhang W, Zhou Y, Li F, Wei H, Peng J. 2016. Recent Advances in Understanding Amino Acid Sensing Mechanisms that Regulate mTORC1. *International journal of molecular sciences* 17
Zhou C, Ma K, Gao R, Mu C, Chen L, et al. 2017. Regulation of mATG9 trafficking by Src- and ULK1-mediated phosphorylation in basal and starvation-induced autophagy. *Cell Res* 27: 184-201
Zhu X, Ohtsubo M, Bohmer RM, Roberts JM, Assoian RK. 1996. Adhesion-dependent cell cycle progression linked to the expression of cyclin D1, activation of cyclin E-cdk2, and phosphorylation of the retinoblastoma protein. *J Cell Biol* 133: 391-403
Zoncu R, Bar-Peled L, Efeyan A, Wang S, Sancak Y, Sabatini DM. 2011. mTORC1 senses lysosomal amino acids through an inside-out mechanism that requires the vacuolar H(+)-ATPase. *Science* 334: 678-83

Acknowledge

Here I would like to thank everybody who helped me during my Ph.D..

Special thanks to Dr. Siegfried Ussar who accepted me in the lab for the understanding and support no matter on academic or living. I learnt a lot from his thought-provoking guidance and deep academic achievement.

Many thanks to PD Dr. Marcel Scheidleler who would like to be my mentor for his genuine advice and generous help.

Also thanks to Prof. Johannes Becker for his rigorous suggestion and thanks to Prof. Martin Klingenspor who would like to be my second adviser.

I would also thank all the members who provide help for my thesis, especially Andreas Israel for his patient help on experimental technique.

Thanks to the collaboration groups who contribute to mass spectrometry, electron microscope analyses and PAT2 knockout mice generation.

In the past several years, I have experienced a lot from the dark side of this society that I have never met. Thanks to everyone who gave me warmth in that cold summer. Maybe several years later, when I look back this period I could find I also gain something from it. These things may be the shining wealth leading the road, just like the sparkling lakes in Alpes reflecting gorgeous sceneries. The original aspiration should never be changed.

Finally I would thank my family for the constant support and encouragement.